Radiation hydrodynamic models and simulated observations of radiative feedback in star forming regions

Thomas James Haworth

Submitted by Thomas James Haworth to the University of Exeter as a thesis for the degree of Doctor of Philosophy in Physics, October 2013.

I certify that all material in this thesis which is not my own work has been identified and that no material has previously been submitted and approved for the award of a degree by this or any other University.

Signed: .....
Thomas James Haworth

Date: .....

Abstract

This thesis details the development of the radiation transport code TORUS for radiation hydrodynamic applications and its subsequent use in investigating problems regarding radiative feedback. The code couples Monte Carlo photoionization with grid-based hydrodynamics and has the advantage that all of the features available to a dedicated radiation transport code are at its disposal in RHD applications. I discuss the development of the code, including the hydrodynamics scheme, the adaptive mesh refinement (AMR) framework and the coupling of radiation transport with hydrodynamics. Extensive testing of the resulting code is also presented.

The main application involves the study of radiatively driven implosion (RDI), a mechanism where the expanding ionized region about a massive star impacts nearby clumps, potentially triggering star formation. Firstly I investigate the way in which the radiation field is treated, isolating the relative impacts of polychromatic and diffuse field radiation on the evolution of radiation hydrodynamic RDI models. I also produce synthetic SEDs, radio, Hα and forbidden line images of the bright rimmed clouds (BRCs) resulting from the RDI models, on which I perform standard diagnostics that are used by observers to obtain the cloud conditions. I test the accuracy of the diagnostics and show that considering the pressure difference between the neutral cloud and surrounding ionized layer can be used to infer whether or not RDI is occurring. Finally I use more synthetic observations to investigate the accuracy of molecular line diagnostics and the nature of line profiles of BRCs. I show that the previously unexplained lack of dominant blue-asymmetry (a blue-asymmetry is the expected signature of a collapsing cloud) in the line profiles of BRCs can be explained by the shell of material, swept up by the expanding ionized region, that drives into the cloud. The work in this thesis combines to help resolve the difficulties in understanding radiative feedback, which is a non–linear process that happens on small astrophysical timescales, by improving numerical models and the way in which they are compared with observations.

There came such a clear opening of the night sky,
The deep glass of wonders, the dark mind
In unclouded gaze of the abyss
Opened like the expression of a face
I looked into that clarity where all things are
End and beginning, and saw
My destiny there: 'So', I said, 'no other
Was possible ever. This
Is I. The pattern stands so forever.'

What am I? Bound and bounded,
A pattern among the stars, a point in motion
Tracing my way. I am my way: it is I
I travel among the wonders.
Held in that gaze and known
In the eye of the abyss,
'Let it be so', I said,
And my heart laughed with joy
To know the death I must die.

-Night Sky, Kathleen Raine

Contents

List of Figures

List of Tables

Declaration

This thesis contains work published as papers. Chapters 5, 6 and 7 are based on papers that have been published in the Monthly Notices of the Royal Astronomical Society (MNRAS). These are Volume 420, Issue 1, pp. 562-578, Volume 426, Issue 1, pp. 203-217 and Volume 431, Issue 4, pp. 3470-3484 respectively. I am first author on these papers and my co-authors partake supervisory (DMA and TJH) and historical code development (DMA, DAR, TJH) roles. Chapter 3 is a description of some features of the radiation transport and hydrodynamics code TORUS. In that chapter I make it explicitly clear which components were contributed to by myself and which are a necessary summary of contributions from others.

Acknowledgements

Here I try to acknowledge those who provided me with the conditions to make the work of last three years a success.

First, of course, Tim Harries my supervisor. His supervision style gave me the freedom to explore my own ideas (to both fruitful and fruitless ends) with the oversight to guide me towards more realistic or relevant projects whenever I strayed for too long. He has always provided the right feedback and advice (be it regarding science, a paper, my presentation style or future career) to keep me improving and challenging myself. Next, David Acreman, the system administrator of the university of Exeter supercomputer ZEN and unofficial additional supervisor of myself. With no formal requirement to do so, Dave has always been happy to listen to and discuss problems of both a computational and astrophysical nature. I hope that the rightful co-authorship of some of the work that contributes to this thesis and my thanks made his effort worthwhile. Thanks to you both Tim and Dave.

I have also had a lot of support from my family. Over the last three years I have found it particularly helpful, on tougher (or simply duller) days, looking at photos from some of our excursions when I visit. Walks in Hockley woods, strawberry picking and build-a-bear for Anna's birthday are just some examples that make me smile.

I also thank my fiancée Laura Davies. After 4 years apart during undergraduate studies with me in Exeter and Laura in Durham I know that she was not overjoyed that I remained in Exeter a further three years to complete my PhD. She could have easily made this work impossible, but has had the patience and understanding to see me through. Knowing that she is waiting for me to finish has also been an excellent motivational factor. I also wish to thank Laura's family for making me so welcome, housing and feeding me whenever I was able to visit and helping to make this long distance relationship (and by extension the PhD) possible.

The calculations presented in this thesis were performed using the University of Exeter Supercomputer, part of the DiRAC Facility jointly funded by STFC, the Large Facilities Capital Fund of BIS, and the University of Exeter. I was funded by an STFC studentship.

TJH
Exeter, U.K.
28th September 2013

"One must still have chaos in oneself to be able to give birth to a dancing star."

Friedrich Nietzsche, Thus spoke Zarathustra: part I (1883)

1 Introduction

Star formation epitomizes the breadth and complexity of problems studied in astrophysics. From galactic and extragalactic influences to molecular cloud motions, feedback from massive stars to gravitational collapse of protostellar cores through to microphysics. Although a broad picture of star formation has been established, the processes on these different spatial scales (spanning at least 10^{31} orders of magnitude) influence one another, making a complete picture of star formation impossibly difficult to obtain at present. The problem is made even more difficult since the physics required to study these systems is also diverse and interdependent, including quantum mechanics, thermodynamics, hydrodynamics, radiation transport, electromagnetism and gravitation. Therefore the analysis of processes at different scales have been divided into separate fields, which inform one another as they develop. In addition to the problems associated with establishing a global picture of star formation, within each of these sub–fields lies a myriad of unanswered questions. In this Chapter I provide an overview of some key results and unanswered questions regarding star formation. In particular I discuss progress in understanding the effect of feedback from massive stars on the surrounding material and therefore subsequent star formation in star forming regions, which is the subject addressed in this thesis.

1.1 Star Formation

As already mentioned the details of star formation now span many fields in astrophysics, within which are many unanswered questions. At the level of the protostar the mechanism for high mass star formation (Yorke & Sonnhalter 2002; Hoare & Franco 2007; Kuiper et al. 2012) and the link between young protostars, their discs and subsequent planet

formation is still unclear (e.g. Bally et al. 1998; Richling & Yorke 1998; Terquem et al. 2000; Artymowicz 2000; Leinhardt 2008; Bate 2011; Santos-Lima et al. 2013). At the level of the star forming region unknowns include the role of cloud turbulence (e.g. Mac Low & Klessen 2004) and the numerous potential effects of feedback from stars in sculpting the surrounding gas and influencing further star formation (e.g. Bisbas et al. 2011; Dale & Bonnell 2011, 2012a). It is also uncertain as to what extent star formation occurs in a hierarchical nature outside of what are thought to be the main star forming complexes (Bressert et al. 2010). On larger scales still questions include how star formation rates and efficiencies are determined, as well as how the gas that comprises star forming regions gets accumulated (e.g. Dobbs et al. 2012; Miura et al. 2012). Furthermore, there is ongoing research into what extent there is a universal initial mass function (IMF) that describes the distribution of stellar types and, if there is one, what governs it (e.g. Chabrier 2003; Davé 2008; Bate 2009; Bastian et al. 2010). At even larger scales it is not yet fully established what the effect of star formation rates, efficiencies and feedback has on galactic evolution (e.g. Scannapieco et al. 2006; Dobbs et al. 2011; Kim et al. 2013) and the re-ionization of the universe (e.g. Dove et al. 2000).

Clearly there is too much to discuss in one Chapter, in the subsequent discussion of some components of star formation I therefore focus on those features of star formation most relevant to this thesis, namely the processes on the scales of molecular clouds – the sites of star formation.

1.1.1 Star Forming Regions

Naturally in order to form stars one needs material from which to make them. The classic picture of a star forming region is therefore quite unsurprisingly a collection of gas and dust (potential material for star formation) and young stars that have already formed. An example is the Tarantula nebula in the Large Magellanic Cloud (LMC), a composite image of which is given in Figure 1.1, created using Hubble space telescope data and data from the ESO 2.2-meter telescope in La Silla.

Gaseous constituents of star forming regions include low density fully ionized gas (H II regions) that result from the emission of ionizing photons by massive young stars into their surroundings. Neutral gas usually resides externally to H II regions, however isolated collections of dense, neutral gas can also exist interior to the boundary and are observed as dark blobs, so called Bok–globules (Bok & Reilly 1947). Bok–globules are thought to be the detached tips of neutral pillars of material (Gritschneder et al. 2009b, 2010; Tremblin et al. 2012a; Gahm et al. 2013).

H II regions often appear as bubble–like cavities. Some results suggest that the hot ionized region about massive young stars is at higher pressure than the neutral surroundings and therefore expands, sweeping up material at the edge of the ionized region and clearing out a low density bubble (Zavagno et al. 2006; Dale et al. 2007). Alternative theories propose that a low density bubble might have already existed and that the void is subsequently filled by ionizing photons (Dale & Bonnell 2011; Walch et al. 2012).

Figure 1.1: An HST/ESO image of the Tarantula nebula. It consists of a number of young stars, a complex gas distribution including low density bubbles and and bright irradiated material. *Credit: NASA, ESA, D. Lennon and E. Sabbi (ESA/STScI), J. Anderson, S. E. de Mink, R. van der Marel, T. Sohn, and N. Walborn (STScI), N. Bastian (Excellence Cluster, Munich), L. Bedin (INAF, Padua), E. Bressert (ESO), P. Crowther (University of Sheffield), A. de Koter (University of Amsterdam), C. Evans (UKATC/STFC, Edinburgh), A. Herrero (IAC, Tenerife), N. Langer (AifA, Bonn), I. Platais (JHU), and H. Sana (University of Amsterdam)*

Bounding the H II region is a transitional zone known as a photodissociation region (PDR), where the species able to survive move from ionized, to atomic, to molecular gas as the strength of the radiation field is reduced. PDRs are rich, dynamic chemical laboratories that give rise to a range of strong emission features that can be used to infer the constituents of the star forming region (e.g. Nagy et al. 2013). PDRs also provide a useful signature of the interplay between massive stars and their surroundings (e.g. Urquhart et al. 2009), particularly when kinematic information can be yielded from line profiles (e.g. Okada et al. 2012). Many codes have been developed to model PDRs to help interpret observations (Röllig et al. 2007). Treatment of PDRs in numerical models is beyond the scope of this thesis as they are complex and computationally expensive to model and are expected to have only a small effect on the dynamic evolution of star forming regions compared to treatment of the ionized and neutral gas alone.

The neutral gas in star forming regions is primarily molecular hydrogen but also contains atomic hydrogen, helium, metals and other molecular species. Neutral gas is not uniformly distributed around ionized bubbles, being instead clumpy and filamentary (Molinari et al. 2010; Palmeirim et al. 2013; Gomez & Vazquez-Semadeni 2013; Polychroni et al. 2013). Typically neutral gas in star forming regions is at temperatures of around 10-30 K and the ionized gas around $7000 - 10^4$ K. Densities in H II regions are typically of order 10–100 $\mathrm{m_H\,cm^{-3}}$ and in neutral gas are typically of order 10–10^6 $\mathrm{m_H\,cm^{-3}}$.

In addition to atomic and molecular species there is also dust: carbonaceous or silicate grains or polycyclic aromatic hydrocarbons. Dust plays an important role in catalysing the formation of molecular hydrogen. Hydrogen atoms stick to the dust grains and diffuse through them until they react with one another (Vidali et al. 2005). Dust also plays an important role in the evolution of the radiation field, scattering shorter wavelength (bluer) photons more efficiently and giving rise to interstellar reddening. Dust can also absorb (and be dissociated by) ionizing photons. If a source of dust could be replenished within an H II region (e.g. through the destruction of cloudlets) then this could reduce the number of ionizing photons available for photoionizations and thus reduce the extent of the ionized gas (Everett & Churchwell 2010).

Excluding interacting starburst galaxies where star formation occurs in a widespread fashion throughout a galaxy, star forming regions are typically (but not exclusively, for example the Tarantula nebula mentioned previously is in the LMC) found in the arms of spiral galaxies. A classic example is the whirlpool galaxy (M51, Lord & Young 1990; Bik et al. 2003), a Hubble image of which is given in Figure 1.2. The spiral arms of M51 consist of dark dust lanes and bright regions of active star formation. It is thought that either spiral arms are sites of star formation due their higher surface densities (e.g. Casoli & Combes 1982) or possibly that material entering the arms is shocked, dissipating kinetic energy and forming dense molecular clouds that might form stars (Roberts 1969). In the arms material is accumulated in clumps leading to either gravitational contraction of an isolated cloud, or collisions between clouds, that may induce star formation (e.g. Elmegreen 2011a; Duarte-Cabral et al. 2011; Moore et al. 2012; McLeod & Whitworth

Figure 1.2: An HST image of M51. Note the bright spots along the spiral arms which are active sites of star formation. *Credit: NASA and The Hubble Heritage Team (STScI/AURA)*

2013).

Although the bright star forming regions observed in the arms of spiral galaxies are believed to be the main sites of star formation, recent work has suggested that it might occur in a more hierarchical manner that extends away from the main star forming complexes (Bastian et al. 2007; Elmegreen 2008; Bressert et al. 2010). In this paradigm, less extreme but more extensive isolated star formation may account for the formation of a substantial number of observed stars. To what extent this is the case is a subject of ongoing research (Gieles et al. 2012).

1.1.2 The formation of low to intermediate mass stars

There are main two competing theories regarding the mechanism for the formation of stars of mass less than around 4 solar masses: gravitational collapse and competitive accretion (Luhman 2012).

In the gravitational collapse scenario a cloud exceeds the Jeans mass

$$M_J = \frac{\pi}{6} \frac{c_{\rm s}^3}{G^{3/2}\rho^{1/2}} \tag{1.1}$$

where $c_{\rm s}$, ρ and G are the sound speed, density of the gas and gravitational constant respectively. The Jeans mass as given by equation 1.1 is that at which the gravitational

potential energy term dominates the kinetic in the scalar virial theorem with no surface pressure or magnetic fields ($2T + U = 0$ where T and U are the kinetic and potential energies). In practice there will be additional effects to consider such as external pressures, turbulence and support from magnetic fields (McKee & Zweibel 1992; Ballesteros-Paredes 2006).

Once the Jeans mass is exceeded cloud then contracts. If the contraction is isothermal then the sound speed remains constant and, as the density increases, the Jeans mass decreases. Therefore an isothermally contracting cloud may potentially fragment further as the Jeans mass is again exceeded on smaller scales (Shu et al. 1987; Padoan & Nordlund 2002). Generally more massive cores go on to form more massive stars, though some will fragment to form multiple stars. The key point regarding this mechanism is that the mass of the star is determined by the core from which it forms and subsequent accretion does not change the stellar mass much.

Conversely in competitive accretion the protostellar mass changes a lot through accretion from material external to the initial core – usually through filamentary accretion flows (Bonnell et al. 2001; Bate et al. 2003). The larger cores with higher gravitational potential accrete more material, starving smaller cores and keeping their mass low. The lowest mass objects are those which are ejected from the system and so do not accrete. Competitive accretion models have had some success in reproducing the IMF for low mass stars ($M < 4\,\mathrm{M}_\odot$) as well as properties of multiple systems such as multiplicity as a function of the mass of the more massive star and the radial separation distribution of binaries (Bate 2012). More massive stars would have to form through either a longer term or more extreme version of competitive accretion, or through some other scenario such as gravitational collapse.

Both of these mechanisms are sensitive to the turbulent structure of the ISM (McKee & Ostriker 2007). Turbulence can lead to dense condensations, that might undergo gravitational collapse, however it also gives rise to filaments which are a key feature of competitive accretion. Turbulence can also support against the large scale collapse of a cloud if the turbulent energy is comparable to the gravitational energy. Ionizing radiation from more massive stars nearby may also play a role by removing the material surrounding a protostar, restricting its mass (Hester et al. 1996).

1.1.3 From dense core to star

Consider a dense core is formed that will go on to form a single star (though note that further fragmentation may occur as discussed earlier in this section). The process of collapse is governed by the relative strengths of the gravitational potential and thermal support (Larson 1969). Small initial angular motions and conservation of angular momentum causes a collapsing cloud to flatten in to a disc with a denser central region (e.g. Shu et al. 1993; Matsumoto et al. 1997; Bate 2011). If the collapse is adiabatic then the temperature and therefore sound speed increases meaning that Jeans mass increases, preventing further collapse. Energy must therefore be extracted from the cloud in order for it to cool and

continue contracting.

Initially during contraction gravitational potential energy is radiated away from the system until the cloud becomes dense enough to be optically thick to the escaping radiation. At this point the cloud heats up, preventing further collapse until warm dust emission at far infrared wavelengths (to which the cloud is optically thin) facilitates sufficient extraction of energy for gravitational collapse to recommence. Further collapse results in increased temperatures in the inner regions of the core, however collapse continues since energy is used in the photodissociation of molecular hydrogen and subsequent photoionization of atom hydrogen and helium. Convection in the hot core (Palla & Stahler 1991) and photon escape through optically thin regions also provide means of extracting energy.

Once the internal pressure of the central object is sufficiently high to be in hydrostatic equilibrium with the surroundings it is known as a protostar. During the protostellar phase the mass of the protostar continues to increase as material is accreted from the disc (Hartmann 2009). Disc accretion also gives rise to collimated bipolar outflows which are driven perpendicularly to the disc by the star's magnetic field (Burrows et al. 1996; Hartmann 2009). These outflows are useful observational signatures for identifying young stellar objects (YSOs) in star forming regions (e.g. Smith et al. 2004; Ohlendorf et al. 2012).

Eventually the disc is dispersed, likely through viscous accretion and photo–evaporation (Alexander et al. 2006; Williams & Cieza 2011; Owen et al. 2011), and accretion ceases. Thereafter the star is on the pre-main sequence (PMS) and heated by gravitational contraction until the beginning of hydrogen fusion when the star moves on to the main sequence (MS).

1.1.4 The formation of high mass stars

Compared to low to intermediate mass stars the formation mechanism of high mass stars is poorly understood (Hoare & Franco 2007; Zinnecker & Yorke 2007). The main issue is identifying the mechanism whereby the stellar mass can keep increasing despite the star emitting strong radiative flux which will have an associated large radiation pressure that will oppose accretion. From analysis of this pressure Kahn (1974) predicted an upper limit for stars of approximately $40\,M_{\odot}$, however stars have now been discovered with up to hundreds of solar masses (Crowther et al. 2010). It is therefore likely that the mass grows through some kind of disc accretion, which is only subjected to a fraction of the stellar luminosity. This is supported by the fact that young high mass stars have outflows which are believed to be associated with discs (Lada 1985). Example mechanisms could be accretion through the disc mid plane only, with shielding from the outer layers or ultra-high accretion rates that dominate the radiation pressure. Krumholz et al. (2009) propose that the outflows can give rise to Rayleigh–Taylor instabilities, causing material to stream down onto the protostar out of the plane of the disc. Recent work by Kuiper et al. (2012) has shown that this might be a result of using a flux limited diffusion (FLD) treatment of the radiation transport. A more sophisticated hybrid ray tracing–FLD method Owen

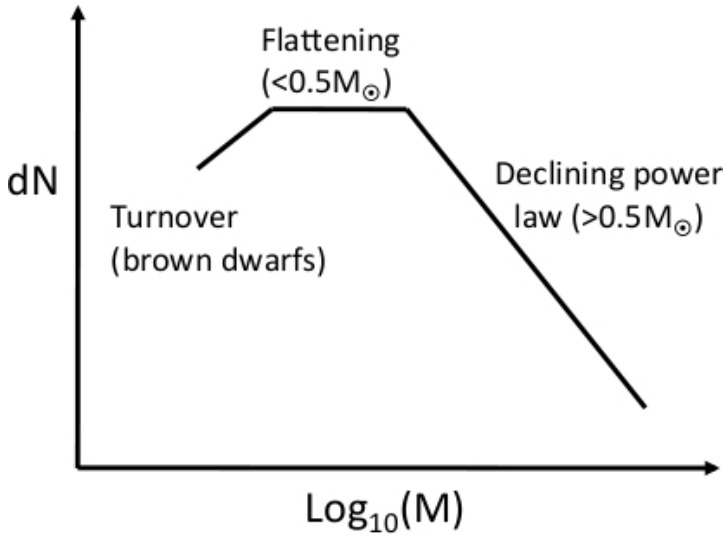

Figure 1.3: A schematic of the IMF. It consists of a declining power law for stars above around $0.5\,M_\odot$. For stars of lower mass there is a flattening and turnover for brown dwarfs.

et al. (2012b); Kuiper & Klessen (2013) blows out full cavities, removing the possibility of material streaming down onto the protostar through Rayleigh–Taylor instability.

Massive stars have a dramatic effect on their surroundings through radiative and kinematic feedback (see section 1.2) and by extension potentially the extent and rate of star formation. A future understanding of where, when (in relation to other stars) and how high mass stars form in star forming regions is therefore going to be critical for establishing a more complete picture of star formation.

1.1.5 The initial mass function

The initial mass function (IMF) is the apparently invariant distribution of stellar masses observed (Bonnell et al. 2007). The distribution consists of a declining power law slope for stars of mass greater than around $0.5\,M_\odot$ (Salpeter 1955) with a flattening for stars of lower mass and a turnover towards brown dwarfs (Kroupa 2002; Chabrier 2003). As an illustration of the form of the IMF, for a declining power law of the type

$$dN \propto m^{-\alpha} dm \tag{1.2}$$

the Salpeter (1955) slope is $\alpha = 2.35$. A schematic of the IMF is given in Figure 1.3. Why the IMF does not vary significantly between different collections of stars (except perhaps towards the galactic center, Paumard et al. 2006) is an active area of research. It could be a natural consequence of the nature of turbulence in the interstellar medium (Padoan et al. 1997; Padoan & Nordlund 2002; Kroupa 2012). Another contender for explaining the universality of the IMF is competitive accretion (Bonnell et al. 2001), whereby stars forming close to one another exhibit preferential accretion on to the higher mass stars, further promoting their growth. In contrast the lower mass stars are starved of material, hindering their mass growth.

Another unanswered question regarding the IMF is at what point in the star forming process is the mass distribution set? It may be that there is a direct correlation between the distribution of cores in a star forming region and the IMF, which has triggered interest in the core mass function (CMF, e.g. Nutter & Ward-Thompson 2007; Goodwin et al. 2008; Chabrier & Hennebelle 2010; Hopkins 2012; Holman et al. 2013).

Understanding the IMF is important for developing a complete theory of star formation. For example, being able to describe the expected number of high mass stars will also yield information regarding the expected level of kinematic and chemical feedback (see section 1.2) on galactic scales. This would allow more realistic parameterizations and sub–grid models to be included in larger scale simulations. The IMF also provides a result that should be reproducible by any model of the star formation processes.

1.1.6 Star formation rate and efficiency

In addition to the IMF there are two other important quantities, the star formation rate and efficiency. The star formation efficiency is the fraction of gas in a region that is converted to stars. The star formation rate is the mass converted into stars per unit time in a given system (usually an isolated star forming region or on a galactic scale). On galactic scales the projected surface star formation rate is related to the gas surface density by the Kennicutt–Schmidt (Schmidt 1959; Kennicutt 1998) law

$$\Sigma_{SFR} \propto (\Sigma_{gas})^n \tag{1.3}$$

where n is typically around 1.4–1.5 (Kennicutt 1998). However this relation does not hold on inhomogeneous smaller scales (i.e. that of a star forming region Onodera et al. 2010). The star surface star formation rate is usually calculated based on the H α luminosity (Kennicutt 1983). Feedback effects may both induce or inhibit star formation, for example by triggering collapse of clouds or dispersing material (e.g. Bisbas et al. 2011; Dale et al. 2007; Dale & Bonnell 2011, 2012a; Walch et al. 2012). This will modify the rate and efficiency with which stars are formed on smaller scales. Relating small scale star formation models to galactic star formation laws is an area of ongoing research (e.g. Bonnell et al. 2013).

1.2 Feedback

Feedback refers to the influence of stars on the surrounding gas in both sculpting the material and inducing or impeding the further formation of stars. This is primarily due to massive (OB) stars which influence the surroundings via strong outflows and winds, the emission of large amounts of ionizing radiation and a supernova explosion at the end of their lifetime. The full cumulative impact and relative importance of these processes on star formation and the evolution of star forming regions is yet to be established and answering this is a key focus of modern research in to star formation. In subsequent

discussion I refer to feedback from stellar winds and supernovae as kinematic (since it is the emission of matter particles from the stellar source that influences the surroundings) and feedback from ionizing photons as radiative.

1.2.1 Stellar Winds

Stellar winds are flows or ejecta of charged or neutral gas from the upper atmosphere of stars. They are prevalent about all massive stars, where the large radiation pressure acts upon atoms through a number of extreme-ultraviolet spectral line absorptions (Conti et al. 2008). This absorption takes place primarily in metals and momentum is transferred to the other constituents of the wind (hydrogen and helium) through collisions. Winds from typical O stars can reach up to around $2000 - 3000\,\mathrm{km\,s^{-1}}$ and can carry a lot of mass ($10^{-6} - 10^{-5}\,\mathrm{M_\odot\,yr^{-1}}$) and momentum away from the star. This not only affects the stellar evolution, but the winds also potentially interact with the material in the vicinity of the star (Castor et al. 1975; Weaver et al. 1977). The wind region initially expands freely, sweeping up material until a sufficiently large amount is present to halt further expansion. The resulting shocked regions then continue to expand, resulting in a bubble wind-region bordered by accumulated material. These bubbles are typically of order tens of parsecs in size, expanding at velocities of order $10\,\mathrm{km\,s^{-1}}$ with a shell thickness around a parsec (Conti et al. 2008). The action of winds and the expanding shell may induce star formation by disrupting stable conglomerations of material, however it may also impede star formation by dispersing material or driving turbulence which supports against collapse. Rather than being emitted spherically, the winds of young massive stars are often in the form of strongly collimated bipolar outflows. It is not presently understood how these bipolar outflows are formed (i.e. whether they are due to magnetic fields or radiation pressure) or what the relative extent of their feedback influence is compared to other mechanisms (e.g. Matzner 2001; Maury et al. 2009; Kuiper et al. 2012).

1.2.2 Supernovae

At the end of the life of a sufficiently massive star ($M > 8M_\odot$) it will explode as a core collapse supernova. The mass-luminosity relation for stars of mass $2\mathrm{M_\odot} < \mathrm{M_*} < 20\mathrm{M_\odot}$ is

$$L_* = M_*^{3.5} \tag{1.4}$$

where L_* and M_* are the stellar luminosity in units of solar luminosity and mass in units of solar mass respectively. Given that the luminosity is the rate of energy emission E/t and the energy radiated away over the stellar lifetime equals the total fraction f of mass converted to energy fM_*c^2, the mass-luminosity relation can be written as

$$\frac{fM_*c^2}{t_*} = M_*^{3.5}. \tag{1.5}$$

Hence the stellar lifetime t_* scales with the -2.5^{th} power of the mass. A star of mass $10\,\mathrm{M}_\odot$ with $f = 1$ will thus have a lifetime of only 9×10^6 years. More massive stars lead even shorter lives.

Given their short lifetimes, stars of mass greater than $8M_\odot$ in star forming regions will likely feed back the 10^{51} erg of energy associated with a type II supernova directly into their star forming region before it has dispersed by some other means. The result of this may be to completely cease star formation in the immediate surroundings, as all material is dispersed, though this may also trigger new waves of star formation in neighbouring gas complexes and even affect the overall distribution of material in a galaxy (e.g. Woltjer 1972; Conti et al. 2008; Hensler 2011; Dobbs et al. 2011; Acreman et al. 2012). Feedback in other forms, such as from stellar winds or ionizing radiation could alter the effectiveness of supernova feedback. For example by opening channels through which energy and material can easily escape, density structures in a star forming region could survive one or more supernovae (Rogers & Pittard 2013).

1.2.3 Radiative Feedback

In contrast to kinematic mechanisms, radiative feedback effects are the result of the radiation emitted by stars into the surrounding material. In the time independent case a star in a uniform density hydrogen-only medium will ionize a spherical 'Strömgren sphere' with radius radius r_s^o given by:

$$r_\mathrm{s}^\mathrm{o} = \left(\frac{3}{4\pi} N_\gamma \frac{1}{n_\mathrm{e} n_\mathrm{p} \alpha^{(2)}} \right)^{\frac{1}{3}} \tag{1.6}$$

Where N_γ is the number of ionizing photons from the source per second, n_e is the electron number density, n_p the proton number density and $\alpha^{(2)}$ is the recombination coefficient into all states except the ground state.

The time-dependent evolution of the ionized region is not so simple. Initially the ionization front propagates rapidly. It can be assumed that the material is ionized as soon as the high energy radiation reaches it and so the front propagates at approximately the speed of light over one mean free path. This phase of ionization front propagation results in little to no significant bulk material motions as the ionization front propagation is much faster than the speed of sound c_s.

In the second phase of evolution, the hot ionized region expands into the surrounding, cool, material as a consequence of the pressure difference between the two regions. Once the ionization front expansion velocity drops below c_s, a shock moves ahead of the ionization front into the neutral material. Spitzer (1998) demonstrates that the ratio of the inwards velocity of material towards the ionizing star through the shock wave u_in to that through the ionization front u_out is given by

$$\frac{u_\mathrm{in}}{u_\mathrm{out}} = \frac{2\rho_\mathrm{I}}{\rho_\mathrm{II}} \frac{V_\mathrm{s}}{V_\mathrm{i}} \tag{1.7}$$

where V_s, V_i are the shock and ionization front velocities respectively and ρ_I, ρ_II are the densities of the ionized (region I) and non-ionized (region II) regions respectively. Assuming that $\rho_\mathrm{I} \approx \rho_\mathrm{II}$, the velocity of material into the shell is always more than double that towards the star through the ionization front, causing material to be swept up in the region between them. It is also important to note that the difference between the ionization front and shock velocities is small until pressure equilibrium is approached, with their fractional difference being given by

$$\frac{V_\mathrm{s} - V_\mathrm{i}}{V_\mathrm{s}} = \left(\frac{\rho_\mathrm{I}}{\rho_\mathrm{II}} - \frac{V_\mathrm{i}}{2V_\mathrm{s}}\right). \tag{1.8}$$

For $\rho_\mathrm{I} \approx \rho_\mathrm{II}$, $V_\mathrm{i}/V_\mathrm{s}$ is almost unity where equation 1.8 applies, i.e. where the pressure difference between the ionized and unionized regions is sufficiently large. The thickness of the shell into which material is swept up is therefore relatively thin. Spitzer (1998) further demonstrates that the analytical radius of an H II region in the phase two expansion at time t is given by

$$r_\mathrm{I} = r_\mathrm{I}^\mathrm{o}\left(1 + \frac{7}{4}\frac{c_\mathrm{I}t}{r_\mathrm{I}^\mathrm{o}}\right)^{4/7} \tag{1.9}$$

up until the radius where pressure equilibrium is approached

$$r_\mathrm{f} = \left(\frac{2T}{T_\mathrm{e}}\right)^2 3r_\mathrm{s}^\mathrm{o} \tag{1.10}$$

where c_I is the speed of sound in the ionized gas and T, T_e are the temperature inside and external to the H II-region. Equation 1.9 is constructed using the thin shell approximation, where the shell is assumed to be infinitesimally thick.

Of the two phases of expansion of the accumulated shell of material in the second phase is the most effective at sculpting the star forming region and potentially inducing or inhibiting star formation. There are two main radiative feedback mechanisms that have been identified; the compression or implosion of pre-existing density inhomogeneities and instability (gravitational or thin shell) in the shell of material that is swept up.

Compression of pre–existing density structures

For the class of radiative feedback in which the radiative shock impacts pre-existing structures there are two main identified mechanisms, radiatively driven implosion (RDI) and radiative round-up. RDI refers to the implosion of large-scale existing density structures to form stars. The radiative shock drives into the cloud and compresses it to the point of gravitational instability. This has been subject to a large amount of theoretical study (Sandford et al. 1982; Bertoldi 1989; Bertoldi & McKee 1990; Lefloch & Lazareff 1994; Kessel-Deynet & Burkert 2003; Miao et al. 2006; Gritschneder et al. 2009a; Henney et al. 2009; Bisbas et al. 2011; Mackey & Lim 2011; Tremblin et al. 2012a). The cloud structure

resulting from RDI in numerical models is bow shaped at early times (or if the cloud is subject to only low ionizing flux) and cometary or pillar–like at late times (or if the cloud is exposed to higher ionizing flux). The resulting elongated or bow–shaped clouds point towards the ionizing sources and the rocket motion resulting from photo–evaporative flows at their surface propels them away from the ionizing source.

Observationally, bright-rimmed clouds (BRCs) are usually assumed to provide evidence for RDI, however this result is only qualitative (Sugitani et al. 1991; Lefloch et al. 1997). BRCs are classified based on their morphology, moving from class A through to B or C as they become more curved or even cometary. Searches for age gradients in the stars associated with BRCs are hoped to offer further support, the idea being that as the BRC is propelled away from the ionizing source, any stars formed within it are left behind. Identifying age gradients is difficult since radiation from the triggering star may disrupt the discs of young stars, making them appear bluer and therefore older than they actually are (e.g. Chauhan et al. 2009; Beltrán et al. 2009; Choudhury et al. 2010; Chauhan et al. 2011b). Alternative approaches to identifying RDI entail analyzing the dynamical state of the cloud to see if it is being compressed (e.g. Thompson et al. 2004; Urquhart et al. 2006; Morgan et al. 2009). Further evidence for RDI is offered in this thesis (see Chapters 5, 6 and 7) and a new means of identifying it based on molecular line profiles is proposed in Chapter 7.

In contrast to affecting a large scale body, radiative round-up applies to smaller scale turbulent systems. Radiation propagates more quickly into low density regions, heating them and causing compression of higher density regions. The result is a number of finger-like objects that resemble observed phenomena known as pillars (or elephant-trunks) that are usually associated with star formation (Gritschneder et al. 2009b, 2010; Ercolano & Gritschneder 2011b; Ercolano et al. 2012; Tremblin et al. 2012a). The problem with confirming whether or not this mechanism is actually responsible for the formation of elephant trunks is that other mechanisms such as thin-shell instabilities also result in similar objects and distinguishing between them observationally is difficult (e.g. Schneps et al. 1980; Carlqvist et al. 2003; Reach et al. 2004; Gahm et al. 2006).

Radiative instability feeback

The expanding shock about an H II-region sweeps up material into a thin shell, as mentioned above in 1.2.3. Once sufficient material has been accumulated the shell will become locally gravitationally unstable and collapse to form stars. This mechanism is known as collect and collapse. Despite being well studied theoretically (e.g. Dale et al. 2007), the search observationally for convincing evidence of collect and collapse is still continuing, with apparently positive findings from, for example, Deharveng et al. (2005) and Zavagno et al. (2006), where massive fragments and YSOs are identified in a ring around a central H II region. Thompson et al. (2012) also find a statistical over density of massive YSOs in at the periphery of bubble H II regions around massive stars, which is suggestive of triggering, but whether the mechanism is collect and collapse or simply distributed RDI

is an open question.

Thin–shell instabilities in the ionization front could also play a role in determining the gas evolution and star formation in star forming regions. The two main mechanisms where this could be the case are Rayleigh-Taylor (Rayleigh 1900; Taylor 1950a) or Vishniac (Vishniac 1983) instabilities. Each give rise to finger-like objects that resemble elephant trunks (as discussed in the previous section on radiative impact feedback) with dense tips at which point stars could form.

1.2.4 Outstanding problems in feedback

In this Chapter I have provided an overview of some key features of star formation and feedback mechanisms. Understanding the link between the two (if any) is a key focus of modern research. Do feedback processes need to be accounted for in order to understand the bulk of star formation, or do they only affect the evolution of a small fraction of the stellar population? I summarise some immediate problems regarding feedback as follows.

1. The relative importance of stellar winds, supernovae and ionizing radiation with regard to modifying the star formation rate, efficiency and IMF is unknown. Furthermore, is the effect of each feedback mechanism the same for both star forming regions and on galactic scales? Research also still also needs to be done in to how the different feedback mechanisms influence one another. For example supernova feedback might be reduced if channels in the gas are developed by winds and ionizing radiation (Rogers & Pittard 2013). Dale et al. (2013) also recently found that feedback from stellar winds is less effective than ionizing radiation.

2. There is a problem comparing theoretical models with observations.

   - For example, in section 1.2.3 I mentioned three mechanisms that give rise to elephant trunk–like objects: RDI, radiative round up and thin–shell instabilities. There needs to be a way of distinguishing between these different mechanisms. A promising method of distinction comes from analysis of the velocity structure over the pillar (Gritschneder et al. 2010).
   - Feedback processes are quick (<1 Myr), nonlinear processes in regions of complex geometry that are only viewed at a snapshot in time and from one viewing angle in observations. It is therefore intrinsically difficult to compare an observation with raw output from a dynamic simulation. Coincidence at a point in time between one or more YSOs and a cloud that is apparently interacting with a nearby massive star is not enough to conclusively prove triggering (Dale & Bonnell 2011).

3. The theoretical understanding of feedback processes comes predominantly from numerical models. Due to the complex nature of the calculations, they have necessarily had to use a number of untested simplifying assumptions. These assumptions include (among others) the treatment of the radiation field, the composition of the gas and

the assumption of photoionization equilibrium. It is necessary to test the impact of such approximations in our models to better understand the effects of feedback and to help close any gap between models and observations.

The first point is the most extensive, spans multiple fields of research and will take substantial time to be fully resolved. The second and third points are problems which I study in this thesis. I approach the problem of comparing models and observations using synthetic observations from the results of radiation hydrodynamic models. This allows for a more rigorous comparison of simulations and observations and may also yield observationally testable predictions that might not otherwise be found. I systematically constrain the effects of assumptions used in numerical models using test calculations.

This thesis concerns the development of the Monte Carlo radiation transport code TORUS to incorporate hydrodynamics for the purpose of radiation hydrodynamic calculations and its subsequent application to problems in radiative feedback. This approach to radiation hydrodynamics has the advantage that many features only usually available to a dedicated radiation transport code can be included, being restricted only by the computational expense of the calculation. This means that I can test a range of radiation transport and microphysics approximations. TORUS can also be used produce synthetic observables from the results of radiation hydrodynamic calculations. This allows for a more rigorous comparison with observations than comparing the raw computational grid, testing of observational techniques and possibly observationally testable predictions that might be used to distinguish between different models of radiative feedback in real systems.

An overview of the key features of TORUS for this thesis and discussion of my contributions to the code is given in Chapter 3. I then describe and present results for a series of benchmark tests of TORUS in Chapter 4. The effects of assumptions regarding the radiation field in numerical models of RDI are addressed in Chapter 5. Specifically I investigate the relative impacts of treating polychromatic and diffuse field radiation (that from recombination events) over a monochromatic radiation field with no diffuse field. This is my first contribution to addressing problem 3 from the list above. In Chapters 6 and 7 I produce synthetic observables from the results of my RDI calculations and use them to test observational diagnostics and look for observational signatures of RDI. This includes simulated spectral energy distributions, atomic line and radio continuum imaging and molecular line data cubes.

By constantly improving the models and the way in which the results are compared with observations the existing disparity between theory and observation of radiative feedback may eventually be resolved. It is my hope that the work in this thesis will be seen as having provided a contribution to this endeavour.

"It is good to have an end to journey towards; but it is the journey that matters, in the end."

Ursula Le Guin, The Left Hand of Darkness (1969)

2

Hydrodynamics and radiative transfer

2.1 Radiation Hydrodynamics I

Radiation hydrodynamics refers to the study of systems in which material motions and the evolution of the radiation field are not independent. The two radiation hydrodynamic extremes are the hydrodynamically–driven limit, where motion causes matter to radiate, and the radiation-driven limit, where radiation induces bulk motion of material. In the former instance, a sufficiently strong shock can cause the material that it is driving into to heat up and radiate. This occurs via collisions between particles in the shock. An example of this effect is the glow that can be seen when a space shuttle re-enters the atmosphere. In the latter case, the radiation field is energetic enough to ionize the gas. This causes an increase in the temperature, and therefore pressure, of the gas. A force will then be exerted on the material proportional to the induced pressure gradient, causing a bulk motion. If the radiation field is strong enough, direct radiation pressure from photons may also affect the flow of material.

In general a first estimate as to the importance of radiation on gas motion in a system is given by the ratio of the material internal energy density to the radiation energy density R, which for an ideal gas at uniform temperature is

$$R = \frac{3k_{\mathrm{B}}}{2a_{\mathrm{R}}}\frac{N}{T^3} \tag{2.1}$$

Where k_{B} is the Boltzmann constant, a_{R} is Stefan's radiation constant, N is number density of the material and T is the temperature. When R is very small, i.e. when temperatures are high and/or densities are low, radiation will be the dominant mechanism and vice versa for hydrodynamic dominance. Star forming regions contain ionized atomic hydrogen regions

(H II regions) that consist of low density, high temperature gas. Radiation hydrodynamic processes in star forming regions are therefore typically in the radiation–driven limit.

Addressing radiation hydrodynamic problems requires consideration of both hydrodynamic and radiative transfer theory. I now outline some of the key concepts regarding these topics in preparation for their discussion in the context of a numerical code in Chapter 3.

2.2 Hydrodynamics

There are two main approaches to analytical hydrodynamics. The Eulerian formulation, which is of greatest importance in this thesis, considers the flow of material through control volumes of fixed dimensions and location in space. In contrast the Lagrangian formulation works in the frame of the flow field, for example tracking the evolution of parcels of material.

2.2.1 The Eulerian Hydrodynamics Equations

The equations of Eulerian hydrodynamics can be derived by the application of conservation laws to the flow of material through a fixed control volume element dV in space. Take, for example, the conservation of mass M. It can be assumed a priori that the only way that the mass in the control volume, given by $M = \int \rho dV$, can vary is if material passes through the surface bounding the control volume dS. That is, no material is spontaneously created or destroyed within dV. Taking the time derivative of the mass in the control volume, and considering the discussion above, results in

$$\int \partial_t M = \int \partial_t \rho dV = -\int \rho \mathbf{u} \cdot d\mathbf{S} \tag{2.2}$$

where the negative sign on the right hand side is chosen so that outflowing material ($\rho \mathbf{u} \cdot d\mathbf{S} > 0$) will lead to a negative time derivative of the mass. Applying the divergence theorem

$$\int \mathbf{A} \cdot d\mathbf{S} = \int \nabla \cdot \mathbf{A} dV \tag{2.3}$$

equation 2.2 becomes

$$\int \partial_t \rho dV = -\int \nabla \cdot (\rho \mathbf{u}) dV. \tag{2.4}$$

Finally, noting that the above relation holds for any choice of control volume, the integrals can be dropped leaving a partial differential equation representing the conservation of mass, usually referred to as the 'continuity equation'

$$\partial_t \rho + \nabla \cdot (\rho \mathbf{u}) = 0. \tag{2.5}$$

It is straightforward to see that the continuity equation is conceptually correct, since if material is converging ($\nabla \cdot (\rho \mathbf{u}) < 0$) the density will increase with time and vice versa for diverging material.

A similar approach can be applied to the conservation of momentum, replacing that quantity varying in time M with the momentum Mu. There is however, an added complication in this instance, since there is an additional effect due to external momentum transfer upon the control volume, i.e. the force exerted by the external pressure P has an influence. An additional term therefore arises that is the integral of the external pressure over the control volume surface

$$\int \partial_t(M\mathbf{u}) = \int \partial_t(\rho\mathbf{u})dV = -\int (\rho\mathbf{u})\mathbf{u}\cdot d\mathbf{S} - \int Pd\mathbf{S}. \tag{2.6}$$

This additional pressure term adds a further complication, since at this stage it is not possible to apply the divergence theorem to equation 2.6 as was done with the continuity equation. This is resolved by introducing the unit tensor $\mathbf{I}$

$$\mathbf{I} = \begin{pmatrix} 1 & 0 & ... & 0 \\ 0 & 1 & ... & 0 \\ \vdots & \vdots & \ddots & \vdots \\ 0 & 0 & ... & 1 \end{pmatrix} \tag{2.7}$$

which puts equation 2.6 in the form

$$\int \partial_t(M\mathbf{u}) = \int \partial_t\rho\mathbf{u}dV = -\int (\rho\mathbf{u})\mathbf{u}\cdot d\mathbf{S} - \int P\mathbf{I}\cdot d\mathbf{S}. \tag{2.8}$$

The divergence theorem and the independence of choice of control volume for equation 2.8 can then be applied in the same manner as for the continuity equation. Further note that $\nabla.\mathbf{I} = \nabla$ (the grad operator), thus the equation for conservation of momentum (equation 2.8) becomes

$$\partial_t\rho\mathbf{u} + \nabla\cdot((\rho\mathbf{u})\mathbf{u}) + \nabla P = 0. \tag{2.9}$$

Equation 2.9 exhibits the expected properties that momentum varies in time as it converges and diverges or is in the presence of a pressure gradient.

Finally, the conservation of energy equation is derived in a similar manner to those for the conservation of mass and momentum. Denote the specific (per unit mass) internal energy e and the specific kinetic energy $u^2/2$. The total specific energy is then

$$e_{tot} = u^2/2 + e \tag{2.10}$$

and the total energy is $\int Me_{tot}$. Using exactly the same procedure as before, taking the time derivative and incorporating a term due to external effects the variation of the total energy is dV is

$$\int \partial_t(Me_{tot}) = \int \partial_t\rho e_{tot}dV = -\int \rho e_{tot}\mathbf{u}\cdot d\mathbf{S} - \int (P\mathbf{u})\cdot d\mathbf{S}. \tag{2.11}$$

This instance is more straightforward than the momentum equation as at this point the divergence theorem can be applied instantly. Doing so and dropping the integrals due to

the independence of control volume choice equation 2.11 becomes

$$\partial_t \rho e_{tot} + \nabla \cdot ((\rho e_{tot} + P)\mathbf{u}) = 0. \tag{2.12}$$

So the energy varies in time in relation to the convergence or divergence of the energy and pressure flux.

Equations 2.5, 2.9 and 2.12 are the Eulerian equations of hydrodynamics. These conservation equations are summarised below

$$\boxed{\begin{aligned} \partial_t \rho + \nabla \cdot (\rho \mathbf{u}) &= 0 \\ \partial_t \rho u + \nabla \cdot ((\rho \mathbf{u})\mathbf{u}) + \nabla P &= 0 \\ \partial_t \rho e_{tot} + \nabla \cdot ((\rho e_{tot} + P)\mathbf{u}) &= 0. \end{aligned}} \tag{2.13}$$

and form the basis of the hydrodynamics scheme developed in TORUS.

There are further layers of complexity that can be added to the right hand sides of these equations, such as artificial viscosity, gravitational, magnetic or radiation source terms, some of which will be considered later in this Chapter. A more detailed discussion of this derivation is given in Dullemond & Johansen (2007).

2.2.2 Viscosity

The equations of hydrodynamics derived briefly in section 2.2.1 apply to material that is considered a bulk fluid. There are many interactions occurring at the sub–fluid level which are therefore not accounted for, in particular the dissipative collisional interactions between particles known as viscosity. Viscosity can play an important part in the evolution of material near shock fronts, providing a non-hydrodynamic source of change in the momentum and energy. This cannot be directly modelled in either an analytical or numerical sense due to the complexity and sub-resolution limit domain over which viscous processes take place respectively. Rather, a viscous term (the coefficient of viscosity, or viscous stress tensor) σ is included in the equations of hydrodynamics which modifies the pressure gradient to give what are known as the Navier-Stokes equations. The momentum equation is modified to

$$\partial_t \rho u + \nabla \cdot ((\rho u)u) + \nabla P = \sigma \tag{2.14}$$

and the energy equation is modified to

$$\partial_t \rho e_{tot} + \nabla \cdot ((\rho e_{tot} + P - \sigma)u) = 0. \tag{2.15}$$

Clearly the role of viscosity is to resist the bulk pressure gradient in the conservation of momentum equation and the convergence and divergence of energy in the conservation of energy equation.

What form does σ take? By comparing the change in momentum of particles travelling across a shock front moving in the $+x$ direction, Zel'Dovich & Raizer (1967) show

that the xx component of the coefficient of viscosity is given by

$$\sigma = \frac{4}{3} nvml(\partial_x u) \tag{2.16}$$

where n, v, m, l and u are the number density, the average thermal velocity, the mass and mean free path of particles that can traverse the shock. σ is thus dependant on the flux of particles through the shock and the alteration to their propagation velocity following their traversal of the shock.

The foundations of Eulerian hydrodynamics have now been introduced, the discussion regarding hydrodynamics is continued in Chapter 3, where the translation from these equations to a numerical algorithm is detailed.

2.3 Atomic and radiative processes

Radiation can influence the hydrodynamic evolution of a system. This primarily occurs via either radiation pressure, whereby the photon momentum is transferred to the gas, or photoionization, which modifies the ionization and temperature structure of the gas. There are also atomic processes which alter the state of the radiation field, for example electronic recombination, in which new photons are emitted when electrons relax into less excited atomic configurations. In this section I summarize some of the key relevant atomic and radiative processes that occur in star forming regions. It is beyond the scope of this thesis to derive each equation, rather the focus is the qualitative behaviour and key features of each process. Including the equations helps to inform this qualitative picture. This discussion is based primarily on Zel'Dovich & Raizer (1967), Osterbrock (1989) and Peraiah (2001).

2.3.1 The equation of radiative transfer

Radiant energy at point r with direction unit vector $\hat{n}$ can be described by the specific intensity $I_\nu(r, \hat{n}, t)$, which is the amount of energy emitted into solid angle $d\Omega$ through surface element da per unit time from radiation of frequency between ν and $\nu + d\nu$, i.e.

$$I_\nu = \frac{dE_\nu}{\cos\theta \, d\nu \, da \, d\Omega \, dt} \tag{2.17}$$

where θ is the angle that $\hat{n}$ makes with the surface da.

The radiation field along a path (a beam or ray) is simply determined by the relative degrees of absorption and emission along the beam. The nature of the processes that contribute to absorption and emission is discussed in more detail in subsequent sections. For now it is suffice to note that the cumulative affect of absorption and emission at specific frequency are characterized by a the specific opacity κ_ν and the specific emissivity j_ν respectively. For radiation propagating a distance ds through a medium of density ρ

the initial intensity I_ν will be attenuated due to absorption by a factor

$$dI_\nu = -\kappa_\nu \rho I_\nu ds = -I_\nu d\tau \tag{2.18}$$

where τ is a dimensionless quantity known as the optical depth. At a given frequency, opaque systems are optically thick whereas transparent systems are optically thin. The quantity $\kappa_\nu \rho$ is represented by the absorption coefficient α_ν.

The contributors to the emissivity relevant to this thesis are continuum emission (which in its most basic form can be considered to be blackbody emission) and line emission from atomic or molecular transitions. For radiation propagating a distance ds through an emitting medium the intensity is increased by a factor

$$dI_\nu = j_\nu ds. \tag{2.19}$$

The ratio of the emission to absorption coefficients is known as the source function $S_\nu = j_\nu/\alpha_\nu$. Generally, along a given path the change in intensity is simply the difference between the increase due to emission and attenuation due to absorption.

$$dI_\nu = -\kappa_\nu \rho I_\nu ds + j_\nu ds. \tag{2.20}$$

The radiative transfer equation is then

$$\frac{dI_\nu}{ds} = -\kappa_\nu \rho I_\nu + j_\nu \tag{2.21}$$

or in terms of optical depth, noting that $d\tau = \alpha_\nu ds$

$$\frac{dI_\nu}{d\tau} = -I_\nu + S_\nu \tag{2.22}$$

where S_ν is the source function defined above as the ratio of emission to absorption coefficients. Equation 2.22 is the analytical basis of problems in radiative transfer. This equation is difficult to solve since the intensity depends on the opacity and emissivity, which in turn can be modified by the radiation field (as discussed in subsequent sections in this Chapter). Analytical solutions are difficult to obtain without a number of assumptions, therefore problems in radiative transfer are typically solved using numerical codes.

2.3.2 Photoionization

Electrons in atoms can occupy a number of energy states, each of which is represented by an integer n (the principle quantum number) and has a corresponding energy relative to the ground state (the lowest level state for the electron in the atom). Through an increase in energy electrons may move into higher energy states. This can occur via collisions with other particles or though the absorption of a photon. In conjunction with spontaneous emission of radiation or further collisions, electrons may also move into lower energy states.

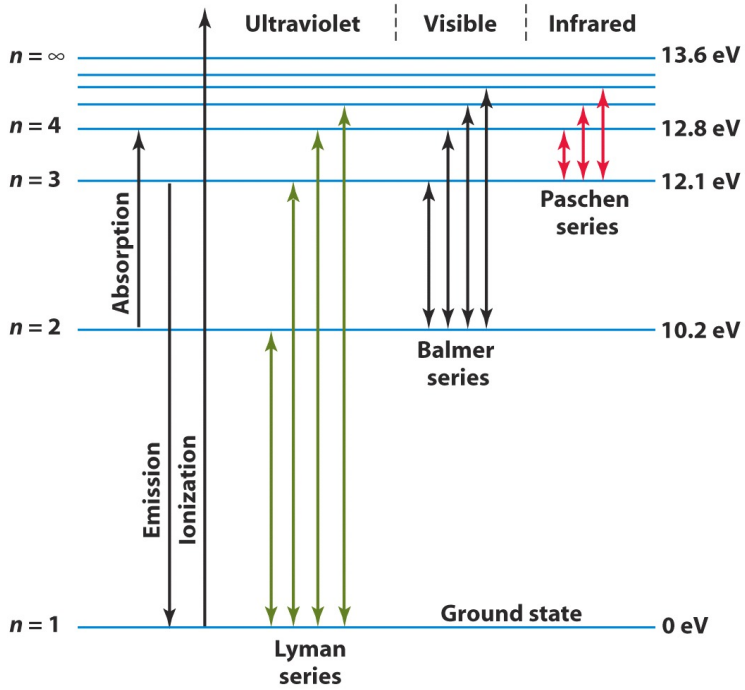

Figure 2.1: A Grotrian diagram of some of the energy levels of atomic hydrogen and the corresponding wavelength range in which photons are emitted following electron transitions between these levels. *credit: Dave Koerner, Northern Arizona University.*

An illustration of these radiative processes (excluding collisional excitation and forbidden line transitions) is given in Figure 2.1, which shows some energy levels of atomic hydrogen and some example transitions. Collections of transitions which involve the same lower energy state are referred to as transition series. For example the collection of transitions in to the ground state of hydrogen are referred to as the Lyman series.

In an extreme case of absorption, bound electrons in atoms can be removed following the atomic interaction with photons of energy greater than the electron binding energy (effectively moving the electron in to $n = \infty$ level). For example, photoionisation of atomic hydrogen will result following the absorption of photons of energy greater than 13.6 eV. This results in a change in the ionization state of the system and the resulting ion and electron increase the kinetic energy of the system by a factor

$$\Delta E_{\mathrm{K}} = h\nu - \phi \tag{2.23}$$

where ϕ, ν and h are the binding energy of the ionized electron, the ionizing photon frequency and the Planck constant respectively. This energy is distributed between the newly formed electron/ion pair.

Some key qualitative features of photoionization can be extracted from the governing analytic equations. The derivations are lengthy and so will not be given here, however for further details see Zel'Dovich & Raizer (1967) section V.1.5 and Osterbrock (1989). The equations describing photoionization are derived assuming the principle of

detailed balance (the balance between a particular process and its reverse process in thermal/photoionization equilibrium). These equations may therefore not be valid if a departure from thermal/photoionization equilibrium occurs. The photoionization rate per unit volume of hydrogen atoms by photons in the frequency range ν to $\nu + d\nu$ is given by

$$R_{\mathrm{p}} = n(H^0) \int_{\nu_0}^{\infty} \frac{4\pi J_\nu}{h\nu} a_{\nu,n}(H^0)\, \mathrm{d}\nu \tag{2.24}$$

where $n(H^0)$, J_ν and $a_{\nu,n}$ are the atomic hydrogen number density, the equilibrium radiation density and the cross section for photoionization of atomic hydrogen with an electron in state n respectively. From Zel'Dovich & Raizer (1967), the photoionization cross section for atomic hydrogen is given by

$$a_{\nu,n} = \frac{64\pi^4}{3\sqrt{3}} \frac{e^{10} m Z^4}{h^6 c \nu^3 n^5} = 7.9 \times 10^{-18} \frac{n}{Z^2} \left(\frac{\nu_n}{\nu}\right)^3 \tag{2.25}$$

where e, Z and ν_n are the electron charge, atomic charge and the minimum frequency required to transition an electron in the nth state to continuum energy levels. The key result from equation 2.25 is that it varies with the inverse cube of the photon frequency and has a maximum at $\nu = \nu_n$. Hard radiation, photons with higher frequency than ν_n, will hence propagate further into a medium before causing photoionization. Furthermore, the photoionization rate (equation 2.24) actually varies in proportion with the inverse fourth power of the frequency and is therefore increasingly small for higher frequencies. This also governs the form of the opacity as a function of frequency. The exact form of the inverse frequency variation of photoionization cross section may deviate slightly for different atoms, e.g. $a_{\nu,n}$ decreases more slowly for nitrogen and more rapidly for sodium than the inverse cube (Zel'Dovich & Raizer 1967).

The mean free path l of a photon before absorption (and therefore potentially photoionization) is determined by the absorption cross section $a_{\nu,n}$ via

$$l = \frac{1}{n(H^0) a_{\nu,n}}. \tag{2.26}$$

The energy gain due to photoionization G of species X_i is given by

$$G(X_i) = n(X_i) \int_{\nu_0}^{\infty} \frac{4\pi J_\nu (\nu - \nu_0)}{\nu} a_{\nu,n}(X_i) d\nu = n_e n(X_i^+) a_{\nu,n}(X_i) \frac{3}{2} kT \tag{2.27}$$

where ν_0 is the minimum frequency required to ionize species X_i and the term $(3/2)kT$ is the mean kinetic energy of electrons freed through photoionization. Note that the rate of energy input depends on the mean intensity and that photoionization events heat the gas.

2.3.3 Recombination

Recombination refers to the process of ionic electron capture, which is accompanied by the emission of a photon of energy equal to the difference between the electron kinetic

energy and its post-capture atomic binding energy. Radiation emitted in association with recombinations contributes to what is known as the diffuse field. The vast majority of recombination events in H II regions result in the formation of atomic hydrogen from a proton and electron. Recombinations directly into the ground state (n = 1) will always result in emission of diffuse field photons with energy greater than the Lyman limit. These photons can further ionize atomic hydrogen. Recombination into states above the ground state will result in the subsequent emission of one or more diffuse field photons as the electron de-excites into the ground state. These photons will have insufficient energy to further ionize atomic hydrogen and unless they photoionize some other species with lower photoionization potential will escape the H II region, extracting energy.

As in section 2.3.2, I present some key equations from, e.g., Zel'Dovich & Raizer (1967) and Osterbrock (1989) which are derived assuming detailed balance. The recombination rate per unit volume for a hydrogen only gas is given by

$$R_{\mathrm{r}} = n_e n_p \alpha(H^0, T) \tag{2.28}$$

where n_e, n_p and $\alpha(H^0, T)$ are the electron density, proton density and recombination coefficient respectively. Note that the recombination rate is dependent upon the existing ionization state (n_e, n_p) of the gas, solving the balance between the recombination and photoionization rates therefore requires an iterative procedure. In thermal equilibrium and therefore under the assumption of detailed balance, the recombination rate of hydrogen is given by the ionization equilibrium equation, which in the notation of Osterbrock (1989) is

$$n\left(H^0\right) \int_{\nu_0}^{\infty} \frac{4\pi J_\nu}{h\nu} a_\nu \left(H^0\right) d\nu = n_e n_p \alpha \left(H^0, T\right). \tag{2.29}$$

This ionization equilibrium equation allows the calculation of the ionization structure of a system in photoionization equilibrium from a knowledge of the radiation field energy density ($4\pi J_\nu / h\nu$). In radiation hydrodynamic calculations photoionization equilibrium can be assumed to be the case for systems where the characteristic recombination timescale t_{rec} is less than the hydrodynamic time step, e.g. for hydrogen

$$t_{\mathrm{rec}} = \frac{1}{n_e \alpha(H^0, T)}, \tag{2.30}$$

(see Chapter 3). Where this is not the case time-dependent approaches to photoionization have been developed numerically (e.g. Perna & Lazzati 2002; Krumholz et al. 2007; Harries 2011). The energy loss $L_{\mathrm{r}}(X_{\mathrm{i}})$ due to recombinations for each species X_{i} is the rate of kinetic energy extraction, or the energy-averaged recombination coefficient

$$L_{\mathrm{r}}(X_{\mathrm{i}}) = n_{\mathrm{e}} n(X_{\mathrm{i}}^{+}) kT \alpha(X_{\mathrm{i}}, T). \tag{2.31}$$

Since the cooling rate due to recombinations is proportional to the number density, contributions to the cooling due to recombination from species heavier than hydrogen and helium are negligible (for example, hydrogen is typically around 5000 times more abundant

than carbon by mass).

2.3.4 Collisional Excitation And Forbidden Line Cooling

Collisional interactions can excite bound electrons into higher energy bound states. In even the best Earth laboratory vacuums, where densities are around 10^5 molecules per cubic centimetre, subsequent collisions would occur sufficiently rapidly to de-excite the electron. In H II regions, where densities are only a few particles per cubic centimetre, collisions occur only on order of $1 - 10^3$ s. In this time the excited atom resides in a so called 'meta-stable' state. In a meta–stable state the excited electron moves through low, but finite, probability transitions that are not allowed by quantum mechanical electric dipole transition rules. Namely that the angular momentum, spin-orbit and magnetic moment quantum numbers L, J and m_j respectively, do not obey the electric dipole selection rules

$$\begin{aligned} \Delta L &= \pm 1 \\ \Delta J &= 0 \\ \Delta m_j &= 0, \pm 1. \end{aligned} \tag{2.32}$$

The collisionally excited electrons do not transition by these routes because there are no accessible states via them. Rather de-excitation occurs via the finite probability magnetic-dipole or electric quadrupole transitions which can have lifetimes of milliseconds to many years as opposed to 10^{-8} s for normal transitions. The details of these additional selection rules are extensive and given in Appendix 3 of Osterbrock (1989). The important point is that these forbidden transitions are between states which differ by only small amounts of energy relative to recombinations and so result in emission of a cascade of low energy diffuse field photons of sufficiently long wavelength that material of the star forming region will be optically thin and most photons will escape without further interaction. This forbidden line cooling is therefore a very efficient way of removing energy from a star forming region, dominating the cooling contribution from recombination despite comprising of order one in 10^7 diffuse field emission events. Forbidden line transitions are denoted by square brackets, for example the famous [O III] 4959Å or 5007Å lines. Observations of these lines were initially attributed to a new, unobserved species that only exists in nebulae (Huggins & Miller 1864), eventually called 'nebulium'. Their eventual explanation, provided by Bowen (1927), was an important contribution to the development of quantum mechanics.

Once again assuming detailed balance, the number of collisonally induced excitations from electrons in a given velocity range is matched by the number of collisional de-excitations that produce electrons in that velocity range. The following equations are taken from Osterbrock (1989). The collisional de-excitation rate per unit volume is given by

$$q_{21} = n_{\rm e} n_2 \left(\frac{2\pi}{kT}\right)^{1/2} \frac{h^2}{m^{3/2}} \frac{\Upsilon(1,2)}{\omega_2} \tag{2.33}$$

where $\Upsilon(1,2)$ is the velocity-averaged collision strength for transitions from a lower level

1 to a higher level 2. This is given by

$$\Upsilon(1,2) = \int_0^\infty \Omega(1,2,E)\mathrm{e}^{-E/kT} d\left(\frac{E}{kT}\right) \tag{2.34}$$

where $\Omega(1,2,E)$ is the energy specific collision strength. The velocity averaged collision strength is derived using the Boltzmann distribution of thermodynamic equilibrium and hence the distribution of electron velocities. The collisional excitation rate is related to the de-excitation rate via

$$q_{12} = \frac{\omega_2}{\omega_1} q_{21} \mathrm{e}^{-h(\nu_2-\nu_1)/kT} \tag{2.35}$$

where ω_i is the statistical weight of level i. As intuitively expected, the collisional de-excitation rate is lower in low temperature, low density gasses. The balance of the excitation and de-excitation rates determine the level of collisional energy loss L_c via

$$L_c = n_e n_1 q_{12} h(\nu_2 - \nu_1) \left[\frac{1}{1 + \frac{n_e q_{21}}{A_{21}}}\right] \tag{2.36}$$

where A_{21} is a spontaneous transition rate coefficient (the Einstein A coefficient) for transitions from level 2 to 1. If collisional de-excitation is low, then forbidden line cooling is strong, however once collisional de-excitation is established it can rapidly dissipate this cooling. Species that undergo collisional excitation (e.g. O^+) have lower abundances than hydrogen and helium, but also have lower excitation potentials. If the electron density is sufficiently low to allow collisional excitation ($< 1000\,\mathrm{cm}^3$, as is the case in H II regions) collisional excitation processes will therefore happen more frequently than photoionization of hydrogen and helium and can dominate the cooling.

2.3.5 Bremsstrahlung radiation

Deceleration of free electrons through electromagnetic interactions results in the emission of free-free or Bremsstrahlung radiation, this typically occurs when a free electron is deflected by an ion. A schematic of the process is given in Figure 2.2. Free-free emission is continuous and contributes only weakly to the cooling in a star forming region. It does, however, typically dominate the emission from H II regions at radio wavelengths which is important for observations (and for the simulated observations that I calculate in Chapter 6). The free-free emissivity is approximately given by, in the notation of Osterbrock (1989),

$$j_{ff} = 1.42 \times 10^{-27} \frac{1}{4\pi} Z^2 T^{1/2} g_{ff} n_e n_+ \,[\mathrm{erg\,cm^{-3}\,s^{-1}}] \tag{2.37}$$

where n_e, n_+ are the number density of electrons and ions respectively, Z is the charge of the ion causing deflection, T is the gas temperature and g_{ff} is the Gaunt factor. The Gaunt factor is a slight modification to classically derived estimates for quantum mechanical processes in continuous emission. For star forming regions the Gaunt factor is typically $1.0 < g_{ff} < 1.5$. The energy loss due to free-free radiation L_{ff} is given by $4\pi j_{ff}$

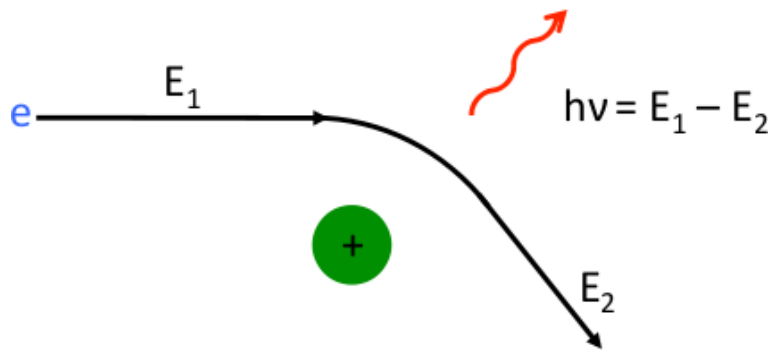

Figure 2.2: A schematic of the Bremsstrahlung emission process. Following an interaction with an ion an electron's path is deflected, causing emission of a photon with energy equal to the difference between the pre (E_1) and post-interaction (E_2) electron energies.

2.3.6 Thermal Equilibrium

The radiative processes summarised in the preceding sections combine to determine the overall ionization and temperature structure of a gas. The resulting thermal balance for a system in equilibrium is that between the energy gain and loss rates

$$G = L_{\rm r} + L_{\rm ff} + L_{\rm c} \tag{2.38}$$

where the loss rates are the sum of values for all recombinations ($L_{\rm r}$), free-free ($L_{\rm ff}$) and collisional ($L_{\rm c}$) processes (see sections 2.3.2, 2.3.3, 2.3.4 and 2.3.5 for a discussion of each term). The heating comes from photoionization. $L_{\rm r}$ is proportional to the product of the electron and ion number density, meaning that it is dominated by hydrogen and helium, the most abundant species. The cooling contribution from free-free processes is typically only minor and comes predominantly from deflection of electrons from hydrogen and helium. In ionized gasses of sufficiently low density for collision de–excitation not to dominate, the cooling is dominated by forbidden line de–excitation from collisionally excited states.

Solving thermal and ionization balance accurately requires an iterative process since both the gain and loss rates depend on the temperature of the system which will change depending on the heating and cooling rate.

2.3.7 Scattering

Scattering of photons by atoms, molecules or (most commonly) dust grains - conglomerations of typically carbonaceous or silicate molecules - alters the propagation direction of the photon. For photon wavelengths much larger than the scattering particle the event is described by Rayleigh scattering, for which the cross section is given by

$$\sigma_R = \frac{2\pi^5}{3}\frac{d^6}{\lambda^4}\left(\frac{n^2-1}{n^2+2}\right)^2 \tag{2.39}$$

where d is the diameter of the scattering particle, λ is the photon wavelength and n is the refractive index of the scattering particle. For wavelengths similar to the particle size one enters the more complicated Mie scattering regime (Mie 1908). Mie theory provides a model for scattering events involving radiation incident on an isotropic sphere in a homogeneous medium. It entails the calculation of a potentially large number of series expansions and so is calculated numerically in practice (see e.g. Barber & Hill 1990).

2.3.8 Radiation pressure

A radiation field imparts a pressure following photon absorption or scattering. Combining the definition of pressure as rate of change of momentum divided by the surface area A over which the force is imparted with the De Broglie momentum expression one gets

$$\mathbf{P} = \frac{1}{A}\frac{d(h/\lambda)}{dt}\hat{u} \tag{2.40}$$

where h is the Planck constant, λ is the photon wavelength and $\hat{u}$ is the unit vector of the pressure force. Given that the photon energy is hc/λ this can be simply re-written as

$$\mathbf{P} = \frac{1}{Ac}\frac{dE}{dt}\hat{u} = (\phi/c)\hat{u}. \tag{2.41}$$

where ϕ is the energy flux through A, E is the photon energy and c is the speed of light. According to these equations higher frequency (energy) photons will impart a larger radiation pressure. The radiation pressure term of equation 2.41 is incorporated into the hydrodynamic momentum and energy conservation equations (equations 2.9 and 2.12 respectively).

2.4 Radiation Hydrodynamics II

In the preceding sections of this Chapter, I have provided an overview of some key concepts in hydrodynamics and radiation transport theory. There are a number of methods available for combining these areas to solve radiation hydrodynamics problems, each of which have their own distinct strengths and weaknesses. In this section I provide an overview of some of the main techniques.

2.4.1 The analytic approach

The analytical equations of radiation hydrodynamics are complex. The basic addition to the equations of hydrodynamics at first glance appear simple, involving an additional radiation pressure term $P_{\rm rad}$ in the momentum conservation equation and a radiant energy flux $F_{\rm rad}$ in the energy conservation equation

$$\begin{aligned} \partial_t \rho u + \nabla \cdot ((\rho u)u + P_{\rm rad}) + \nabla P &= 0 \\ \partial_t \rho e_{tot} + \nabla \cdot ((\rho e_{tot} + P)u + F_{\rm rad}) &= 0. \end{aligned} \tag{2.42}$$

However, the additional terms become extensive in multi-dimensional systems or complex geometries, making analytical solutions to problems difficult to achieve except in the most simple scenarios. Changes to the ionization and temperature structure are also not included in the above equations. A number of analytic approaches have been developed to facilitate some solutions, however the results are limited and discussion of this would have to be extensive and would diverge from the focus of this thesis. Rather, numerical approaches to radiation hydrodynamic problems are both of relevance and, in some ways, more straightforward. The reader interested in the analytical approach is directed towards the texts of Mihalas & Mihalas (1984) and Castor (2004).

2.4.2 Numerical approaches

The alternative approach to analytic methods for solving radiation hydrodynamic problems is numerical calculation. Historically this has entailed incorporating radiative effects into existing hydrodynamic codes. For example, the inclusion of ionizing radiation in the smooth particle hydrodynamics (SPH - a numerical technique based on the Lagrangian formulation of hydrodynamics) codes VINE (Gritschneder et al. 2009a) and SEREN (Bisbas et al. 2009). Generally the inclusion of radiative effects entails interspersing the hydrodynamic time steps with radiative transfer calculations, the results of which modify the conditions and influence the next hydrodynamics step. This separation is known as operator splitting.

The disadvantage of including radiative effects in a hydrodynamics code is that it is very difficult to treat the radiation field without making a number of assumptions compared to static radiative transfer calculations. This is because a thorough treatment is both difficult to implement as an addition to a hydrodynamics code and is computationally expensive. For example, prior to the work in this thesis the majority of codes assumed that ionizing radiation is monochromatic (though polychromatic effects are estimated in Yorke & Sonnhalter 2002; Mellema et al. 2006; Kuiper et al. 2010) and ignored diffuse field radiation under the assumption that it is immediately re-absorbed (the on the spot approximation). Calculations have also only included hydrogen, ignoring the effects of forbidden line cooling. Inclusion of diffuse field effects was attempted for ionization+VINE (iVINE) by comparing photoionization calculations of simulation snapshots with those using the Monte Carlo photoionization code MOCASSIN and paramaterizing the diffuse field effect based on the differences. However, this was shown to be subject to a large degree of error and also gave rise to anomalous heated regions (Ercolano & Gritschneder 2011b).

Typically radiation hydrodynamic calculations have used flux-limited diffusion or ray tracing to model the radiation field. Flux limited diffusion applies in systems where the mean free path of photons is very short or very long and the gradient in specific intensity is small, however can fail to provide an accurate solution in multi-dimensional complex geometries (Turner & Stone 2001). Flux limited diffusion has recently been demonstrated to yield significantly modified results to more thorough treatments of the radiation field, for example Kuiper et al. (2012). Ray tracing does permit higher accuracy solutions

but becomes very slow where multiple ionizing sources are present since the calculation duration scales as the number of sources multiplied by the number of iterations required for convergence (Mellema et al. 2006). An ongoing development and promising alternative to the technique advanced in this thesis is the implementation of hybrid methods that combine both ray tracing and flux limited diffusion techniques (e.g. Kuiper et al. 2012; Owen et al. 2012b; Kuiper & Klessen 2013).

The technique pioneered in this thesis combines Monte Carlo photoionization with hydrodynamics. As with the existing techniques, photoionization and hydrodynamic calculations are performed sequentially using operator splitting. However this new approach has the advantage that all of the features available to a dedicated radiation transport code can be incorporated in the photoionization stage of the calculation. This means that a much more sophisticated treatment of the radiation field can be managed, for example polychromatic radiation, the diffuse field, helium and metals. It also scales well with an arbitrary number of ionizing sources in the calculation and has the additional advantage that the resulting radiation hydrodynamic calculations can also be processed using the same radiative transfer code to produce synthetic observables. The disadvantage, and the reason that this approach has not been attempted to date, is that Monte Carlo radiative transfer (MCRT) is computationally expensive. The solution to this is the excellent scalability of MCRT in parallel computing. The details of the algorithm and the points alluded to above are given in the next Chapter.

"I wish to God these calculations had been executed by steam!"

Charles Babbage (1821)

3

TORUS: Radiation Transport And Hydrodynamics Code

Declaration

This Chapter contains a lot of material that is relevant and necessary for this thesis but that was developed by others. The main hydrodynamics, photoionization and their coupled radiation hydrodynamic algorithms were initially developed by Tim Harries. The octree grid structure was initially implemented by Neil Symington and the self–gravity has been exclusively developed by Tim Harries. I make further note of what I worked on throughout this Chapter, but generally my role was testing and ongoing development of the coupling of photoionization with hydrodynamics. For example resolving the problem of odd–even decoupling, implementing periodic photon packet boundaries and developing the photon packet bundling scheme discussed in this Chapter. I also worked extensively on the parallelization of the photoionization scheme, including MPI, openMP and hybrid parallelization. Furthermore, I developed the existing adaptive mesh refinement grid for hydrodynamics, including checking conservation, implementing flux interpolation, interpolation of quantities to child cells using Shepherd's method, optimising refinement sweeps and updating the grid refinement criteria. In addition I made the photoionization routine more concise and efficient by consolidating the photon packet variables into a photon packet structure. I also extensively tested the code, which is discussed in the next Chapter.

3.1 Introduction

TORUS (Transfer Of Radiation Under Sobolev, or Transfer Of Radiation Using Stokes) is a Monte Carlo radiative transfer code. It was initially designed to perform three dimensional calculations, including treatment of polarization and Mie or Rayleigh scattering. In this form it was used to analyse synthetic spectral line observations of stellar winds that are rotationally distorted by rapid stellar rotation or which contain clumps (Harries 2000). With the addition of dust treatment it was also used to model observations of the Wolf-Rayet (WR) star binary WR137 in a 3D model that departs from spherical symmetry in an effort to provide an explanation for observed polarization variability (Harries et al. 2000). Over the last 13 years it has developed and been applied to models of accretion on to T Tauri stars (Vink et al. 2005; Symington et al. 2005), discs around Herbig AeBe stars (Tannirkulam et al. 2008), Raman-scattered line formation in symbiotic binaries (Harries & Howarth 1997), dust emission and molecular line formation in star forming regions (Kurosawa et al. 2004; Rundle et al. 2010), synthetic galactic HI observations (Acreman et al. 2010a) and has been coupled with an SPH code to perform radiation hydrodynamic calculations (Acreman et al. 2010b). Over the course of these projects the code has evolved into something spread across over a hundred modules and comprising of order 150000 lines of Fortran 2003. The result is a code that is extremely flexible, relies very little on external libraries and can be applied to a vast range of problems.

The next installment in the evolution of TORUS is the transition to a self-contained radiation hydrodynamics code. Developing, debugging and testing this is a major component of the work undertaken in this Thesis. In this rest of this Chapter I detail the radiation hydrodynamics scheme now implemented in TORUS as well as some further essential details relating to the code for applications in this thesis. At the time of writing the radiation hydrodynamics in TORUS is still evolving. The future TORUS developer should therefore exercise caution when comparing the information in this Chapter with what there is in the code.

Using operator splitting, the hydrodynamics and radiation transport in a radiation hydrodynamics calculation can be performed sequentially. This makes for conceptually straightforward approach, as the hydrodynamic and photoionization components of the calculation can be detailed and coded and tested independently before being combined.

3.2 Hydrodynamics

In section 2.2 the basics of analytical Eulerian hydrodynamics were presented. In this section I provide an overview of how this translates into a numerical implementation in TORUS. Note that, unless specified otherwise, this section is based on existing established theory and algorithms. Some key resources in studying both analytical and numerical aspects of hydrodynamics are the highly recommended lecture notes of Dullemond & Johansen (2007) and the books Zel'Dovich & Raizer (1967), Mihalas & Mihalas (1984)

and Castor (2004).

3.2.1 Flux conserving finite volume hydrodynamics

Calculating the solution to hydrodynamics problems using a finitely powerful computational machine requires discretization of the continuous differential hydrodynamics equations of section 2.2.1, since they cannot be infinitely resolved. This is analogous to splitting space on the computational domain into a series of the control volumes mentioned in section 2.2.1.

For simplicity, first consider a one-dimensional domain which is split into a number of cells that have their central coordinates labelled by the index i and are of uniform spacing Δx. A cell consists of a central grid point and a boundary which it shares with the neighbouring grid point. For example, on a grid of fixed spacing the boundaries would be at $\pm\frac{\Delta x}{2}$. An arbitrary quantity (e.g. the density, ρ) in the ith cell at the nth time step is represented by q_i^n. The quantity $q_i^n u_i^n$ is the flux of this quantity through the cell centre, i.e. u_i^n is the velocity at the cell centre. Using this notation, the continuity equation can be written in discrete form, for example

$$\frac{\partial \rho}{\partial t} = -\frac{d(\rho u_x)}{dx} \tag{3.1}$$

could be re-written as

$$\frac{\rho_i^{n+1} - \rho_i^n}{\Delta t} = -\frac{(\rho_{i+1}^n u_{i+1}^n - \rho_{i-1}^n u_{i-1}^n)}{x_{i+1} - x_{i-1}} \tag{3.2}$$

for a step in time Δt.

Each of the Eulerian hydrodynamics equations has one term that is simply the flux gradient. In the case of the continuity equation this is the density flux and for the momentum it is the flux of $q = \rho u$. In the above example the value of q_i^{n+1} is updated using the flux gradient across the $i \pm 1^{\text{th}}$ cells, the so called centered differencing scheme. This method is known to be unstable because the future values at a position in space depend on both the upstream and downstream flow, allowing downstream information to propagate back upstream. A solution to this is upstream differencing, in which the flux f at the upstream cell interface is calculated for each cell

$$f_{i-1/2}^n = q_i^n u_{i-1/2}^n \tag{3.3}$$

where $u_{i-1/2}^n$ is the average of the ith and $i-1^{th}$ cell centre velocities. The flux gradient is then calculated between the $i+1/2$ and $i-1/2$ cell boundaries. A general equation, which can be used to represent the non-pressure terms in the conservation of mass ($q_i^n = \rho_i^n$), momentum ($q_i^n = (\rho u)_i^n$) and energy ($q_i^n = (\rho e)_i^n$) and does not depend on downstream flow, is then

$$q_i^{n+1} = q_i^n - \Delta t \frac{f_{i+1/2}^n - f_{i-1/2}^n}{x_{i+1/2} - x_{i-1/2}}. \tag{3.4}$$

Without further modification, this is known as a donor-cell advection scheme. Note that when formulating this it has been assumed that quantities vary linearly between grid points. Such a scheme is known as piecewise-linear.

The additional pressure corrections for the energy (equation 2.12) and momentum (equation 2.9) conservation are subsequently calculated using similar discrete partial differential equations that consider the pressure gradient. For example, the momentum is updated using

$$(\rho u)_i^{n+1} = (\rho u)_i^{n+1} - \Delta t \frac{P_{i+1/2} - P_{i-1/2}}{x_{i+1/2} - x_{i-1/2}}. \tag{3.5}$$

If implemented properly, the advantage of a technique such as this where fluxes are defined at cell interfaces is that by virtue of considering flow from one cell into another, it guarantees the conservation of the physical quantities being advected - something desirable in any physical model. These equations will be developed into more complex forms throughout this Chapter, but comprise the most basic level of the hydrodynamics scheme in TORUS.

3.2.2 The Courant-Friedichs-Lewy condition

If the time step in a hydrodynamic calculation is too large the result will become unstable (and likely incorrect). This is because the algorithm discussed in the previous section considers only the nearest neighbour cells when performing an advection. So, if the timestep is large enough to send material further than the nearest neighbour cells the algorithm will be erroneous. To resolve this, the time step is limited so that material can never propagate further than one neighbouring cell. The maximum allowed timestep for material moving with velocity u on a grid of spacing Δx, is given by the Courant-Friedichs-Lewy (CFL) condition

$$\Delta t \leq \frac{\Delta x}{u + c_s} \tag{3.6}$$

where c_s is the gas sound speed, the value of which depends on the equation of state of the model. For an isothermal calculation

$$c_s = \sqrt{\frac{P}{\rho}} \tag{3.7}$$

where P and ρ are the gas pressure and density respectively. For an adiabatic equation of state

$$c_s = \gamma(\gamma - 1)e \tag{3.8}$$

where γ is the adiabatic index and e is the specific thermal energy.

Usually only a fraction of this maximum is used. This fraction is known as the CFL constant or CFL parameter. For the hydrodynamic calculations in this thesis the default CFL parameter is 0.3.

3.2.3 Odd-Even Decoupling

In section 3.2.1 it was noted that the pressure terms in the equations of conservation of momentum and energy are treated after the flux advection update (equation 3.4) using equation 3.5. This considers the pressure gradient across the $i+1^{\text{th}}$ cell to the $i-1^{\text{th}}$ cell for each cell i. Importantly, the pressure in i plays no role in this part of the calculation. This can lead to two independent pressure fields that are offset by one cell, an effect termed 'odd-even decoupling', which manifests itself as a 'checkerboard' pattern in models. Odd-even decoupling halves the effective resolution of the model pressure field and lowers its accuracy so needs to be avoided. Interpolating the pressures to get cell interface values, for example

$$\rho u_i^{n+1} = \rho u_i^{n+1} - \frac{\Delta t}{\Delta x}\left(\frac{P_{i+1}^n + P_i^n}{2} - \frac{P_i^n + P_{i-1}^n}{2}\right) \tag{3.9}$$

is insufficient as the contributions from i cancel.

Rhie-Chow interpolation (Rhie & Chow 1983) is a solution to the odd-even decoupling problem, whereby the advecting velocities are modified to properly account for the ambient pressure field. In this scheme the velocity from the pressure gradient in the cells in contact with $i-1/2$ is subtracted from, and the velocity from the next two cells ($i+1$ and $i-2$) is added to, the interface velocity i.e.

$$u_{i-1/2} = \frac{u_i + u_{i-1}}{2} \tag{3.10}$$

becomes

$$u_{i-1/2} = \frac{u_i + u_{i-1}}{2} - \frac{\Delta t}{2\left(\rho_{i-1} + \rho_i\right)}\frac{P_i - P_{i-1}}{\Delta x} + \frac{\Delta t}{2}\left(\frac{1}{\rho_i}\frac{P_{i+1} - P_{i-1}}{2\Delta x} + \frac{1}{\rho_{i-1}}\frac{P_i - P_{i-2}}{2\Delta x}\right) \tag{3.11}$$

where Δx is the size of the ith cell. Equation 3.11 does not modify the actual pressure distribution and removes the possibility of odd-even decoupling. The significant effects of including Rhie-Chow interpolation are demonstrated in Figure 3.1, where comparisons of pre and post Rhie-Chow models of the formation of Kelvin-Helmholtz instabilities are shown (the Kelvin-Helmholtz instability model is detailed in Chapter 4). The checkerboard effect in the upper panel is clearly visible.

3.2.4 Flux limiting

If there is a large gradient in a quantity (i.e. a shock) then a piecewise-linear scheme may cause an overshoot in interpolated quantities and incorrectly estimate the conditions in a region of the grid that is not at the cell centre. This can result in numerically induced oscillations. This is resolved by implementing a flux limiter. The requirements of a flux limiter are that it should remove oscillations near sharp shocks whilst leaving low amplitude physical features unchanged. The flux limiter does this by modifying the assumed slope based on the surrounding cells. In practice, with the inclusion of a flux

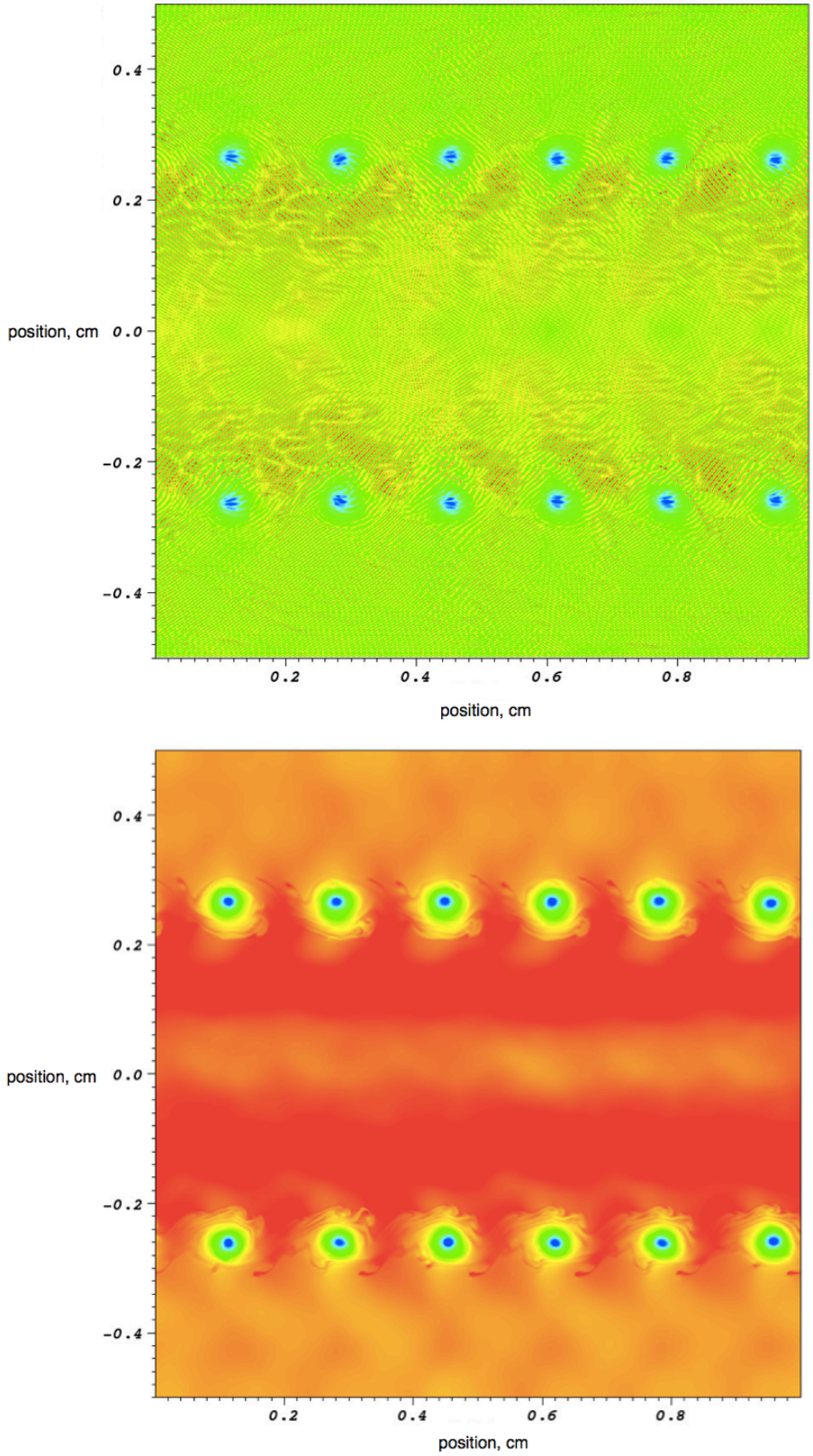

Figure 3.1: A comparison of pre (top) and post (bottom) Rhie–Chow interpolation ρe (density times specific energy) distributions for a Kelvin-Helmholtz instability model. The details of this model are discussed in section 4.2.3, the purpose of this plot is simply to illustrate the checkerboard pattern that arises due to odd–even decoupling in the upper frame and the result of preventing odd–even decoupling using Rhie–Chow interpolation.

limiter the interface flux is modified to include an extra term

$$f^n_{i-1/2} = q^n_i u^n_{i-1/2} + \frac{\Delta t}{2\Delta x}\left| u_{i-1/2}\left(1 - \frac{u_{i-1/2}\Delta t}{\Delta x}\right)\right| (\sigma_i\,(q_i - q_{i-1})) \tag{3.12}$$

where σ_i, the flux limiting function, is one of the many previously developed flux limiting schemes, the default used by TORUS is the 'superbee' (Roe 1985)

$$\sigma_i = \mathbf{MAX}(0.0, \mathbf{MIN}(1.0, r), \mathbf{MIN}(2.0, r)) \tag{3.13}$$

where r is given by

$$r = \begin{cases} \frac{q_{i-1}-q_{i-2}}{q_{i+1}-q_{i-1}} & u_{i-1/2} > 0.0 \\ \frac{q_{i+1}-q_i}{q_{i+1}-q_{i-1}} & u_{i-1/2} < 0.0 \end{cases}. \tag{3.14}$$

Snapshots from a Sod shock tube test model (this model is detailed in Chapter 4) both with (labelled superbee) and without (labelled donorcell) the superbee flux limiter are given in Figure 3.2. It is clear that the calculation that includes the flux limiter yields a much more accurate solution. The slight dip in density near the rarefaction wave at the center of the result arises because the flux limiter is only supposed to remove oscillations near sharp shocks, so as not to dissipate physical structures.

The TORUS hydrodynamics algorithm is also total variation diminishing (TVD). The total variation (TV) for a discrete numerical advection scheme gives a measure of the growth of oscillations in the calculation. At a particular time step on a grid of N cells the TV for a quantity q is given by

$$\mathrm{TV} = \sum_{\mathrm{i}}^{\mathrm{N}} \left|\mathrm{q_{i+1}} - \mathrm{q_i}\right|. \tag{3.15}$$

If local maxima and minima are being developed then the total variation will increase. The algorithm is TVD if it satisfies the relation

$$\mathrm{TV}\left(\mathrm{q}^{\mathrm{n+1}}\right) \leq \mathrm{TV}\left(\mathrm{q}^{\mathrm{n}}\right) \tag{3.16}$$

across time steps. Being TVD means that unphysical oscillations should not arise and with suitable choice of flux limiter oscillations should only be suppressed near sharp shocks.

3.2.5 Pressure and the equation of state

The pressure in a given cell depends on the equation of state of the system. Two commonly used options are an isothermal or adiabatic equation of state. If isothermal, the pressure P is simply given by

$$P = \frac{k_{\mathrm{B}}T}{\mu m_{\mathrm{H}}} \tag{3.17}$$

where k_{B}, T, μ and m_{H} are the Boltzmann constant, temperature, mean particle weight and the hydrogen mass respectively. This isothermal equation of state applies in systems

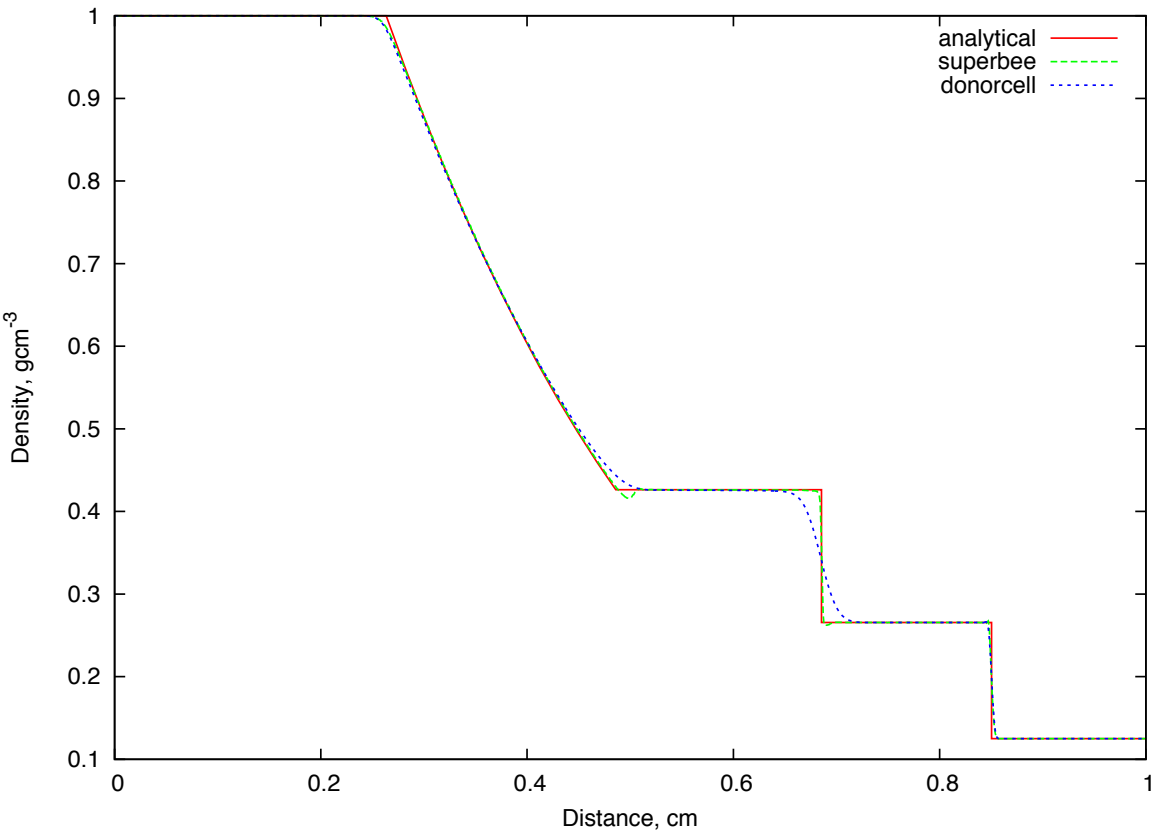

Figure 3.2: A comparison of the analytical Sod shock tube test result and those calculated numerically with the superbee flux limiter (green dashed line) and with no flux limiter (donorcell, blue dotted line). The Sod shock tube test is discussed in more detail in section 4.2.1.

where the temperature is constant in a cell and dominates the pressure. This is used in radiation hydrodynamic calculations in this thesis, with the temperature derived directly from the photoionization calculation.

For an adiabatic equation of state, the pressure in a cell is given by

$$P = (\gamma - 1)\rho(e - \frac{1}{2}u^2) \tag{3.18}$$

where $(e - \frac{1}{2}u^2)$ is the difference between the total and kinetic energy (the thermal energy) and γ is the adiabatic index - the ratio of isobaric to isochoric specific heats. This adiabatic equation of state is used in hydrodynamic-only calculations in this thesis.

3.2.6 Artificial Viscosity

Numerical schemes cannot resolve the viscous processes that occur on smaller scales than grids can feasibly resolve. These dissipative forces are important in shocks, which are discontinuous and therefore not well described by the continuous Eulerian hydrodynamics equations. Without viscosity oscillatory artifacts can appear in the post shock region of the grid, the effects of viscosity therefore need to be paramaterised.

The basic scheme used by TORUS, which is applied to in hydrodynamic models in this thesis, is von Neumann-Richtmeyer artificial viscosity (von Neumann & Richtmyer 1950). Under this, if the advecting velocity at $i - 1$ is greater than that at $i + 1$ then the pressure in cell i is modified based on the momentum flux across the cell

$$P_i = P_i + \Gamma \tag{3.19}$$

where the term Γ is given by

$$\Gamma = \frac{1}{4}\eta^2\rho_i\left(u_{i+1} - u_{i-1}\right)^2 \tag{3.20}$$

and the parameter η is a customisable value for which the default in TORUS is 0.3.

3.2.7 Hydrodynamic Boundary conditions and ghost cells

Grid based hydrodynamics requires a knowledge of the physical conditions in the $i + 1^{\text{th}}$ and, depending on which flux limiter is being used, the $i - 1^{\text{th}}$ and $i - 2^{\text{th}}$ cells. This means that cells near the edge of the computational domain require some dummy, or 'ghost', cells from which they can obtain these quantities. Ghost cells form a layer two cells thick around the outside of a computational domain and the values that they contain depend on the choice of boundary conditions. Some standard boundary conditions are as follows:

1. reflecting: For reflective boundaries the ghost cells mirror the values of their opposite cells and reverse the velocity. This scheme is illustrated in Figure 3.3, where cells labelled by the same letter contain the same values.

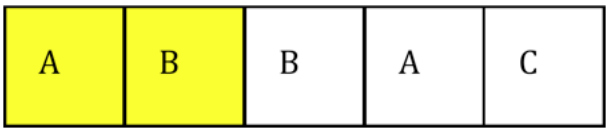

Figure 3.3: A schematic of the ghost cell behaviour at a reflecting boundary. Cells labelled by the same letter share the same values. The ghost cells are highlighted in yellow.

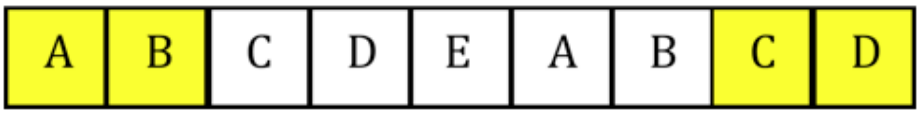

Figure 3.4: A schematic of the ghost cell behaviour at periodic boundaries. Cells labelled by the same letter share the same values. The ghost cells are highlighted in yellow.

2. periodic: For periodic boundaries, the ghost cells at one edge match the values of the cells at the edge of the computational domain on the other side of the grid. Periodic boundaries are used when it is assumed that the system being modelled continues indefinitely in each of the periodic directions, i.e. what exits the right hand side of the grid, enters the left hand side of the grid. This scheme is illustrated in Figure 3.4.

3. free outflow no inflow: Free outflow no inflow boundaries allow material to flow freely off of the computational grid, however no material may re-enter the grid. Ghost cells take on their neighbour values and no velocities are allowed so that no material escapes the ghosts back on to the main computational domain.

4. Inflow: Material streams onto the grid from the inflow boundary in a manner specified dependent on the system being modelled. This condition can be used for co-moving frame calculations.

5. Inflow Gradient: Similar to the inflow condition, only there is a gradient across the boundary for the incoming material. In comoving frame models this is analogous to the system propagating through the surroundings at an arbitrary angle, rather than perpendicularly.

6. Zero gradient: The ghosts both have the same values as the outermost cell of the computational domain, the velocities are not reversed. This allows the inflow of material onto the grid.

3.2.8 The hydrodynamics algorithm

The features discussed in the preceeding sections of this Chapter combine to form the bulk of the hydrodynamics algorithm used by TORUS. In this section I briefly mention how they fit together to do this. For a more detailed discussion see Dullemond & Johansen (2007), on which the most basic level of the hydrodynamics in this thesis is based.

Consider a grid of cells, each of which is populated by values for each advecting quantity (e.g. ρ, ρu, ρe) either from the last time step or via initialized values. At this start point the boundary conditions have also been enforced. For one hydrodynamic time step in a single direction the calculation comprises the following components

1. The duration of the time step is calculated using the CFL condition, equation 3.6.
2. The pressure in each cell is constructed using one of the equations from section 3.2.5, without yet taking in to account artificial viscosity.
3. The interface velocities at $i-1/2$ are constructed for each cell. The $i+1/2$ velocity for cell i is simply the $i-1/2$ velocity of its neighbour $i+1$. Rhie-Chow interpolation is applied at this stage (see section 3.2.3).
4. ρ, $\rho(u, v, w)$ and ρe are all advected using equation 3.4. Their fluxes are constructed using equation 3.12, including the use of a flux limiter.
5. Boundary conditions are imposed using one of the schemes from section 3.2.7.
6. The pressure is re-constructed, this time taking in to account artificial viscosity (see section 3.2.6).
7. ρu and ρe are updated due to pressure effects (e.g. equation 3.5).

The process is repeated until the sum of the time steps taken equals the total simulation time. For multidimensional calculations, e.g. in three dimensions, the convention is followed in which half a time step in the x-direction is performed, followed by full individual time steps in the y and z–directions, followed by another half time step in the x-direction.

3.3 Monte Carlo Photoionization

Photoionization calculations in this thesis use an iterative Monte Carlo photon packet propagating routine, similar to that of Ercolano et al. (2003) and Wood et al. (2004) which in turn are based on the methods presented by Lucy (1999).

Photon packets are collections of photons for which the total energy ϵ remains constant, but the number of photons contained varies for different frequencies ν. These are initiated at stars in the model, with frequencies selected randomly based on the emission spectrum of the star. The constant energy value ϵ for each photon packet is simply the total energy emitted by stars (luminosity L) during the duration Δt of the iteration divided by the total number of photon packets N:

$$\epsilon = \frac{L\Delta t}{N}. \tag{3.21}$$

The initial propagation vector (u, v, w) of a photon packet from an isotropic source is

determined randomly, using:

$$\begin{aligned} w &= 2r_1 - 1 \\ t &= \sqrt{1 - w^2} \\ \theta &= \pi(2r_2 - 1) \\ u &= t\cos(\theta) \\ v &= t\sin(\theta) \end{aligned} \tag{3.22}$$

where r_1 and r_2 are random numbers. The photon packet will then propagate for a path length l determined by a randomly selected optical depth until its next event, which will either involve an interaction with the material after traversing a random optical depth given by

$$\tau = -\ln(1 - r) \tag{3.23}$$

(as detailed in Harries & Howarth 1997) or the crossing of a cell boundary.

If the photon packet fails to escape a cell after travelling τ then its propagation ceases and an absorption event occurs. At this point, there are two possibilities based on the assumed effect of diffuse field radiation. The diffuse field is that of photons emitted following recombination events. The first possibility is the on the spot (OTS) approximation. Under the OTS approximation; diffuse field photons are assumed to contribute negligibly to the global ionization structure following absorption. This is justified in regions of simple geometry, for example where density gradients are small. In MC photoionization once a photon packet is absorbed it is ignored, being assumed to either have been re-emitted with a frequency lower than that required for photoionization, or provide negligible further contribution to the ionization structure by causing further photoionization on only small scales. If the diffuse field is treated then, using the principle of detailed balance, after an absorption event a new photon packet is immediately emitted from the same location with a new isotropically random direction and a new random frequency based on the temperature dependent emission spectrum. This process repeats until the photon packet escapes the grid. In systems with periodic hydrodynamic boundary conditions it may also be desirable to have periodic photon packet boundary conditions so that the material near to the boundaries is not subject to an unrealistic asymmetric ionizing flux. For periodic photon packet boundaries in TORUS each photon packet that has not undergone an absorption event may re-emerge on the opposite site of the grid following escape. In order to avoid long loops for packets of low frequency photons each packet is only allowed to traverse a periodic boundary once, if it does so a second time it is considered to have escaped. For each cell in the grid the sum of the paths $\sum l$ that photon packets traverse is recorded.

Note that the energy density dU of a radiation field is given by

$$dU = \frac{4\pi J_\nu}{c} d\nu \tag{3.24}$$

where c is the speed of light and J_ν is the specific intensity and frequency ν. A photon packet traversing a path l in a particular cell contributes an energy $\epsilon(l/c)/\Delta t$ to the time-averaged energy density of that cell. Thus by summing over all paths l the energy density of a given cell (volume V) can be determined, and the by equation 3.24 the mean intensity may be estimated:

$$\frac{4\pi J_\nu}{c} d\nu = \frac{\epsilon}{c\Delta t}\frac{1}{V}\sum_{d\nu} l. \tag{3.25}$$

This is then used to obtain ionization fractions by solving the ionization balance equation (Osterbrock 1989)

$$\frac{n(X^{i+1})}{n(X^i)} = \frac{1}{\alpha(X^i)n_e}\int_{\nu_1}^{\infty}\frac{4\pi J_\nu a_\nu(X^i)d\nu}{h\nu} \tag{3.26}$$

where $n(X^i)$, $\alpha(X^i)$, $a_\nu(X^i)$, n_e and ν_1 are the number density of the ith ionization state of species X, recombination coefficient, absorption cross section, electron number density and the threshold frequency for ionization of species X^i respectively. In terms of Monte Carlo estimators (equation 3.25), equation 3.26 is given by

$$\frac{n(X^{i+1})}{n(X^i)} = \frac{\epsilon}{\Delta t V\alpha(X^i)n_e}\sum\frac{la_\nu(X^i)}{h\nu} \tag{3.27}$$

This approach has the advantage that photon packets contribute to the estimate of the radiation field without having to undergo absorption events (being only required to cross a cell boundary), thus even very optically thin regions are properly sampled. Photoionization calculations are performed iteratively, doubling the number of photon packets per iteration until the temperature and ionization fractions converge. The hydrogen, helium and C IV recombination rates used by TORUS are calculated based on Verner & Ferland (1996). Other radiative recombination rates are calculated using fits to the results of Nussbaumer & Storey (1983), Pequignot et al. (1991) or Shull & van Steenberg (1982). The photoionization cross sections of all atomic species in this thesis are calculated using the PHFIT2 routine from Verner et al. (1996).

TORUS performs photoionization calculations that incorporate a range of atomic species and in which thermal balance in each cell is calculated by iterating on the temperature until the heating and cooling rates match. Similarly to the photoionization calculation (equation 3.27), the heating rate in a given cell is calculated based on the sum of trajectories of photon packets through the cell. This is used to estimate the heating contributions from photoionization of hydrogen and helium (see section 2.3, Wood et al. 2004) and the heating of dust (section 2.3, Lucy 1999). These three terms sum to give the total heating rate.

The cooling rate is initially calculated for the maximum and minimum allowed temperatures in the calculation (30000 K and 10 K respectively by default in TORUS). This is then refined by bisection until the cooling rate matches the heating rate. The cooling processes considered are that from free–free radiation, hydrogen and helium recombination, dust cooling and collisional excitation of hydrogen and metals (see section 2.3).

In many radiation hydrodynamic calculations to date a simplified thermal balance calculation is used and the only species considered are atomic and ionized hydrogen (e.g. Gritschneder et al. 2009a; Bisbas et al. 2009). For comparison with other codes in RHD applications TORUS can also optionally use this simplified thermal balanced. The temperature is calculated by interpolating between pre-determined temperatures, $T_{\rm n}$ and $T_{\rm io}$, ascribed to the state of fully neutral and fully ionized gas respectively as a function of the newly calculated fraction of ionized atomic hydrogen in the $i^{\rm th}$ cell η_i

$$T_i = T_{\rm n} + \eta_i (T_{\rm io} - T_{\rm n}). \tag{3.28}$$

Typical values to use in this simplified thermal balance calculation are $T_{\rm n} = 10\,{\rm K}$ and $T_{\rm io} = 10000\,{\rm K}$ (the defaults in TORUS).

3.3.1 Pros and cons of the Monte Carlo method

Monte Carlo radiative transfer has some significant advantages over alternative methods. It naturally translates to multidimensional problems with complex geometries. It is also comparatively straightforward to modify and add additional physical processes to (e.g. the diffuse radiation field). These practical reasons aside it is also conceptually appealing compared to other methods, mirroring the actual physical process of photons traversing the system. Its primary weakness, however, is that it is computationally expensive and can experience noise related issues which can make a converged solution difficult to achieve. To resolve this a number of optimization and variance reduction techniques are employed, detailed in section 3.6.

3.4 Self Gravity

3.4.1 The Gas Field

The effect of gravity in astrophysical systems is of course important. In a star forming region it is responsible for the global collapse of clouds and the further contraction of denser regions to form stars. Self gravity of the gas field is included in TORUS by solving Poisson's equation

$$\nabla^2 \phi = 4\pi G \rho \tag{3.29}$$

where ϕ and ρ are the gravitational potential and matter density respectively.

Poisson's equation is solved by iterative calculation of a linearized form of equation 3.29 (a linear approximation of the function) using a multigrid Gauss-Seidel method. The multigrid approach can decrease the convergence time for the self gravity calculation since the number of iterations for convergence on a raw grid is proportional to the number of cells. By starting with very few cells and re-applying the coarse converged solution to the next level of refinement progressively a converged solution at the finest level of the grid can be more rapidly calculated. Firstly the gravitational potential is updated at the coarsest

computed level of the grid, which is always at least the fourth level of refinement, this continues until the maximum level (the details of the grid are given in section 3.7). For each level the update is a two stage process. In three dimensions, the first stage updates take the form

$$\phi_{i,gas}^{n+1} = \phi_{i,gas}^{n} + S_f \left(\frac{1}{6} \left(\sum_{k=1}^{6} \frac{d\phi_{k-i,gas}}{dx_{k-i}} - 4\pi G \rho_i^n \right) - \phi_{i,gas}^{n} \right) \tag{3.30}$$

for each of the k neighbours sharing cell faces with the cell at i. The above correction is iterated over at each level until the fractional change is within some tolerance, for which TORUS uses 10^{-4}. S_f is a customizable factor that determines the impact of each corrective iteration called 'successive over-relaxation', the value for which adopted by TORUS is 1.2.

Once equation 3.30 is applied at each level the second order term of the gravitational potential update occurs at the finest level only. This uses the potential gradient between the updating cell and its neighbours

$$\phi_{i,gas}^{n+1,'} = \phi_{i,gas}^{n+1} + (1 - S_f)\phi_{i,gas}^{n} + S_f \left(\phi_{i,gas}^{n} + \left(\Delta T \sum_{k=1}^{6} \frac{d^2\phi_{k-i,gas}}{dx_{k-i}^2} - 4\pi G \rho_i^n \Delta T \right) \right) \tag{3.31}$$

This second order correction is again iterated over until the fractional change across all cells is less than 1×10^{-4}.

Dirichlet boundary conditions are imposed at the start of each depth of the Gauss-Seidel iterations of equation 3.30. They are also applied following the final sweep of equation 3.30 before moving to solving equation 3.31. With Dirichlet boundary conditions the solution for the gravitational potential interior to the boundaries must match a previously calculated solution at the boundaries. This boundary solution is calculated using a multipole expansion with Legendre polynomials of the matter interior to the boundary. Multipole expansions are used to represent angularly varying functions. When employing Dirichlet boundary conditions TORUS includes multipole expansion terms up to the quadrupole.

3.4.2 Contribution To Dynamics

The gravitational potential is included as a source term in the hydrodynamical equations in a similar way to the pressure field contribution discussed in section 3.2.1. For example modifying the momentum to

$$\rho u_i^n = \rho u_i^n - \frac{\Delta t}{2\Delta x} \left(\phi_{i+1}^n - \phi_{i-1}^n \right). \tag{3.32}$$

Note that the same update is applied to ρe.

3.5 Radiation Hydrodynamics

The hydrodynamics and photoionization schemes outlined in sections 3.2 and 3.3 are combined using operator splitting to perform radiation hydrodynamics calculations. A photoionization calculation is initially run to convergence, this generally allows subsequent calculations to run relatively quickly given that they are usually minor perturbations of the previous state. We then perform photoionization and hydrodynamics steps sequentially. In TORUS, the photoionization calculation for a time step is always calculated prior to the hydrodynamics calculation. The hydrodynamics algorithm does not remain completely unchanged in radiation hydrodynamic calculations, advecting the ionization and dust fractions as well as the usual hydrodynamic quantities.

This operator splitting technique is flexible and relatively conceptually straightforward. It is however very computationally expensive, requiring a large number of Monte-Carlo photoionization calculations that render the gravitational and hydrodynamic components of the calculation negligible in comparative computational cost. Fortunately the propagation of photon each photon packet in an iteration is independent, MCRT can therefore be efficiently parallelized.

3.6 Optimization and Parallelization

3.6.1 Domain decomposition

TORUS uses Message Passing Interface (MPI) to decompose the computational grid into n subsets which are each managed by individual processors (threads). N = n + 1 threads are required in total, with the zeroth ($n = 0$) master thread performing governing and collating operations. Each dimension of the domain is split into halves or quarters, i.e. a two dimensional model can be split across 4 or 16 threads with N = 5 or 17, whereas a three dimensional model can be split into cubes across 8 or 64 threads with N = 9 or 65. This type of parallelization is called 'distributed memory'; each thread has its own memory and performs calculations independently of the rest of the grid. Threads communicate with one another where necessary and collate results. An illustration of domain decomposition of a two dimensional model is given in Figure 3.5 where the domains are distinguished by different colours. Domain decomposition can help to alleviate problems with memory intensive calculations and, assuming the communications between threads are not too extensive, provide a reduction in computation time.

3.6.2 Photon Packet Bundling

The domain decomposed photoionization routine initially comprised each thread propagating one photon packet at a time and communicating that packet to the appropriate neighbouring thread once a domain boundary is crossed. This involved threads doing nothing while waiting to receive photon packets, and a large number of inter-thread communications. The associated large communication overhead can dramatically increase

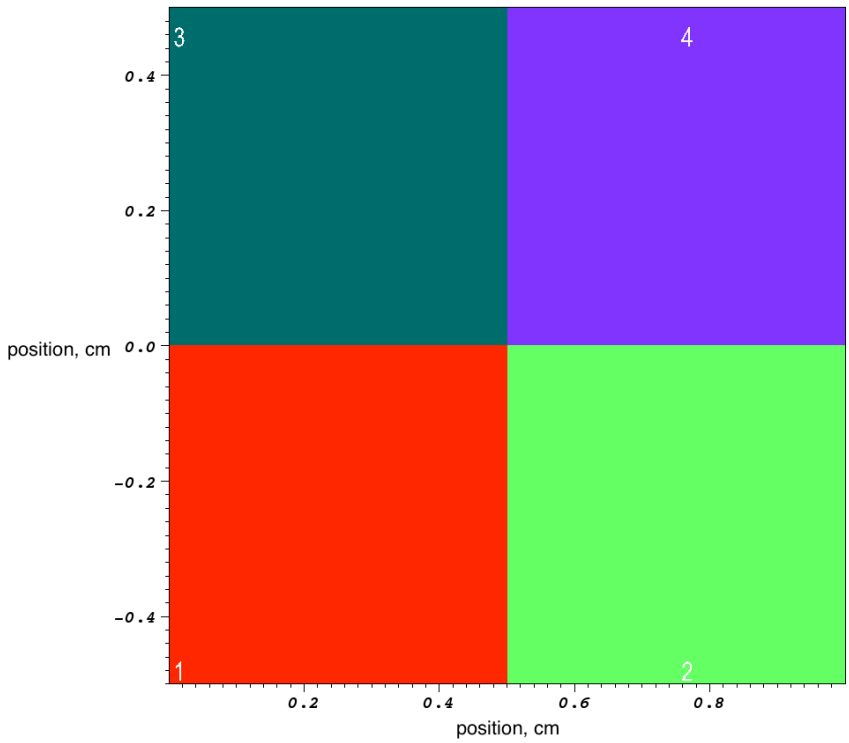

Figure 3.5: An illustration of a two by two domain decomposition of a two dimensional grid. The MPI thread numbers are included in each colored domain box.

computation time. I implemented a modification in which photon packets are communicated in stacks to decrease the communication overhead and therefore computation time. The new scheme proceeds as follows.

The zeroth thread initiates photon packets, selecting which photon source they are initiated from, an appropriate set of packet properties (e.g. frequency, position, direction...) and which thread the photon packet will need to be sent to (the thread that hosts the photon source). It then adds the newly created packets to a stack until the number destined for any one thread matches a predefined stack limit, the default for which in TORUS is 200. The photon stack is then communicated to the appropriate thread, which begins propagating photons from the stack. Now when a photon packet crosses an MPI thread boundary the domain threads do not wait for one another, but rather add the photon packet to their own "to send" stacks. They can then proceed to propagate the next packet in their own "to propagate" stack. Once a domain stack has a "to send" stack of size equal to the stack limit it will communicate it to the appropriate thread. Likewise, once a domain thread has a zero sized stack, it will await the next one. In order to avoid deadlocks between threads, where two are trying to send stacks to one another with neither trying to receive, the domain threads communicate stacks using buffered sends. Under this, the stack is sent to a temporary buffer until it is ready to be received.

The final aspect of the new scheme is treatment of the point at which the number of photon packets that remain to be propagated is less than the stack size limit. Without a special case when reaching this point, packets on a given thread would otherwise never leave. To avoid hanging, the zeroth thread stops waiting for the "to send" stack size to reach the limit for any one receive thread and just sends whatever is already accumulated once it establishes that the following condition has been met

$$N_{\gamma,\mathrm{tot}} - N_{\gamma,\mathrm{sent}} < \zeta N \tag{3.33}$$

where $N_{\gamma,\mathrm{tot}}$, $N_{\gamma,\mathrm{sent}}$, ζ, and N are the total number of photon packets to be used in the iteration, the number of photon packets sent to the domain threads so far, the stack limit and the number of threads respectively. Once all photon packets are distributed by the zeroth thread, it then tells each domain thread to start "panic sending". In the panic send phase, all domain threads send whatever they have in their to send stack to the appropriate threads and will eventually communicate photon packets one at a time. It should be noted that this panic time usually comprises only a small part of the photoionization calculation.

In order to efficiently implement this and make the whole photoionization module simpler and easier to read I created a photon packet data type that contains all of the appropriate properties of the packet:

```
type PHOTONPACKET
    type(VECTOR) :: rVec
    type(VECTOR) :: uHat
    real(double) :: Freq
```

```
    real(double) :: tPhot
    real(double) :: ppw
    integer :: destination
    logical :: sourcePhoton
    logical :: crossedPeriodic
end type PHOTONPACKET
```

where `rVec`, `uHat`, `freq`, `tPhot`, `ppw`, `destination`, `sourcePhoton` and `crossedPeriodic` are the packet position, propagation direction, frequency, propagation time, weight, MPI thread destination (when a boundary has been crossed), an indicator as to whether or not the photon packet is diffuse and an indicator as to whether or not the packet has crossed a periodic boundary respectively. This is particularly useful when sending the packets between threads as each quantity related to the photon packet can be sent in one go using the custom data type rather than being sent individually (e.g. as doubles, logicals and integers). I constructed a custom MPI data type to facilitate communication of the photon packet types following Gibson (2009). A standard MPI send/receive operation between two threads would comprise one thread executing a command such as

```
call MPI_SEND(thingToSend, 1, MPI_LOGICAL, destinationThread, tag, &
Communicator,  ierr)
```

and the other executing the command

```
call MPI_RECV(thingToReceive, 1, MPI_LOGICAL, sendingThread, tag, &
Communicator, status, ierr).
```

Following this exchange the thread `destinationThread` will populate the `thingToReceive` variable with `sendingThread`'s `thingToSend` value. The `MPI_LOGICAL` refers to the data type of the information being sent, in this case a logical. It could however also be an integer, real, double precision or character. For photon packets, a send/receive pair could be required for each of the photon packet attributes. By specifying custom MPI data types an entire photon packet can be sent at once. Firstly a custom MPI data type for the vector custom type is created using

```
    call MPI_TYPE_CONTIGUOUS(3, MPI_DOUBLE_PRECISION, MPI_VECTOR, ierr)
    call MPI_TYPE_COMMIT(MPI_VECTOR, ierr).
```

This sets up a new data type `MPI_VECTOR` consisting of three regular `MPI_DOUBLE_PRECISION` MPI types. The photon packet stack type is more difficult as it contains components of different data types, including logicals, doubles, vectors and an integer

```
    !MPI datatype for the photon_stack data type
    oldTypes = (/ MPI_VECTOR, MPI_VECTOR, MPI_DOUBLE_PRECISION, &
         MPI_DOUBLE_PRECISION, MPI_DOUBLE_PRECISION, &
         MPI_INTEGER, MPI_LOGICAL, MPI_LOGICAL/)
```

```
call MPI_GET_ADDRESS(toSendStack(1)%rVec, displacement(1), ierr)
call MPI_GET_ADDRESS(toSendStack(1)%uHat, displacement(2), ierr)
call MPI_GET_ADDRESS(toSendStack(1)%freq, displacement(3), ierr)
call MPI_GET_ADDRESS(toSendStack(1)%tPhot, displacement(4), ierr)
call MPI_GET_ADDRESS(toSendStack(1)%ppw, displacement(5), ierr)
call MPI_GET_ADDRESS(toSendStack(1)%destination, displacement(6), ierr)
call MPI_GET_ADDRESS(toSendStack(1)%sourcePhoton, displacement(7), ierr)
call MPI_GET_ADDRESS(toSendStack(1)%crossedPeriodic, displacement(8), ierr)

do iDisp = 8, 1, -1
   displacement(iDisp) = displacement(iDisp) - displacement(1)
end do

call MPI_TYPE_CREATE_STRUCT(count, blockLengths, displacement, &
      oldTypes, MPI_PHOTON_STACK, ierr )
call MPI_TYPE_COMMIT(MPI_PHOTON_STACK, ierr).
```

This block of code sets up the memory structure for the new `MPI_PHOTON_STACK` type, which is basically a sequence of the individual types interspaced with buffering memory blocks.

The stack size limit affects the speed at which the model runs. If it is too small, the number of communications between MPI threads will slow down the calculation, whereas if it is too big there will be a significant delay between stack sendings and the domain threads will not be used efficiently, also slowing down the calculation. The optimum stack size will also depend on the number of photon packets that will be propagated in the photoionization calculation in total. In addition, the level of domain decomposition will also have an influence on the optimum stack size.

A number of single iterations runs with varying stack limit, decomposition level and photon packet number were executed to derive the optimum default stack size of 200 photon packets. A more effective use of this bundling would be to keep track of the efficiency with which the photon packets are propagating whilst varying the stack size to hone in on an optimum value. Given that the number of photon packets may vary between photoionization iterations the average time per photon packet t_{ppp} is used as comparison, i.e. if the time for the iteration is t_{photo} and the total number of photon packets is N_{monte}

$$t_{\mathrm{ppp}} = \frac{t_{\mathrm{photo}}}{N_{\mathrm{monte}}}. \tag{3.34}$$

If the latest iteration took, on average, longer per photon packet then it is possibly using a less efficient photon packet stack size and should change it. The user can specify the initial guess for the stack size and the default increment/decrement over which the stack

size should change `dStack`. If the optimization procedure is currently following a particular line of improvement but then reduces in efficiency then it needs to turn back and head towards the last, better timing. In order to facilitate this, the update size and direction are modified depending on the outcome of the average time comparison.

3.6.3 Multiple grid copies

Tim Harries implemented a parallelization option in which multiple copies of the domain decomposed MPI grid are used. In a photoionization calculation the total number of photon packets is divided among the grid copies. Each copy performs photon packet transports in isolation and then the resulting path lengths through each cell are collated once the propagation of all packets is completed. This permits more flexible resource usage and very efficient scaling in computation time with grid copies. Doubling the number of grid copies effectively halves the photoionization calculation wall time. Such efficient scaling of the most computationally expensive part of the calculation justifies massive levels of parallelization which, depending on the model, can result in the photoionization step no longer being the limiting factor (i.e. it is comparable to the duration of a hydrodynamics step).

3.6.4 openMP and Hybrid parallelization

In addition to MPI parallelization that uses domain decomposition and multiple grid copies, TORUS has also been developed to include shared memory parallelization using openMP. In the shared memory scheme the photon packets on each domain are propagated in parallel.

The shared and distributed parallelizations can also be coupled in a hybrid scheme. In hybrid parallelization the first thread (or some fraction of the threads) on each computational node is assigned a distributed memory role (i.e. is a domain decomposing thread). The other threads on each node are shared memory. openMP and hybrid parallelization is found not to scale as efficiently as using multiple grid copies (at least for calculations up to around 500 cores), but offers an extra degree of flexibility that might justify more massively parallel calculations when using multiple grid copies becomes less efficient.

3.7 Adaptive mesh refinement

Modelling of any system will require using a sufficiently high level of resolution to capture all of the (realistically capturable, c.f. viscosity) important processes. To some extent this can be achieved for a grid based code by using finer and finer grids across the entire of the computational domain, this does however become rapidly very computationally expensive, being both slow and requiring a lot of memory. An alternative is that of adaptive mesh refinement (AMR) under which portions of the grid that are automatically determined to require higher resolution are refined and those which are determined to be acceptably described using lower resolution are unrefined (coarsened). This is achieved by varying

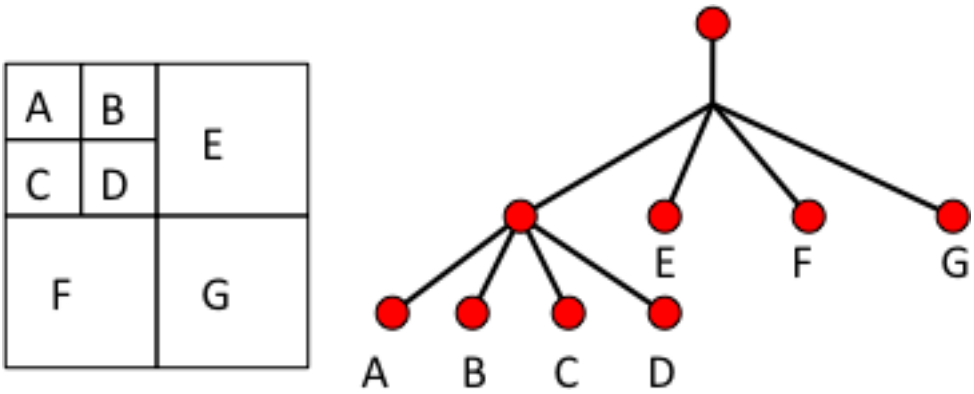

Figure 3.6: An illustration of the AMR grid quadtree structure for a two dimensional grid. The tree nodes are marked on the tree in red and each cell corresponds to a node on the tree without children.

the depth of the tree data structure that makes up the grid on a branch-to-branch basis in a similar manner to Teyssier (2002), as opposed to using an unstructured grid (Löhner 1987) or block-structured AMR (Fryxell et al. 2000).

TORUS stores the computational grid in an octree, a tree in which each node has eight branches to child nodes (cells) that will either be occupied by an active cell or null. Navigation through the grid is then achieved by moving recursively through the octree. An illustration of the tree for a two dimensional adaptive grid, in which the it is a quadtree, is given in Figure 3.6.

A refinement event involves an octree node that has no children forming a number of children appropriate to the dimensionality of the problem. For example, in three dimensions a cubic cell will split into 8 cubic children and in two dimensions a square cell will split into 4 square children. The child cells inherit the parent cell's values, which are distributed among the children using an interpolation based on the values in surrounding cells. This is covered in more detail in section 3.7.1.

A coarsening event comprises the merging of a number of children appropriate to the dimensionality of the problem (as above) into a single parent cell. This is equivalent to nullifying the child cells at the bottom of this component of the octree, renewing their parent. For a coarsening event the parent cell inherits the averages of its children's values. An illustration of refinement and coarsening steps is given in Figure 3.7. The condition that no newly-refined set of children can be re-coarsened until the next hydrodynamic step is completed is imposed to ensure that a refined cell is not immediately re-coarsened.

In the refinement phase of the calculation, one or more MPI threads will go into a checking/refining state and the others will go into a serving state. Those that are checking/refining traverse the grid cells on their domain checking for cells that need to be refined using any specified criterion given in sections 3.7.2 and 3.7.3.

The condition that no two neighbouring cells differ by more than one level of refinement is also imposed. As well as making the code more straightforward, this constraint also reduces sporadic effects due to large jumps in refinement (Teyssier 2002). For the

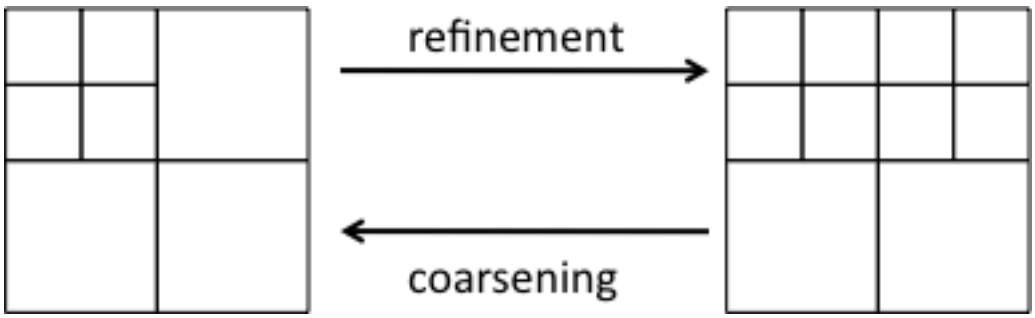

Figure 3.7: An illustration of refinement and coarsening on an adaptive grid. Refinement leads to the replacement of large cells by multiple higher resolution cells whereas coarsening results in the replacement of multiple high resolution cells by larger cells.

cells at domain boundaries the values of cells on other domains will be required, these are obtained by sending a request to the appropriate serving thread which will then return the values. This will be covered in more detail in section 3.7.1.

3.7.1 Adding new child cells with interpolation

When refining a 'parent' cell into a collection of 'children' each quantity within the parent needs to be distributed among the new children. As well as satisfying conservation laws, the way in which the quantities are distributed should reflect the ambient surroundings rather than just being split evenly across the new cells. This requires some sampling and interpolation of the surrounding values. Initially this was done by moving to each corner of the parent cell and probing each of the cells in contact with that corner (including the parent) for values. Averaging the corner values for each quantity then provides a measure for how the parent quantities should be split among the children. This corner scheme, however, exhibits grid noise as the probing does not take into account the relative distances to the cells used in the averaging, thus a coarse low density cell at a diagonal to a high density shock will greatly skew the way in which values are distributed.

Shepard's method (Shepard 1968) provides a more sophisticated interpolation scheme that is relatively straightforward to implement as there are existing modules available for use. Shepards method is a way of assigning a value to an arbitrary position in space based on a collection of other values at varying positions relative to the target point. The value a at a target point r when given a collection of N values in space $a_i(r_i)$ is given by

$$a = \sum_{i=0}^{N} \frac{W_i(r_i)u_i(r_i)}{\sum_{j=0}^{N} W_j(r_j)} \tag{3.35}$$

where W_i is given by

$$W_i = \frac{1}{|r_i - r|^p} \tag{3.36}$$

and is a weighting function based on the distance of the sample point from the target point. Modifying the value p determines how the distance from the target point to an input point influences the contribution from that input point, for example larger p values

put greater significance on the values that are spatially closer to the cell that is being refined. The modules used to implement are the pre-existing two and three dimensional Shepard method codes of Renka (1988a) and Renka (1988b). TORUS had to be developed to return all points (cell centres) within a given radius to pass to the Shephard method routines. It does this by moving through the grid recursively and using all the points that lie within a given search radius. When doing this search only the state of the grid prior to any refinement in the current sweep is used (i.e. the old parents are always used rather than newly refined cells), so that the order of refinement across the grid doesn't have any influence on the resulting grid structure. It is important that a sufficiently large number of input points are used in the Shepherd's method interpolation to accurately interpolate from the surroundings (for example if a fixed radius were used it is possible large cells could be missed). Proper spatial sampling is guaranteed by doubling the search radius if the number of points falls below some critical value, in 3D this minimum number of points is set to 10.

3.7.2 Photoionization loop refinement

Photoionization calculations involve a number of iterations. A refinement/coarsening sweep can be applied to the grid between these iterations to improve the resolution only where the ionization fraction is varying sufficiently rapidly to warrant it. This involves considering the fractional difference in ionization fraction between cells. If it exceeds some pre-defined limit then a refinement is considered necessary. For the species y of ionization fraction $X(y)$, the condition

$$\left|\frac{X(y)_i - X(y)_{i\pm1}}{X(y)_i}\right| - \delta_{\rm lim} \begin{cases} > 0 & \text{Split} \\ \\ \leq 0 & \text{Do not split} \end{cases} \tag{3.37}$$

determines whether or not refinement takes place, where $\delta_{\rm lim}$ is the fractional difference refinement limit. Conversely, if the fractional difference is below some other limit then a coarsening event can occur. In addition to taking place between photoionization iterations, refinement can also occur based on the ionization fraction in a refinement sweep between hydrodynamic steps.

3.7.3 Hydrodynamics based refinement

Hydrodynamical refinement/coarsening takes place between hydrodynamic time steps. Inter-cell fractional differences of any quantity on the grid can be used to decide refinement. If the fractional difference between the density, temperature, ionization fraction or speed between two cells varies by more than some user-specified limit then a splitting event takes place. For a general quantity q and fractional difference limit $\delta_{\rm lim}$ the criterion is

$$\left|\frac{q_i - q_{i+1}}{q_i}\right| - \delta_{\rm lim} \begin{cases} > 0 & \text{Split} \\ \\ \leq 0 & \text{Do not split} \end{cases} \tag{3.38}$$

This check is performed across all neighbouring cells unless a refinement event is decided (after which further checks are unnecessary). Another option for refinement is to refine if the cell mass reaches some specified fraction of the Jeans mass (equation 1.1).

Unrefinement

For both the photoionization and hydrodynamical considerations, coarsening steps take place less frequently than refinement steps (e.g. one coarsening sweep for every five refinement sweeps). This is to ensure that sufficient resolution is definitely achieved where required, rather than being immediately re-coarsened.

The unrefinenent check is a multi–stage process. Firstly, if the following is satisfied for the set of child cells that would be coarsened

$$|\frac{q_{max} - q_{min}}{q_{mean}}| > l \tag{3.39}$$

for quantity q and tolerance l, then the cells are not allowed to coarsen. This check is made for ρ, ρe, ρu, ρv and ρw and the default tolerance is 5×10^{-2}. There is also a check to ensure that the cell currently being considered for unrefinement is not already coarser than its neighbours since TORUS follows a convention in which neighbouring cells can differ by no more than one level of refinement (see also section 3.7.4). Finally there is also a check between each cell and all of its $k^{\rm th}$ neighbours (regardless of whether they are on the same octal) whereby satisfying the following

$$|\frac{q_{mean} - q_k}{q_{mean}}| > l \tag{3.40}$$

for the density and velocity fields prevents a coarsening. This final criterion is imposed because it is likely that such cells will be about to refine.

3.7.4 Evening up the grid

The hydrodynamics scheme used by TORUS requires that neighbouring cells never differ in refinement by more than one level. This makes the code implementation more straightforward and also prevents artifacts which can arise when there are large jumps in resolution, such as those observed in the propagation of a shock through a fine to coarse interface (Teyssier 2002). Therefore, following refinement/coarsening sweeps the grid is monitored to ensure that all cells satisfy this condition. If they do not, then additional cells are refined where appropriate.

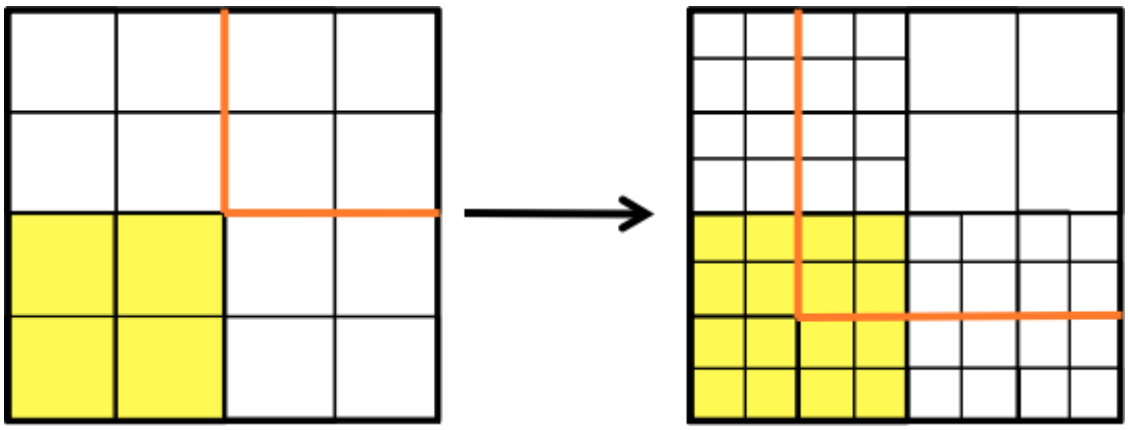

Figure 3.8: An illustration of the introduction of cells onto the main computational domain when corner ghost cells are refined. The interface between the main computational domain and ghost cells is marked in red and the corner cells which are detached from the grid are marked in yellow. Following refinement, yellow cells are on the main computational domain.

3.7.5 Corners and edges

Corners and edges require special treatment to ensure that boundary conditions are enforced correctly. It is important that the ghosts are of equal refinement to their boundary partners (i.e. the cells that determine the quantities in the ghost cell). For example, in the case of reflecting boundaries the four cells nearest the edge must match in refinement: the two ghosts and their domain cell partners. This condition is enforced whilst performing the check that no two neighboring cells differ by more than one level of refinement (evening up the grid, section 3.7.4).

Corners are more complicated than other ghost cells. For a grid that does not change its structure, the corner cells have no influence whatsoever on what occurs in the main computational domain. This is because their boundary partners are also all ghost cells. Now, if there is a refinement of the corners some component of this totally disconnected part of the grid moves onto the computational domain and introduces anomalous values. This is illustrated in Figure 3.8. Another problem arises when using different boundary conditions for each edge of the grid as it is not obvious which boundary condition the corner would use. For the sake of simplicity, development time and confidence in derived results, corners on AMR grids are currently forced to the highest level of refinement possible in the model and are not allowed to coarsen. Most other AMR codes have the ghosts completely isolated from the computational domain and the ghost corners do not even exist. Such an implementation is difficult (but not impossible) in TORUS because of its octree structure.

3.7.6 Optimizing the refinement sweeps

The most basic way of performing the refinement sweep is to traverse the cells in a domain until a split is found and the proceed to the next domain. This repeats until a traversal of all domains has occurred without a splitting event. While one domain is checking for

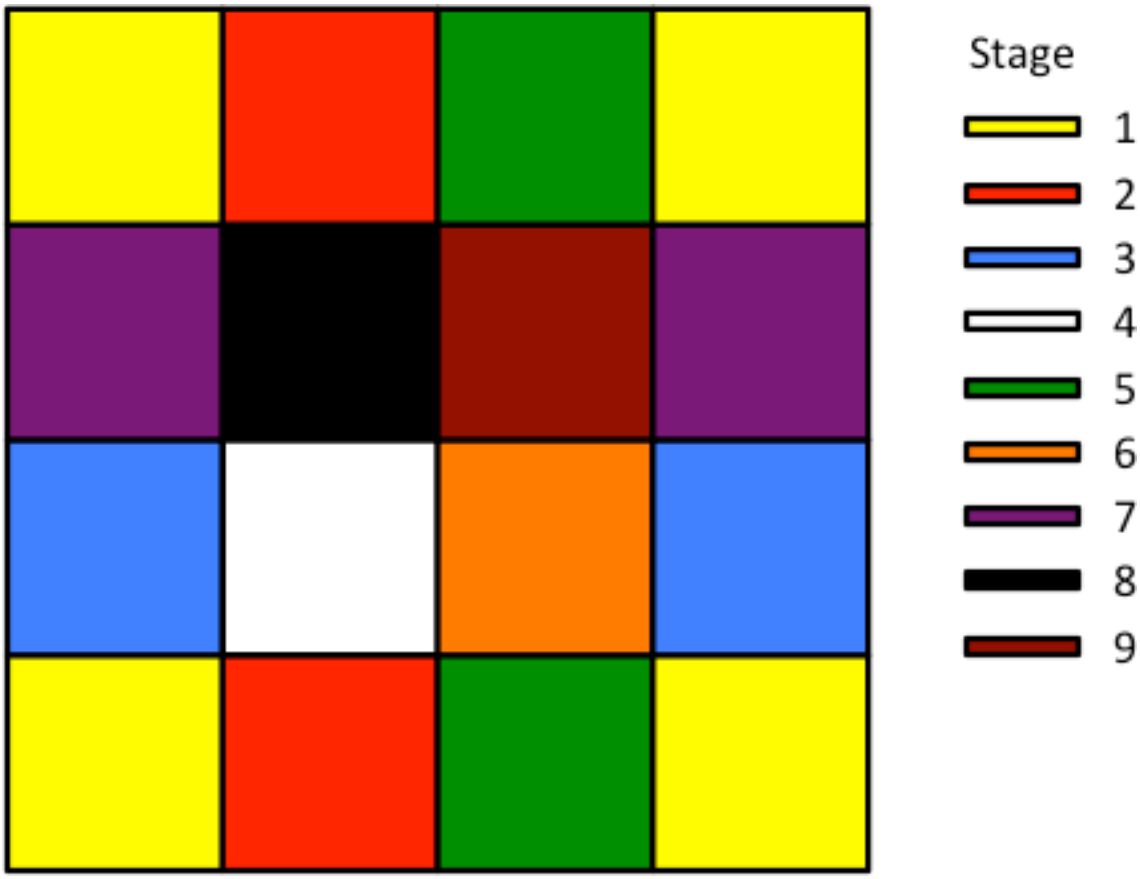

Figure 3.9: An illustration of the stages in which the evening up could be synchronised for different threads over a 16-way decomposition.

cells to be split, the others establish a hydrodynamic values server, which can be queried by the splitting domain for cell values outside of its own domain. This serving of all threads but one is not very efficient. Rather in each case there are combinations of threads which can check for splitting simultaneously without interfering with the serving of other threads. For example, assuming that the search will never extend between the directly neighbouring domains, a two dimensional grid with 16-level domain decomposition could perform checking for the bottom right and bottom left domains without rendering either with serverless requests. Finding efficient combinations of domains to check for splits simultaneously is a simple way to improve the efficiency of the AMR grid processing.

I construct an array of size equal to the number of domains, with each element containing a number that denotes the stage at which that domain undergoes split checking. The split checking then loops up to the maximum stage number rather than the total number of domains, this maximum stage should therefore be as small as possible. A straightforward scheme for a two dimensional 16-way decomposition is given in Figure 3.9. This scheme can also be applied to every second layer in a three dimensional model (interlaced with layers that follow some other ordering).

In a three dimensional 64-way domain decomposition this reduces the splitting loop from 64 to 18 components, a speedup of approximately a factor of 3.5, and a two dimen-

sional 16-way decomposition into 9 components.

3.7.7 Grid Shuffling

It is important for the grid to capture the initial model configuration properly so that initial deficiencies in the resolution do not propagate as the model evolves. For example if there is an interface between materials of different density that is not well resolved then the resulting motion of the material will not be planar, retaining some memory of the initial grid state.

One way to avoid this is to hard code initial grid configurations for specific geometries. However, this is not ideal as it is cumbersome to repeatedly modify and requires a special instance for each model geometry. To improve on this I developed a system called grid shuffling. Under this scheme in the initialization stage of the calculation there is a cycling between adding the initial physical parameters to the grid and a refinement of the grid. Starting from the coarsest possible grid (excluding the corners) the starting conditions are applied and the grid is refined when necessary according to the criteria specified in section 3.7.3, the grid is then repopulated using the same starting values and the process repeats for

$$n = (\text{maxDepthAMR} - \text{minDepthAMR}) + 2 \tag{3.41}$$

cycles. This ensures that the starting grid makes full use of the available resolution and captures starting features in a way consistent with the way that they will be treated in the subsequent evolution of the model. Figure 3.10 shows a starting grid for a two dimensional diagonal Sod shock tube in a box that has no forced starting refinement but has undergone grid shuffling. The grid shuffling has clearly identified the zone boundary in which the higher density material refines and, by refining and repopulating the grid, has ensured that the transition zone is as smooth as possible.

3.7.8 Coarse to fine interpolation

On an adaptive mesh, advection across a coarse to fine cell interface should account for the ambient flux gradient to more accurately capture the fluid behaviour. A 2D schematic of a coarse to fine interface is given in Figure 3.11. The coarse cell outgoing flux F_{out} is the sum of the fluxes into the upper F_u and lower F_l neighboring cells

$$F_{\text{out}} = F_u + F_l. \tag{3.42}$$

Fine cells (B and E from Figure 3.11) in contact with the coarse cell (cell A) are referred to as neighbors and those that are used in establishing the flux gradient (F and G) are called the community cells. In two dimensions the ambient flux gradient, for example

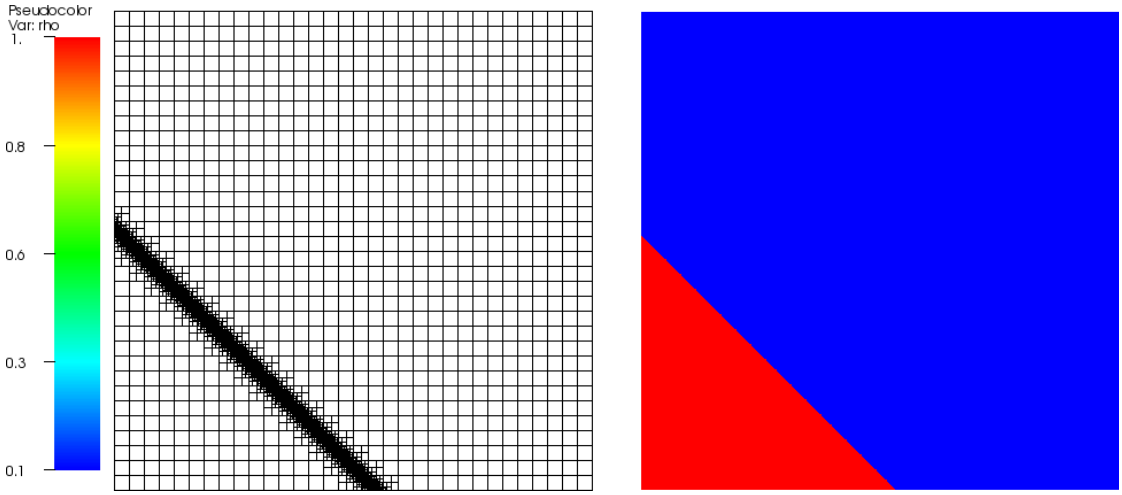

Figure 3.10: An illustration of the grid shuffling applied to the starting conditions of a diagonal Sod shock tube test. On the left is the starting grid state and on the right is the density distribution.

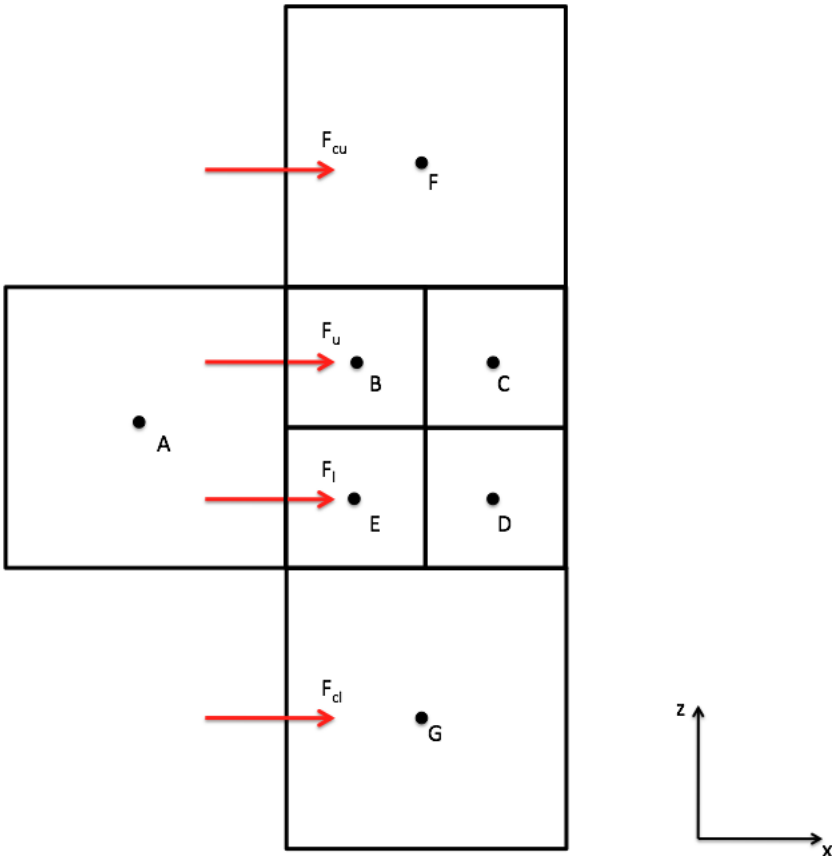

Figure 3.11: A schematic of a coarse (cell A) to fine (cells B and E) interface and surrounding cells that are used to determine how the outgoing flux from cell A is distributed to B and E when advecting in the x-direction.

when advecting in the x-direction, is simply

$$\frac{\Delta F}{\Delta z} = \frac{F_{cu} - F_{cl}}{z_F - z_G}. \tag{3.43}$$

The amount by which the fine cells have their incoming fluxes modified is then

$$\begin{aligned} dF_u &= \tfrac{\Delta F}{\Delta z}\left(z_B - z_A\right) \\ dF_l &= \tfrac{\Delta F}{\Delta z}\left(z_E - z_A\right). \end{aligned} \tag{3.44}$$

The sign of dF is determined by the sign of the flux gradient and the condition $dF_B = -dF_E$ for flux conservation is automatically satisfied.

The migration to three-dimensional flux interpolation is surprisingly quite straightforward. Exactly the same process is applied as in the two dimensional case, only it has to be repeated; once for the each dimension perpendicular to the direction in what advection is currently occurring. Once both flux gradients have been established the total modification factor is then the sum of the two modification factors.

3.8 Further Implementation

In this section I detail any further miscellaneous features in TORUS that I have developed or are important for future reference throughout this thesis.

3.8.1 Warm Starts For Different Decompositions

TORUS dumps the state of the computational grid at regular, specifiable intervals. Modifications to the code were required to accommodate changing the decomposition scheme from that used to write a given grid and that used when re-reading it. For example, with limited initial resources available a model can still make some progress at low, slower decomposition before moving to higher decomposition when the resources become available. This works by sweeping recursively throughout the entire octree after reading in the grid and redistributing MPI thread labels.

3.8.2 MPI Thread Checking

Domain decomposed models in TORUS require one of the possible number of MPI threads which is dependant on the geometry. For example 512+1, 64+1 or 8+1 MPI threads for three dimensional models. TORUS checks whether one of these configurations is being used and returns the viable options for a given dimensionality if an incorrect number of MPI threads has been specified. The allowed decompositions come in intervals of $2mn_D + 1$ where m is an integer and n_D is the number of dimensions, however only small values of m are supported.

3.8.3 Input File Units

When running a calculation using TORUS, the user specifies all of the calculation details in an input parameters file. These input files previously assumed that numerical values are in terms of the units used in the calculations. This is not ideal as an unfamiliar user will not necessarily be aware of what these units are. A dedicated module and a number of other routines were added to allow the user to specify the units intended after the numerical value in the parameters file. For inputs which have units, for example the end time of a simulation, an entry in the inputs file would include a third term as follows

```
tend 1.d16 s
```

where `s` denotes an entry in seconds. This value will be read in and then converted to the units used in the calculation. In the event that no unit is added it is assumed that the TORUS defaults are being used. Because different physical quantities use different default units, each quantity also has an associated *unit type*. For example, the default dust grain size entry ($1\,\mu$m) is different to the default wavelength size (1 Å). There are therefore unit types 'dust' and 'wavelength' which ensure that the appropriate conversion is applied to the quantity in the parameters file. A list of all units and unit types is given in Appendix A.

3.9 Summary

In this Chapter I have primarily introduced the hydrodynamics and photoionization schemes in TORUS and their coupling to perform radiation hydrodynamic calculations. TORUS uses a grid based finite–volume total variation diminishing hydrodynamics scheme that employs the superbee flux limiter by default. Photoionization is treated using the Monte Carlo approach (Lucy 1999; Ercolano et al. 2003). I also briefly described the treatment of self–gravity, which was developed by Tim Harries. Furthermore, I have decribed some of the parallelization and optimization techniques that are used to make the computationally expensive coupling of hydrodynamics with Monte Carlo radiation transport feasible. I also discussed developments of the TORUS octree grid structure to include an adaptive mesh in hydrodynamic/radiation hydrodynamic calculations.

"I guess once you start doubting, there's no end to it."

Batou, Ghost in the shell (1995)

4 Benchmark Testing

4.1 Introduction

Before using TORUS to study new problems, it is essential to test the veracity of the code by ensuring that it can reproduce well established results. There are a number of test cases that have a well understood result, usually with an analytic solution and confirmation from a number of different numerical codes. In this Chapter I present the details and results of some of these tests when performed by TORUS. The modular fashion in which TORUS is written allows for the testing of small components of the code in isolation. The tests here check the hydrodynamic, photoionization, radiation hydrodynamic, AMR grid and imaging components of TORUS. The fixed–grid hydrodynamic tests, H II40 Lexington Benchmark and H II region expansion benchmark in this Chapter all appeared in Haworth & Harries (2012), MNRAS, 420, 562.

4.2 Hydrodynamics Tests

First the hydrodynamic tests. At this stage a fixed grid is used rather than the AMR to ensure that the algorithm is working in its most basic form.

4.2.1 Sod Shock Tube

The Sod shock tube test is a simple 1-dimensional model, initially comprising two equal volumes separated by a partition. Both partitions, the left hand partition and right hand partition, contain ideal gases at zero velocity with different densities and hence different initial pressure and energy. A schematic of this system is given in Figure 4.1.

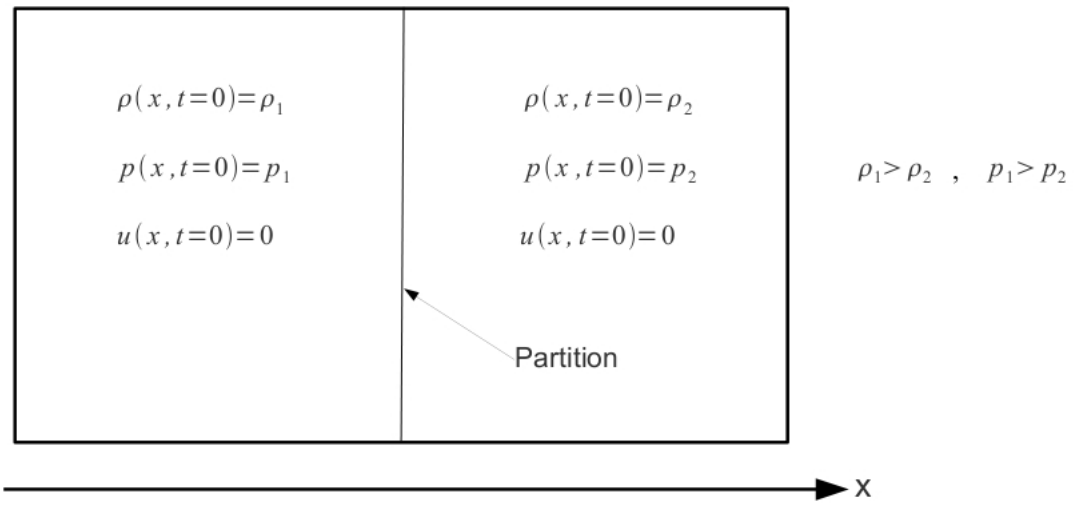

Figure 4.1: A schematic of the initial state of the Sod shock tube test. It initially consists of two equal volumes separated by a partition. The left hand volume is at higher density and pressure.

At time $t = 0\,\mathrm{s}$, the partition is removed and the system allowed to evolve. The state after a time t is detailed by Sod (1978). In order to pass this test TORUS should reproduce the correct density distribution, in agreement with the analytical solution, at a given point in time.

The model uses an adiabatic equation of state, with adiabatic index $\gamma = 7/5$. Unless otherwise stated, a value of 0.3 is used for the Courant–Friedrichs–Lewy (CFL) parameter in all hydrodynamics models throughout this thesis (see section 3.2.2). In this model the boundary conditions are reflective and 1024 cells are used for the grid.

A summary of the model parameters is given in Table 4.1 and the result as computed by TORUS at $t = 0.2\,\mathrm{s}$ is shown in Figure 4.2.

Table 4.1: Sod shock tube parameters.

Variable (Unit)	Value	Description
ρ_1 ($\mathrm{g\,cm^{-3}}$)	1	Initial density in the left hand partition
ρ_2 ($\mathrm{g\,cm^{-3}}$)	0.125	Initial density in right hand partition
γ	7/5	Adiabatic index
P_1 ($\mathrm{dyn\,cm^{-2}}$)	1	Initial pressure in left hand partition
P_2 ($\mathrm{dyn\,cm^{-2}}$)	0.1	Initial pressure in right hand partition
E_1 ($\mathrm{erg\,cm^{-3}}$)	2.5	Initial energy density in left hand partition
E_1 ($\mathrm{erg\,cm^{-3}}$)	2.0	Initial energy density in right hand partition
E.O.S.	Adiabatic	Equation of state
L (cm)	1	Computational domain size
n_{cells}	1024	Number of grid cells

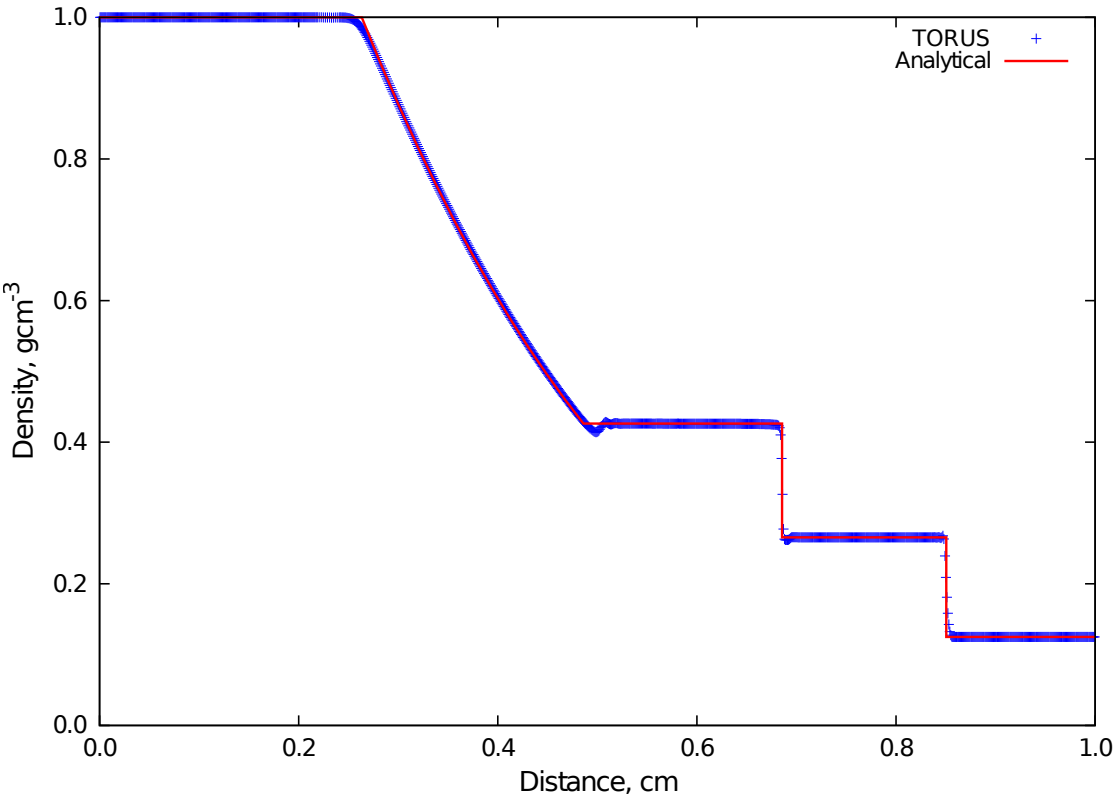

Figure 4.2: The density distribution of the Sod shock tube test at time $t = 0.2\,\mathrm{s}$, showing both the result given by TORUS (blue crosses) and the analytical solution (red line).

The features in this result are, from right to left; the initial density in the right hand partition, a shock wave which forms as a result of the low density material recoiling away from the high density material, a contact discontinuity between the high density material of the left hand partition and the low density material of the right hand partition, a rarefaction wave formed because the contact discontinuity acts as a piston drawing left hand material to the right and the initial density of the left hand partition.

It is clear from visual inspection of Figure 4.2 that TORUS is in excellent agreement with the analytical solution. The slight density dip at the rarefaction wave-contact dis-

continuity interface arises because TVD flux limited schemes only smooth out oscillations near sharp shocks. This is a necessary compromise, so that existing physical oscillations are not unphysically damped (see section 3.2).

4.2.2 Sedov-Taylor Blast Wave

A suitably large amount of energy released into a suitably small region of space will result in a very strong shock wave (a 'blast wave'). For most of the evolution of a blast wave, it can be described using self-similarity relations as detailed by Sedov (1946) and Taylor (1950b). Eventually the gas cools and propagates under its previously gained momentum and the pressure difference between any uncooled interior gas and the cooler surroundings.

The Sedov-Taylor blast wave test is an extreme model, which tests the advection scheme beyond the demands that will be made of it in star formation applications. In this 2-dimensional model a large amount of energy is injected into a circular region, radius 0.01 cm, of a constant density ideal gas, causing a blast wave. In order to pass this test TORUS must reproduce the correct density distribution, compared to the self-similar analytical solution, at a given point in time.

The initial ratio of thermal energy in the circular region to the rest of the grid is $3 \times 10^8 : 1$. Until recently the extreme nature of this model required that a CFL parameter value of 0.08 was required in order to capture the early stages of evolution without numerical instability arising. It is this version of the code for which the test results here are presented. In the versions of the code beyond the work included in this thesis, Tim Harries has added criteria in addition to the courant condition discussed in section 3.2.2, for example calculating a limiting time–step based on the pressure gradient. This should resolve the need to manually adjust the courant parameter in more recent calculations. The boundary conditions used in this test are all reflective and the grid comprises 512^2 cells. The analytical solution used for comparison is generated using the code of Haque (2006). A full table of parameters is given in Table 4.2 and a comparison of the density distribution at time $t = 0.03$ s, as calculated both by TORUS and analytically, is given in Figure 4.3. TORUS demonstrates a good level of agreement with the analytical solution but, as with all numerical schemes, suffers from numerical diffusion. This is responsible for the slight broadening of the shock and reduction in the peak amplitude compared to the analytical solution.

4.2.3 Kelvin-Helmholtz instability

Kelvin-Helmholtz (KH) instabilities are vortices that form at an interface between two materials due to shear forces (Von Helmholtz 1868; Kelvin 1871). Adaptations to SPH codes have recently found to be required in order to form KH instabilities by Agertz et al. (2007) and Price (2008), thus reproducing these has proved to be an important test of hydrodynamical algorithms.

The 2-dimensional system modelled here follows Price (2008), comprising two fluids in contact at different density and velocity, such that the ratio of their densities is 2:1

Table 4.2: Sedov-Taylor parameters.

Variable (Unit)	Value	Description
γ	7/5	Adiabatic index
v (cm s^{-1})	0	Initial velocity
ρ (g cm^{-2})	1	Initial surface density
$r_{\rm i}$ (cm)	0.01	Energy dump zone radius
$\mathrm{E_{Blast}}$ (erg cm^{-2})	3183.1	Dump zone surface energy density
$\mathrm{E_o}$ (erg cm^{-2})	1×10^{-5}	Ambient surface energy density
E.O.S.	Adiabatic	Equation of state
L(cm)	1	Computational domain size
$n_{\rm cells}$	512^2	Number of grid cells

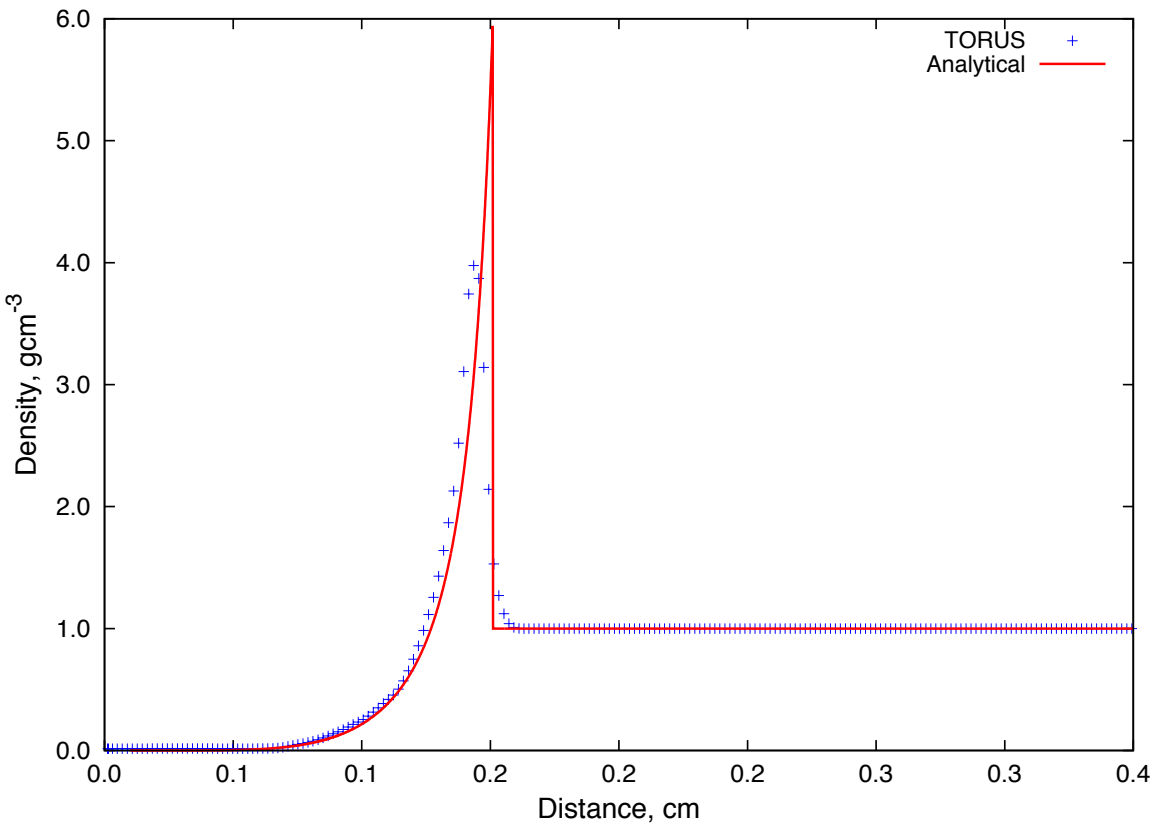

Figure 4.3: Density distribution of the Sedov-Taylor blast wave at $t = 0.03$ s showing both the result given by TORUS (blue crosses) and the analytical solution (red line).

and their velocities are equal in magnitude but in opposite directions. Periodic boundary conditions are used at the $\pm x$ boundaries and reflective conditions at the $\pm z$ boundaries, corresponding to housing the system in a pipe that extends indefinitely in $\pm x$. At time $t = 0$ s the interface between these fluids is subject to a perturbation of the form

$$u = \begin{cases} A\sin(-2\pi(\mathrm{x}+1/2)(1/6)), & |z-0.25| < 0.025 \\ \\ A\sin(2\pi(\mathrm{x}+1/2)(1/6)), & |z+0.25| < 0.025. \end{cases} \tag{4.1}$$

vortices should then form within a characteristic KH timescale given by

$$\tau_{KH} = \frac{2\pi}{\omega}. \tag{4.2}$$

Where, for materials in contact with density ρ_1 and ρ_2 and velocities v_1 and v_2 subject to a periodic perturbation of wavelength λ

$$\omega = \frac{2\pi}{\lambda}\frac{(\rho_1\rho_2)^{1/2}|v_1 - v_2|}{(\rho_1+\rho_2)}. \tag{4.3}$$

A full table of parameters used for this test is given in Table 4.3.

Table 4.3: Kelvin-Helmholtz parameters.

Variable (Unit)	Value	Description
γ	5/3	Adiabatic Index
ρ_1 ($\mathrm{g\,cm^{-2}}$)	1	Ambient fluid initial surface density
ρ_2 ($\mathrm{g\,cm^{-2}}$)	2	Central fluid initial surface density
u_1 ($\mathrm{cm\,s^{-1}}$)	-0.5	Ambient fluid initial velocity
u_2 ($\mathrm{cm\,s^{-1}}$)	$+0.5$	Central fluid initial velocity
E.O.S	Adiabatic	Equation of State
A	0.025	Constant in perturbation equation
λ (cm)	1/6	Wavelength of perturbation
L (cm)	1	Computational domain size
n_{cells}	512^2	Number of grid cells

Using these parameters and equations 4.2 and 4.3 we obtain a KH timescale of approximately 0.35 seconds, the time within which vortices should form. A plot of the density distribution as calculated by TORUS at τ_{KH} is given in Figure 4.4 and clearly demonstrates that primary and secondary vortices have formed within the KH timescale. If this model proceeds further the whole system eventually becomes unstable. This test has also been successfully performed using density ratios of 5:1 and 10:1.

4.2.4 Rayleigh-Taylor instability

Rayleigh-Taylor instabilities can arise where a material is 'on top' of a second lower density material in a gravitational potential and the interface between them is subject to a perturbation or when a low density material drives into a high density one and the interface

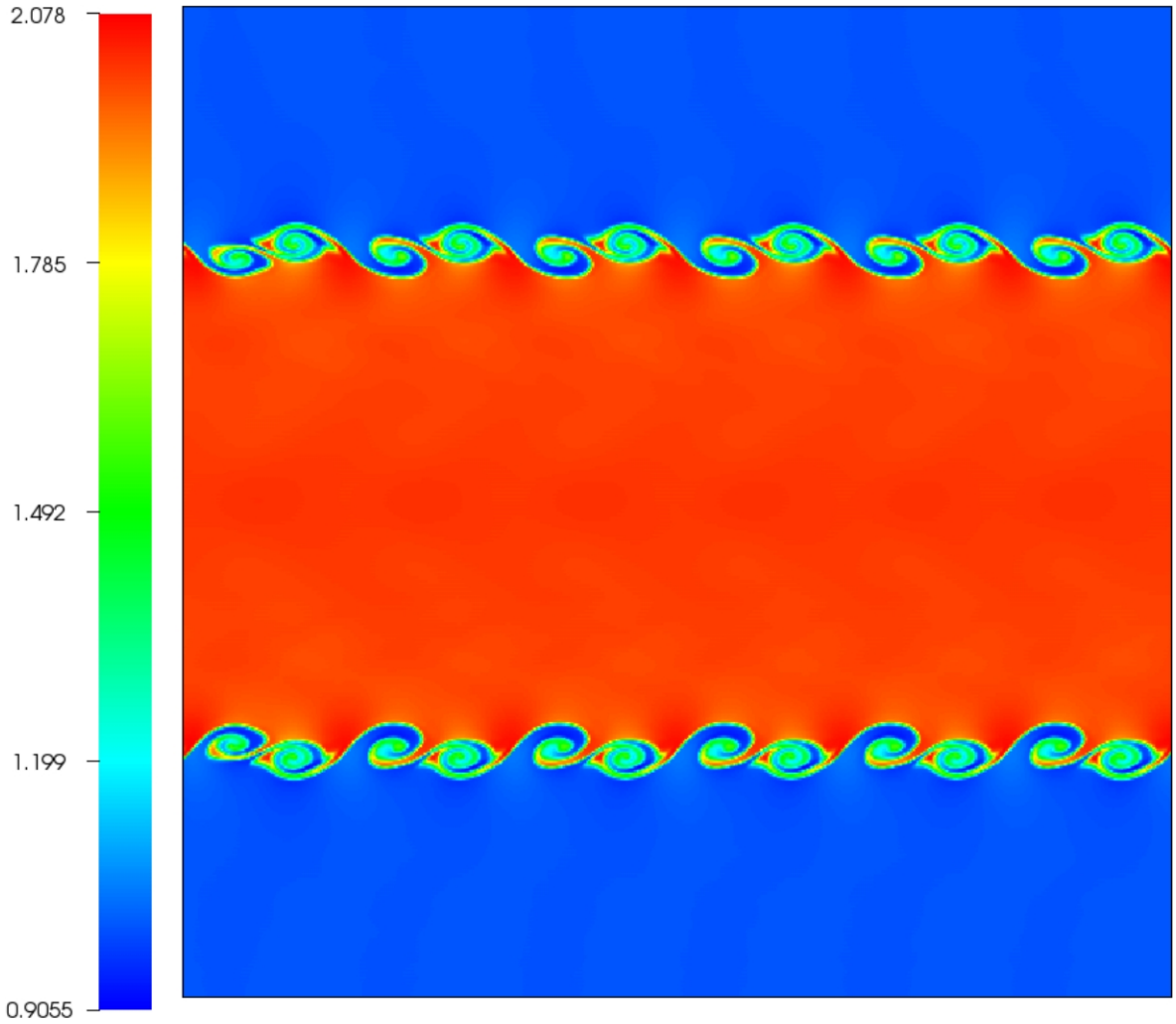

Figure 4.4: The surface density distribution in $\mathrm{g\,cm^{-2}}$ at $\tau_{\mathrm{KH}} = 0.35\,\mathrm{s}$ across the $1\mathrm{cm}^2$ domain of the Kelvin-Helmholtz instability model. Primary and secondary vortices are clearly visible at this point. This calculation uses periodic boundary conditions.

is again subject to perturbation (Rayleigh 1900; Taylor 1950a). They are manifested as 'Rayleigh-Taylor fingers' that propagate into the low density material along which Kelvin-Helmholtz instabilities may form. This gives rise to a characteristic mushroom shape. The following test uses system parameters selected so that they should give rise to this characteristic structure.

At time $t = 0\,\mathrm{s}$ the interface between two different density materials in a $1\,\mathrm{cm}^2$ box in the presence of a gravitational field is subject to a small disturbance of magnitude $-0.055\,\mathrm{cm\,s^{-1}}$ across a finite range $0.45 < x < 0.55$ of the interface, the system is then left to evolve. The ratio of the upper to lower densities is 2:1. We use periodic boundary conditions at the $\pm x$-direction bounds and reflective at the $\pm z$-direction bounds. The

gravitational potential ϕ at height z is given by

$$\phi(z) = gz \tag{4.4}$$

where g is the acceleration due to gravity, in this test equal to $0.1\,\mathrm{cm\,s^{-2}}$. A summary of parameters used in this test is given in Table 4.4.

Table 4.4: Rayleigh-Taylor parameters.

Variable (Unit)	Value	Description
ρ_1 ($\mathrm{g\,cm^{-2}}$)	2	Surface density of upper material
ρ_2 ($\mathrm{g\,cm^{-2}}$)	1	Surface density of lower material
g ($\mathrm{cm\,s^{-2}}$)	0.1	gravitational acceleration
E.O.S.	Adiabatic	Equation of state
L ($\mathrm{cm^2}$)	1	Computational domain size
n_{cells}	512^2	Number of grid cells

Figure 4.5 shows the distinctive mushroom-shape formed via this method at time $t = 5\,\mathrm{s}$. The main body of the mushroom is the Rayleigh-Taylor finger, at the tip of which Kelvin-Helmholtz instabilities have formed.

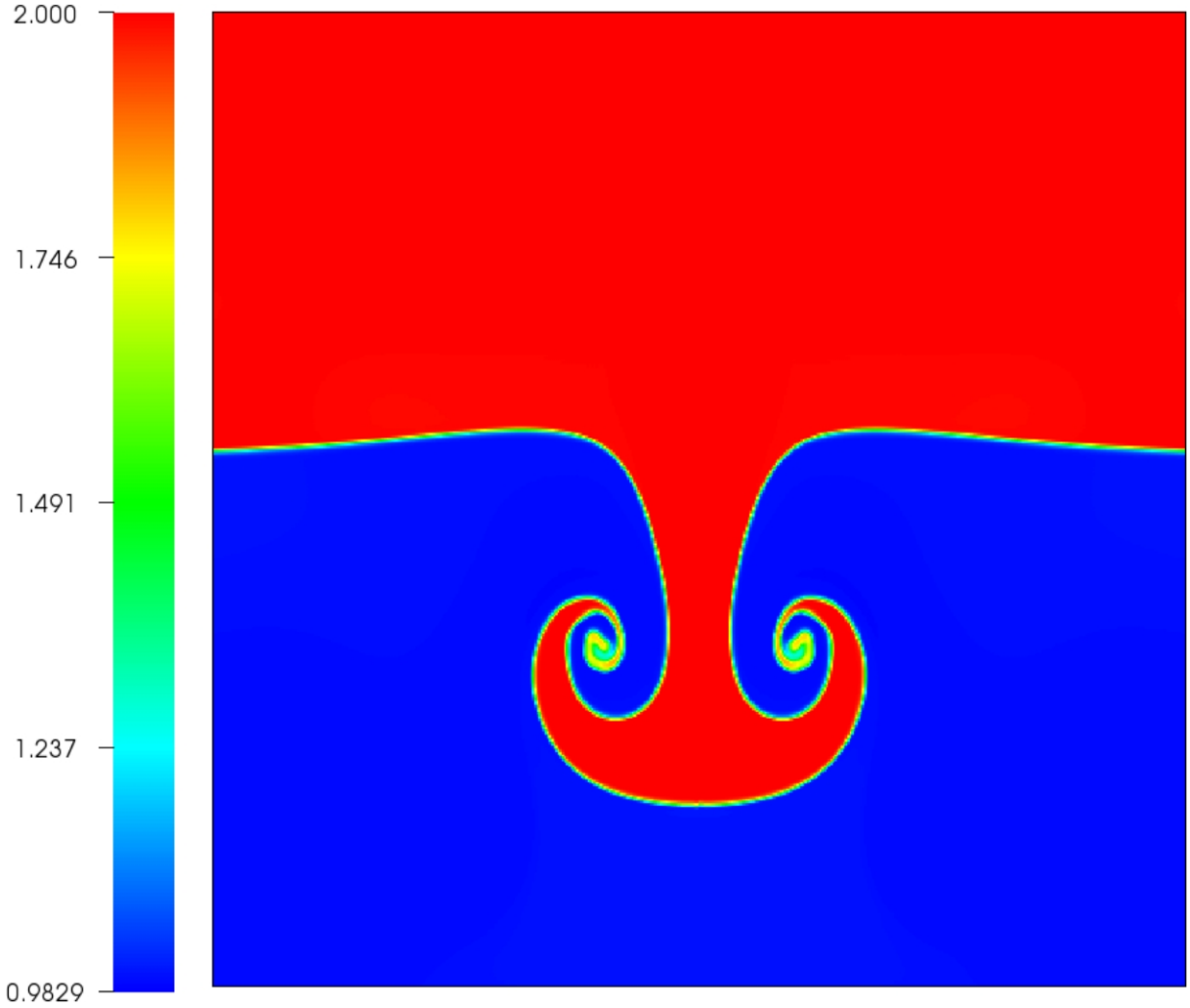

Figure 4.5: Surface density distribution in $\mathrm{g\,cm^{-2}}$ at time $t = 5\,\mathrm{s}$ showing the 'mushroom' formed in our $1\,\mathrm{cm}^2$ domain size, Rayleigh-Taylor instability model. It comprises a penetrating column of material with Kelvin-Helmholtz instabilities forming where the materials flow past one another.

4.3 Self Gravity Tests

4.3.1 Collapse Of A Uniform Sphere

This test follows, in three dimensions, the collapse of an initially uniform sphere to form an $n = 1$ polytrope. A polytropic cloud is one in which the pressure P varies according to the following relation:

$$P = K\rho^{1+\frac{1}{n}} \tag{4.5}$$

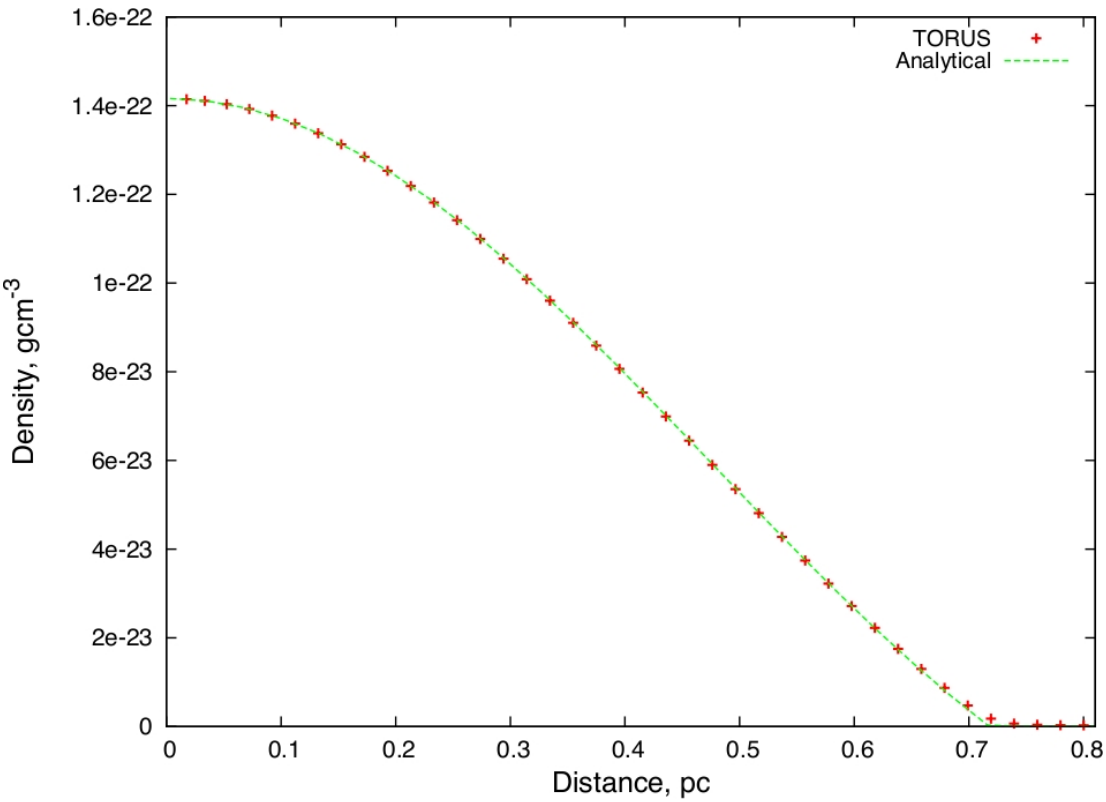

Figure 4.6: The analytical and TORUS -computed resulting density distribution for the collapse of a uniform density sphere to form an $n = 1$ polytrope.

where n is the index of the polytrope, ρ is the density and K is a constant. The corresponding solution to Poisson's equation for a self-gravitating polytropic fluid is given by the Lane-Emden equation, which details the variation in pressure and density in terms of dimensionless variables ζ and θ:

$$\frac{1}{\zeta^2}\frac{d}{d\zeta}\left(\zeta^2\frac{d\theta}{d\zeta}\right) + \theta^n = 0. \tag{4.6}$$

θ and ζ are given by equations 4.7 and 4.8:

$$\theta^n = \frac{\rho}{\rho_c} \tag{4.7}$$

and

$$\zeta = r\left(\frac{4\pi G\rho_c^2}{(n+1)P_c}\right)^{1/2} \tag{4.8}$$

where r, ρ_c and P_c are the radial position, central density and pressure respectively.

The solution to the Lane-Emden equation for an $n = 1$ polytrope is simply a sinc function, which should be the form of the resulting density distribution once collapse has occurred. This model employs reflecting boundary conditions. A summary of the parameters used for this test is given in Table 4.5. The model was run with significant artificial viscosity in order to strongly damp the oscillations that would otherwise occur.

Table 4.5: The self-gravity test parameters.

Variable (Unit)	Value	Description
M_{sphere} ($M_\odot$)	1	Mass of initial sphere
r_{sphere} (pc)	1	Radius of initial sphere
γ	2	Adiabatic index
E.O.S.	Polytropic	Equation of state
K	4.1317×10^{29}	Equation 4.5 constant
n_{cells}	128^3	Number of grid cells

The resulting radial density distribution following collapse as calculated both analytically and by TORUS is given in Figure 4.6 and demonstrates that TORUS is in excellent agreement with the expected result.

4.4 Photoionization Tests

4.4.1 The Hii40 Lexington Benchmark

The HII40 Lexington benchmark is a one dimensional test in which the equilibrium temperature and ionization structure of an HII region heated by a star at 40000 K is calculated and compared with the output of one of the many codes that reproduce the accepted result (see Ferland 1995). Here we calculate a comparison set of results using the one dimensional semi-analytic code Cloudy (Ferland et al. 1998), one of the original contributors to the benchmark. The system modelled comprises a star at 40000 K at the left hand edge of the grid, size 4.4×10^{19}cm comprising 1024 cells. This test incorporates more species than only hydrogen and does not rely on the simplified thermal balance calculation of equation 3.28, rather the temperature of the cell is determined through comparison of the heating and cooling rates as described in section 3.3. It also includes treatment of the diffuse field. A full list of parameters used for this benchmark is given in Table 6.1.

The resulting temperature and ionization fractions as calculated using both TORUS and Cloudy are shown in Figure 4.7. TORUS is consistent with the Cloudy temperature distribution to within 10% and is generally much better than this. The higher temperature calculated by TORUS in the inner regions is in agreement with the result obtained in Wood et al. (2004). The hydrogen and helium ionization fractions agree extremely well, this is of particular importance with regard to the hydrogen-only radiation hydrodynamics models presented in Chapter 5 of this thesis (Haworth & Harries 2012). The other ions match to within similar levels of agreement as Ercolano et al. (2003) and Wood et al. (2004).

Table 4.6: Lexington benchmark parameters.

Variable (Unit)	Value	Description
T_{eff}(K)	40000	Source effective temperature
$R_*(R_\odot)$	18.67	Source radius
n_{H} (cm^{-3})	100	Hydrogen number density
$\log_{10}$(He/H)	-1	Helium abundance
$\log_{10}$(C/H)	-3.66	Carbon abundance
$\log_{10}$(N/H)	-4.40	Nitrogen abundance
$\log_{10}$(O/H)	-3.48	Oxygen abundance
$\log_{10}$(Ne/H)	-4.30	Neon abundance
$\log_{10}$(S/H)	-5.05	Sulphur abundance
L (cm)	4.4×10^{19}	Computational domain size
n_{cells}	1024	Number of grid cells

Discrepancies in the result of this benchmark are usually attributed to differences in the atomic data used by the codes that are being compared.

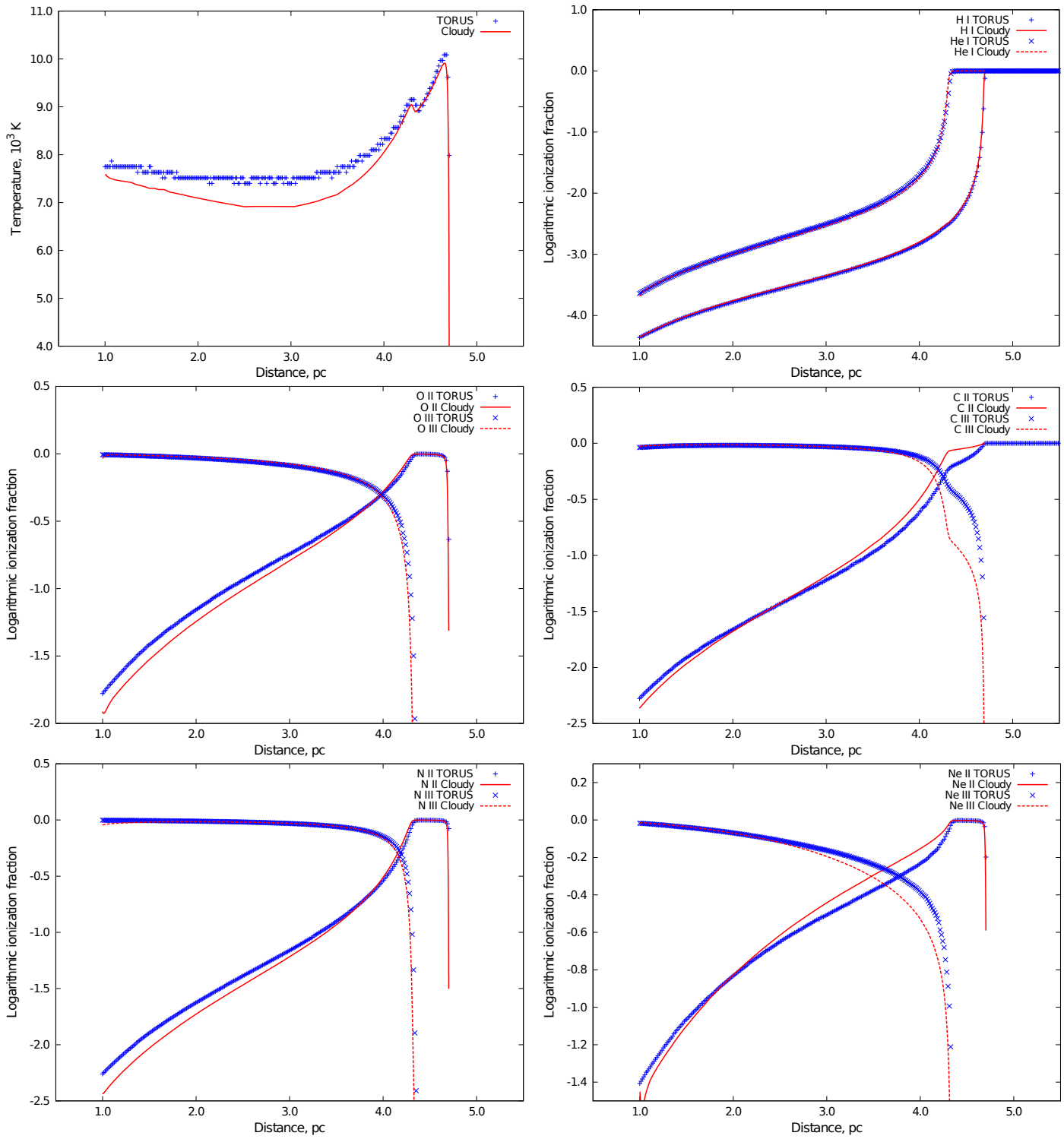

Figure 4.7: Top Left: The temperature distribution for the Lexington benchmark. Top Right: Hydrogen and helium ionization fractions. Middle Left: Oxygen ionization fractions. Middle Right: Carbon ionization fractions. Bottom Left: Nitrogen ionization fractions. Bottom Right: Neon ionization fractions.

4.5 Radiation Hydrodynamics Tests

4.5.1 Hii-Region expansion

In section 1.2.3 it was noted that there are two different regimes for evolution of an HII region, the R-type in which the ionization front propagation is rapid and little material motion occurs and the D-type in which a shock wave propagates into the neutral material ahead of the ionization front due to the pressure difference between the hot ionized and cold neutral regions.

In this test the D–type expansion is modelled in three dimensions, using the analytical solution (equation 1.9) as a comparison. The evolution of the R–type expansion, prior to is ignored because the calculations here assume photoionization equilibrium. The system consists of a star at 40000 K with a blackbody emission spectrum at the centre of a 11.36 pc^3 box of neutral hydrogen with reflective boundary conditions. We perform a radiation hydrodynamics calculation as outlined in Chapter 3 and follow the evolution of the ionization front position, defined as the point where the atomic hydrogen ionization fraction $X(\mathrm{HI}) = 0.5$, from $r_{\mathrm{I}} = r_{\mathrm{I}}^{\mathrm{o}}$ with time. Table 4.7 lists the parameters used in this test

Table 4.7: Parameters used for the HII expansion model.

Variable (Unit)	Value	Description
ρ_{o} ($\mathrm{m_H\,cm^{-3}}$)	100	Initial density
T_{o} (K)	10	Initial temperature of grid
u_{o} ($\mathrm{cm\,s^{-1}}$)	0	Initial velocity throughout grid
γ	5/3	Adiabatic index
E.O.S	Isothermal	Equation of state
T_* (K)	40000	Effective source temperature
R_* ($\mathrm{R_\odot}$)	10	Source radius
L(pc)	11.36	Grid edge length
n_{cells}	128^3	Number of grid cells

The results of this test as calculated both analytically using equation 1.9 and by TORUS are shown in Figure 4.8.

TORUS shows excellent agreement with equation 1.9 shortly after reaching the Strömgren radius. (The discrepancies at early times occur because TORUS evolves from a neutral starting point whereas the analytical solution starts with the ionization front at the Strömgren radius). At late times the evolution starts to deviate from the analytical solution as sufficient material is accumulated for the thin shell approximation to no longer apply.

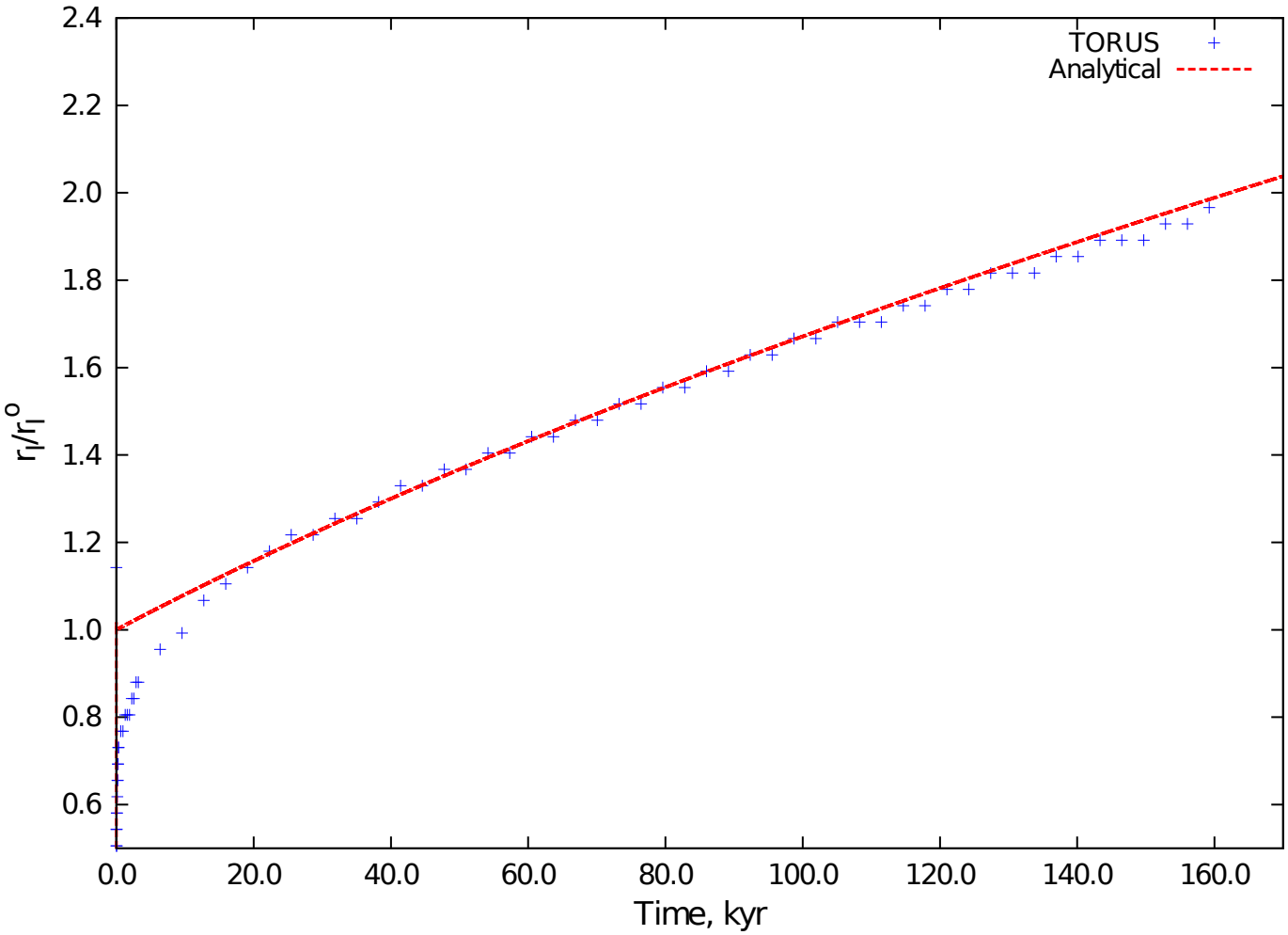

Figure 4.8: The position of the ionization front $r_{\rm I}$ in units of the Strömgren radius $r_{\rm I}^{\rm o}$ in the HII expansion radiation hydrodynamics test. The blue crosses are the position of the ionisation front computed by TORUS and the dashed line is the analytical Spitzer D–type expansion solution.

4.5.2 Validating The Use Of Single Photoionization Iterations

Following the initial, highly converged photoionization calculation the radiation hydrodynamics routine performs only single photoionization iterations sequentially with the hydrodynamic and self gravity components of the calculation. This is under the assumption that over an individual time step the changes to the system are small. The validity of this approach can be checked by taking a snapshot from one of the later components of a radiation hydrodynamics calculation and checking that a complete, converged photoionization calculation provides the same result. Using the results from one the radiatively driven implosion models that will be discussed in Chapter 5, I reset the ionization fraction so that the grid is completely ionized and ran a photoionization calculation over multiple iterations until convergence. I then compare the resulting ionization structure with that from the radiation hydrodynamic calculation. The hydrogen ionization fraction distribution following the renewed photoionization calculation is shown in Figure 4.9. Overlaid

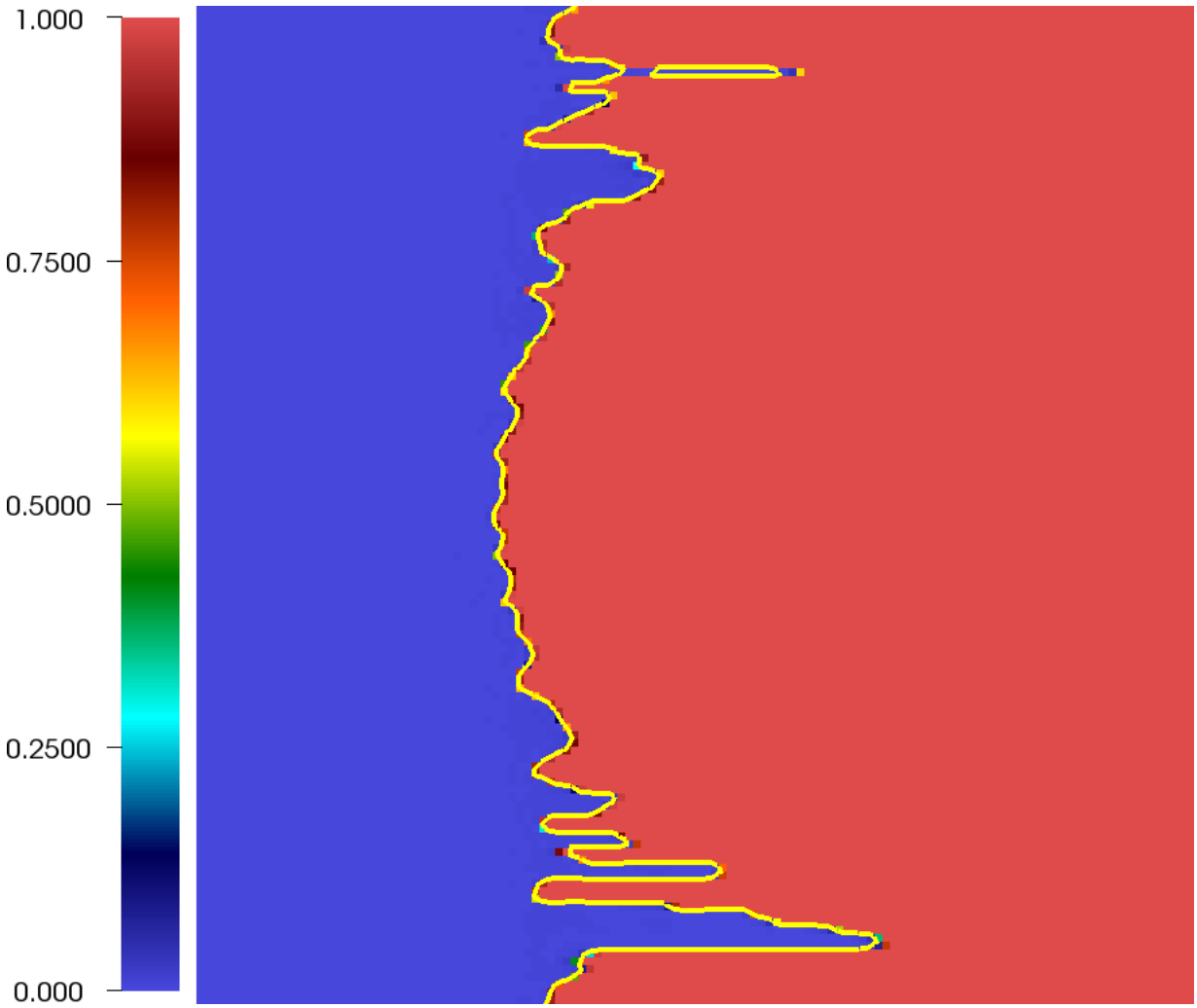

Figure 4.9: A model testing the use of a single photoionization iteration between hydrodynamics steps in radiation hydrodynamic calculations. The yellow contour represents the point in the radiation hydrodynamic calculations where atomic hydrogen is half ionized. The main distribution is that for a full photoionization calculation performed on the radiation hydrodynamic grid state.

is a contour representing the point at which atomic hydrogen is half ionized in the RHD model. It is clear the perturbation to the ionization state between steps is sufficiently small to warrant use of a single photoionization iteration between steps.

4.6 AMR Test

Adaptive mesh refinement is complex and difficult to implement correctly. In particular, it is important to ensure accurate conservation of key physical quantities such as mass and energy. Grid based artefacts should also not arise and will not if refinement and flux interpolation (detailed in section 3.7) are both working properly and the maximum available resolution is sufficiently high.

4.6.1 Diagonal Sod Shock

Here I provide a demonstration of the full AMR scheme using a two dimensional diagonal version of the well known Sod shock tube test that was discussed at the beginning of this Chapter (Sod 1978; Fryxell et al. 2000; Teyssier 2002). Initially, material of surface density $1\,\mathrm{g\,cm^{-2}}$ resides in the region $(x+z) < 0.05$ of a $1\,\mathrm{cm}^2$ box, the rest of which is at a surface density of $0.1\,\mathrm{g\,cm^{-2}}$. The grid refines based on the density distribution with a gradient limit of 7.5×10^{-3}, minimum depth of 5 and maximum depth of 9. After grid shuffling (see section 3.7.7), the system is allowed to evolve, with the high density material moving into the lower density material in a manner that is well studied (and discussed in section 4.2.1). I also run a comparison calculation using the comprehensively tested fixed grid hydrodynamics. The resulting AMR and fixed grid density distributions and the structure of AMR grid at 0.25 s are given in Figure 4.10. Both calculations are visually very similar, giving good agreement as to the positions of the shock and contact discontinuities and the form of the rarefaction wave. The AMR grid has clearly captured the discontinuities effectively, with high refinement also concentrated around the rarefaction wave. Cells upstream of these discontinuities has also visibly coarsened once the discontinuity has passed through. The AMR grid is not applied to the published applications in this thesis (to be used in the near future). Further testing and applications will appear in a future methods paper, Harries et al. (in prep).

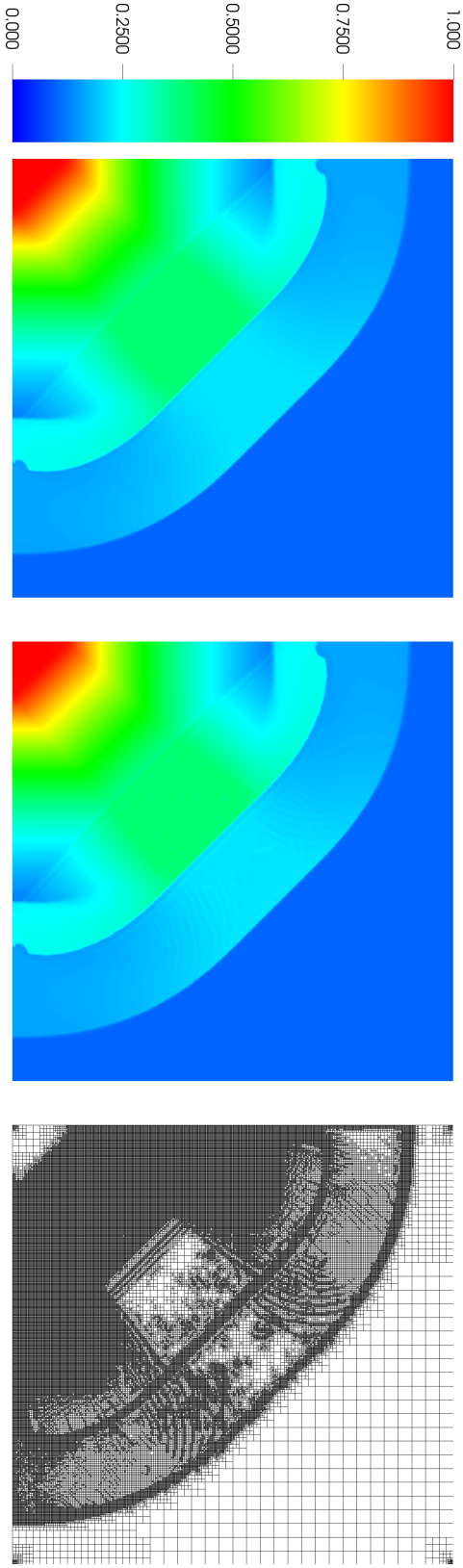

Figure 4.10: The state of the two dimensional diagonal Sod shock model for both fixed and AMR grids at 0.25 s. The top frame is the density distribution of the fixed grid calculation, the central frame the density distribution of the model which uses an adaptive grid and the bottom frame shows the configuration of the AMR mesh.

4.7 Synthetic Imaging Test

TORUS is capable of producing a range of simulated observables, including radio continuum and atomic line imaging, spectral energy distributions (Kurosawa et al. 2004) and molecular line data cubes (Rundle et al. 2010). Further details are provided when these features are used for applications in Chapters 6 and 7. I worked in collaboration with David Acreman to develop the following simple test of free–free continuum synthetic imaging for the TORUS test suite.

4.7.1 The cylinder test

Consider a cylinder of ionized material, surrounded by neutral vacuum, at a distance D from an observer. Assuming isotropic emission and enforcing no absorption, the line of sight intensity as a function of distance from the center to the edge of the cylinder will vary for the observer depending on the amount of material along that line of sight. In this test a synthetic free-free continuum image is generated of the cylinder at 6 microns. The intensity along a cut of the image across the cylinder is then compared with the theoretical intensity variation.

For comparison with a synthetic image it is useful to split the theoretical model into a series of rectangular prisms with the shorter length facing the observer. These shorter lengths are the same size dx as the pixels of the synthetic image. A schematic of the cylinder is shown in Figure 4.11. Two example pixel slices through the cylinder are shown, one through the centre directly opposite the observer at point O, labelled A, and another at some other point, labelled B. The centre of pixel B is at an angle θ to the line connecting the centre of the cylinder and the observer.

Table 4.8: Parameters used for the cylinder image test.

Variable (Unit)	Value	Description
ρ_c ($m_H\,cm^{-3}$)	1000	Cylinder density
ρ_c (cm^{-3})	1×10^{-40}	Cylinder density
N_{phot}	4×10^7	Number of photons used to construct image
$\lambda(\mu m)$	6	Image photon wavelength
Image Type	Free-Free	Radiation source type
N_{pix}	201×201	Number of pixels
D (pc)	50	Observer distance from cylinder center
L (pc)	0.972	Cylinder length
r (pc)	0.972	Cylinder radius

In TORUS the radio continuum thermal free–free emissivity into all angles at frequency ν is calculated using

$$j_\nu = 4\pi \frac{2h\nu^3}{c^2} n_e^2 \alpha(\nu, T) \exp\left(-\frac{h\nu}{k_B T}\right) \tag{4.9}$$

where n_e and $\alpha(\nu T)$ are the electron density and the free–free absorption coefficient for

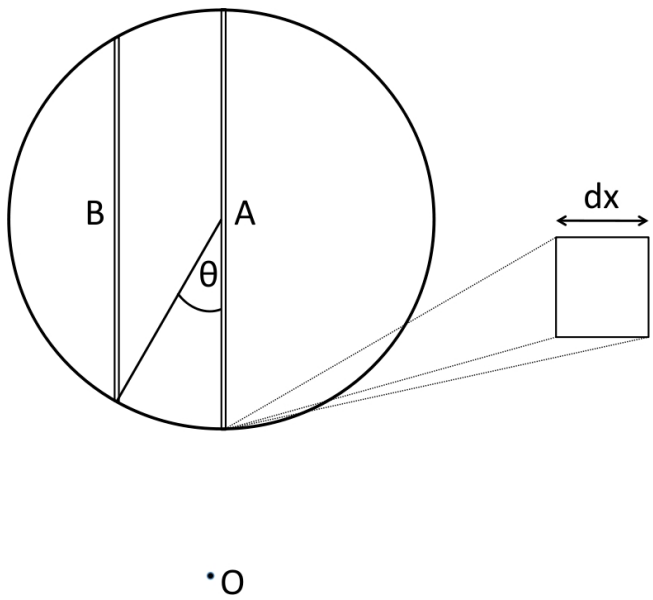

Figure 4.11: A schematic of the cylinder image test model. A cylinder of uniform density, temperature and therefore radio continuum emissivity is split into a series of rectangular prisms that intersect the edge of the cylinder at an angle θ to the central axis. All prisms are of the same width and height dx and the length through the cylinder is a function of θ.

hydrogen. The total emission along one of the prisms is the emissivity multiplied by the prism volume times the solid angle subtended by the pixel, i.e.

$$j_{\text{obs,central}} = \frac{j}{4\pi} 2r\cos(\theta)dx^2 \tag{4.10}$$

gives the intensity in erg/s/ for the pixel, where dx, r and θ are the pixel size, cylinder radius and angle the pixel centre makes with the cylinder central axis (see Figure 4.11).. For cells outside of the cylinder the intensity is set to zero as the vacuum will have negligible emission.

To account for the finite difference in path length between the central position and edges of the cell, the cell edge path lengths are used to provide upper and lower limits for the expected emission. The central value and upper and lower limits on the observed emission in a given cell are determined by

$$\begin{aligned} j_{\text{obs,upper}} &= \tfrac{j}{4\pi} 2\left(dx|\tan(\theta)| + r\cos(\theta)\right)dx^2 \\ j_{\text{obs,lower}} &= \tfrac{j}{4\pi} 2\left(r\cos(\theta) - dx|\tan(\theta)|\right)dx^2 \end{aligned} \tag{4.11}$$

In this test his theoretical distribution is then compared with the intensities across a slice of the synthetic image on pixel by pixel basis.

A list of the parameters used for this test is given in Table 4.8. An example of the resulting synthetic image generated by TORUS is given in Figure 4.12. A plot showing both the theoretical intensity distribution and a synthetic one is given in Figure 4.13 for what would be a vertical cut across the image in Figure 4.12. The intensity profile of

the synthetic image produced by TORUS is in good agreement with the expected intensity distribution. The scatter is due to Monte Carlo sampling noise.

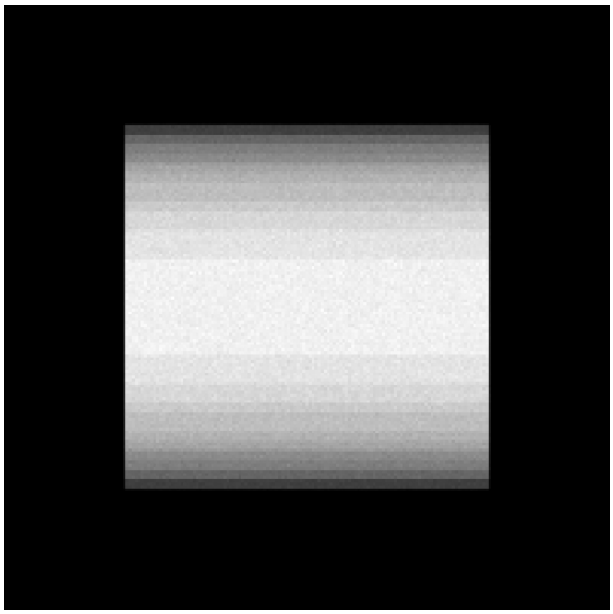

Figure 4.12: An example of a synthetic image generated by TORUS in the cylinder image test.

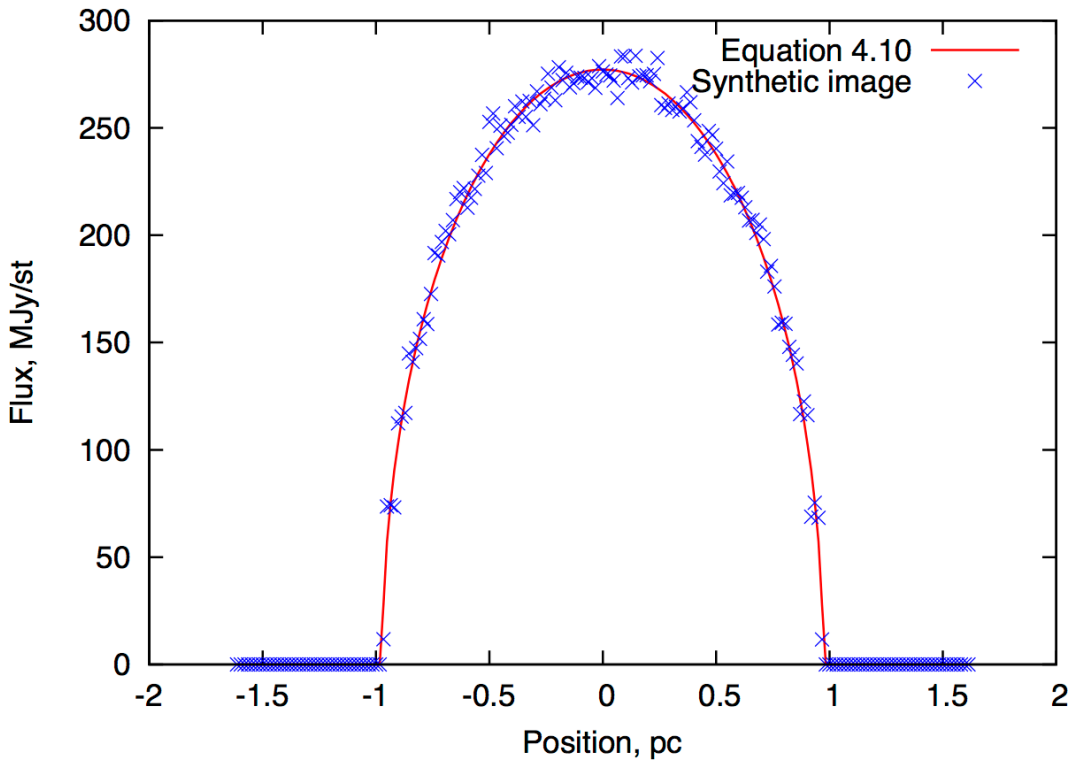

Figure 4.13: A comparison of the theoretical and synthetic image emission intensity profiles for a vertical cut down the centre of the image in Figure 4.12.

4.8 Summary

I have demonstrated that TORUS satisfies a number of benchmark tests. The radiative transfer scheme, including treatment of the diffuse field, is in good agreement with the Lexington benchmark as calculated by Cloudy (Ferland et al. 1998). The hydrodynamics algorithm satisfies the Sod shock tube test and Sedov-Taylor blast wave density distributions at a given point in time and has also been shown to produce Kelvin-Helmholtz and Rayleigh-Taylor instabilities. Furthermore our self-gravity calculation reproduces the same $n = 1$ polytropic density distribution as given by the Lane-Emden equation following the collapse of a uniform density sphere. The radiation hydrodynamics scheme has been shown to agree with the analytical work of Spitzer (1978) for the rate of expansion of an HII region and the use of a single photoionization iteration between hydrodynamics steps has been supported. Furthermore the adaptive mesh has been tested as well as the imaging routine. These results verify that TORUS hydrodynamics, photoionization, AMR and imaging modules reproduce both the standard and additional, newly introduced, benchmarks and is ready for application to new problems.

"It is tempting, if the only tool you have is a hammer, to treat everything as if it were a nail."

Abraham Maslow, The Psychology of Science, (1966)

5

Radiatively driven implosion: the effect of the diffuse radiation field

5.1 Abstract

In this Chapter the effect of including diffuse field radiation when modelling the radiatively driven implosion of a Bonnor-Ebert sphere (BES) is investigated. Radiation-hydrodynamical calculations are performed by combining Monte Carlo photoionization with grid-based Eulerian hydrodynamics using operator splitting. It is found that the diffuse field has a significant effect on the nature of radiatively driven collapse which is strongly coupled to the strength of the driving shock that is established before impacting the BES. This can result in either slower or more rapid star formation than expected using the on-the-spot approximation depending on the distance of the BES from the source object. As well as directly compressing the BES, stronger shocks increase the thickness and density in the shell of accumulated material, which leads to short, strong, photo-evaporative ejections that reinforce the compression whenever it slows. This happens particularly effectively when the diffuse field is included as rocket motion is induced over a larger area of the shell surface. The formation and evolution of 'elephant trunks' via instability is also found to vary significantly when the diffuse field is included. Since the perturbations that seed instabilities are smeared out elephant trunks form less readily and, once formed, are exposed to enhanced thermal compression.

The research detailed in this Chapter has been published in Haworth & Harries (2012), MNRAS, 420, 562.

5.2 Introduction

The majority of stars form in clusters, situated in molecular clouds that range in size from less than a single parsec to several hundred parsecs (Lada & Lada 2003). In order for star formation to occur, gravitational collapse of material has to overcome internal thermal pressure, supersonic material motions (turbulence) and magnetic fields (see e.g. Preibisch & Zinnecker 2007; Hartmann 2009). The presence of OB stars in these systems has a dramatic impact on the surrounding material (and therefore star formation), as they emit large amounts of high energy radiation that photoionizes gas and gives rise to propagating ionization and shock fronts (Elmegreen 2011b). They also inject mechanical energy into the surroundings in the form of high-speed stellar winds and, eventually, supernova explosions. The net impact of radiative feedback from massive stars on star formation efficiency in a molecular cloud is currently unclear, though a number of individual processes that either inhibit or induce further star formation has been identified.

The two main radiative feedback mechanisms that inhibit star formation are the dispersal of material that might otherwise move towards the centre of the molecular clouds' gravitational potential (e.g. Herbig 1962) and the possibility of driving and maintaining turbulence that supports against collapse (e.g. Peters et al. 2008; Gritschneder et al. 2009b).

The two primary established mechanisms for the induction of star formation are consequences of the expanding ionization and shock fronts about a massive star. The first is 'collect and collapse' (Elmegreen & Lada 1977; Elmegreen et al. 1995; Dale et al. 2007) in which material that is accumulated by the expanding ionization front of an H II -region becomes locally gravitationally unstable, fragmenting and collapsing to form stars. This mechanism is supported observationally by, for example, the identification of massive fragments located in a dust ring surrounding the H II region RCW 79 by Zavagno et al. (2006).

The second mechanism is radiatively driven implosion (RDI), (Bertoldi 1989) in which radiatively induced shocks drive into otherwise stable pre-existing density structures and cause them to collapse and form stars. RDI has been modelled by various groups, for example Kessel-Deynet & Burkert (2003), Arthur & Hoare (2006), Gritschneder et al. (2009a), Henney et al. (2009), Bisbas et al. (2011) and produces objects similar to observed bright rimmed clouds (BRCs) in H II regions (Ogura et al. 2002). The rate at which collapse occurs and the associated star forming efficiency of these RDI models has unsurprisingly been found to be very sensitive to the incoming flux.

A variant of collect and collapse, in which the trigger for fragmentation of an ionization front is one of the many possible hydrodynamic or radiation hydrodynamic instabilities has also been explored (e.g. Vishniac 1983; Garcia-Segura & Franco 1996; Williams 2002; Mizuta et al. 2006). When sufficiently perturbed, faster moving components of the ionization front will funnel material transversely to the direction of I-front propagation, depositing it in the path of slower moving components (Vishniac 1983; Garcia-Segura & Franco 1996). This results in a collection of pillar-like objects with dense tips, much as is

observed in e.g. the pillars of creation in the Eagle Nebula or the Dancing Queen's Trunk in NGC7822 (see e.g. Schneps et al. 1980; Reach et al. 2004; Chauhan et al. 2011a).

Recently, Gritschneder et al. (2009b) and Gritschneder et al. (2010) used the ray-tracing, smooth particle hydrodynamics (SPH) code, IVINE (Gritschneder et al. 2009a) to consider the effects of a radiation front impinging upon a turbulent neutral medium. They found that radiation could support turbulence, which would prohibit large-scale star formation by supporting against collapse. They also found that ionizing radiation rapidly penetrated lower density regions, heating them up and compressing the remaining higher density structures. This again resulted in pillars with dense cores at the tips where stars might form. They termed this process 'radiative round-up'.

Each of the aforementioned processes has been the subject of numerical modelling. Due to the intensive computational demand of these models, at least in three dimensions, a number of approximations have necessarily been developed. Ercolano & Gritschneder (2011a) provides an overview and evaluation of some of the main approximations, summarised as follows.

a) Considering a monochromatic radiation field, usually Lyman 13.6eV photons, reduces calculation timescales (as with all of these approximations) compared with polychromatic models. This is because the entire source spectrum does not need to be resolved and a single value can be used for the gas opacity. However, this speed up is at the expense of being able to reliably calculate the resulting ionization and temperature structure of the system and neglects effects due to radiation hardening (though radiation hardening effects can be estimated in monochromatic codes, e.g. Mellema et al. 2006).

b) Use of simplified thermal balance calculations, for example calculating the temperature as a simple function of the ionization fraction. This is more straightforward to implement and results in faster calculations than solving the thermal balance by comparing heating and cooling rates.

c) Assuming that the system is in photoionization equilibrium. This is valid where recombination timescales are shorter than the dynamical timescales of the gas.

d) The 'on the spot' (OTS) approximation. Under this scheme diffuse field photons, those generated in recombination events, are not treated. This is justified in regimes where diffuse field photons will not propagate very far and therefore not modify the global ionization structure significantly. It is however, questionable in regions of low or rapidly varying density. Because diffuse field photons are emitted isotropically, it is possible that shadowed regions will not be exposed to a realistic amount of ionizing radiation when modelled under the OTS approximation.

It is not yet clear what impact these approximations have on both the inhibiting and inducing mechanisms described above. In an effort to understand the effect of the diffuse field, Ercolano & Gritschneder (2011a) compared snapshots from the radiative round-up models run by IVINE, with full radiative transfer calculations using the Monte-Carlo radiative transfer code MOCASSIN (Ercolano et al. 2003) and noted significant differences

between the ionization and temperature structures calculated by the two codes. Ercolano & Gritschneder (2011b) subsequently attempted to account for the thermal effects of the diffuse field in IVINE by identifying shadowed regions and assigning them a parameterised temperature as a function of density based on comparisons of IVINE and MOCASSIN snapshots. Using this shadowing scheme a significant effect on the resulting pillar structures was observed. Far fewer pillars were formed and those that remained were narrower, denser and often cut off from the parent molecular cloud due to their paramaterized increased exposure to ionizing radiation from the diffuse field. This leads to earlier triggering of star formation and reduces the efficiency of radiation driven turbulence. This shadowing scheme is not without drawbacks, being susceptible to erroneous heating of true shadowed regions. The spread in temperatures at a given density calculated by MOCASSIN also results in quoted typical errors in parameterized temperature of approximately 50%. It is certainly clear from this work that a more comprehensive knowledge of the effects of the diffuse field would be valuable. It will be necessary to establish just how different the result of a radiation hydrodynamics calculation can be when incorporating the diffuse field directly, to validate or reassess the use of simplified radiation handling in radiative feedback simulations.

In this Chapter I use the radiation hydrodynamics code TORUS (Harries 2000; Kurosawa et al. 2004; Harries et al. 2004; Acreman et al. 2010a; Harries 2011) to investigate the effects on radiatively driven implosion of a more sophisticated treatment of the diffuse field than previously applied in a radiation hydrodynamics calculation. Specifically, we will systematically deduce the relative effects of using a monochromatic OTS, polychromatic OTS and polychromatic-diffuse radiation field on the overall nature of collapse.

5.3 Numerical Method

The TORUS radiation hydrodynamics code has already been extensively detailed in Chapter 3 and tested in Chapter 4. This work was a first application and publication using the radiation hydrodynamics scheme, including the domain decomposed photoionization, hydrodynamics and self gravity (Haworth & Harries 2012).

For the radiation hydrodynamics models in this first application a simplified thermal balance calculation is used and the only species considered are atomic and ionized hydrogen. This is to allow for comparison with previous works that use these schemes such as Gritschneder et al. (2009a) and Bisbas et al. (2009). It also results in a less computationally expensive calculation. The temperature is calculated by interpolating between pre-determined temperatures, $T_{\rm n}$ and $T_{\rm io}$, ascribed to the state of fully neutral and fully ionized gas respectively as a function of the newly calculated fraction of ionized atomic hydrogen in the $i^{\rm th}$ cell η_i

$$T_i = T_{\rm n} + \eta_i (T_{\rm io} - T_{\rm n}) \tag{5.1}$$

For the work in this thesis $T_{\rm n} = 10\,{\rm K}$ and $T_{\rm io} = 10000\,{\rm K}$ for all models that use this simplified thermal balance calculation.

5.3.1 Implementation

Despite the high computational cost of the TORUS radiation hydrodynamics scheme, it is extremely scalable (as discussed extensively in section 3.6). The computational domain is decomposed into subdomains over which the components of the radiation hydrodynamics calculation are computed by an individual processor (thread). In three dimensions subdomains take the form of cubes of equal volume, which at present can be either 1/8, 1/64 or 1/512 of the total domain volume. An additional master thread performs governing and collating operations, giving a total of 65 threads for each of the three-dimensional models performed here. At lower dimensionality the grid can be decomposed in a similar manner into equally sized squares (2D) or lines (1D).

In the photoionization component of a calculation, photon packets are communicated between threads in stacks rather than individually to reduce the communication latency overhead, as discussed in section 3.6.2. TORUS stores quantities using an octree AMR grid, however at the time of running these calculations adaptive refinement and coarsening of the grid was not yet fully tested in the hydrodynamics routine, a fixed grid was therefore used for the models in this Chapter.

The RDI calculations presented in this Chapter were run on an SGI Altix ICE system using 65 2.83GHz Intel Xeon cores across 9 dual quad-core compute nodes. These typically completed within 600–1000 hours of wall time. The models that include the diffuse field did not necessarily take the longest time to complete, as the additional hydrodynamic and photoionization calculations required for models that develop the highest velocity material motions outweigh the additional time taken for each photoionization calculation when the diffuse field is included.

5.4 Model setup

The calculations in this Chapter are of the radiatively driven implosion of a Bonnor-Ebert sphere (a sphere in which the density varies according to the Lane-Emden equation, equation 4.6) using three different treatments of the radiation field so as to distinguish their relative contributions to the evolution of the system. The three different radiation fields used are:

a) a monochromatic radiation field with the OTS approximation

b) a polychromatic radiation field with the OTS approximation

c) a polychromatic radiation field with the diffuse field, as outlined in section 3.3.

The details of the starting conditions are very similar to that of Gritschneder et al. (2009a). A Bonnor-Ebert sphere (BES) of radius 1.6 pc resides at the centre of a $1.5 \times 10^{19}\,\mathrm{cm}^3$ ($4.87^3\,\mathrm{pc}^3$) grid of 128^3 cells. A BES is a solution to the Lane-Emden equation (see section 4.3.1) where $n = \infty$, resulting in an isothermal sphere where $P \propto \rho$ that is truncated at some radius and embedded in a medium of external pressure to prevent the cloud expanding.

The BES has a core number density of $10^3\mathrm{cm}^{-3}$, with the material surrounding the

BES having a number density equal to that at the BES edge (such a BES is known as 'incomplete'). My model domain is slightly larger than that used by Gritschneder et al. (2009a) so that the evolution of larger extent of any shadowed region can be studied. The resolution of these models is currently limited by computational cost, however the number of grid cells here is equivalent to that used in the successful H II region expansion test of section 4.5.1. This model is also on a smaller length scale than that of the H II region expansion test so the resolution will be sufficiently high. As mentioned in section 5.3.1, use of the AMR grid that will enable the calculation of models at higher resolutions in future work.

The primary photon source is a star that lies outside the grid in the $-x$ direction. The radiation field is assumed to enter the grid plane parallel at the $-x$ boundary, at which photon packets are initiated at random locations and the flux is modified to account for geometric dilution.

As well as considering the three different radiation schemes mentioned above, the three different flux regimes considered in Gritschneder et al. (2009a) are also treated. These are denoted high, medium and low flux and correspond to the BES being located just within, on the edge of and just beyond the Strömgren radius respectively. The fluxes and corresponding stellar properties that were used to generate these different flux regimes are given in Table 5.1, along with the other parameters used for this model.

In all of the models presented in this Chapter, the hydrodynamic boundary conditions are periodic at $\pm y$ and $\pm z$ and free outflow/no inflow at $\pm x$. Dirichlet boundary conditions are used for the self-gravity calculation and the radiation field boundaries are free outflow/no inflow. Using this boundary condition for the radiation field can lead to reduced sampling at the domain boundaries, where material will be subject to non-symmetric diffuse flux. A solution to this in the form of periodic photon packet boundary conditions is discussed in Chapter 6.

The free fall time for this cloud is approximately 3 Myr, estimated using $1/(\sqrt{G\rho_{\max}})$ where $\rho_{\max}$ is the central density and G is the gravitational constant. This is a factor of 15 longer than the total simulation time of 200 kyr. Radiation hydrodynamics will thus dominate gravitational effects in the evolution of the system. The state of the computational grid is saved every 5 kyr.

5.5 Results and Discussion

5.5.1 Initial properties

The initial ionization state of the system for all three flux regimes and photoionization schemes is shown in Figure 5.1. At this stage there is already a noticeable difference between them in the extent of their un-ionized regions. The top row from Figure 5.1 represents the starting point that would be obtained by most pre-existing models (specifically, it is a zoomed out version of Gritschneder et al. 2009a). The middle row is the start

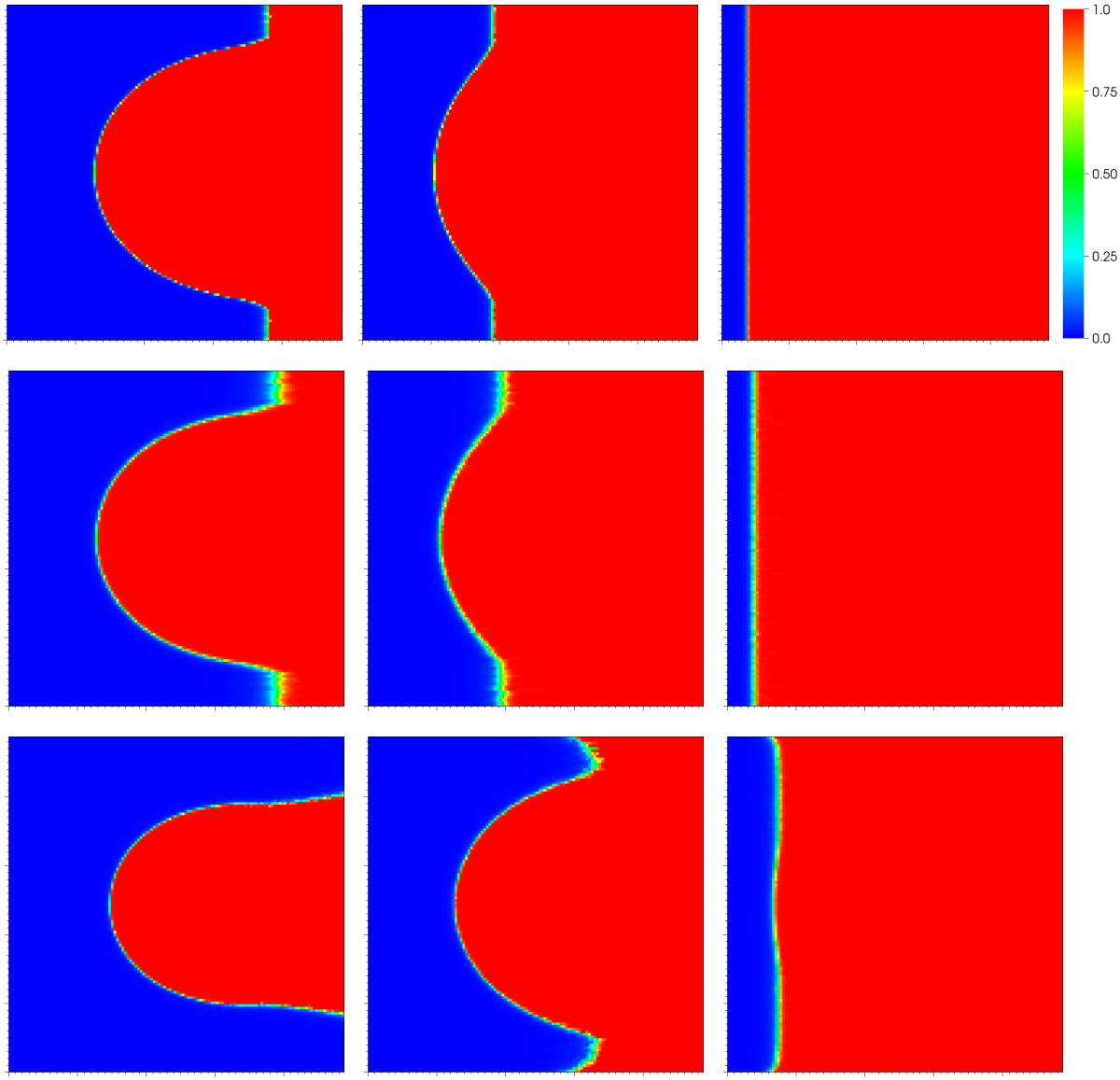

Figure 5.1: Top row) The hydrogen ionization fraction for the OTS monochromatic model. Middle row) The hydrogen ionization fraction for the OTS polychromatic model. Bottom row) The hydrogen ionization fraction for the model which includes the diffuse field. Columns are, from left to right, high, medium and low flux regimes. Each frame is a slice through the computational grid, which is a cube with sides 4.87 pc long. Major ticks are separated by 1 pc.

Table 5.1: Parameters used for the RDI of a BES model.

Variable (Unit)	Value	Description
R_c (pc)	1.6	Cutoff radius
n_{max} (cm^{-3})	1000	Peak BES number density
T_o (K)	10	Initial temperature of grid
γ	1	Adiabatic index
E.O.S	Isothermal	Equation of state
Φ_{lo} (cm^{-2})	9.0×10^8	Low ionizing flux
D_{lo} (pc)	$(-10.679, 0, 0)$	Source position (low flux)
Φ_{med} (cm^{-2})	4.5×10^9	Intermediate ionizing flux
D_{med} (pc)	$(-4.782, 0, 0)$	Source position (medium flux)
Φ_{hi} (cm^{-2})	9.0×10^9	High ionizing flux
D_{hi} (pc)	$(-3.377, 0, 0)$	Source position (high flux)
L(pc^3)	4.87^3	Grid size
n_{cells}	128^3	Number of grid cells
CFL	0.3	CFL parameter

point for the models in which a polychromatic radiation field is considered, but the OTS approximation is still applied. In comparison with the top row, it is clear that the extent of the ionized region has increased slightly and the transition region has been smoothed out. This is due to hard radiation, which penetrates more deeply since the photoionization cross section approximately decreases in proportion to the inverse cube of the photon frequency (see section 2.3.2 and Osterbrock 1989). The bottom row is the starting H I fraction for the models that include the diffuse field. In all three flux regimes the extent of the ionized region is significantly different to that of the other two sets of models. At high flux material in the wings of the model is completely ionized, the medium flux model I-front has significantly wrapped itself around the BES and the low flux model I-front now grazes the BES. Note that the curved I-front wings towards the edge of the low and medium flux models arise because these models do not include periodic photon packet boundary conditions and so these regions are subject to a non-symmetric diffuse ionizing flux.

The logarithmic density distribution for the high, medium and low flux models over all three treatments of the radiation field, are shown side by side at 50, 100, 150 and 200 kyr in Figures 5.2, 5.3 and 5.4 respectively. In each of these figures the monochromatic models are represented by the left hand column, the polychromatic models by the central column and the polychromatic-diffuse models by the right hand column. It is clear that there are some marked differences between the evolutions of the system under the different radiation treatments. A case-by-case study of the evolution of the separate models is given below in sections 5.5.3, 5.5.4 and 5.5.5.

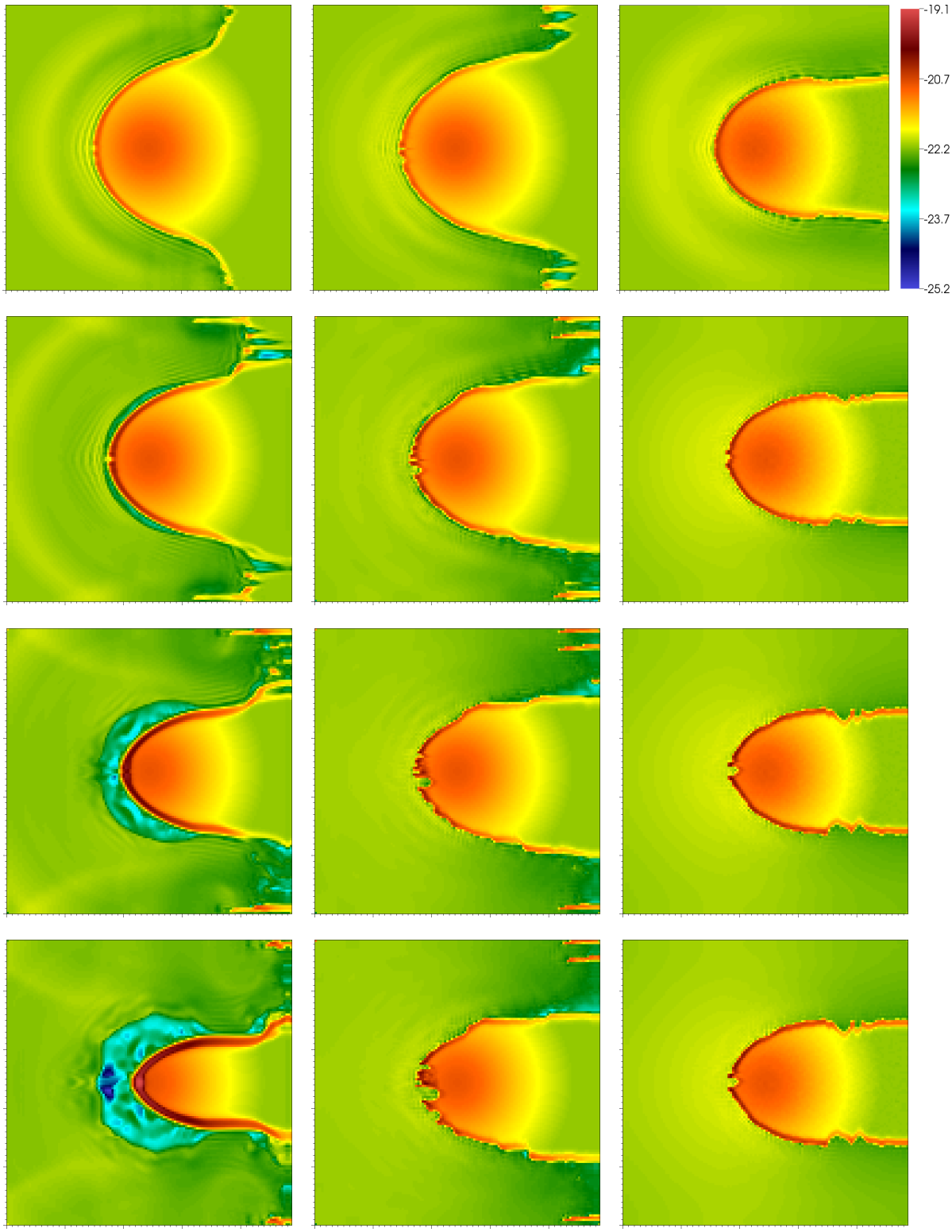

Figure 5.2: The high flux model logarithmic density distributions (cgs). Left column) Monochromatic models. Middle column) Polychromatic models. Right column) Polychromatic-diffuse models. Time is increasing from top to bottom, with snapshots at 50, 100, 150 and 200 kyr. Each frame is a slice through the computational grid, which is a cube with sides 4.87 pc long. Major ticks are separated by 1 pc.

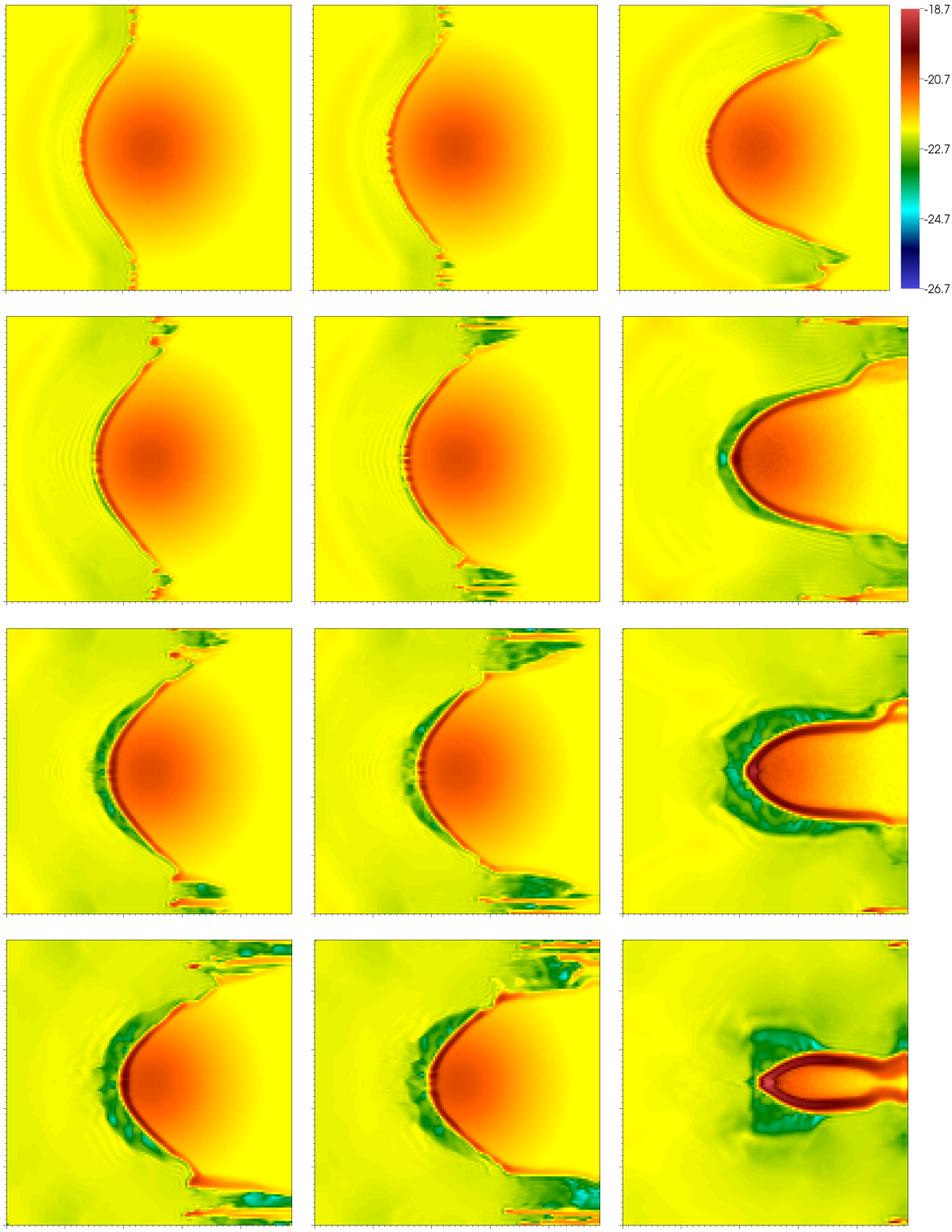

Figure 5.3: The medium flux model logarithmic density distributions (cgs). Left column) Monochromatic models. Middle column) Polychromatic models. Right column) Polychromatic-diffuse models. Time is increasing from top to bottom, with snapshots at 50, 100, 150 and 200 kyr. Each frame is a slice through the computational grid, which is a cube with sides 4.87 pc long. Major ticks are separated by 1 pc.

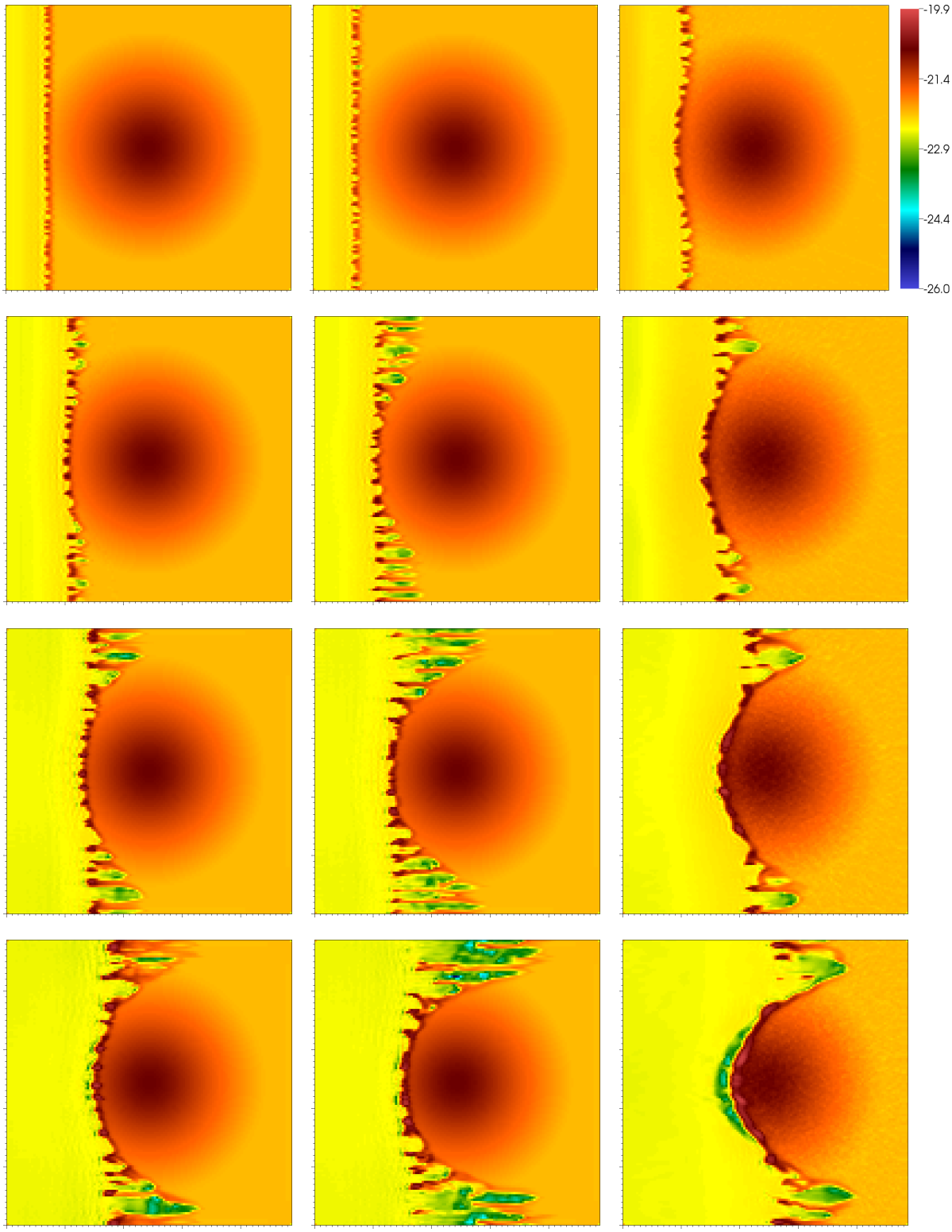

Figure 5.4: The low flux model logarithmic density distributions (cgs). Left column) Monochromatic models. Middle column) Polychromatic models. Right column) Polychromatic-diffuse models. Time is increasing from top to bottom, with snapshots at 50, 100, 150 and 200 kyr. Each frame is a slice through the computational grid, which is a cube with sides 4.87 pc long. Major ticks are separated by 1 pc.

5.5.2 The formation and evolution of instabilities

A number of the models presented here are subject to the formation of instabilities. These arise when the thin shell swept up by the ionization front propagates though the lower density regions of the computational domain such as in the wings or (in the low flux regime) prior to driving into the BES.

There are two main sources of perturbation that may seed these instabilities. The first is 'angle of incidence' Williams (2002) in which regions of the I-front that are not entirely perpendicular to the incoming radiation field are subject to varying ionizing flux and therefore differential acceleration. This may occur as the I-front wraps around the BES. The second is numerically induced perturbation via noise in the calculated ionization fraction. As mentioned in section 3.3 the induced temperature, and therefore pressure, is directly proportional to the calculated ionization fraction (equation 5.1). The resulting pressure gradient then determines the induced advecting velocity. If a thin shell of material does not encounter any disruption in its propagation (like encountering a high density component of a BES) then even a small amount of numerical spread in the ionization fraction along the I-front will eventually lead to it bending on small scales and therefore induce thin shell instabilities (Vishniac 1983; Garcia-Segura & Franco 1996). Once the I-front structure is disrupted, the faster propagating components will lose mass by transfer to the cool neutral neighboring material perpendicular to the direction of the I-front propagation. This leads to an accumulation of material ahead of the slower moving components of the I-front, which further brakes the expansion in these regions. This transport of material also reduces the density in the faster moving components of the I-front, allowing photoionizing radiation to propagate more deeply (c.f. equation 1.6) and accelerate these components of the front further. Improving the accuracy of the ionization fractions in the front will delay the onset of numerically induced instabilities, however they should eventually arise for any non-analytical radiation hydrodynamics code if the I-front is allowed to propagate for long enough without being disrupted by some other means. For example, increasing the number of photon packets by a factor of 100 (a factor 10 improvement in signal-to-noise) allows the I-front to propagate only one cell further before the onset of instability.

It is clear that other radiation-hydrodynamical methods should also seed these instabilities. For example, combining SPH hydrodynamics with ray-tracing will lead to a 'noisy' I-front due to the random-variation of the SPH representation of the density field. Grid-based codes with ray-tracing radiation-transfer will also be susceptible to instabilities as the angular sampling of the radiation field may not coincide perfectly with the axes of the underlying hydrodynamical grid. Of course within star forming regions themselves density perturbations will inevitably lead to the growth of instabilities.

Regardless of the seed of these instabilities in the simulations, their evolution occurs in a manner consistent with the instability studies referenced above and result in 'elephant trunk' structures. Their evolution also highlights interesting differences between the dif-

ferent treatments of the radiation field, the details of which are discussed in the following sections.

5.5.3 High flux models

The high flux density evolutions are given in Figure 5.2 and broadly exhibit two different behaviours. In the polychromatic OTS and polychromatic-diffuse models the system is initially ionized to the extent that a strong shock cannot form quickly enough to effectively drive into the BES. A shock does move away from the ionisation front, but is quickly braked by the BES. Not much material is accumulated in the shell before this point, meaning that only a weak photo–evaporative flow is established (Bertoldi & McKee 1990). The evolution of the resulting structure is then a consequence of rocket motion as heated, dense, material is evaporated away from the surface of the cloud into the low density external material (Oort & Spitzer 1955). The tunnelling of material at the tip and along the length of these models into the cometary structure occurs where there are differences between rocket-motion velocities due to either variations in the accumulated density or the density internal to the shell. An interesting difference between the OTS and diffuse field models is also revealed in the rocket-driven phase, with the OTS model being accelerated only along components facing the ionizing source and the diffuse field model being accelerated across the entire cometary surface due to diffuse-driven photo-evaporation.

On the other hand, the monochromatic OTS model does form a strong shock sufficiently rapidly to effectively drive into the BES, this leads to greater compression and accumulation of material into a relatively thick shell around the edge of the resulting bow structure. To illustrate the early braking of the polychromatic models, the difference in the velocity field between the monochromatic OTS and diffuse models at 50 kyr is illustrated in Figure 5.5. At this point the monochromatic model is still driving a shock into the BES and accumulating material, whereas the polychromatic-diffuse model is beginning a photo-evaporative flow.

In the OTS model, sufficient material is rapidly accumulated for a short, strong, photoevaporative flow to occur prior to substantial braking of the bow. The resulting rocket-motion is therefore much stronger than normal photo-evaporative flow, giving rise to the ejection of a significant amount of material that accelerates the existing shock and carves out a low density wake. Subsequent ejections also occur episodically along the length of the bow that is exposed to ionizing radiation. The result is a disrupted region surrounding the tip of the bow structure in which densities can be excavated to levels lower than the ambient surroundings. A possible cause of the episodic nature of this process is that the outer shell density oscillates about some critical value as the shell sequentially accumulates and ejects. This ‘episodic photo-evaporative ejection’ further drives the collapse very effectively and contracts the bow perpendicularly to the ejection direction, tapering the head of the cometary structure. Figure 5.6 shows the disrupted region around the tip of the bow of the monochromatic model at 180, 185 and 190 kyr and

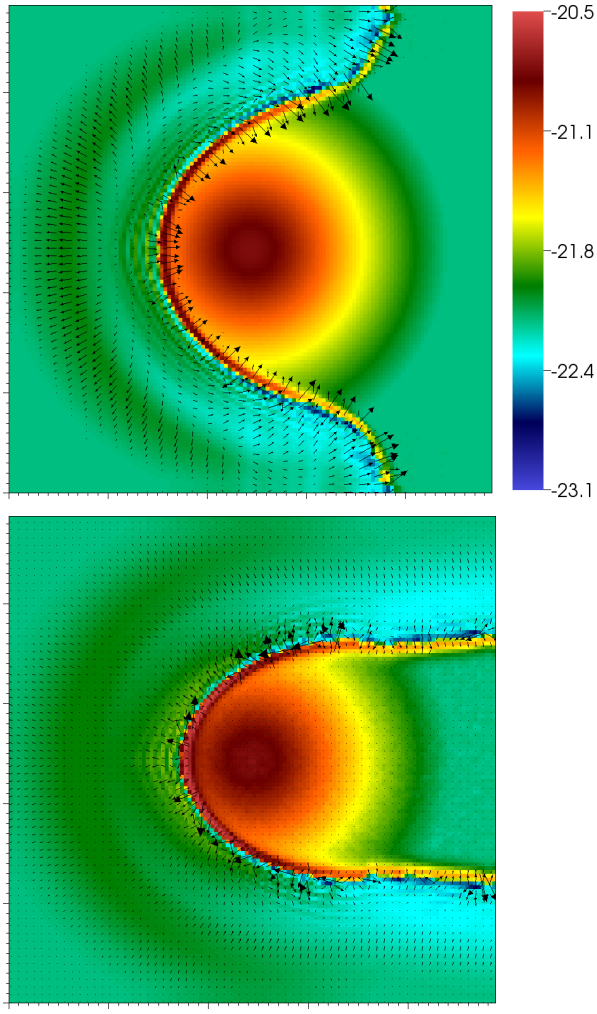

Figure 5.5: The logarithmic density field in $\mathrm{g\,cm^{-3}}$, with velocity vectors, for the high flux models at 50 kyr. This demonstrates the difference between the driving shock of the monochromatic OTS model (top frame) and the photo-evaporative flow of the polychromatic-diffuse model (bottom frame). Each frame is a slice through the computational grid, which is a cube with sides 4.87 pc long. Major ticks are separated by 1 pc. Typical shock (upper frame) and outflow (lower frame) velocities are 5-7 $\mathrm{km\,s^{-1}}$ and 1-4 $\mathrm{km\,s^{-1}}$ respectively.

illustrates the motion of discrete knots of material away from the surface, rather than a continuous stream.

The evolution of the maximum cell densities for each high flux model are shown in the top frame of Figure 5.7. This can be used in conjunction with the appropriate density map to illustrate the rate at which material is collected. Here the maximum density evolution highlights the differences between the two different behaviours noted above. In the polychromatic and polychromatic-diffuse models the maximum density increases at a declining rate and eventually plateaus. The monochromatic model continues accumulating material as it is effectively rocket-driven towards the core of the BES, finishing with a maximum density approximately 4.5 times that of the other models. Star formation at this flux regime will actually occur more slowly when polychromatic radiation or the diffuse field is accounted for than in the simplified calculation.

The formation of thin shell instabilities has little to no impact in the evolution of these models, appearing only in the wings of the polychromatic and monochromatic OTS models and are simply swept off the grid.

5.5.4 Medium flux models

The medium flux density evolution is presented in Figure 5.3 and exhibits the largest difference between the final states of the OTS and diffuse field models. The OTS models both develop shocks that drive effectively into the BES, resulting in rapidly formed high density bow structures. The accumulated density is high enough to give rise to a scaled down version of the episodic photo-evaporatively driven collapse exhibited by the high flux monochromatic model and leads to the same rocket-motion that continues driving material towards the centre of the BES and tapers the bow head. In the wings of the OTS models instabilities form via the mechanism described in section 5.5.2 and propagate linearly, having no effect of the rate of collapse and eventually being swept off of the grid. Note that the low density regions in the wake of these instabilities are not due to photo-evaporative flow, rather they have been excavated by the high velocity instability shocks, with the material funnelled laterally to form knots and elephant trunks.

The diffuse field model behaves slightly differently, resembling a more effectively collapsed version of the monochromatic OTS high flux model. Again a strong shock is developed which drives into the BES and transitions to episodic photo-evaporatively driven collapse. The major difference lies in the wings of the model, which effectively drive into the side of the BES resulting in a final bullet-like structure with a very high density at what was the core of the BES. The reason for this is that a photo-evaporative flow can establish itself along a greater extent of the bow, into regions that would otherwise be shadowed from heating, because of the diffuse radiation field. This results in a whip-like progression of photo-evaporation along the trunk as the shell sequentially becomes dense enough to readily eject material and ceases in the tail regions when the diffuse ionizing flux becomes too low to cause heating. This will most likely result in much more rapid star formation in the model that includes the diffuse field. The evolution of the maximum

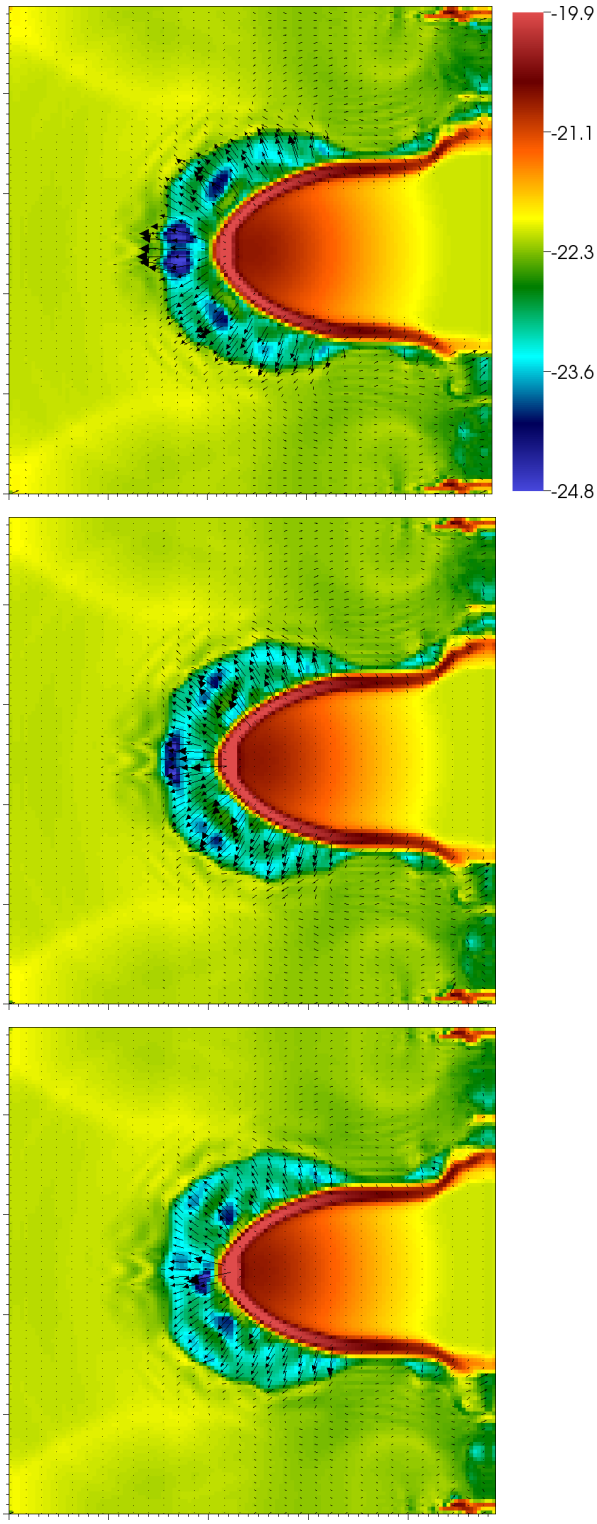

Figure 5.6: Logarithmic density snapshots in $\mathrm{g\,cm^{-3}}$ with velocity vectors for the high flux monochromatic model at 180, 185 and 190 kyr from top to bottom. This illustrates the ejection of distinct knots of material and the evolution of the disrupted region around the tip of the bow. Each frame is a slice through the computational grid, which is a cube with sides 4.87 pc long. Major ticks are separated by 1 pc. Typical velocities in the outflow region of each frame are 25-35 $\mathrm{km\,s^{-1}}$.

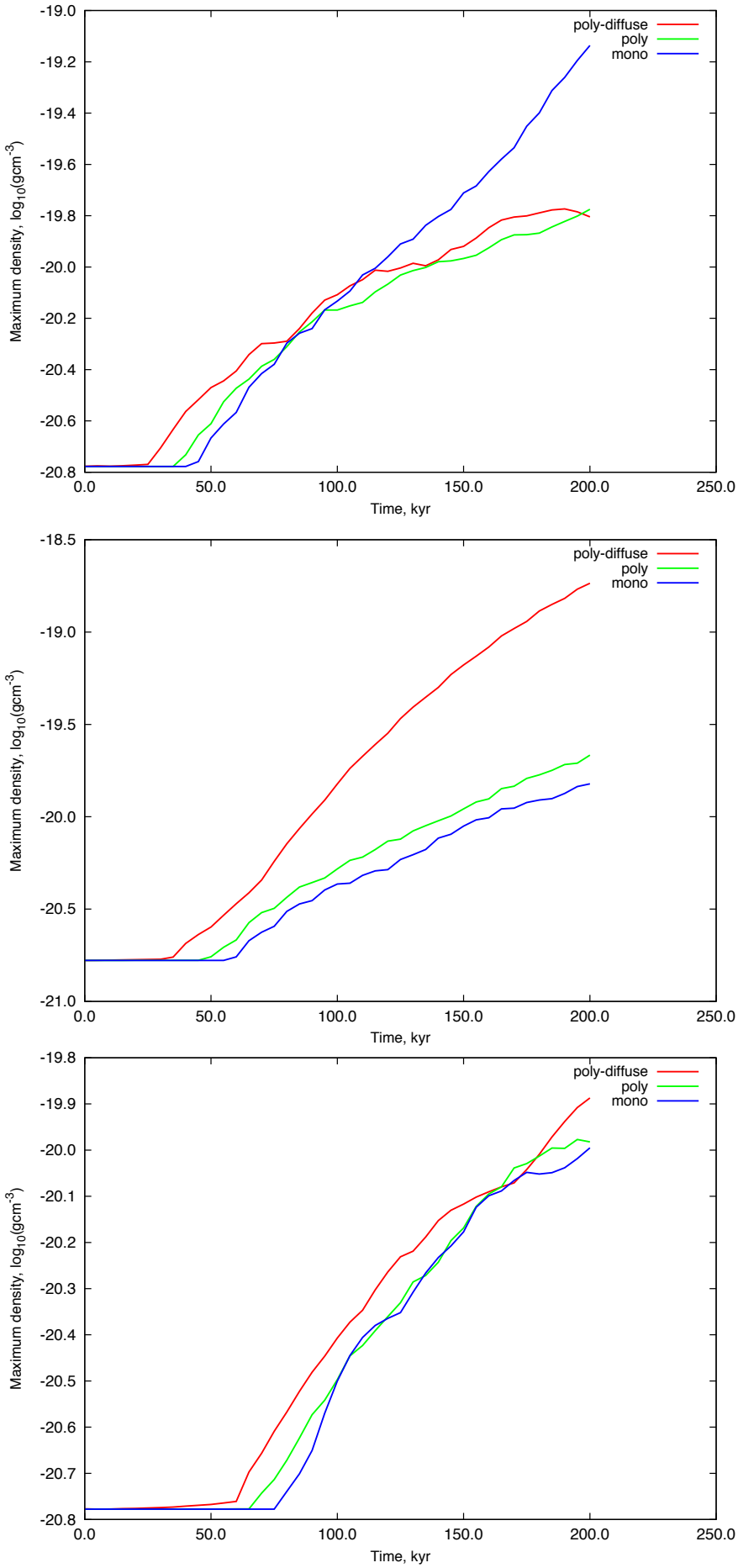

Figure 5.7: The evolution of maximum logarithmic density on the grid with time for the high (top), medium (centre) and low (bottom) flux models.

cell density for these medium flux models is shown in the middle frame of Figure 5.7. This clearly highlights the fairly extreme difference between the OTS and diffuse field models, with a final difference in maximum density at 200 kyr of well over a factor of 10.

5.5.5 Low flux models

The low flux density evolutions are given in Figure 5.4. These models exhibit the largest susceptibility to thin shell instability as instabilities can begin developing across the entirety of the I-front before it impacts the BES. Once the I-front impacts the BES the growth of instabilities is halted, resulting in high density knots along the rim of the resulting bow structure. Those that continue in the wings of the model are elongated into elephant trunks with high density tips via the mechanism described in section 5.5.2. The evolution of these elephant trunks varies with each treatment of the radiation field. The polychromatic OTS trunks are more elongated than the monochromatic ones because hard radiation carves out a path more rapidly. Any compression of the trunks in the OTS models is due to thermal pressure. In the polychromatic-diffuse model, diffuse field radiation effectively drives into the material perpendicular to any displacement in the ionization front and therefore actually prevents the formation of a number of potential trunks by smoothing out dimples. Those trunks that do form will also continue to be both compressed thermally and exposed to diffuse ionizing radiation.

The RDI process for the OTS models occurs very weakly, with more material being accumulated through instability than compression. The diffuse field model drives into the BES more effectively, forming a smoother high density bow compared to the knotted structures of the other models and manages to initiate some photo-evaporative flow. The maximum cell density evolution for the low flux models is given in the bottom frame of Figure 5.7. At 200 kyr the diffuse field model has accumulated only a slightly larger maximum density than the OTS models, though it is clear from Figure 5.4 that it has achieved this order of density over a relatively large volume. The diffuse field model will most likely form stars first and on a larger scale than the models that use the OTS approximation.

These low flux results, comprising a bright rimmed cloud with pillars along its wings, bear resemblance to observed systems such as IC 1848E, as shown in Figure 1 of Chauhan et al. (2011a). In the aforementioned work, instability was suggested as the formation mechanism of the elephant trunks in this region of IC 1848E, my unstable radiatively driven shock driving into a pre-existing density structure supports this hypothesis.

5.5.6 Comparison with iVine

There are some differences between the results obtained here and those of Gritschneder et al. (2009a), the work on which the RDI model parameters in this Chapter are based. In particular the maximum density evolutions derived by TORUS are much weaker, to the extent that no clear gravitational collapse has occurred by 200 kyr. This discrepancy is attributed to the difference in grid size, combined with the use of periodic boundary

conditions. A significant proportion of the compression of the BES in the IVINE models arises because hot gas is advected off the edge of the periodic boundary and impacts the cloud on the opposite side of the grid (see section 4.1.2 of Gritschneder et al. 2009a). This effect is justified by the authors as they assume that the molecular cloud completely surrounds the triggering star, however the effect will still give rise to differences in the results obtained by my models and theirs since motion of the hot gas has longer to decay over my larger grid and is also impeded by the elephant trunks that have formed in the wings of my models. In my models, lateral compression of the BES due to motion in the hot gas through the boundaries has negligible effect and as such the BES can be considered to be isolated.

With regard to the effect of the diffuse field, a comparison with the results found using IVINE/DIVINE (Ercolano & Gritschneder 2011b) is not straightforward as the systems being modelled are very different. However the results here broadly agree that treating the diffuse field can lead to higher density resulting structures. This is particularly prevalent in the medium flux model (section 5.5.4). In the low flux model (section 5.5.5), where elephant trunks of a similar form to those created in the IVINE/DIVINE models arise, there is further agreement in that inclusion of the diffuse field increases the density and decreases the number of elephant trunks that form. In addition, there is agreement that these trunks are narrowed, sometimes to the extent that the head of the trunk can become completely detached.

5.6 Conclusions

It is clear that a direct treatment of the diffuse field has a significant impact upon the evolution of radiation hydrodynamics calculations on parsec scales. Not only is the effectiveness of RDI sensitive to the way in which the radiation field is treated, the formation and evolution of elephant trunk structures via instability also varies.

At low and intermediate flux regimes inclusion of the diffuse field results in more efficient RDI, with both more widespread accumulation of material and, particularly in the medium flux case, a higher final maximum density. In the high flux regime however, the material around the BES is ionized so rapidly in the diffuse and polychromatic OTS models that only a weak shock forms and RDI does not occur effectively. Generally, it is found that the extent to which RDI occurs depends strongly on the strength of the shock that is accumulated prior to driving into the BES. Regardless of the ionizing flux, if only a weak driving shock has formed collapse will occur slowly. When sufficient material is accumulated a photo-evaporative flow is found to occur before the driving shock is braked, reinforcing the shock with the resulting rocket motion. This occurs in short, sharp, bursts with the reason for this episodic behaviour hypothesised as being due to the refilling time for material in the dense shell. The high velocity ejecta carve out material around the head of the cometary structure resulting in a low density disrupted bubble. This rocket motion has a significant effect on the collapse of the BES: with the inclusion of the diffuse

field, it can occur across a large part of the otherwise shadowed region and significantly narrow the resulting cometary structure.

Elephant trunks that arise due to thin shell instability are harder to form in the presence of the diffuse field as the dimples that seed them are smoothed out, and those that do form are then subject to the expected combination of thermal compression and diffuse field photoionizing radiation. Despite this the formation of elephant trunks, as the result of instability in a radiatively driven shock, still occurs and provides a mechanism for the formation of systems such as that discussed in Chauhan et al. (2011a).

The radiation-hydrodynamical effect of the diffuse field is cumulative and significant, and is strongly coupled to the hydrodynamical evolution of the system. This implies that the treatment of the diffuse field should be accurate throughout a simulation, as consistent deficiencies could lead to a systematic change in the overall radiation hydrodynamical evolution of the system.

5.7 Summary

In this Chapter the radiation hydrodynamics module of the TORUS code has been used to investigate the effects of using a monochromatic OTS, polychromatic OTS and polychromatic-diffuse field on the radiatively driven implosion of a Bonnor-Ebert sphere. I have found that incorporating the diffuse field into this model over three flux regimes leads to significantly different results to those obtained using the OTS approximation. At intermediate and low flux regimes the rate of compression is higher than that without inclusion of the diffuse field, whereas at high flux compression actually occurs more slowly when the diffuse or polychromatic OTS field is considered because there is little opportunity for a material shock to drive into the BES. In the event of accumulation of sufficient material, photo-evaporative flow or ejection has been identified as a mechanism which can drive collapse very effectively. This photo-evaporative flow is particularly effective at driving and compressing the tail of the cometary structure when the diffuse field is treated. The formation of elephant trunk structures via instability also occurs much less readily with the inclusion of the diffuse field as perturbations to the ionization front are smeared out. In conclusion, in order to properly address quantitative questions regarding triggered star formation a thorough treatment of the diffuse field is necessary in radiation hydrodynamics models. These low flux results, comprising a bright rimmed cloud with pillars along its wings, bear resemblance to observed systems such as IC 1848E, as shown in Figure 1 of Chauhan et al. (2011a). In the aforementioned work, instability was suggested as the formation mechanism of the elephant trunks in this region of IC 1848E, my unstable radiatively driven shock driving into a pre-existing density structure supports this hypothesis.

I have shown that the way that the radiation field is treated can have important consequences for the way in which RHD calculations evolve. There are other approximations, discussed at the start of this Chapter, which also require testing. For example,

the assumption of photoionisation equilibrium or considering hydrogen–only gas. I am investigating this as part of my ongoing research. In the rest of this thesis I now focus on simulated observations using the results of the models in this Chapter. To test observational diagnostics and to make observationally verifiable predictions of signatures of RDI.

"Would you be so kind as to provide the Proposal Code(s)/Project ID(s) for the VLA observations reported in the paper, HAWORTH et al. "Testing diagnostics of triggered star formation" recently posted to astro-ph?"

Anonymous

6

Testing continuum and atomic line diagnostics of triggered star formation

6.1 Abstract

In this Chapter I produce synthetic images and SEDs from radiation hydrodynamical simulations of radiatively driven implosion from Chapter 5. The imaged bright rimmed clouds (BRCs) are morphologically similar to those actually observed in star forming regions. Using nebular diagnostic optical collisional line ratios, simulated Very Large Array (VLA) radio images, Hα imaging and SED fitting I compute the neutral cloud and ionized boundary layer gas densities and temperatures and perform a virial stability analysis for each cloud. I determine that the neutral cloud temperatures derived by SED fitting are hotter than the dominant neutral cloud temperature by $1-2\,\mathrm{K}$ due to emission from warm dust. This translates into a change in the calculated cloud mass by $8-35\,\%$. Using a constant mass conversion factor (C_ν) for BRCs of different class is found to give rise to errors in the cloud mass of up to a factor of 3.6. The ionized boundary layer (IBL) electron temperature calculated using diagnostic line ratios is more accurate than assuming the canonical value adopted for radio diagnostics of $10^4\,\mathrm{K}$. Both radio diagnostics and diagnostic line ratios are found to underestimate the electron density in the IBL. Each system is qualitatively correctly found to be in a state in which the pressure in the ionized boundary layer is greater than the supporting cloud pressure, implying that the objects are being compressed. I find that observationally derived mass loss estimates agree with those on the simulation grid and introduce the concept of using the mass loss flux to give an indication of the relative strength of photo-evaporative flow between clouds. The effect of beam size on these diagnostics in radio observations is found to be a mixing of the

bright rim and ambient cloud and H II region fluxes, which leads to an underestimate of the cloud properties relative to a control diagnostic.

The research detailed in this Chapter has been published in Haworth et al. (2012), MNRAS, 426, 203.

6.2 Introduction

A central problem in the study of star formation and galaxy evolution is the effect of stellar feedback on star formation rates, efficiencies, and the initial mass function (IMF) (e.g. Dobbs et al. 2011; Elmegreen 2011c; Bate 2012; Elmegreen 2012; Kennicutt & Evans 2012, and references therein). Stellar winds drive into the surrounding material which is expected to either induce star formation by triggering collapse in otherwise stable conglomerations or alternatively to hinder star formation by dispersing material and driving turbulence (example theoretical, observational and synthetic observational studies include Matzner 2001; Smith & Rosen 2005; Arce et al. 2010; Offner et al. 2011). Supernova feedback is another kinematic mechanism whereby the explosions of massive stars locally disperse potential star forming material, but may cause large-scale collapse of nearby gas clouds (see Hensler 2011, and references therein). Young stars, specifically the most massive (i.e. OB), emit large amounts of ionizing radiation into the surrounding gas. This quickly ionizes and heats the surroundings, generating shocks that sweep up material into a shell that can either become locally gravitationally unstable (the collect and collapse scenario - Deharveng et al. 2005; Zavagno et al. 2006; Dale et al. 2007) or drive into pre-existing density structures and compress them to form stars, a process known as radiatively driven implosion (RDI).

RDI has been subject to a large amount of numerical modelling which has repeatedly demonstrated that the compression and implosion of clouds is possible (e.g. Sandford et al. 1982; Bertoldi 1989; Lefloch & Lazareff 1994; Kessel-Deynet & Burkert 2003; Miao et al. 2009; Gritschneder et al. 2009a; Bisbas et al. 2011; Dale & Bonnell 2012b; Haworth & Harries 2012). The resulting objects are usually bow shaped thin dense shells or cometary structures, in qualitative agreement with studies such as the northern hemisphere bright rimmed cloud (BRC) survey of Sugitani et al. (1991), which found that BRCs can be broadly classified by their rim morphology, being either: type A (moderately curved), type B (tightly curved) or type C (cometary).

A number of bright rimmed clouds has been identified in the vicinity of which are collections of young stars (studies include Sugitani et al. 1991; Ogura et al. 2002; Thompson et al. 2004; Lee & Chen 2007; Beltrán et al. 2009; Morgan et al. 2009; Chauhan et al. 2009; Choudhury et al. 2010; Chauhan et al. 2011b; Thompson et al. 2012), these are often cited as examples of triggered star formation via RDI and have been studied using a range of techniques. One of the most popular signatures of triggered star formation is an age gradient in YSOs, with bluer (and therefore supposedly older) sources located in closer proximity to the triggering star. Beltrán et al. (2009) study the BRC IC 1396N in the

Cep OB2 association and caution against this approach, as a collection of stars of similar age may exhibit an apparent observational age gradient if they are sequentially exposed to high ionizing flux and stripped of their circumstellar environment.

An alternative to studying stellar age gradients is to analyze the neutral cloud and ambient ionized gas properties. Lefloch & Lazareff (1994) calculated semi-analytic two dimensional models of RDI and included figures of the system emissivity which were found to have similar morphology to the BRC types observed in star forming regions. They further compared the cloud and ionized boundary layer (IBL) pressures using a multiwavelength molecular line and radio emission study of CG5 in IC1848 (Lefloch et al. 1997) and found greater pressures in the IBL by approximately a factor of 10, indicative of shock compression. They also calculated an estimate of the incident ionizing radiation flux and mass loss rates, finding values of $4.8 \times 10^9\,\mathrm{cm}^{-2}\,\mathrm{s}^{-1}$ and $105\,\mathrm{M}_\odot\,\mathrm{Myr}^{-1}$ respectively. Thompson et al. (2004) and Morgan et al. (2004) performed a similar analysis on a larger number of clouds, finding that for only a small number the IBL is at higher pressure and that more frequently the objects are in pressure balance. The aforementioned studies suggest that greater external pressure will lead to the eventual dispersal of the cloud, whereas clouds that are overpressured relative to the surroundings will stall the shock until enough material is accumulated and the pressure sufficiently increased to continue driving into the cloud. The presence of photo-evaporative flow in Lefloch & Lazareff (1994) and Thompson et al. (2004) is also an important factor in identifying RDI. In addition to calculating the mass loss rate, striations in Hα imaging about the BRC is identified as an indication of such a flow.

In this Chapter I use the final state of the RDI models generated in Haworth & Harries (2012) (Chapter 5 that incorporated the diffuse field. These calculations considered the RDI of a Bonnor-Ebert sphere at three distances from the triggering star and gave rise to clouds that appear to be type A (the low flux model), B (the high flux model) and type B-C (the medium flux model). These models also vary in the nature of the driving shock, with the medium and low flux models being driven by a photoionizing shock/photo-evaporative flow and the high flux model in pressure balance. With these final grid states I perform synthetic Hα and radio continuum imaging, as well as generate synthetic SEDs to perform standard diagnostics that look for RDI. I also explore the use of long slit spectroscopy to calculate diagnostic forbidden line ratios, determine the nebular conditions and infer the stability of the BRCs. In addition I investigate the observational characteristics of photo-evaporative flows and mass loss rate calculations. This is all performed from the unique perspective in which the actual conditions of the system are known. Through this process I aim to guide observers towards unambiguous signatures of triggered star formation in BRCs and to investigate the accuracy and applicability of these standard diagnostic techniques.

6.3 Numerical Method

6.3.1 Overview

The grid based radiation transport and hydrodynamics code TORUS (Chapter 3 Harries 2000; Acreman et al. 2010a; Harries 2011; Haworth & Harries 2012) is used to perform the calculations in this Chapter. Using the final states of the models which included the diffuse field in Haworth & Harries (2012) I perform photoionization calculations with additional atomic species. Dust is then added to the resulting grids as part of post processing and the final grid states are used to generate SEDs and images for diagnostics.

6.3.2 Photoionization

The photoionization routine follows that detailed in Chapter 3 and the papers Ercolano et al. (2003), Wood et al. (2004) and Haworth & Harries (2012). The diffuse field is included in models in this Chapter. I also include periodic photon packet boundary conditions, without which the ionizing flux at the edges of the grid can be underestimated if the model geometry is periodic. However, in order to avoid long loops for low frequency packets which have a small probability of interaction, each photon packet is only allowed to cross a periodic boundary once. Ionization balance in all calculations is determined by solving the ionization balance equation (Osterbrock 1989) and photoionization equilibrium is assumed. In this Chapter I include treatment of a range of atomic constituents: hydrogen, helium, carbon, nitrogen, oxygen, neon and sulphur. Thermal balance is calculated by finding the temperature at which the heating and cooling rates match in the manner described in Wood et al. (2004). Hydrogen and helium heating is treated as well as recombination, free-free and collisional line cooling.

6.3.3 Synthetic Imaging and SEDs

Synthetic images are generated by accumulating photon packets from the grid in a 2D array of collecting bins. The basic method follows the Monte Carlo scheme detailed in Hillier (1991) and Harries (2000), an example application is Kurosawa et al. (2004). For an observer location (which can be specified arbitrarily) relative to the grid, a pixel array is generated. The emissivity across the grid is then calculated and can include dust continuum, free-free continuum, forbidden and recombination line radiation. The image is constructed by propagation of photon packets from dust, gaseous and stellar sources, with each packet carrying power P given by

$$P = \frac{L_* + W_{\rm tot}}{N_{\rm monte}} \tag{6.1}$$

where L_*, $W_{\rm tot}$ and $N_{\rm monte}$ are the total stellar source emission, the total emission from the gas and dust and the number of photon packets used in the image generation respectively.

The Monte Carlo method is subject to Poisson noise analogous to that inherent in the collection of photons in real imaging, therefore we employ variance reduction tech-

niques to reduce the calculation time required to reach adequate signal to noise. To improve sampling in the gas the probability of a photon packet originating from a stellar source is fixed at 0.1 and the packet assigned an appropriate weight w. Following initial generation and each scattering event of photon packets, an additional packet is forcibly directed towards the observer with a modified weighting the, so called, 'peel-off' technique (Cashwell & Everett 1959; Yusef-Zadeh et al. 1984). Once a photon packet escapes the grid in the direction of the observer it changes the flux F_γ in whichever pixel it intersects to

$$F_{\gamma+1} = F_\gamma + \frac{Pw\mathrm{e}^{-\tau}}{4\pi} \tag{6.2}$$

where w is the photon packet weight and τ is the optical depth along the packet's path to the observer. The accumulated photon packet contributions are converted into a final image in distance independent units of mega Janskys per steradian.

Spectral energy distributions are also generated via Monte Carlo radiative transfer in a similar manner. Rather than contributing to a 2D pixel array photon packet intensities are binned by frequency to form the SED (see Kurosawa et al. 2004).

Dust properties

Dust is not directly included in the photoionization calculations in this Chapter, rather it is added to all cells where the temperature is less than 1500 K prior to image/SED generation (e.g. Dullemond et al. 2001). Unless otherwise specified, a dust to gas mass ratio of 1×10^{-2} is used in all images generated in this Chapter. The dust model used assumes spherical silicate dust particles that follow a standard interstellar medium power-law size distribution (e.g. Mathis et al. 1977). The optical constants are taken from Draine & Lee (1984). A pre-tabulated Mie-scattering phase matrix is used. The wavelength dependency of the dust opacity (per gram of dust) and albedo are given in Figures 6.1 and 6.2 respectively.

6.3.4 Radio Imaging

Synthetic images generated at radio wavelengths using the method described in section 6.3.3 will have a sub-pixel beam and a Poisson noise level determined by the number of photon packets used in the image generation, at a level that is possibly lower than the Gaussian noise associated with radio imaging. I therefore modify images at these wavelengths as part of post processing. The image is smoothed to a Gaussian beam using ACONVOLVE from CIAO v4.1 (Fruscione et al. 2006) to a size appropriate to the half power beamwidth (HPBW) of the simulated instrument. It is assumed that the Gaussian smoothing outlined above extinguishes the effects of Poisson noise (which is relatively small) and then Gaussian noise is added to the image separately using the STARLINK ADDNOISE routine. The emulated exposure time, beam size and noise level are chosen to be typical of those for a given instrument.

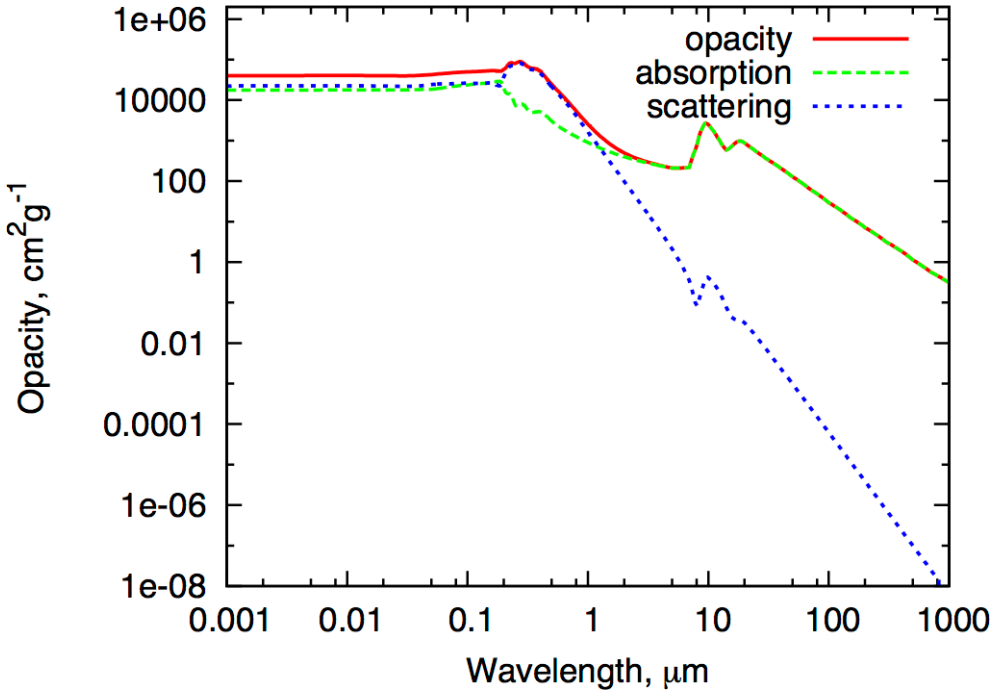

Figure 6.1: The dust model opacities (absorption, scattering and total) as a function of wavelength. Note that the opacity is per gram of dust.

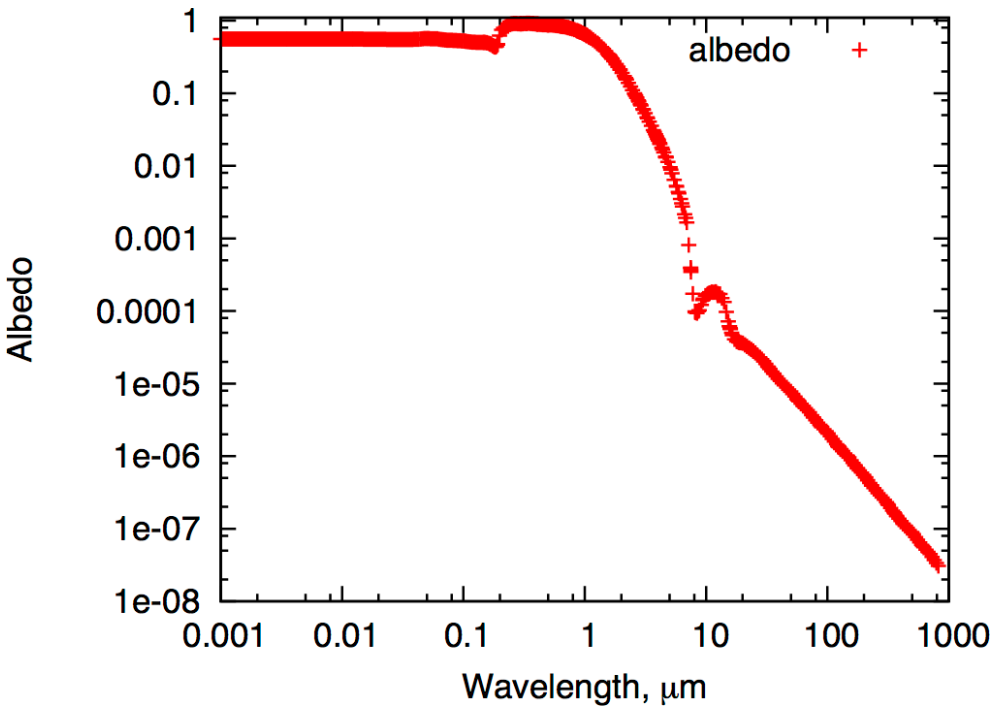

Figure 6.2: The dust model albedo as a function of wavelength.

6.4 Diagnostic Techniques

To determine what an observer would infer following observations of my model clouds a range of standard diagnostic techniques are employed that are used to determine the ionized and neutral gas properties.

6.4.1 Neutral cloud properties from SED fits

In this work no molecular lines are treated. The neutral cloud gas properties are therefore obtained by fitting the submillimetre thermal dust continuum tail of the object SED with a greybody function of the form

$$F_\nu = \Omega B_\nu(T_\mathrm{d})\left(1 - \mathrm{e}^{-\tau_\nu}\right) \tag{6.3}$$

where Ω, $B_\nu(T_\mathrm{d})$ and τ_ν are the solid angle subtended by the region for which the temperature is being derived, the frequency specific Planck function at dust temperature T_d and the optical depth at frequency ν respectively (Hildebrand 1983; Dent et al. 1998; Thompson et al. 2004; Morgan et al. 2008). A procedure is adopted in which the optical depth at a given frequency is paramaterized in terms of a reference frequency and optical depth i.e.

$$\tau_\nu = \tau_\mathrm{ref}\left(\frac{\nu}{\nu_\mathrm{ref}}\right)^\beta \tag{6.4}$$

(e.g. Hildebrand 1983). The reference wavelength is chosen to be 850 μm and a value of 2 is adopted for β, the index specifying the frequency dependency of the dust emissivity, following Hildebrand (1983), Thompson et al. (2004) and Morgan et al. (2008). The reference optical depth is calculated using the equation for submillimetre optical depth from Hildebrand (1983)

$$\tau_\nu = F_\nu\left[\pi\theta_\mathrm{R}^2 B_\nu(T_\mathrm{d})\right]^{-1} \tag{6.5}$$

where θ_R is the angular radius of the region over which the flux is being integrated in radians. The SED is fitted using a chi-square minimization. Although a fit could be performed across an entire calculated spectrum, I typically do so over only a small range in the manner of observational studies such as Thompson et al. (2004). The cloud mass is then found using the established method of Hildebrand (1983), whereby the total gas and dust mass of the cloud is given by

$$M = \frac{d^2 F_\nu C_\nu}{B_\nu(T_\mathrm{d})} \tag{6.6}$$

where d is the distance of the cloud from the observer and C_ν is a mass conversion factor. I use the flux density at 850 μm. A value for C_ν (specifically C_ν at 850 μm or 345 GHz, C_{345}) needs to be appropriately selected (Hildebrand 1983; Draine & Lee 1984; Ossenkopf & Henning 1994; Kerton et al. 2001). Typically, smaller values of C_ν apply to cold, high

density, regions and larger values to low density regions (e.g. the diffuse ISM). As an example, the value selected by Thompson et al. (2004) for 850 μm analysis of clouds with assumed densities of $10^5\,\mathrm{cm}^{-3}$ is $50\,\mathrm{g\,cm}^{-2}$. An expression for C_ν is given by Hildebrand (1983)

$$C_\nu = [N_\mathrm{H}/\tau_\nu]\, m_\mathrm{H}\mu \tag{6.7}$$

where N_H is the column density, m_H the hydrogen mass and μ is the mean particle mass relative to hydrogen, which I assume to be 1.36 in neutral gas following, e.g. Hildebrand (1983); Blitz & Rosolowsky (2006). C_ν can also be expressed in terms of the opacity κ_ν and the gas and dust densities

$$C_\nu = \frac{1}{\kappa_\nu}\left[\frac{\rho_\mathrm{gas} + \rho_\mathrm{dust}}{\rho_\mathrm{dust}}\right] \tag{6.8}$$

which has the advantage that the dust to gas ratio and opacity is defined by TORUS. At 850 microns the value of C given by equation 6.8 is $240\,\mathrm{g\,cm}^{-2}$. The model clouds are not supported by turbulent motions owing to the ideal starting conditions. I assume that the sound speed in the neutral gas is isothermal and is calculated using the fitted dust temperature.

6.4.2 Ionizing flux, mass loss rates and IBL electron densities from radio emission

The conditions in the IBL of the BRC are calculated following the standard radio diagnostics of Lefloch et al. (1997) which are used in, for example, Morgan et al. (2004), Thompson et al. (2004) and Urquhart et al. (2006). This technique does not constrain the temperature in the IBL so the standard value of 10^4 K is assumed, following the aforementioned studies.

An observational estimate of the ionizing flux Φ per square centimetre per second impinging upon the BRC can be made from the 20 cm free-free emission integrated flux from the IBL by rearranging equation 6 from Lefloch et al. (1997)

$$\Phi = 1.24 \times 10^{10} F_\nu T_\mathrm{e}^{0.35} \nu^{0.1} \theta^{-2} \tag{6.9}$$

where T_e is the electron temperature of the ionized gas in K, θ is the angular diameter in arcseconds of the region over which the flux is integrated and F_ν is the integrated flux in mJy at frequency ν in GHz.

The electron density can also be calculated using

$$n_\mathrm{e} = 122.41 \sqrt{\frac{F_\nu T_\mathrm{e}^{0.35} \nu^{0.1} \theta^{-2}}{\eta R}} \tag{6.10}$$

where η is the thickness of the ionized boundary layer as a fraction of the cloud radius and R is the cloud radius in parsecs (Lefloch et al. 1997). Bertoldi (1989) give η typically ≈ 0.2 which is the value adopted by Morgan et al. (2004), Thompson et al. (2004) and

Urquhart et al. (2006), I therefore also assume this value. The electron density allows the ionized boundary layer gas pressure to be derived using

$$P_{\rm i} = 2\rho_{\rm i} c_{\rm i}^2 \tag{6.11}$$

where $P_{\rm i}$, $\rho_{\rm i}$ and $c_{\rm i}$ are the pressure, density and sound speed in the ionized boundary layer (e.g. Morgan et al. 2004; Thompson et al. 2004). I assume that in the ionized regions where these diagnostics are applied that $\rho_{\rm i} = n_{\rm e} m_{\rm H}$ and that the sound speed is isothermal, i.e. $c_{\rm i} = \sqrt{k_{\rm B} T_{\rm e}/\mu m_{\rm H}}$, where $k_{\rm B}$ is the Boltzmann constant and μ is the mean particle mass relative to hydrogen, here assumed to be 0.6 in the IBL, the value for ionized gas of solar composition.

The mass loss rate from the cloud due to ionized gas streaming away from the surface (photo-evaporative flow) is calculated using

$$\dot{M} = 4.4 \times 10^{-3} \Phi^{1/2} R^{3/2} {\rm M}_\odot {\rm Myr}^{-1} \tag{6.12}$$

where R is the cloud radius in parsecs (Lefloch & Lazareff 1994; Thompson et al. 2004). Haworth & Harries (2012) identified strong photo-evaporative flows from some of the RDI model clouds that are studied here and so will provide a valuable test of the equation 6.12 estimate.

6.4.3 H α emission

I generate images of H α recombination emission as it has previously been used to identify photo-evaporative flow via striations perpendicular to the bright rim (Thompson et al. 2004). Imaging at this wavelength (6563 Å) is also useful for tracing ionized gas and is regularly used as a basis for identifying regions over which to perform long slit spectroscopy (e.g. Tüllmann et al. 2003).

6.4.4 IBL properties from optical collisional line ratios

The conditions of H II regions and planetary nebulae have long been studied using ratios of forbidden lines that are sensitive to the electron density or temperature (e.g. Osterbrock 1989; Spitzer 1998; Caplan et al. 2000; Deharveng et al. 2000; Lagrois et al. 2012, and references therein). Single forbidden lines have been used in studies to identify pre main sequence (PMS) stars in and around BRCs as an indicator of triggered star formation (e.g. Lee et al. 2005; Lee & Chen 2007). However, the line ratios have not yet been applied to calculating the IBL properties and hence the relative pressures of the IBL and the neutral cloud. I therefore derive the ionized gas conditions using these diagnostic ratios, in addition to the radio analysis, to assess their future use as a tool for identifying RDI.

Forbidden line intensities are usually obtained by performing slit spectroscopy of the system (e.g. Tüllmann et al. 2003). I emulate this form of analysis by generating synthetic images at a range of forbidden line wavelengths and calculating the intensity

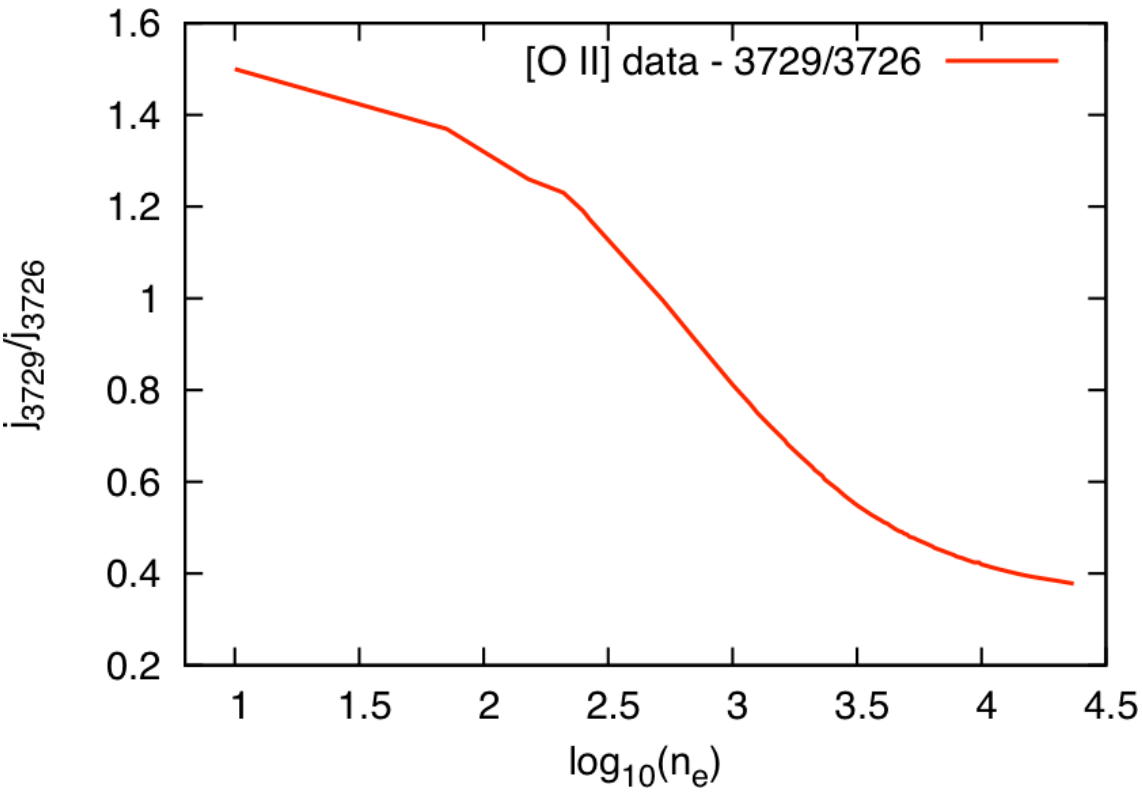

Figure 6.3: The [O II] (3729 Å/3726 Å) ratio variation with logarithmic electron density.

across a pseudo-slit region on the image. This is akin to choosing the intensity at a specific wavelength on the slit spectrum.

I calculate the electron density using the [O II] 3729Å/3726Å ratio by linearly interpolating between the tabulated ratio and electron density values given in Table 2 of Wang et al. (2004) as well as some values from Table 5.2 of Osterbrock (1989). I assume a maximum ratio of 1.5, determined by the ratio of the level statistical weights (Osterbrock 1989) and use a corresponding minimum electron density of $10\,\mathrm{cm}^{-3}$. The resulting variation in the collisoinal line ratio as a function of logarithmic electron density is given in Figure 6.3. This electron density value is then used in one of the many low density limit ($n_\mathrm{H} < 10^5\,\mathrm{cm}^{-3}$) expressions available for the ratio value as a function of temperature and electron density for a temperature sensitive line (e.g. Osterbrock 1989). The [O III] line ratio

$$\frac{j_{\lambda 4959} + j_{\lambda 5007}}{j_{\lambda 4363}} = \frac{7.90\exp(3.29\times 10^4/T)}{1 + 4.5\times 10^{-4} n_\mathrm{e}/T^{1/2}} \tag{6.13}$$

the [N II] line ratio

$$\frac{j_{\lambda 6548} + j_{\lambda 6583}}{j_{\lambda 5755}} = \frac{8.23\exp(2.50\times 10^4/T)}{1 + 4.4\times 10^{-3} n_\mathrm{e}/T^{1/2}} \tag{6.14}$$

and the [Ne III] line ratio

$$\frac{j_{\lambda 3869} + j_{\lambda 3968}}{j_{\lambda 3343}} = \frac{13.7 \exp(4.30 \times 10^4/T)}{1 + 3.8 \times 10^{-5} n_{\rm e}/T^{1/2}} \tag{6.15}$$

are all used in this Chapter.

Hence from one electron density sensitive line ratio and one temperature sensitive ratio an estimate of the electron density and temperature in the ionized gas can be obtained. With an estimate of the temperature and electron densities the pressure is calculated using equation 6.11. This method has the advantage that the temperature of the ionized gas is determined directly, rather than being assumed to be 10000 K as is the case for the radio diagnostics (e.g. Thompson et al. 2004).

6.5 Testing

The TORUS radiation hydrodynamics scheme is tested extensively in Chapter 4 and Haworth & Harries (2012). There are also numerous applications of the imaging and SED generating routines available in the literature (e.g. Harries et al. 2004; Kurosawa et al. 2004). Tests of the ratio diagnostics and the SED fitting are given here.

6.5.1 Diagnostic line ratio testing: the H ii40 Lexington benchmark

The H II40 Lexington benchmark involves, in one dimension and assuming no time evolution, calculating the temperature and ionization structure of the gas surrounding a star at 40000 K (see Ferland 1995, and section 4.4.1). Given the well studied nature of this temperature distribution it is an ideal test of the accuracy of the forbidden line ratio diagnostics. I perform a photoionization calculation of a three dimensional version of the H II40 benchmark with the ionizing star set at the grid centre and apply forbidden line ratio diagnostics to synthetic images of the converged system. Given the large amount of neutral foreground material and the low dust fraction in the hot H II region, the dust to gas ratio in this test is set to a negligibly small value. The model resolution, number of image pixels and slit size are chosen to match that of the RDI grids, images and emulated slit spectroscopy of BRCs used later in this Chapter. A list of the parameters used in the H II40 benchmark and associated imaging is given in Table 6.1.

The converged temperature state of the grid is given in Figure 6.4 and a colour composite image comprising Hα (red) the 5007 Å [O III] line (green) and the 3968 Å [Ne III] line (blue) is given in Figure 6.5, upon which is marked the region covered by the spectroscopic slit. In addition to the slit location in Figure 6.5, I repeat the diagnostics for slit positions at $\pm 1, 2$ pixels in the x-direction to determine the level of uncertainty when using a single slit position to infer the conditions. The average electron density calculated using the [O II] diagnostic ratio and temperature calculated using the [O III], [N II] and [Ne III] diagnostic ratios are given in Table 6.2. The prescribed hydrogen number density is 100 cm^{-3}, which is slightly higher than the inferred electron density. The HI

Table 6.1: Parameters for the H II40 Lexington benchmark which is used to test diagnostic line ratios.

Variable (Unit)	Value	Description
$T_{\rm eff}$(K)	40000	Source effective temperature
$R_*(R_\odot)$	18.67	Source radius
$n_{\rm H}$ (cm^{-3})	100	Hydrogen number density
$\log_{10}$(He/H)	-1	Helium abundance
$\log_{10}$(C/H)	-3.66	Carbon abundance
$\log_{10}$(N/H)	-4.40	Nitrogen abundance
$\log_{10}$(O/H)	-3.48	Oxygen abundance
$\log_{10}$(Ne/H)	-4.30	Neon abundance
$\log_{10}$(S/H)	-5.05	Sulphur abundance
L (pc^3)	16^3	Computational domain volume
$n_{\rm cells}$	128^3	Number of grid cells
$n_{\rm pix}$	401^2	Synthetic image pixels
N_γ	10^8	Photon packets used in synthetic image generation
$L_{\rm s}$ (pixels)	100	Spectroscopic slit length
$W_{\rm s}$ (pixels)	2	Spectroscopic slit width

Table 6.2: The Lexington H II40 test average conditions from diagnostics using a spectroscopic slit at 5 locations.

Ratio	$n_{\rm e}$ (cm^{-3})	$T_{\rm e}$ (K)
[O II], j_{3729}/j_{3726}	88 ± 2	–
[O III], $(j_{5007} + j_{4959})/j_{4363}$	–	$7215\pm^{6}_{7}$
[N II], $(j_{6583} + j_{6548})/j_{5755}$	–	$8366\pm^{4}_{3}$
[Ne III], $(j_{3968} + j_{3869})/j_{3343}$	–	$7474\pm^{6}_{9}$

fraction throughout the grid is not uniformly zero, however this accounts for less than 1 cm^{-3}. Comparing the linear interpolation between the [O II] data points with a more sophisticated fit also only leads to an improvement of 3 cm^{-3}. The remaining discrepancy is therefore believed to be characteristic of the diagnostic ratio.

Although there is some variation between the calculated temperatures, they all lie within the 7000-10000 K range expected from Figure 6.4. The actual average temperature of the volume through the H II region covered by the slit is 7769 K, within 600 K of each diagnostic and within 85 K of the diagnostic average. Based on the uncertainties in individual diagnostics calculated in this test, further electron densities derived in this Chapter using the [O II] line ratio are conservatively calculated to the nearest 10 cm^{-3} and individual temperatures derived using the [O III], [N II] and [Ne III] line ratios are calculated to the nearest 10 K.

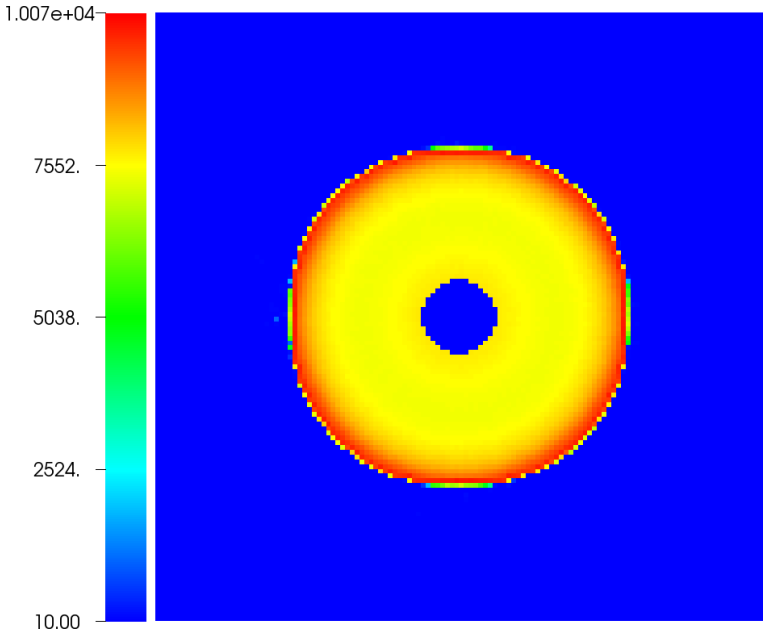

Figure 6.4: A slice through the three dimensional temperature distribution of the H II40 Lexington test. The colour scale indicates the temperature in Kelvin. The image is 4 pc to a side.

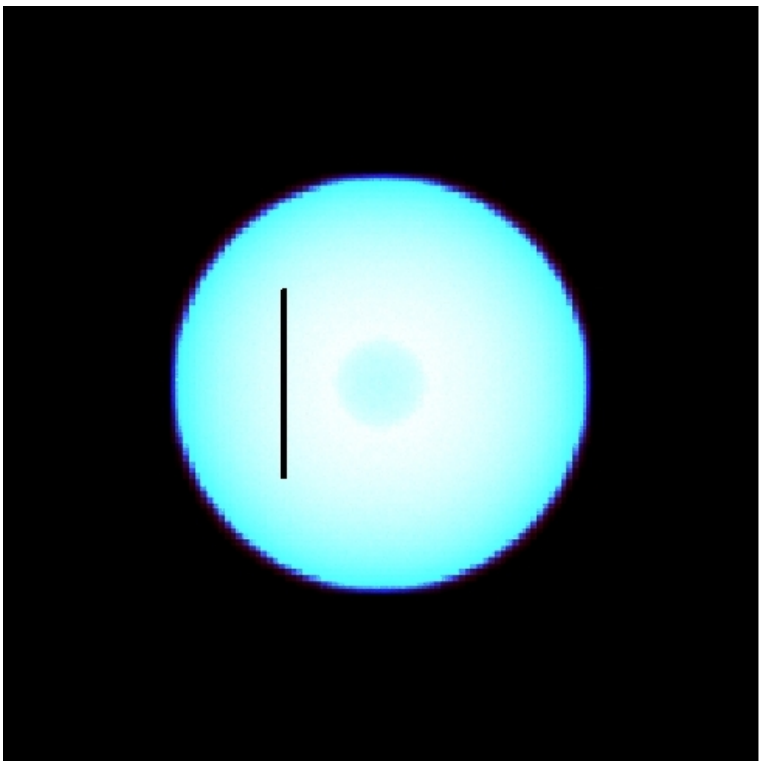

Figure 6.5: A colour composite image of the H II40 test using Hα (red), the [O III] 5007 Å line (green) and the [Ne III] 3968 Å line (blue). Overlaid is the slit region used to emulate slit spectroscopy.

Table 6.3: Cold uniform sphere fitted masses.

C_{345} ($g\,cm^{-2}$)	Mass $M_\odot$
50	9.9
100	19.8
200	39.6
214	42.4
250	49.5

6.5.2 SED greybody fit testing: a cold uniform sphere

To test the cloud masses and temperatures derived by greybody SED fitting I consider the simple system that is a three dimensional uniform density sphere at constant temperature, surrounded by vacuum. I choose a density of 100 hydrogen atoms per cubic centimetre and a cloud radius of 1.6 pc (equivalent to the cut-off radius of the starting Bonnor-Ebert sphere in the models of Haworth & Harries 2012). The density in the surrounding material is set to a negligibly low value so that it will not contribute to the SED. The model is prescribed a uniform temperature distribution of 10 K throughout the grid.

I produce an SED for an observer situated 1000 pc from the grid. The spectrum is fitted in the manner described in section 6.4.1 from 450 μm to 850 μm following Thompson et al. (2004) and is shown in Figure 6.6. The value of β used in equation 6.4 is fixed at 2, meaning that the only free parameter in the fitting is the dust temperature. The resulting calculated temperature is 9.5 K, within 5 per cent of the prescribed value.

The total mass of this cloud is 42.4 $M_\odot$. I use a range of values for C_{345} to calculate a fitted mass from the SED, the results of which are given in Table 6.3. I find that the most appropriate value of C_{345} for number densities of order 100 cm^{-3} at low temperatures is 214 $g\,cm^{-2}$. Given that the dust to gas ratio (prescribed at 1:100) and opacity is known (from figure 6.1) using equation 6.8 I estimate the value of C_{345} (that at 850 μm, 345 GHz) to be 240 $g\,cm^{-2}$. This differs from the best value found above by 11 per cent. This difference is accounted for by the slight underestimate of the dust temperature given by the SED fit, which appears in the denominator of the mass calculation in the planck function. The ratio of the planck function at 345 GHZ using temperatures of 10 and 9.5 K does recover a difference of 11 per cent.

C_{345} can also be estimated using equation 6.7. The average column density over the uniform sphere is $1.3 \times 10^{20}\,cm^{-2}$, the optical depth calculated using equation 6.5 is 2.2×10^{-6} and the corresponding C_{345} value using equation 6.7 is 131 $g\,cm^{-2}$, which differs from the expected value by 45 per cent. The reason for the discrepancy in the estimate derived using equation 6.7 is likely due to averaging the large variations in column density across the sphere, from its maximum value at the centre to approximately zero at the edge. Given that densities of order $100\,m_H\,cm^{-3}$ are typical of the neutral clouds in the RDI models, I retain the presently inferred value of $C_{345} = 214\,g\,cm^{-2}$ in further SED fitting in this Chapter. I note that a simple linear scaling can be used to transform between

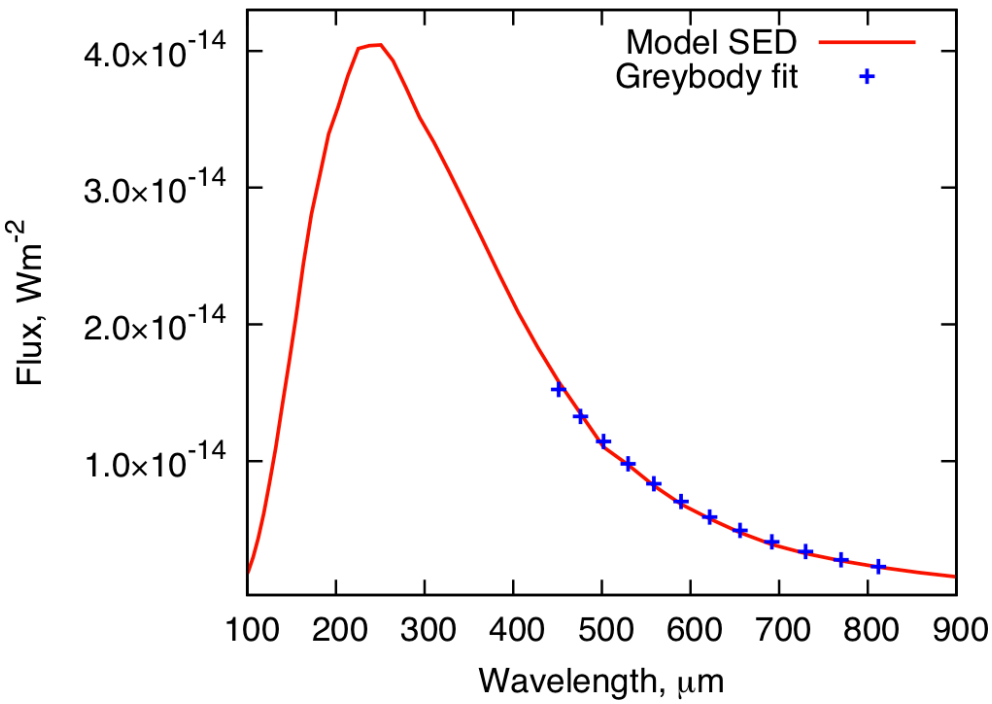

Figure 6.6: The uniform cloud model SED (red line) and the greybody fit (blue crosses).

6.6 Results and Discussion

6.6.1 The numerical models

I add atomic species to the final state (after 200 kyr of evolution) of the RDI models in Chapter 5 and perform photoionization calculations. The three models, each of which comprised a Bonnor-Ebert sphere (BES) exposed to a different level of ionizing flux (high, medium and low), underwent thermal and photo-evaporative compression. The low flux model exhibited thermal compression of the BES and intermediate strength photo-evaporative flow, resulting in a type A bow. Instabilities in the ionization front also led to the formation of finger like objects in the wings of the low flux model. The medium flux model quickly accumulated a dense shell of material resulting in strong photo-evaporative flow that compressed the cloud to a type B-C cometary bow. The high flux model rapidly established pressure balance and exhibited only weak photo-evaporative flow, leaving what resembles a type B bow. A summary of the key parameters of these models is given in Table 6.4.

The temperature state of each model following the full photoionization calculation is given in Figure 6.7. In each model, typical ionized gas temperatures range from $7000 - 10000$ K and neutral temperatures are essentially uniform at 10 K. Of the cells with an HI ionization fraction greater than 0.5 and temperature less than 1500 K (i.e. the neutral cloud): 97%, 96% and 98% are at 10 K for the low, medium and high flux models respectively. By mass 96%, 95% and 98% of the cloud is at 10 K for the low, medium and high flux models respectively.

The low and medium flux models have retained a cold neutral gas morphology sim-

Table 6.4: Key RDI model parameters.

Variable (Unit)	Value	Description
$D_{\rm low}$ (pc)	$(-10.68, 0, 0)$	Source position (low flux)
$D_{\rm med}$ (pc)	$(-4.78, 0, 0)$	Source position (medium flux)
$D_{\rm hi}$ (pc)	$(-3.38, 0, 0)$	Source position (high flux)
T_* (K)	40000	Source effective temperature
R_* ($\rm R_\odot$)	10	Source radius
$\Phi_{\rm low}$ ($\rm cm^{-2}\,s^{-1}$)	9×10^8	Low ionizing flux at the left grid edge
$\Phi_{\rm med}$ ($\rm cm^{-2}\,s^{-1}$)	4.5×10^9	Medium ionizing flux at the left grid edge
$\Phi_{\rm hi}$ ($\rm cm^{-2}\,s^{-1}$)	9×10^9	High ionizing flux at the left grid edge
L($\rm pc^3$)	4.87^3	Grid size
$n_{\rm cells}$	128^3	Number of grid cells
$n_{\rm pix}$	401^2	Synthetic image pixels
$\theta_{\rm pix}(''$)	2.5	Angular width per pixel
N_γ	10^8	Photons packets used in synthetic image
$D_{\rm o}$ (pc)	1000	Observer distance
dust/gas	1×10^{-2}	Dust to gas ratio
$\log_{10}$(He/H)	-1	Helium abundance
$\log_{10}$(C/H)	-3.66	Carbon abundance
$\log_{10}$(N/H)	-4.40	Nitrogen abundance
$\log_{10}$(O/H)	-3.48	Oxygen abundance
$\log_{10}$(Ne/H)	-4.30	Neon abundance
$\log_{10}$(S/H)	-5.05	Sulphur abundance

ilar to that at the end of their radiation hydrodynamic evolution. Because the disruption to the original BES significantly modified the density distribution in the low and medium flux regimes by excavating and accumulating material, the addition of helium, metals (and therefore forbidden line cooling) and more sophisticated thermal balance have little effect on the extent of the ionized region. This is not the case for the high flux model, which weakly modified the density distribution, achieving early pressure balance and establishing only weak photo-evaporative flow. As a result the enhanced cooling has shifted the ionization front away from the cloud structure that was formed in the radiation hydrodynamics calculation to a new position similar to that of the low flux model. This additional cooling in weakly disrupted gas is also responsible for the cool regions towards the edge of the medium flux grid. These alterations to the extent of the ionized regions hint at the importance of including additional atomic processes such as forbidden line cooling in radiation hydrodynamics calculations. Although the effect is small in the low and medium flux model, any diagnostic procedure applied to the high flux model will not be examining the pressure balanced system generated in Haworth & Harries (2012), but a new one in which D-type expansion about the H II region is yet to occur.

The low and medium flux models both exhibit slightly cooler regions where strong photo-evaporative flow occurs. This is the yellow region mirroring the central part of the bow of the top frame of Figure 6.7 for the low flux model and the shovel shaped yellow region about the tip of the cometary object in the middle frame of Figure 6.7 for the medium flux model.

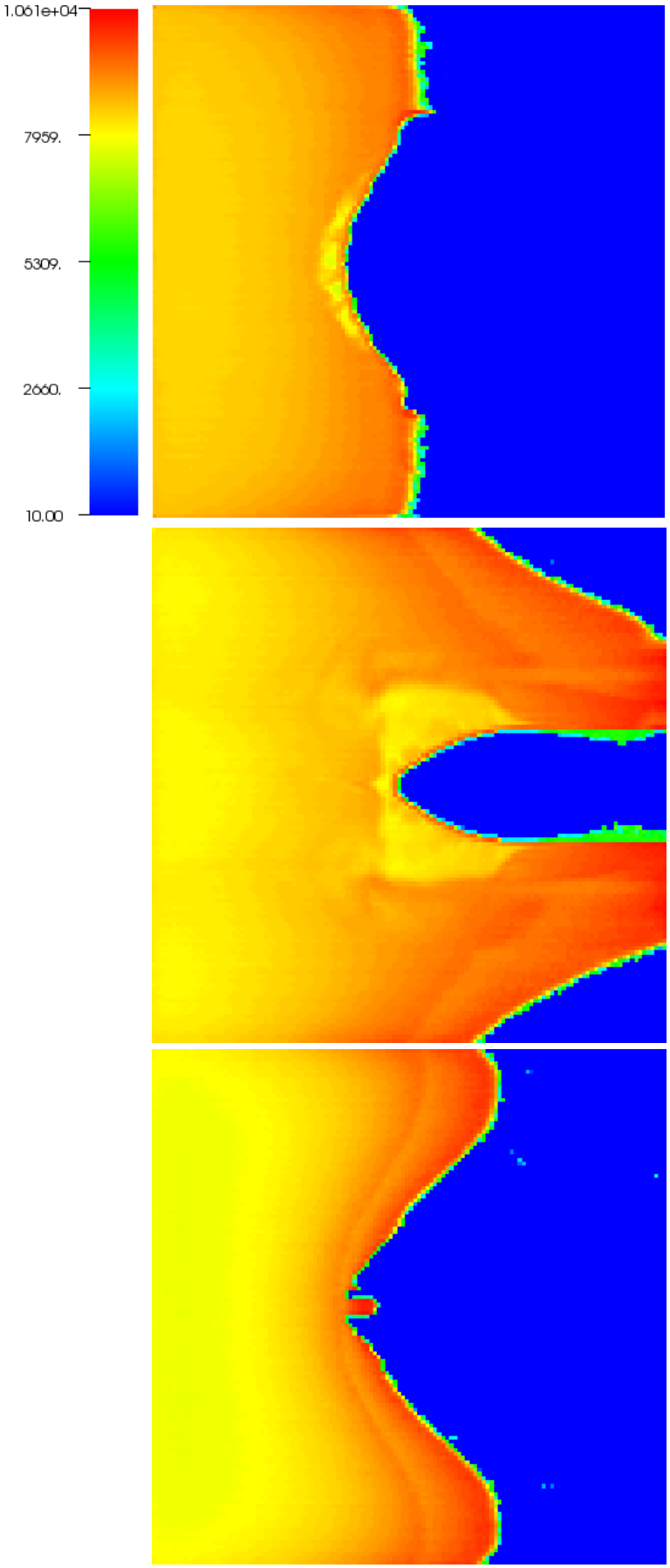

Figure 6.7: The temperature distribution (in Kelvin) for a slice through each model, low flux to high flux from top to bottom. Each image is 4.87 pc to a side.

6.6.2 Optical Image Morphology

A synthetic image of the low flux model using Hα (red), the 5007 Å [O III] line (green) and the 3968 Å [Ne III] line (blue) is given in Figure 6.8. The object clearly resembles a class A, moderately curved, bright rimmed cloud. Hα dominates the emission along the rim, making it appear red. The signature of the photo-evaporative flow is the slightly darker region opposite the bright rim, which has been excavated to slightly lower densities due to the motion of the flow. Bright blue spots are dense gas on the face of the cloud that has been photoionized. From this edge-on inclination the fingers due to instabilities (see section 6.6.1) are not clear because along a given line of sight there are multiple trunks and the average column density is approximately constant. Furthermore, the enhanced cooling due to forbidden line processes means that the ionized regions between the trunks are now neutral, suppressing emission from them. A two colour image in the electron density sensitive lines of [O II] where the observer is inclined by 30 degrees relative to the ionization front is shown in Figure 6.11. Here the fingers and dark photo-evaporative flow region are much more clearly illustrated. The morphological resemblance between this image and that in Figure 1 of Chauhan et al. (2011a) is notable, despite the fact that the additional cooling has made the fingers harder to discern. In Chauhan et al. (2011a) it was suggested that the finger like objects in the wings of the BRC were due to instability, this image and the radiation hydrodynamic model it is generated from qualitatively support this hypothesis.

A synthetic image of the medium flux model using Hα (red), the 5007 Å [O III] line (green) and the 3968 Å [Ne III] line (blue) is given in Figure 6.9. This object resembles a type B-C BRC, having an almost cometary appearance that is again dominated by Hα emission. The ribbing effect interior to the cometary structure is a result of the low resolution used in the radiation hydrodynamics calculation and has no physical significance. The bright ribs are the cells exposed to the direct stellar radiation field and the darker regions are shielded cells, for which radiative heating comes primarily from the diffuse field. Despite being known to have a stronger photo-evaporative flow than the low flux model, it is difficult to distinguish between a dark excavated region and neutral foreground material. Again, I take an image at thirty degrees inclined relative to the ionization front to illustrate this point in Figure 6.12, in which the dark foreground material starts moving out of view. This image suggests that the BRC is situated in the bottom of a basin of ionized gas. Furthermore, a darker region excavated by the photo-evaporative flow is visible around the BRC in these electron density sensitive diagnostic lines.

A synthetic image of the high flux model using Hα (red), the 5007 Å [O III] line (green) and the 3968 Å [Ne III] line (blue) is given in Figure 6.10. Note that the radiation hydrodynamics model did not significantly alter the starting density distribution for this model, accumulating only a small amount of material before achieving pressure balance and establishing a weak photo-evaporative flow. As a result the enhanced cooling due to forbidden line radiation and the more complex thermal balance calculation have increased the size of the neutral gas region, i.e. the Strömgren radius is smaller. The resulting

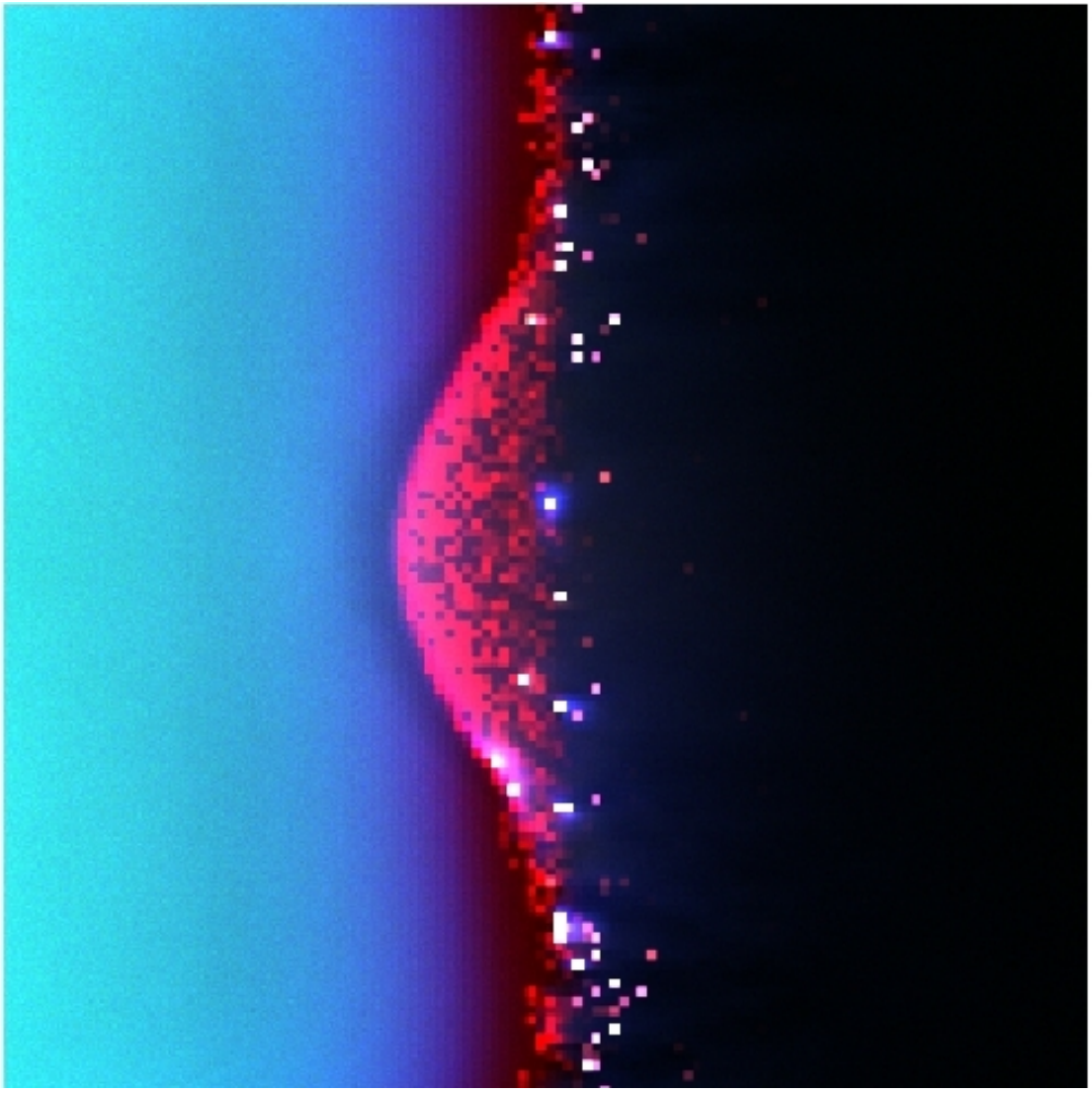

Figure 6.8: A composite colour image of the low flux model using Hα (red), the 5007 Å [O III] line (green), and the 3968 Å [Ne III] line (blue).

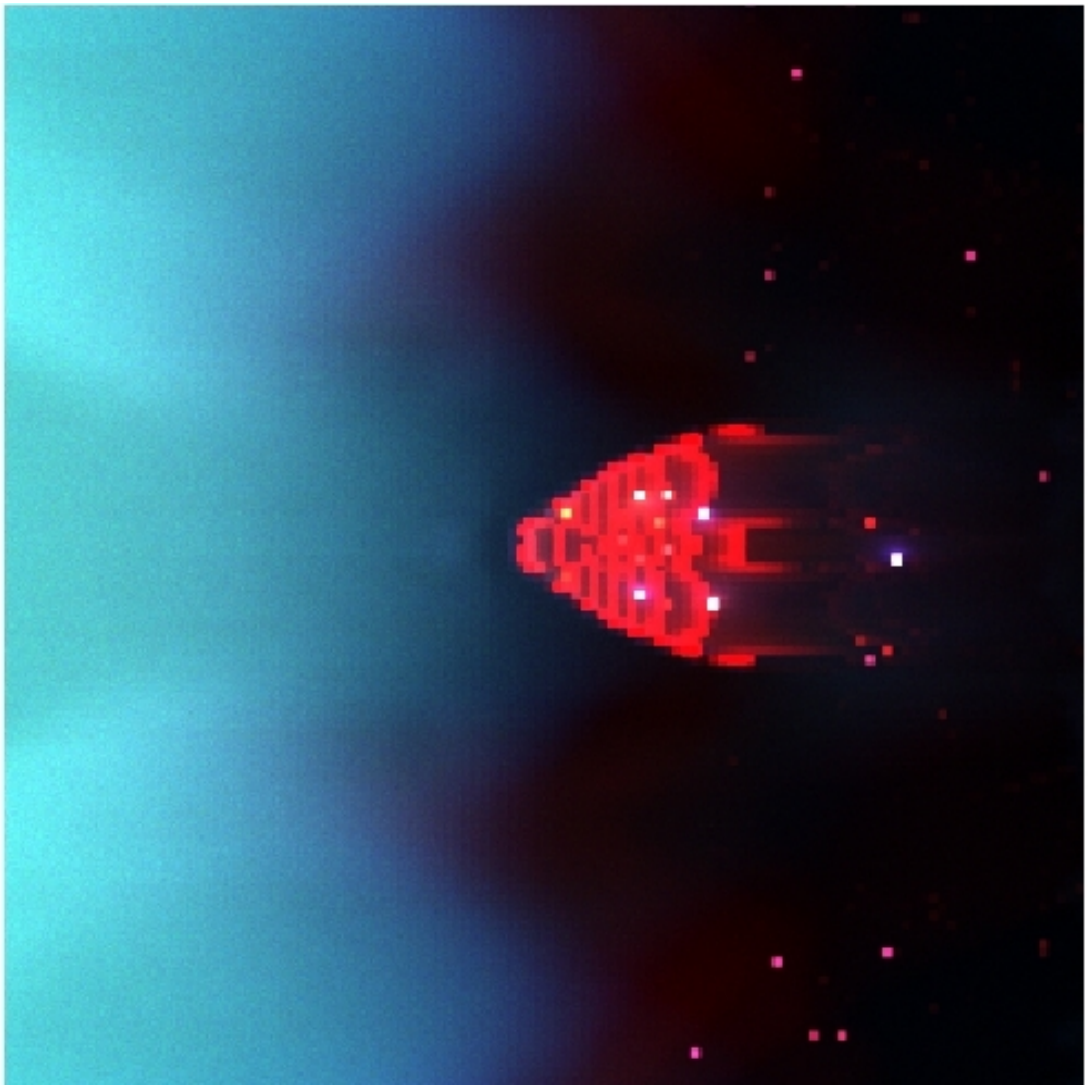

Figure 6.9: A composite colour image of the medium flux model using Hα (red), the 5007 Å [O III] line (green), and the 3968 Å [Ne III] line (blue).

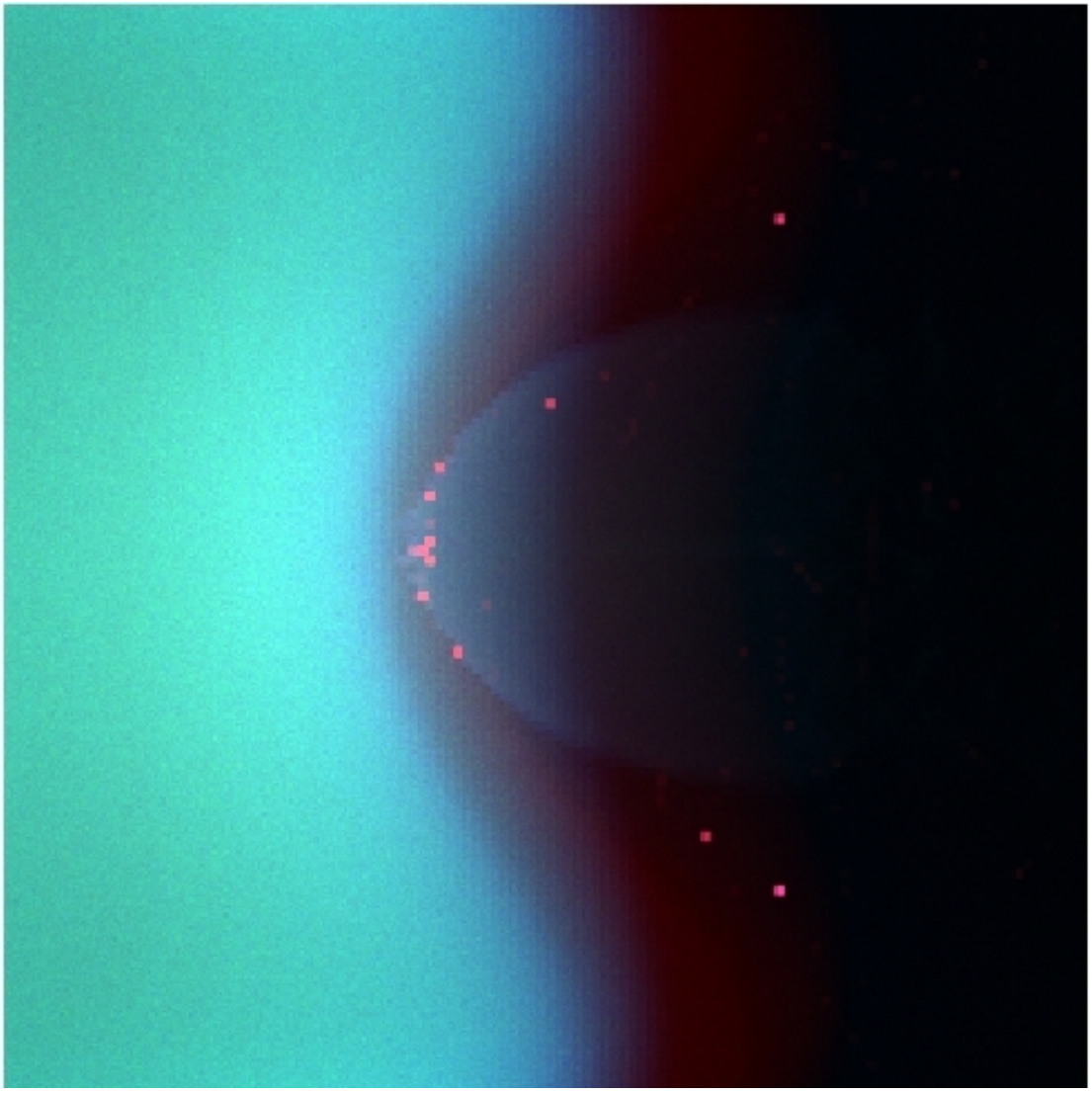

Figure 6.10: A composite colour image of the high flux model using Hα (red), the 5007 Å [O III] line (green), and the 3968 Å [Ne III] line (blue).

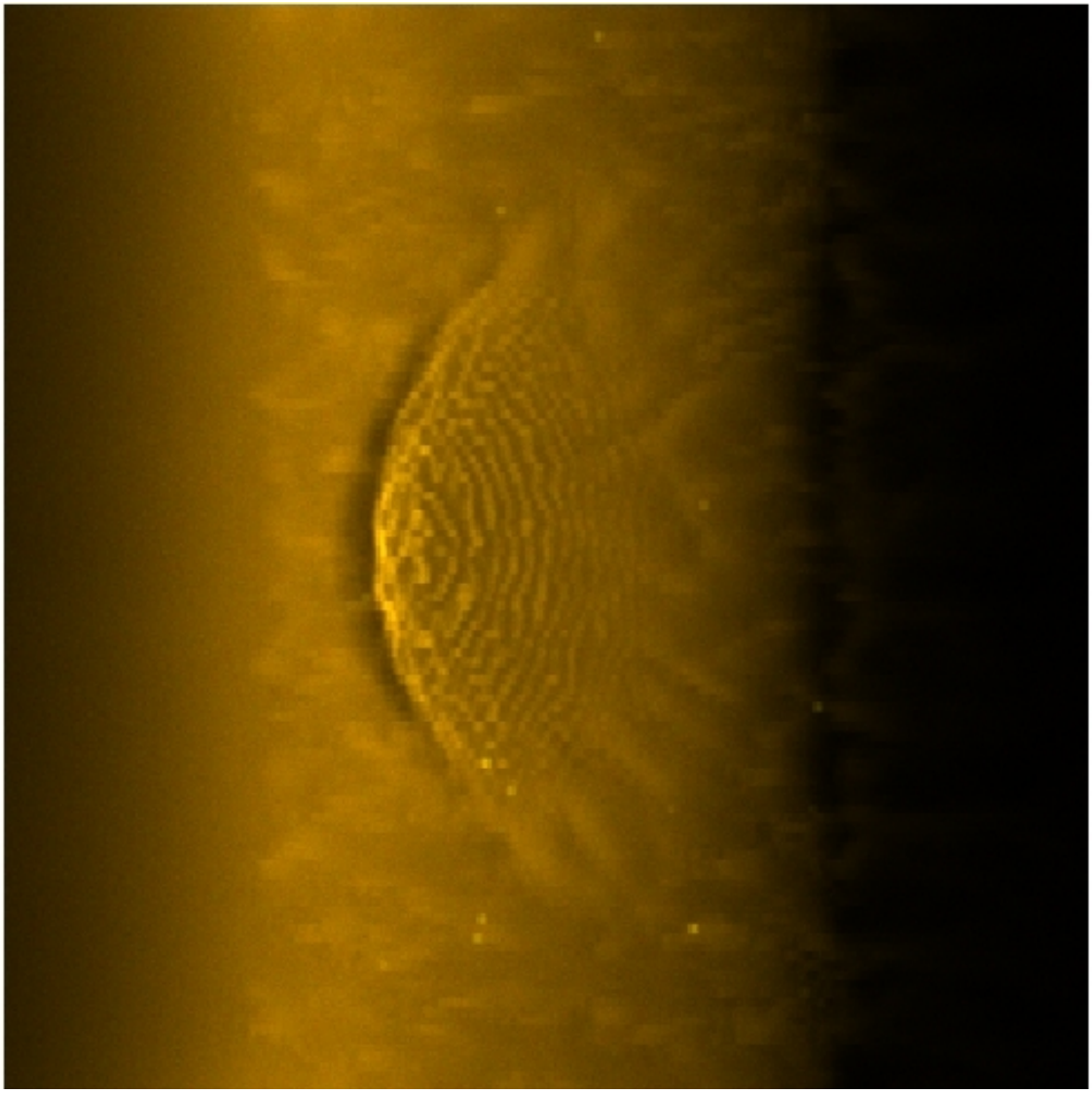

Figure 6.11: A two colour image of the low flux model for an observer inclined thirty degrees relative to the planar ionization front. This image is constructed using the electron density sensitive 3729 Å (red) and 3726 Å (green), [O II] lines.

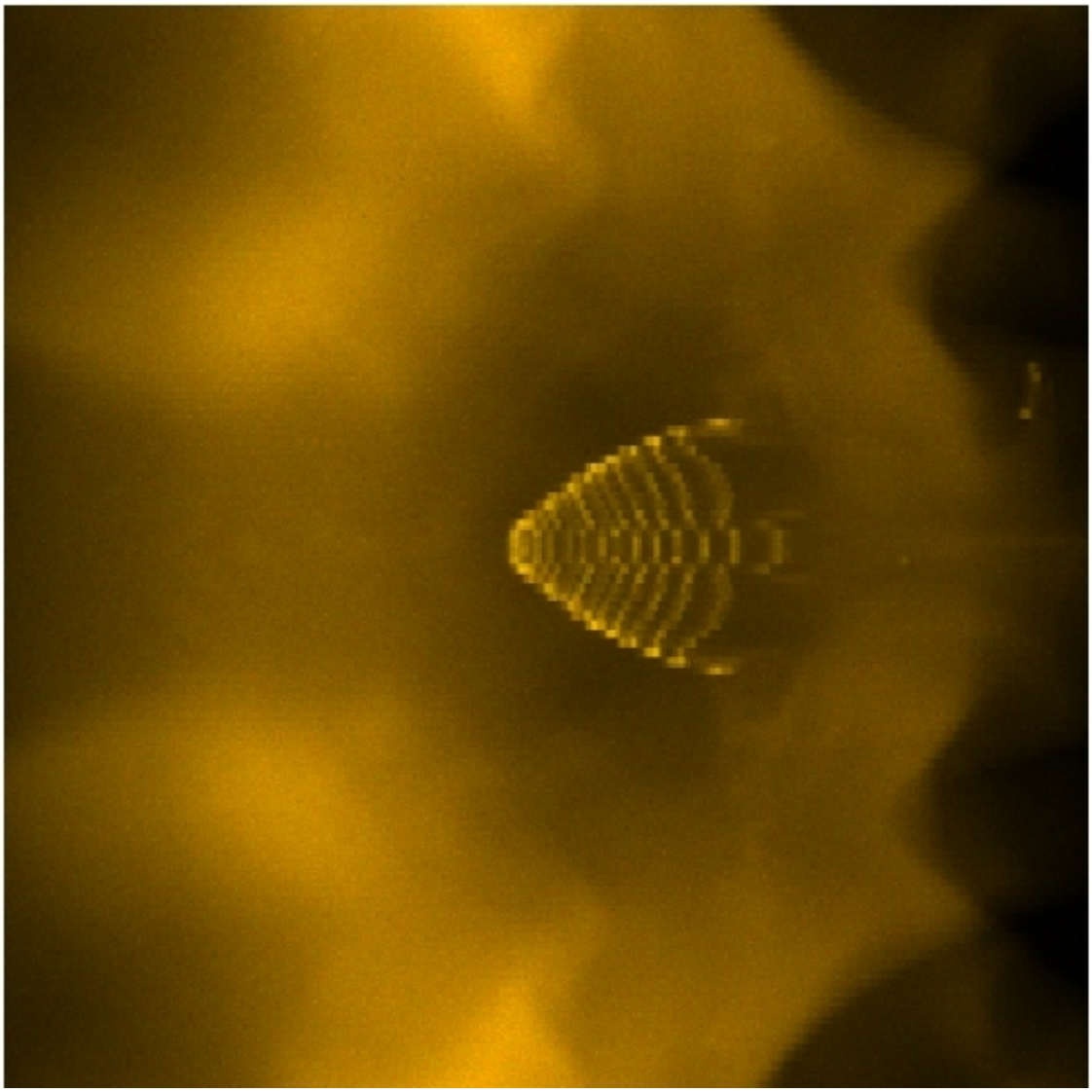

Figure 6.12: A two colour image of the medium flux model for an observer inclined thirty degrees relative to the planar ionization front. This image is constructed using the electron density sensitive 3729 Å (red) and 3726 Å (green) [O II] lines.

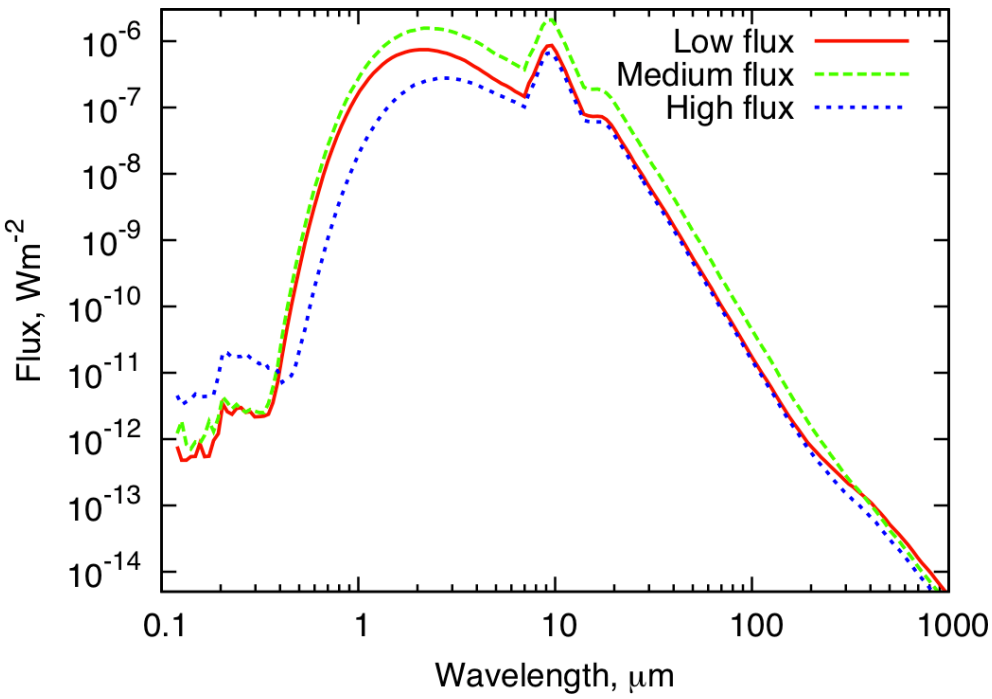

Figure 6.13: A a comparison of the low (solid red line), medium (dashed green line) and high flux (dotted blue line) model spectra.

imaged object has the curvature of a class A BRC, though it is not actually bright rimmed, beneath which hints of the old neutral cloud structure can be seen.

6.6.3 Neutral gas properties

Spectral energy distributions which include dust and free-free emissivities were generated for each converged grid, these are shown in Figure 6.13. Short of the near UV regime (from approximately 380 nm bluewards) scattered stellar photons dominate the signal and the flux decreases in accordance with the star's distance from the grid, i.e. the strongest signal is from the high flux model and the weakest is from the low flux model. Over most of the rest of the spectrum, where direct thermal radiation dominates the SED, the medium flux model consistently has the strongest signal, followed by the low then high flux models. At wavelengths greater than about 370 μm the low flux spectrum has the strongest signal due to the greater spatial extent of the cloud and therefore more widespread dust emission. The 10 μm silicate feature is clearly visible in emission in all SEDs.

The dust temperatures and cloud masses are derived using the greybody fitting method described in section 6.4.1. I use a value of 214 g cm^{-2} for C_{345} (345 GHz, 850 μm) and fit the spectrum between 450 and 850 μm following Thompson et al. (2004). The resulting temperatures and cloud masses for each system are given in Table 6.5. The temperatures are all close to the dominant (that for at least 95% by mass) neutral cloud temperature of 10 K. The derived temperature is increased slightly by $1-2$ K by warmer dust at the interior edge of the bright rim.

Table 6.5: Neutral cloud properties from SED fitting. Included are two choices of C_{345} and the masses calculated using the dominant temperature of 10 K.

Model	Dust temperature (K)	Cloud mass, ($M_\odot$) $C_{345} = 214\,\mathrm{g\,cm^{-2}}$	Cloud mass, ($M_\odot$) $C_{345} = 50\,\mathrm{g\,cm^{-2}}$	Cloud mass, ($M_\odot$) $C_{345} = 214/50\,\mathrm{g\,cm^{-2}}$, T = 10 K	Cloud mass from grid ($M_\odot$)
Low flux	11	144	34	159/37	74
Medium flux	12	75	18	115/27	21
High flux	11	76	18	90/21	77

Table 6.6: HPBW sizes and pixel noise levels for the images based on 30 s VLA exposures.

Configuration	HPBW	rms pixel noise ($\mathrm{mJy\,pixel^{-1}}$)
B	$3.9''$	0.27
C	$12.5''$	2.7×10^{-2}
D	$44''$	2.2×10^{-3}

The calculated neutral mass in the low and medium flux cases are overestimated by a factor of approximately 2 and 3.6 respectively. This is due to the standard practice of using a fixed value of C_{345} (e.g. Thompson et al. 2004; Morgan et al. 2008) which is probably too large in this case. The correct mass would have been inferred using values of 110 and $60\,\mathrm{g\,cm^{-2}}$ for C_{345} in the low and medium flux mass calculations respectively. The inferred mass of the high flux cloud is close to the known value on the computational grid. This is because lower densities were attained in this model making the adopted value of C_{345} more appropriate.

Cloud masses calculated using the commonly adopted value of $50\,\mathrm{g\,cm^{-2}}$ for C_{345} (e.g. Thompson et al. 2004) are also given in Table 6.5. These give a reasonable estimate of the medium flux mass but underestimate the low flux mass by over a factor of two. The large error in the high flux mass when using the lower value of C_{345} is less significant due to the differences discussed in section 6.6.1.

The sensitivity of this calculation to the dust temperature at low values is also illustrated in Table 6.5, where the calculated mass assuming a cloud temperature of 10 K (the dominant temperature in the neutral cloud, see section 6.6.1) is also given for both values of C_{345} used here. In the low and high flux cases the 1 K variation in temperature modifies the calculated masses by a factor in the range $8 - 16\,\%$. The 2 K variation in the medium flux case leads to a change in the calculated mass by about 35 %.

This mass calculation is already treated with caution (e.g. Kerton et al. 2001; Thompson et al. 2004; Morgan et al. 2008) these results suggest that using a fixed value of C_{345} for a range of clouds of different class will induce errors of a factor up to around 3.6 in some of the cloud masses and that the calculation is sensitive to temperature at values around 10 K with a typical difference in the mass of about $15\,\%\,\mathrm{K^{-1}}$.

6.6.4 Radio analysis

20 cm radio images are used to determine the photoionizing flux, IBL electron density and mass loss rate following the discussion in section 6.4.2. Synthetic images at 20 cm are generated, smoothed and subjected to noise in the manner described in sections 6.3.3 and 6.3.4 to be representative of the resolution and noise level of 30 second exposures of the VLA type B, C and D configurations. 30 second exposures using the D configuration are typical of those used in the NRAO VLA Sky Survey (NVSS) (Condon et al. 1998). I assume a bandwidth of 43 MHz and the use of 26 antennae. The rms noise associated with these observations is $0.524\,\mathrm{mJy\,beam^{-1}}$. Table 6.6 summarises the HPBW value and rms pixel noise for each configuration. The regions used to derive the integrated IBL flux are

the circular regions labelled 'B' on Hα images in Figure 6.17. These all have an angular diameter of $1'$. The cloud radii are those of the circular regions marked 'A' on Figure 6.17 and are 1.5, 0.6 and 1.3 pc for the low, medium and high flux models respectively.

The raw radio images, as well as simulated B, C and D configuration, 30 second VLA images are given in Figure 6.16. The colour scale used in each frame is set to match that of the raw image. As the beam size increases, the BRC structure is smoothed out and the brightness of the object is also modified. The calculated ionizing fluxes, electron densities and mass loss rates based on each radio image are summarised in Table 6.7. For each model, using a larger beam reduces the measured flux resulting in underestimates of the cloud properties by up to 25% relative to the unsmoothed image. This is because the compact, bright object flux is partially lost to the surroundings, which are uniformly much dimmer than the BRC.

The ionizing fluxes at the left hand edge of the computational grid are known to be, from low to high flux, 9×10^8, 4.5×10^9 and $9 \times 10^9\,\mathrm{cm^{-2}\,s^{-1}}$. The tabulated values of ionizing flux at the BRC, which are calculated at distance of around 2 pc from the left hand edge of the grid, are therefore of realistic magnitude. There is a discrepancy in that the high flux model ionizing fluxes are only slightly larger than the medium flux, however this is due to the change in ionization structure mentioned in section 6.6.1 that gives rise to an absence of a clear IBL and hence a lower measured flux.

The electron density in the medium flux case has been correctly inferred as being significantly higher than that in the low flux case. The actual number densities in the IBL are in the range $60 - 190$, $200 - 1500$ and $50 - 100\,\mathrm{cm^{-3}}$ for the low, medium and high flux models respectively. In the medium and low flux cases the calculated values lie beneath this range, suggesting that the effect of the IBL on compression might be underestimated. This underestimate arises due to cooler gas in the regions over which the flux is being integrated at the interior of the bright rim. These relatively cool regions arise where there is localised shielding from the stellar radiation field and radiative heating occurs primarily from the diffuse field. This is the cause of the ribbing effect seen in the medium flux images, where the bright contours are those cells directly exposed to the stellar radiation field. Increasing the region over which the flux is integrated amplifies this problem. For example, in the extreme case of integrating the flux over the entire cloud (region A in Figure 6.17) the low flux electron density is reduced to around $15\,\mathrm{cm^{-3}}$. Conversely, reducing the size over which the flux is integrated too much will make the derived values more susceptible to noise.

The inferred mass loss rates are higher for the larger clouds, which have a larger surface over which material can be lost. Providing an actual mass loss rate from the computational grids for comparison is non-trivial, particularly in the low flux case where the boundary between the BRC cloud and the gas in the wings of the model is poorly defined. I therefore calculate the difference between the mass at 195 and 200 kyr in a number of volumes encapsulating the BRCs on the computational grid to provide a range of mass loss estimates. These estimates are also shown in Table 6.7, the high flux model is

neglected due to the changes to the ionization structure discussed in section 6.6.1. Both the low and medium flux mass loss estimates from the grid span just over one order magnitude, encompassing the mass loss rates from the 20 cm emission analysis.

Although in the correct (but broad) range, the mass loss rate as a quantity does not give a proper indication of the relative strengths of the photo-evaporative flows. For example, the medium flux model ejections are clearly more energetic than the low flux ones, giving rise to stronger rocket-motion, more rapid compression of the cloud and leaving a stronger signature in the ambient H II region, but its mass loss rate is similar. A more useful parameter for studying relative photo-evaporative flow strengths is the mass flux

$$M_{\mathrm{f}} = \frac{1}{\Omega}\frac{\dot{M}}{R^2} \tag{6.16}$$

where R is the radius of the cloud and Ω is the solid angle on the cloud bounded by the IBL. For near edge-on inclinations Ω can be approximated assuming cylindrical symmetry. Example mass fluxes are also included in Table 6.7 which (based on the opening angle of the bow) assume that the low flux IBL bounds $2\pi(1 - \cos(\pi/3))$ of the cloud surface and the medium flux cloud IBL bounds 2π of the surface. These mass fluxes imply that the medium flux flow is significantly stronger than that of the low flux model, in agreement with the behaviour from the model grid. The difficulty in using the mass flux as an indicator of relative photo-evaporative flow strengths is determining what fraction of the cloud is covered by the IBL. A first order comparison of the relative mass fluxes of clouds of similar type could be obtained by assuming that the fraction of the cloud bounded by the IBL is the same between types (Sugitani et al. 1991) and that only the radius of the cloud varies.

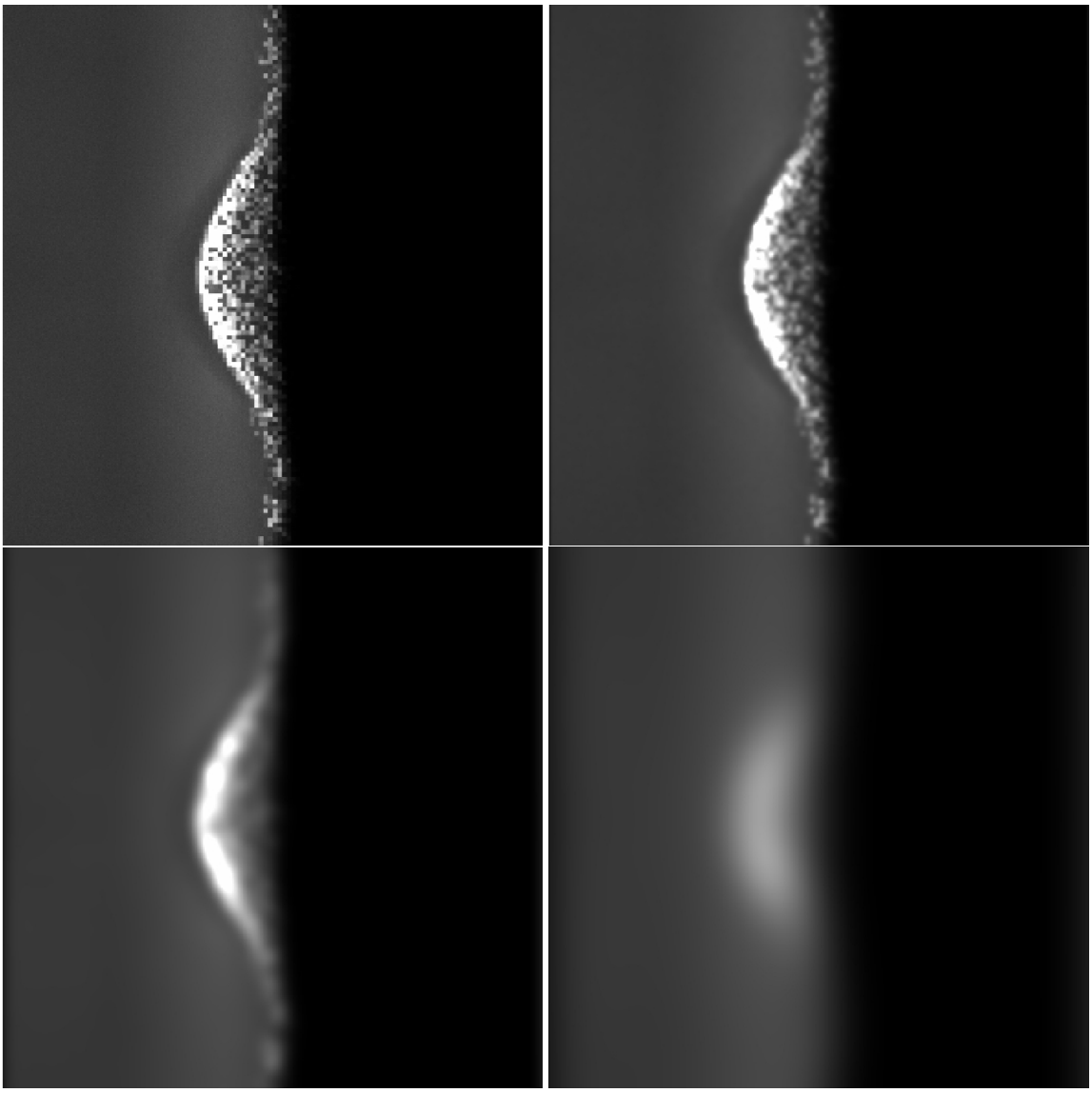

Figure 6.14: Radio images of the low flux models. The top left hand panel is the raw output from TORUS. The other panels, moving clockwise, are the raw image modified to be representative of 30 s exposures using the VLA type B, C and D configurations. The grey scale of each image is set to match that of the raw output image.

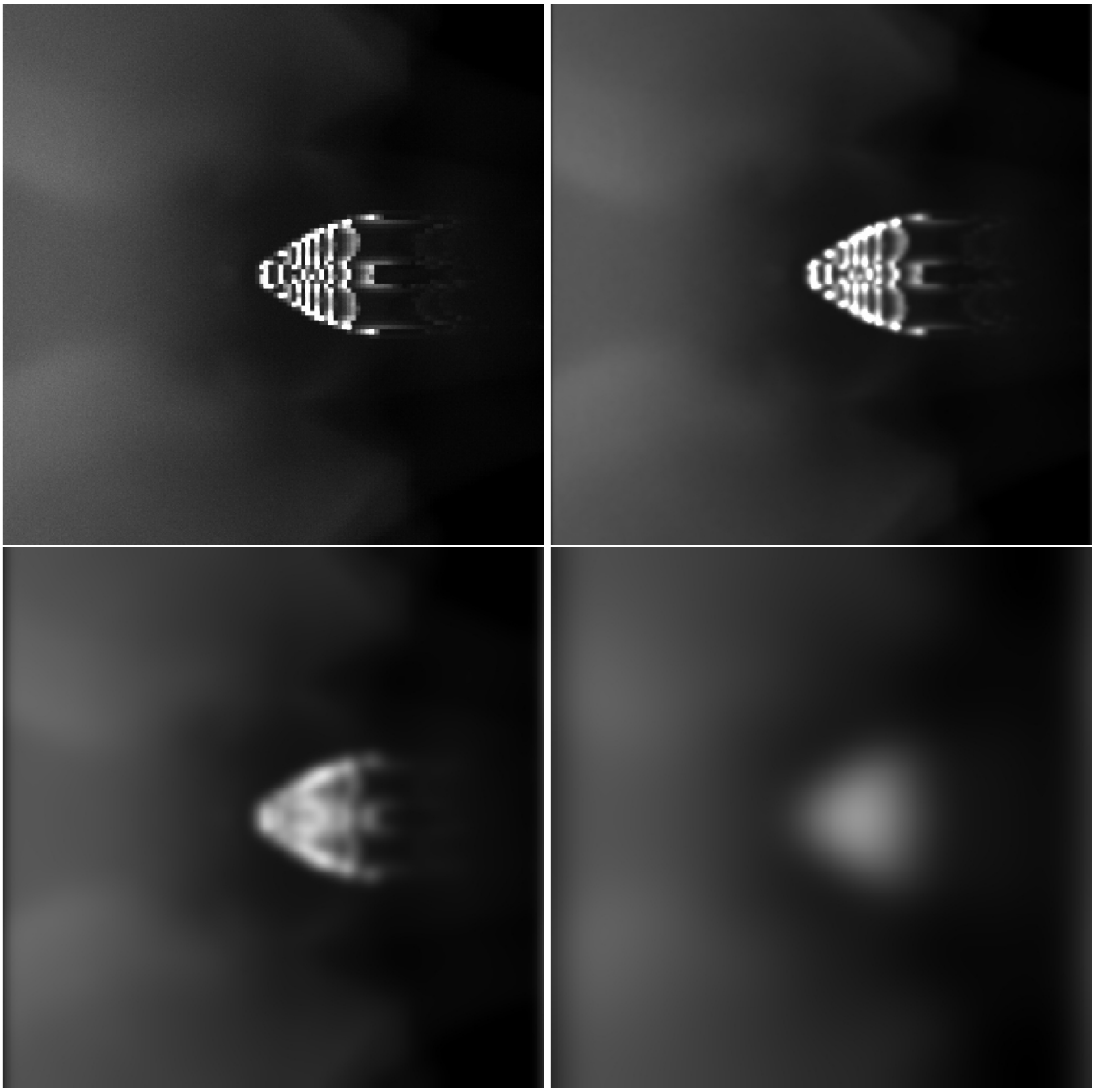

Figure 6.15: Radio images of the medium flux models.The top left hand panel is the raw output from TORUS. The other panels, moving clockwise, are the raw image modified to be representative of 30 s exposures using the VLA type B, C and D configurations. The grey scale of each image is set to match that of the raw output image.

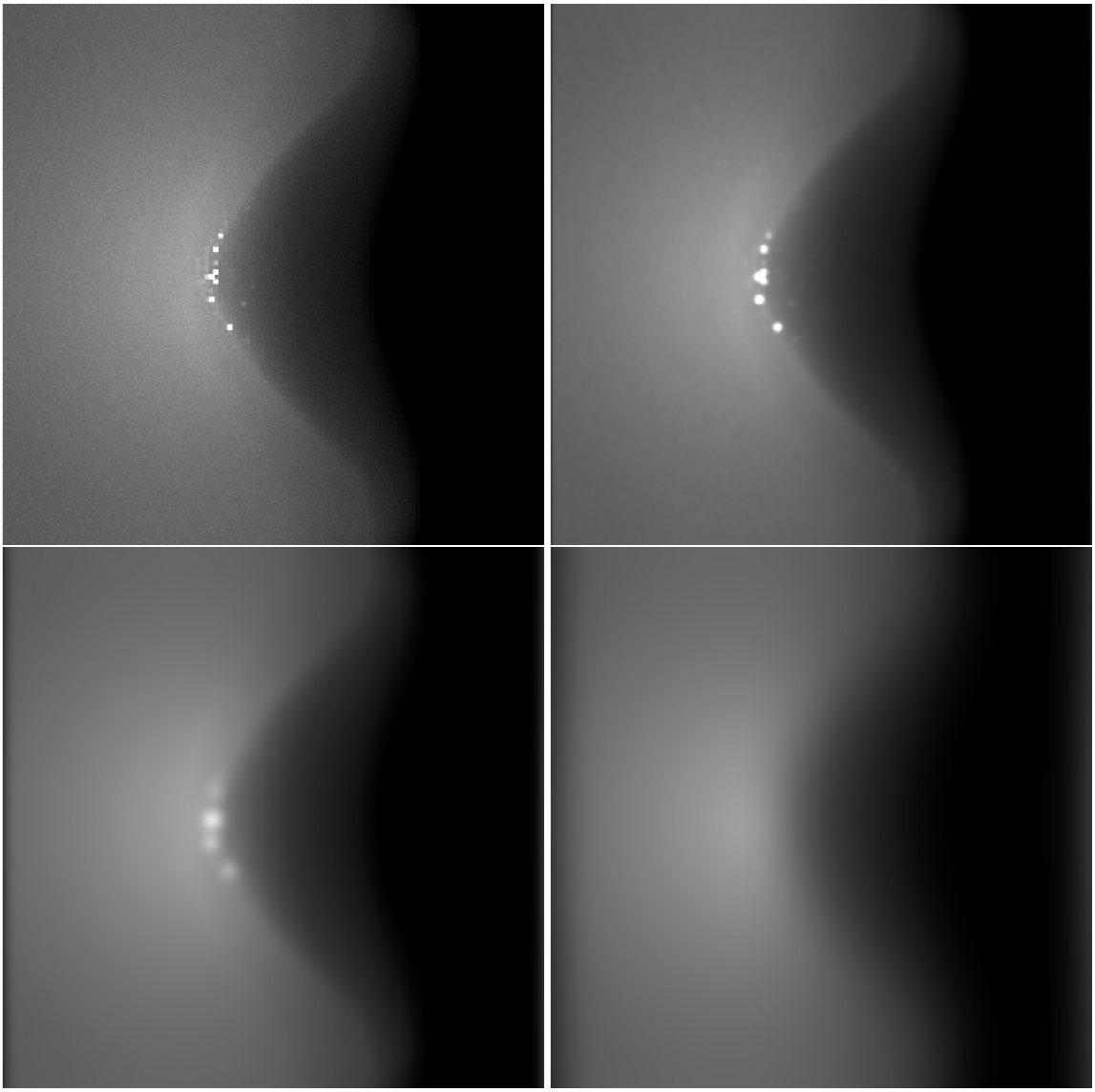

Figure 6.16: Radio images of the high flux models. The top left hand panel is the raw output from TORUS. The other panels, moving clockwise, are the raw image modified to be representative of 30 s exposures using the VLA type B, C and D configurations. The grey scale of each image is set to match that of the raw output image.

Table 6.7: BRC IBL properties from analysis of radio images at 20 cm. The mass loss rate from the model grid is also included.

Model	Configuration	Ionizing flux (Φ, $\mathrm{cm^{-2}\,s^{-1}}$)	Electron density (n_e, $\mathrm{cm^{-3}}$)	Mass loss rate ($\dot{M}$, $\mathrm{M_\odot\,kyr^{-1}}$)	Model mass loss rate ($\dot{M}$, $\mathrm{M_\odot\,kyr^{-1}}$)	Mass flux (M_f, $\mathrm{M_\odot\,Myr^{-1}\,pc^{-2}}$)
Low flux	raw	5.0×10^8	45	0.18	$1.4 \times 10^{-2} - 0.2$	26
Low flux	B	4.9×10^8	45	0.18	$1.4 \times 10^{-2} - 0.2$	25
Low flux	C	4.6×10^8	43	0.17	$1.4 \times 10^{-2} - 0.2$	24
Low flux	D	3.3×10^8	36	0.15	$1.4 \times 10^{-2} - 0.2$	21
Medium flux	raw	1.5×10^9	122	7.8×10^{-2}	$9.8 \times 10^{-3} - 0.1$	35
Medium flux	B	1.4×10^9	119	7.7×10^{-2}	$9.8 \times 10^{-3} - 0.1$	34
Medium flux	C	1.3×10^9	113	7.3×10^{-2}	$9.8 \times 10^{-3} - 0.1$	32
Medium flux	D	8.2×10^8	91	5.9×10^{-2}	$9.8 \times 10^{-3} - 0.1$	26
High flux	raw	1.7×10^9	89	0.27	–	–
High flux	B	1.7×10^9	89	0.27	–	–
High flux	C	1.6×10^9	87	0.26	–	–
High flux	D	1.4×10^9	80	0.24	–	–

6.6.5 Diagnostic line ratio analysis

As discussed in section 6.4.4, I emulate slit spectroscopy by calculating images at specific wavelengths and derive the conditions in the slit region using diagnostic line ratios. The slits are shown in the upper left of Hα images of the models in Figure 6.17 (marked C). Each slit has a width of 2 pixels and a length of 100, 50 and 80 pixels for the low, medium and high flux models respectively. These are placed over the ionized cells closest to the tip of the BRC.

The electron densities and the average of the temperature diagnostics are given in Table 6.8 along with the values calculated using radio diagnostics and those from the model grids. I retain the level of accuracy determined in section 6.5.1. As with the radio diagnostic, the electron density is clearly underestimated in the medium and low flux cases (e.g. hydrogen number densities are of order $60 - 190\,\mathrm{cm}^{-3}$ for the low flux model). These values could be influenced by the low density (of order ten hydrogen atoms per cubic centimetre) region just beyond the BRC that has been excavated by the photo-evaporative flow.

The temperatures derived using the [O III], [N II] and [Ne III] ratios are also given in Table 6.8. The temperature calculations use the electron densities calculated from the [O II] lines, but depend only weakly on this value so the largest error in n_e ($\Delta n_\mathrm{e} = 1460$ in the medium flux case) translates into an error of only 15 K. The separate temperature diagnostics of each model are within 110 K of one another and all lie within the range seen in the temperature maps of Figure 6.7. The actual temperature in the IBL is typically 8000-9000 K so the average temperatures in Table 6.8 are more accurate than assuming a value to 10^4 K. Given that the electron densities are underestimated by both radio and diagnostic line ratio techniques and the inferred IBL temperatures are more accurate using diagnostic line ratios, this technique is a viable tool for the study of RDI.

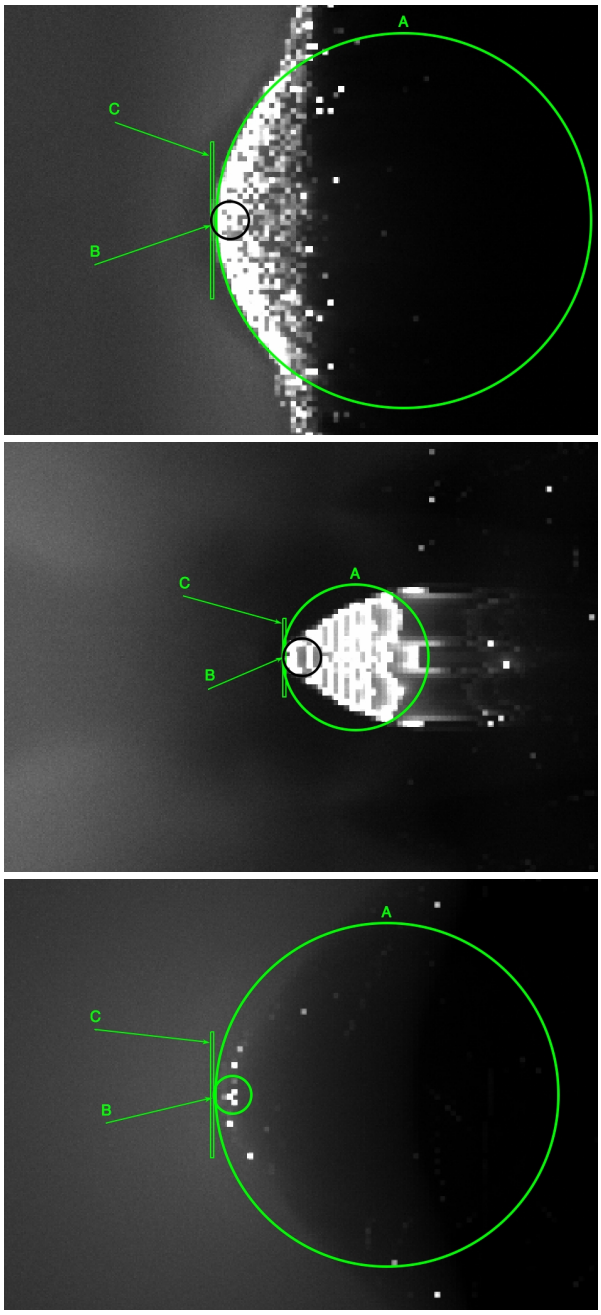

Figure 6.17: Hα images of each model, low to high flux from top to bottom. Overlaid are the regions which are designated as the cloud cross section (those labelled A), the regions over which the radio flux is integrated (those labelled B) and the spectroscopic slits (those labelled C).

Table 6.8: Diagnostic line ratio electron densities and average IBL temperatures. The average electron densities calculated using the radio diagnostic are also included as well as the known conditions from the model.

Model	Line ratio n_e (cm^{-3})	Radio n_e (cm^{-3})	Model n_e (cm^{-3})	Line ratio T_e (K)	Model T_e (K)
Low flux	20	36 – 45	60 – 190	8500	8000 – 9000
Medium flux	40	91 – 122	200 – 1500	8500	8000 – 9000
High flux	60	80 – 91	50 – 100	8380	8000 – 9000

6.6.6 Identifying RDI

If the BRCs are in pressure equilibrium with the IBL then the virial theorem (including a surface term) gives

$$P_{\rm i} = \frac{3c_{\rm s}^2 M_{\rm c}}{4\pi R_{\rm c}^3} - \frac{3GM_{\rm c}}{20\pi R_{\rm c}^4} \tag{6.17}$$

where $M_{\rm c}$, $R_{\rm c}$, $c_{\rm s}$ and $P_{\rm i}$ are the cloud mass, cloud radius, cloud gas sound speed and pressure in the IBL respectively (e.g. Hartmann 2009; Thompson et al. 2004). If the BRC is not in pressure equilibrium then the contracting or expanding nature of the cloud can be inferred from the relative magnitudes of the left and right hand sides of equation 6.17, which will be referred to as the external and supporting pressures ($P_{\rm i}$ and $P_{\rm s}$) respectively.

For the radio method I use the electron densities calculated in section 6.6.4 and make the standard assumption that the ionized gas is at 10000 K. For the diagnostic ratio method I use the electron densities and the average temperatures calculated in section 6.6.5. The neutral cloud properties are those determined in section 6.6.3 using C_{345}=214 g cm^{-2}. Under this virial equilibrium technique a cloud radius needs to be assumed, the circular regions on Figure 6.17 represent the cross section of the spherical clouds used to investigate equilibrium.

The low, medium and high flux clouds have radii of 1.5, 0.6 and 1.3 pc respectively. Given that most of the neutral mass on the grid is concentrated in the BRC, I assume in each stability analysis that all of the SED fitted mass is contained within the highlighted regions. The supporting cloud pressures for each model, from low to high flux are 4.6×10^{-13}, 4.1×10^{-12} and 3.7×10^{-13} dyn cm^{-2} respectively. Typical pressures in the neutral cloud on the radiation hydrodynamic simulation grid are $10^{-13} - 10^{-12}$, $10^{-12} - 10^{-10}$ and $10^{-13} - 10^{-12}$ dyn cm^{-2} in the low, medium and high flux models respectively so the derived pressure values are towards the centre of this range in the low and high flux models and towards the lower end of the range found in the medium flux model.

The external pressures and their ratio relative to the support pressure are given in Table 6.9. The pressures in the IBL from the model grids range from around $0.5-3\times10^{-10}$, $1 - 5 \times 10^{-10}$ and $1 - 2.5 \times 10^{-10}$ dyn cm^{-2} for the low, medium and high flux models respectively. The IBL pressures derived using diagnostic line ratios lie within this range, however because the assumed temperature of 10^4 K is larger than the actual temperature in the IBL the radio diagnostics overestimate the pressure in the IBL in the medium and high flux cases. The low flux electron density was sufficiently underestimated for the pressure to fall into the range on the model grid.

All diagnostics imply that the cloud should be undergoing thermal compression, which is in qualitative agreement with the known model behaviour in the medium and low flux cases. Furthermore, the difference in pressure is weaker in the medium flux case than the low flux case. This reflects the relative behaviours of the clouds, as the rate of compression of the medium flux cloud has started to plateau by this point (200 kyr) in the radiation hydrodynamics calculation. The biggest pressure differences are found in the high flux model. Although this is not in agreement with the pressure supported

system at the time of imaging in the radiation hydrodynamics calculation, the ionization front has been relocated to a point at which D-type driving of the front into the cloud is about to occur as discussed in section 6.6.1. The large pressure difference implies that the system is about to undergo strong compression and, given that this new starting point is further from the BES than in the start point of the hydrogen only radiation hydrodynamics models, it is likely that the resulting BRC following a new calculation with metals would more closely resemble that of the medium flux model. The ratio of external to supporting pressure lies within the range of those found on the computational grid in all cases, but are typically towards the lower end of the range. This is due to a combination of the overestimated neutral cloud masses and the underestimated IBL electron densities.

Table 6.9: IBL pressures and their ratio to the supporting cloud pressure in virial stability analysis. The ratio of IBL to neutral cloud supporting pressures from the model are also included.

Model	Diagnostic method	External pressure ($P_{\rm i}$, $\times 10^{-10}\,{\rm dyn\,cm^{-2}}$)	$P_{\rm i}/P_{\rm s}$	Model $P_{\rm i}/P_{\rm s}$
Low flux	Radio, raw image	2.1	460	50-3000
Low flux	Radio, VLA configuration B	2.1	460	$50-3000$
Low flux	Radio, VLA configuration C	2.0	430	$50-3000$
Low flux	Radio, VLA configuration D	1.7	370	$50-3000$
Low flux	Slit spectroscopy	0.78	170	$50-3000$
Medium flux	Radio, raw image	5.6	140	$1-500$
Medium flux	Radio, VLA configuration B	5.5	130	$1-500$
Medium flux	Radio, VLA configuration C	5.2	130	$1-500$
Medium flux	Radio, VLA configuration D	4.2	100	$1-500$
Medium flux	Slit spectroscopy	1.6	40	$1-500$
High flux	Radio, raw image	4.1	1110	$100-2500$
High flux	Radio, VLA configuration B	4.1	1110	$100-2500$
High flux	Radio, VLA configuration C	4.0	1080	$100-2500$
High flux	Radio, VLA configuration D	3.7	1000	$100-2500$
High flux	Slit spectroscopy	2.3	620	$100-2500$

6.7 Summary and conclusions

I have performed a range of synthetic observations and diagnostics of radiation hydrodynamic RDI model results to investigate the accuracy of diagnostic techniques and to identify signatures of RDI. I have produced SEDs, images that are representative of 30 second VLA radio observations using the type B, C and D configurations (the latter of which is used for the NRAO VLA Sky Survey) and forbidden line images of each model. These synthetic observations have been used to replicate a number of diagnostics to calculate the conditions in the neutral BRC and its IBL. Using these conditions I have performed a virial stability analysis of each system to determine whether the BRCs are being compressed by the IBL. I draw the following conclusions from this work:

1. The synthetic images generated show objects which are morphologically similar to BRCs observed in star forming regions.

2. The neutral cloud dust temperatures derived using greybody fitting of the SED are similar to those calculated in observational studies (e.g. Thompson et al. 2004; Morgan et al. 2008) and are slightly higher than, but within 2 K of, the known dominant cloud temperature (10 K for at least 95% of the cloud by mass). This slight temperature overestimate is due to warmer dust in the cloud. The mass inferred using equation 10a from Hildebrand (1983) (equation 6.6 in this Chapter) at 10 K is found to vary by $8-16\,\%$ with a change of 1 K and by up to 35 % with a change of 2 K. Using a fixed value of C_{345} for clouds of different class is found to induce an error in the calculated mass of up to a factor 3.6.

3. The temperatures derived using diagnostic line ratios at around 8500 K are more accurate than assuming a canonical temperature of 10^4 K as in the radio diagnostics. The electron number densities established using both techniques are underestimates of those in the IBL on the computational grid. Diagnostic line ratios underestimate the electron density due to contamination from the low density region excavated by the photo-evaporative flow. The radio electron density underestimate is due to lower emission from the interior regions of the BRC where some shielding from the stellar radiation field occurs and radiative heating is due to the, relatively weak, diffuse field.

4. The supporting cloud pressures are found to lie within the range on the computational grids for all models. The IBL pressures are found to be within the correct range for the forbidden line ratio diagnostic. However, since the assumed temperature in the IBL is larger than the actual temperature the radio diagnostics overestimate the IBL pressure in the medium and high flux cases. The IBL pressure is greater than that of the supporting cloud for each model, implying that the cloud is being compressed. This behaviour is qualitatively correct for the low and medium flux models, however is not the observed behaviour of the pressure balanced high flux model. The ratio of external to supporting

pressure is found to be towards the lower end of the range of values found on the model grid in each case.

5. The ionization state of the low and medium flux grids following the initial photoionization calculation remained reasonably consistent with that at the end of the radiation hydrodynamic calculations. However, for the high flux model in which the density structure in the system was not significantly altered in the radiation hydrodynamics calculation, the ionization front has moved closer to the star. This is due to the enhanced cooling by forbidden line emission and more comprehensive thermal balance calculation, essentially resetting the model to a point in which D-type expansion of the ionization front is yet to occur. With a greater distance over which to accumulate material, the modified high flux system may well have achieved a stronger photo-evaporative flow and higher levels of compression of the BRC than in the original model. This result indicates the importance of including atomic chemistry in future calculations.

6. The effect of moving to larger beam sizes in radio observations is to contaminate the integrated flux from the BRC with that from the surrounding neutral cloud and H II region. Since both the neutral cloud and H II region are dimmer than the IBL this reduces the integrated flux, resulting in an underestimate of the incident ionizing flux, electron density and mass loss rate relative to that calculated using an unsmoothed comparison image

7. Despite the presence of strong photo-evaporative flows which establish prominent, relatively cool, low density regions on the model grid, they are difficult to detect in the images calculated here. No striations are detected in H α about the BRC, rather the visual indicator of photo-evaporative flow in these systems is darker regions in the vicinity of the BRC, where material is excavated by the flow. It is likely that striations are not observed because the resolution in these calculations was not sufficiently high to resolve them.

8. The estimate for mass loss rate of clouds from Lefloch & Lazareff (1994) is found to be in good agreement with that of the clouds on the computational grid. By using the mass flux, a measure of the relative strengths of the photo-evaporative flows can be calculated, correctly implying that the medium flux model exhibits much stronger flow than the low flux model, despite having a similar mass loss rate.

I have shown that existing diagnostics do give an insight into the conditions of BRCs and can broadly be used to infer whether or not RDI is occurring using virial stability analysis. However, by comparing the inferred conditions to those on the model grids I find that these diagnostics are each subject to significant sources of error. The cumulative effect of these errors is IBL-to-cloud pressure ratios towards the lower end of the known range, suggesting that the effects of shock compression might be underestimated.

"...there at the tiniest point, the smallest thing possible exists, without component parts, but part of something larger, for, lacking in weight or force, it cannot exist alone but must join with other bits to be part of something else, another and larger thing...'

Lucretius, De Rerum Natura, 1st century B.C.

7

Assessing molecular line diagnostics of triggered star formation using synthetic observations.

7.1 Abstract

In this Chapter I investigate observational signatures of triggered star formation in bright rimmed clouds (BRCs) by using molecular line transfer calculations based on radiation-hydrodynamic radiatively-driven-implosion models. I find that for BRCs the separation in velocity between the line profile peak of an optically thick and an optically thin line is determined by both the observer viewing angle and the density of the shell driving into the cloud. In agreement with observations, I find that most BRC line profiles are symmetric and that asymmetries can be either red or blue, in contrast to the blue-dominance expected for a collapsing cloud. Asymmetries in the line profiles arise when an optically thick line is dominated by the shell and an optically thin line is dominated by the cloud interior to the shell. The asymmetries are red or blue depending on whether the shell is moving towards or away from the observer respectively. Using the known motions of the molecular gas in my models I rule out the 'envelope expansion with core collapse' mechanism as the cause of the lack of blue-asymmetry in my simulated observations. I show that the absence of a strong photon dominated region (PDR) around a BRC may not rule out the presence of triggered star formation: if the BRC line profile has a strong blue component then the shell is expected to be driving towards the observer, suggesting that the cloud is being viewed from behind and the PDR is obstructed. This could explain why BRCs such as SFO 80, 81 and 86 have a blue secondary peak and only a weak PDR inferred at $8\,\mu$m. Finally I also test the use of ^{12}CO, ^{13}CO and C^{18}O as diagnostics of cloud mass, temperature and column density. I find that the inferred conditions are in reasonable agreement with those

from the models. Calculating the cloud mass assuming spherical symmetry is shown to introduce an error of an order of magnitude whereas integrating the column density over a given region is found to introduce an error of up to a factor of two.

The research detailed in this Chapter has been published in Haworth et al. (2013), MNRAS, 431, 3470.

7.2 Introduction

Molecular line diagnostics are a widely used tool for investigating the conditions of astrophysical clouds and star formation (e.g. Schneps et al. 1980; De Vries et al. 2002; Urquhart et al. 2006; Narayanan et al. 2008; Rundle et al. 2010; Buckle et al. 2012; Hatchell et al. 2013). Line profiles can yield information about the kinematic motions of the molecular gas (e.g. Lee et al. 2004; Tsamis et al. 2008; Roberts et al. 2010; Stahler & Yen 2010; Lou & Gao 2011) and ratios of line intensities can be used to infer the cloud properties such as optical depth, temperature, column density and mass (e.g. Myers et al. 1983). Combinations of molecular tracers are usually used since different tracers probe different parts of the system. For example the ^{12}CO lines are optically thick, meaning that the outer layers of a cloud are probed. Conversely C^{18}O and HCN lines are optically thin, probing to deeper layers of a cloud.

Bright rimmed clouds (BRCs) are objects which are believed to be formed when shocks generated by nearby massive stars drive into surrounding pre-existing density structures, potentially triggering star formation in the radiatively driven implosion (RDI) scenario (e.g. Sandford et al. 1982; Bertoldi 1989; Lefloch & Lazareff 1994; Kessel-Deynet & Burkert 2003; Gritschneder et al. 2009a; Miao et al. 2009; Mackey & Lim 2010; Bisbas et al. 2011; Tremblin et al. 2012b; Haworth & Harries 2012, and references therein). This is a highly kinematic process in which shock driving is expected to occur, potentially leading to the collapse of the cloud. As such, BRCs have been subjected to a large number of molecular line observations to try and identify RDI (e.g. Lefloch et al. 1997; De Vries et al. 2002; Thompson et al. 2004; Urquhart et al. 2006, 2009; Morgan et al. 2009).

The conditions in the neutral gas of BRCs are frequently calculated based on the ratio of ^{13}CO to C^{18}O intensities following Myers et al. (1983). However alternative combinations of lines can also be used such as CS, HCO$^+$, HCN and other CO isotopologues. Lefloch et al. (1997) used CO, CS and Thompson et al. (2004) used ^{12}CO, ^{13}CO to calculate the conditions of BRCs in IC1848. They then compared the neutral cloud conditions with the ionized boundary layer (IBL) pressure to determine whether or not the clouds are being compressed. Thompson et al. (2004) found that two out of the three clouds studied have possibly been induced to collapse by the effect of radiation from nearby stars. The single system studied by Lefloch et al. (1997) was also found to be in this state, where the IBL pressure was greater than the cloud support pressure. Urquhart et al. (2006) performed a similar pressure comparison on four BRCs from the SFO catalogue (Sugitani et al. 1991; Sugitani & Ogura 1994) using ^{12}CO, ^{13}CO and C^{18}O ($J = 1 \rightarrow 0$) transitions,

finding probable triggering in two of the clouds. Other examples are Morgan et al. (2009) and Urquhart et al. (2009) where CO observations and signatures of photoionization were used to refine the northern and southern hemisphere SFO catalogues respectively, retaining only those clouds in which triggered star formation seems likely. Morgan et al. (2009) and Urquhart et al. (2009) both found that BRCs hosting sites of probable star formation typically had warmer external layers of neutral gas, approximately $20 - 30\,\mathrm{K}$, compared to the central cloud which is at about $10 - 20\,\mathrm{K}$. Urquhart et al. (2009) retained clouds for which a photon dominated region (PDR) was clearly visible, a feature which suggests that photoionization is taking place. These gas studies have been reasonably successful in identifying possible sites of triggering, however none has been conclusive. Additional evidence and tests of the accuracy of the diagnostic techniques are still required before strong conclusions can be drawn about the prevalence of RDI.

A number of features have been identified in molecular line profiles that are believed to be characteristic of specific kinematic processes. For a gas undergoing Maxwell-Boltzmann thermal motions the line profile is described by a Gaussian distribution due to thermal broadening. Deviations from this form can give insight into the bulk motions of the molecular gas. A signature that is commonly interpreted as representing infall comes from observations of optically thick lines such as ^{12}CO. If the optically thick line is sufficiently self-absorbed there will be two peaks in the line profile. For an infalling cloud, the red line profile peak is due to material moving away from the observer in the exterior regions of the cloud and the blue line profile peak is due to material moving towards the observer in the central regions of the cloud. Given that the central regions are at higher density and are therefore more likely to exceed the critical density for the molecular species, a blue-asymmetry (when the blue peak is stronger) is the expected signature of infall (e.g. Lee et al. 2004; Tsamis et al. 2008; Roberts et al. 2010; Stahler & Yen 2010). A second, optically thin, line such as C^{18}O is checked for a single peak to ensure that the two peaks from the optically thick line are from the same cloud rather than a superposition of two distinct objects at different systematic velocities.

Although this blue-asymmetry has been observed for protostars (e.g. Mardones et al. 1997) and pre-stellar cores (e.g. Lee et al. 2001, 2004) it is generally not observed in BRCs. Rather there is usually no clear asymmetry and sometimes even a dominant red-asymmetry (Thompson & White 2004). For example De Vries et al. (2002) use the Five College Radio Astronomy Observatory (FCRAO) to perform a number of molecular line observations of BRCs from the SFO catalogue. They found that a strong blue-asymmetry feature was only observed in one out of seven of the BRCs that they studied. De Vries et al. (2002) proposed that this might be due to the shock heating the cloud from the outside in, which could render the standard infall signatures unobservable.

It is currently unclear what is responsible for the lack of infall signature in the self-absorption peaks of optically thick line spectra of BRCs. There are a number of proposed causes, for example rotation (e.g. Redman et al. 2004), pulsation (e.g. Keto et al. 2006), turbulence in the core (e.g. Lee & Kim 2009; Smith et al. 2012), shock heating (De Vries

et al. 2002) or the envelope expansion with core collapse (EECC) model (e.g. Keto et al. 2006; Gao & Lou 2010; Lou & Gao 2011; Fu et al. 2011). Thompson & White (2004) studied the red-asymmetric BRC SFO 11NE in IC1848 and also attempt to model its line profile by calculating a synthetic profile for a number of possible cloud configurations. They found that an EECC model gave good agreement, suggesting that SFO 11NE is in the expansion phase of RDI identified by Lefloch & Lazareff (1994).

Understanding the reliability of molecular line diagnostics and the reason behind the lack of blue-asymmetry is essential if a more comprehensive picture of the effect of feedback and triggered star formation is to be realised. In Haworth et al. (2012) I tested other diagnostics of BRCs that use continuum and atomic line data. In this Chapter I extend this form of analysis to molecular lines: generating synthetic data cubes and performing standard diagnostics to test their accuracy and applicability, and to address sources of ambiguity when using them to infer whether or not triggered star formation is occurring.

7.3 Numerical method

In addition to the photoionization and hydrodynamics capabilities discussed in Chapter 3, TORUS is also capable of non–LTE molecular line transport. This capability was developed by David Rundle and Tim Harries. The details of the molecular line transfer algorithm are given in Rundle et al. (2010), but I provide a summary here for completeness. I perform a non-LTE statistical equilibrium calculation to determine molecular level populations and use the result to calculate synthetic observations in the form of spectral datacubes. The statistical equilibrium algorithm uses an accelerated Monte Carlo method (Hogerheijde & van der Tak 2000) to calculate the mean intensity in each cell. A cell-centric long-characteristic ray tracing scheme is used in which a number of randomly directed rays are traced from random locations in each cell. The frequencies are also randomly selected from a uniform distribution of width 4.3 turbulent line widths, centred on the rest frequency of a given molecular transition. The specific intensity at the end point of the ray in the cell is determined by integrating the equation of radiative transfer along the path traced by the ray to the edge of the grid. The boundary condition for most rays is the cosmic microwave background (CMB). However for the calculations in this Chapter there is a nearby O star, the effect of which has to be included. I therefore developed the molecular line transfer calculation so that a single ray is forced from each cell towards the star, using the stellar effective temperature as the boundary condition and weighting that ray's contribution based on the assumed probability of it having intersected the star at random. This probability is simply the solid angle subtended by the star divided by 4π.

I include dust in these calculations and assume a canonical value for the dust to gas mass ratio of 1×10^{-2} in all cells that are below a temperature of 1500 K. For cells hotter than this I incorporate sublimation effects by setting the dust abundance to a negligible value. I assume spherical silicate dust grains that follow a standard interstellar medium

size distribution (Mathis et al. 1977). The optical constants are taken from Draine & Lee (1984). Given that BRCs are relatively young (the RHD models simulated 200 kyr of evolution), the dust size distribution and chemistry are not expected to depart much from this canonical interstellar medium model. This is the same dust treatment used in Haworth et al. (2012)/the previous Chapter.

Once a set of rays has been traced, the mean intensity $\bar{J}_\nu$ in each cell is calculated by averaging the specific intensity from the rays, weighted by the line profile function

$$\phi_\nu = \frac{c}{v_{\rm turb}\nu_0\sqrt{\pi}}{\rm e}^{-\Delta v^2/v_{\rm turb}^2} \tag{7.1}$$

where c, ν_0, $v_{\rm turb}$, and Δv are the speed of light, rest frequency of the transition, turbulent velocity and velocity required to Doppler shift ν_0 to ν respectively. Here $v_{\rm turb}$ is imposed as $0.2\,{\rm km\,s^{-1}}$, similar to that used in Rundle et al. (2010) and featured in Offner et al. (2008). The radiation hydrodynamic models of Haworth & Harries (2012) (which are the basis for the statistical equilibrium calculations in this Chapter and are described more in section 7.3.1) exhibited strong systematic bulk motions which dominate turbulence. $\bar{J}_\nu$ in each cell comprises two components, a first that is fixed for the cell during one set of level population iterations which describes the contribution from space external to the cell and a second that varies with the level populations (which affect the source function, S_ν) internal to the cell

$$\bar{J}_\nu = J_\nu^{\rm ext} + J_\nu^{\rm int} = \frac{\sum\limits_i I_\nu^i {\rm e}^{-\tau_{\rm i}}\phi_\nu}{\sum\limits_i \phi_\nu} + \frac{\sum\limits_i S_\nu\left(1-{\rm e}^{-\tau_{\rm i}}\right)\phi_\nu}{\sum\limits_i \phi_\nu} \tag{7.2}$$

where I_ν^i and τ_i are the intensity and optical depth along the $i^{\rm th}$ ray. Equation 7.2 is solved iteratively in conjunction with the equations of statistical equilibrium, which determine the level populations and modify the source function within the cell

$$n_l\left[\sum_{k<l} A_{lk} + \sum_{k\neq l}\left(B_{lk}J_\nu + C_{lk}\right)\right] = \sum_{k>l} n_k A_{kl} + \sum_{k\neq l} n_k\left(B_{kl}J_\nu + C_{kl}\right) \tag{7.3}$$

where n_l, A_{lk}, B_{lk} and C_{lk} are the relative fractional level population of level l, Einstein A (spontaneous absorption/emission) and B (stimulated absorption/emission) coefficients and the collisional rate coefficient for levels l and k at a given temperature. The coefficients are taken from the LAMDA database (Schöier et al. 2005). Initially the J = 0, 1 relative fractional level populations are set to 0.5 and the other levels to 1×10^{-10}.

The ray tracing and level population calculations are performed iteratively. Convergence is checked by comparing level populations from the latest and previous iteration, being achieved where the maximum root mean square fractional difference in all levels is less than a user-specified value, here taken to be 1×10^{-2}. This results in an average

fractional difference of order 10^{-4}–10^{-5} in the J = 2, 1 levels which are those required for the transitions used in this Chapter. Some repeat calculations were performed to check that my convergence criterion was sufficient.

A two-stage calculation is performed in which an initial set of iterations using rays with fixed position, frequency and direction is run until the level populations converge. This is followed by iterations using rays with random position, frequency and direction that double in number until the level populations again converge. The first stage of the calculation converges quickly, but poorly samples both the frequency range and the spatial extent of the grid. The second stage reduces the systematic and random errors associated with using fixed rays. This combination reduces the calculation time compared to using solely random rays. A typical calculation requires around 10 iterations using a starting number of between 400–700 fixed rays per cell (that do not double in number between iterations) followed by 3–4 iterations using random rays which double in number with each iteration. The statistical equilibrium calculation also make use of the convergence-acceleration scheme of Ng (1974), which estimates an updated set of relative fractional level populations by extrapolation based on the level populations from the previous 4 iterations. This convergence acceleration is employed every five iterations.

In this Chapter I investigate molecular line diagnostics and kinematic signatures of the neutral component of BRCs. Due to computational expense it currently not possible to perform 3D radiation hydrodynamic models with chemical evolution (Glover et al. 2010). I therefore use standard values for the molecular abundance relative to hydrogen and neglect PDR and low–temperature chemistry other than to adopt the following conditions. An abundance drop-model is employed at low temperatures for CO and its isotopologues to accommodate freeze-out of molecules on to dust grains (Jørgensen 2004). Under this scheme molecular species in cells at less than 30 K and molecular hydrogen density greater than $3 \times 10^4\,\mathrm{cm}^{-3}$ have their abundance reduced by a factor of 10. The molecular abundance is set to a negligible value where the neutral atomic hydrogen fraction is lower than the conservative value of 0.1 as the gas is ionized and molecules would be dissociated (photodissociation codes assume no ionized atomic hydrogen, e.g. Bisbas et al. 2012; Heiner & Vázquez-Semadeni 2013).

Data cubes comprising two-dimensional spatial data and a series of velocity channels are generated by ray tracing in a similar manner to the primary level-population solver, only the rays are directed towards a pixel array that represents the image plane at the observer position. The cubes are produced in units of spectral radiance, $\mathrm{erg\,s^{-1}\,cm^{-2}\,Hz^{-1}\,sr^{-1}}$, usually simply referred to as the monochromatic specific intensity I_ν and converted into a brightness temperature T_B using the Rayleigh-Jeans approximation

$$T_\mathrm{B} = \frac{I_\nu c^2}{2\nu^2 k_\mathrm{B}} \tag{7.4}$$

where c, ν and k_B are the speed of light, frequency of observation and Boltzmann constant respectively. Extensive testing of the molecular line transfer calculations is included in

Rundle et al. (2010).

7.3.1 The radiation hydrodynamic models

The density, temperature and velocity distribution that provide the basis for the statistical equilibrium and simulated observation calculations are taken from the final grid states of the radiation hydrodynamic RDI models of Haworth & Harries (2012) that were also used in Haworth et al. (2012) and are discussed in the previous two Chapters.

In Haworth & Harries (2012), the models initially consisted of a Bonnor-Ebert sphere (BES) at the centre of the grid with a plane parallel ionizing radiation field impinging upon the left hand edge of the grid. I considered three different distances of the BES from the star responsible for the plane parallel radiation field which, due to the varying levels of flux incident at the left hand edge of the grid, I labelled the 'low', 'medium' and 'high' flux models. The radiation field parameters are all given in Table 7.1. During the radiation hydrodynamic calculation, an ionization front was established which drove into the BES, accumulating a dense shell of material and changing the BES morphology. The outer layer of the shell was also photoionized and ejected in a photo-evaporative outflow. The manner in which compression of the BES proceeded was found to be dependent on the distance of the star, in agreement with previous models such as Gritschneder et al. (2009a) and Bisbas et al. (2011). I also found that inclusion of diffuse field radiation could significantly modify the result of the calculation.

In this Chapter the final states of the most sophisticated RDI models, those which included the diffuse field in Haworth & Harries (2012) and have been subject to a full photoionization and thermal balance calculation in Haworth et al. (2012), are used. A slice through the logarithmically scaled density distribution for each model at 200 kyr (the simulation end time of the RDI models) is given in Figure 7.1. Also included are velocity vectors and a contour corresponding to the point at which the neutral atomic hydrogen fraction is equal to 0.1 (above which molecular species are able to survive, see section 7.3). Where the contour does not trace the dense gas, for example in the wings of the high flux model (the bottom panel of Figure 7.1) the additional cooling from the full photoionization and thermal balance calculation in Haworth et al. (2012) has moved the ionization front. This relocation of the ionization front has a negligible effect on the simulated molecular line diagnostics in this Chapter since it is in regions away from the main cloud (the object of study) that are at low density and therefore low intensity relative to the cloud.

7.4 Simulated Observations

7.4.1 Choice of molecular transitions

Isotopologues of CO are among the most commonly used species in molecular line observations, in particular for observations of BRCs (e.g. Lefloch et al. 1997; De Vries et al.

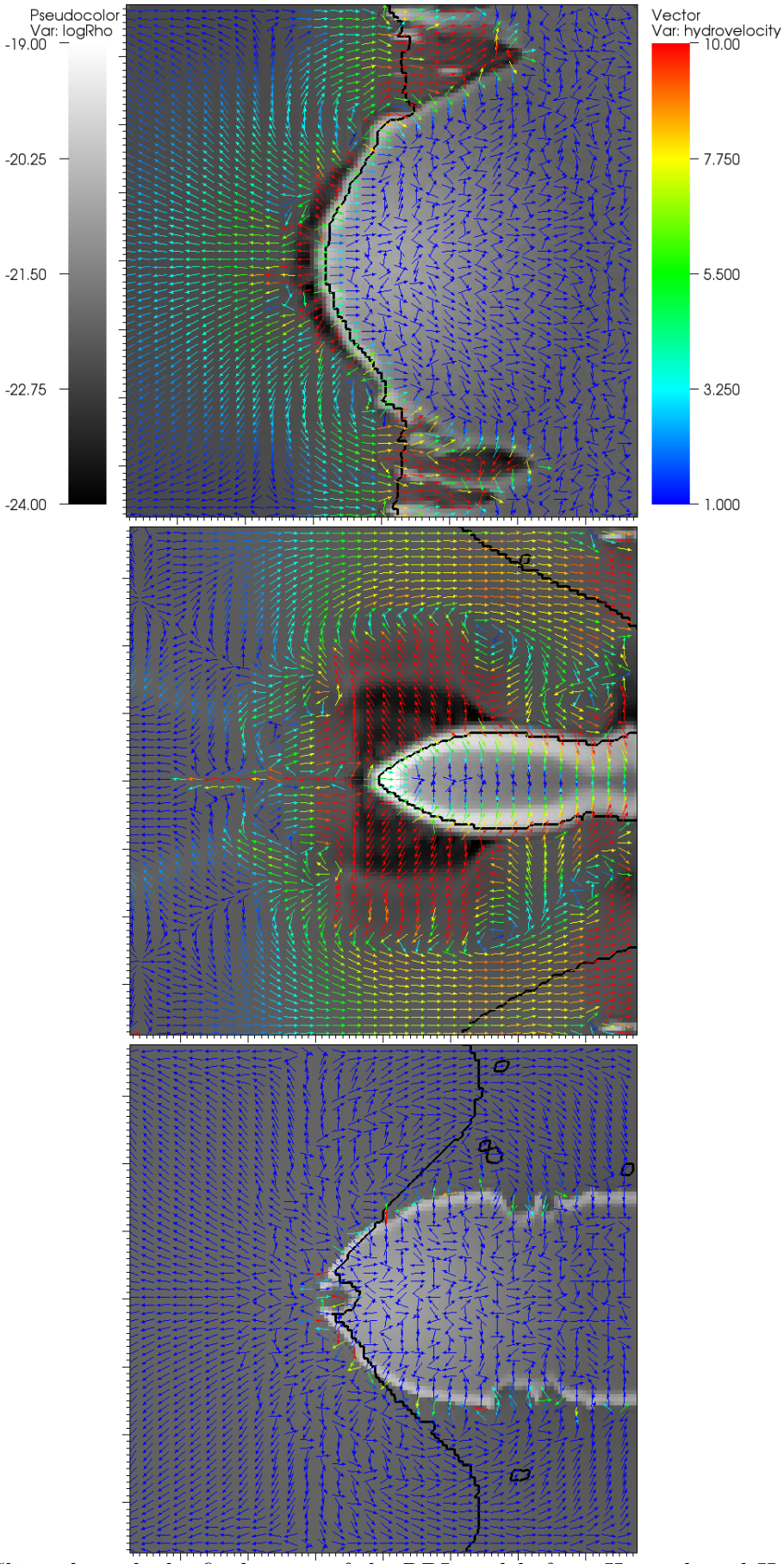

Figure 7.1: Slices through the final states of the RDI models from Haworth and Harries (2012). The panels are from the 'low', 'medium' and 'high' flux models from top to bottom. The greyscale distribution is the logarithmic density, the contour is that at which the neutral atomic hydrogen fraction is equal to 0.1 and the vectors represent the velocity field. Major ticks are separated by 0.65 pc.

Table 7.1: A list of key parameters from the RDI models of Haworth & Harries (2012).

Variable (unit)	Value	Description
R_c (pc)	1.6	Cutoff radius of initial BES
n_{max} (cm^{-3})	1000	Peak initial BES number density
Φ_{low} (cm^{-2})	9.0×10^8	Low ionizing flux
D_{low} (pc)	$(-10.679, 0, 0)$	Source position (low flux)
Φ_{med} (cm^{-2})	4.5×10^9	Intermediate ionizing flux
D_{med} (pc)	$(-4.782, 0, 0)$	Source position (medium flux)
Φ_{high} (cm^{-2})	9.0×10^9	High ionizing flux
D_{high} (pc)	$(-3.377, 0, 0)$	Source position (high flux)
T (K)	40000	Source effective temperature
R ($R_\odot$)	10	Source radius
L(pc^3)	4.87^3	Grid size

2002; Thompson et al. 2004; Morgan et al. 2009). This is because they have a relatively high abundance and low critical density, making them easier to observe. I therefore choose to generate data cubes of ^{12}CO, ^{13}CO and C^{18}O. Analysis of molecular line data requires the use of probes which are sensitive to different conditions in the cloud. ^{12}CO (J = 2→1) is a line which can be optically thick, with ^{13}CO (J = 2→1) and C^{18}O (J = 2→1) being optically thinner variants. These are combined to trace and infer the properties of the molecular gas.

7.4.2 Simulated instruments

I smooth the data cubes that I calculate to a Gaussian beam using ACONVOLVE from CIAO v4.1 (Fruscione et al. 2006) to a size appropriate to the half power beamwidth (HPBW) of the simulated instrument. I choose the beam size given by the Rayleigh criterion, as is the case for the JCMT which has a 15 m dish, resulting in beam sizes of around 22″. For comparison, the beam size of the ^{12}CO (J = 1→0) transition using the FCRAO in De Vries et al. (2002) is 46″. Factors such as instrument and atmospheric noise are not included.

7.5 Calculating the molecular cloud conditions

The optical depth, excitation temperature and column density of the optically thin C^{18}O line can be determined following the method described by Myers et al. (1983) and used by, for example, Urquhart et al. (2004) and Morgan et al. (2009). The source-averaged optical depth of C^{18}O is determined using

$$\frac{T_{13}}{T_{18}} = \frac{1 - e^{-\tau_{13}}}{1 - e^{-\tau_{18}}} \tag{7.5}$$

where T_{13} and T_{18} are the peak brightness temperatures of the source-averaged line profiles of ^{13}CO and C^{18}O respectively, with the background signal subtracted. In this work, the background signal is determined from the average value in the ambient H II region. Equation 7.5 is solved by assuming that the two source-averaged optical depths are related

by their relative abundances

$$\tau_{13} = X_{13/18}\tau_{18} \tag{7.6}$$

where $X_{13/18}$ is the ratio of ^{13}CO to C^{18}O abundances. This abundance ratio is usually estimated based on Galactic abundance distributions and the location of the target in the Galaxy (Langer & Penzias 1990), for example being taken as 10 in Urquhart et al. (2006). Here I use the ratio of prescribed abundances from Table 7.2, giving a ratio of approximately 16 for $X_{13/18}$ and 30 for $X_{12/13}$. I find the remaining single unknown optical depth numerically, using a decimal search.

The gas excitation temperature is estimated for ^{12}CO and C^{18}O via the same approach used in Morgan et al. (2009). The equation of radiative transfer written in terms of optical depth τ, integrated along a path length s and with the background subtracted gives the intensity as a function of the Planck function B_ν, the background intensity I_0 and the optical depth

$$I_\nu(s) = (B_\nu - I_0)\left(1 - e^{-\tau}\right). \tag{7.7}$$

This can be re-written in terms of temperatures as

$$T_\mathrm{B} = \frac{h\nu}{k_\mathrm{B}}\left(\frac{1}{e^{h\nu/k_\mathrm{B}T_\mathrm{ex}} - 1} - \frac{1}{e^{h\nu/k_\mathrm{B}T_\mathrm{cmb}}}\right)\left(1 - e^{-\tau}\right) \tag{7.8}$$

where T_B, T_ex and T_cmb are the brightness, excitation and CMB temperatures respectively and ν is the frequency of radiation emitted following the molecular transition (Rohlfs & Wilson 1996). Equation 7.8 can be rearranged for the excitation temperature to

$$T_\mathrm{ex} = T_\nu \left\{ \ln\left[1 + T_\nu \frac{1 - e^{-\tau}}{T_\mathrm{B} + T_\nu\left(1 - e^{-\tau}\right)e^{\frac{-T_\nu}{T_\mathrm{cmb}}}}\right]\right\}^{-1} \tag{7.9}$$

where T_ν is set to $h\nu/k_\mathrm{B}$. If the ^{12}CO emission is optically thick, which is typically expected to be the case, the term $1 - e^{-\tau}$ tends to 1 and the excitation temperature T_ex of ^{12}CO can be estimated using

$$T_\mathrm{ex} = 11.06\left\{\ln\left[1 + 11.06\frac{1}{T_\mathrm{B} + 0.192}\right]\right\}^{-1}. \tag{7.10}$$

The criterion that ^{12}CO be optically thick can be checked by comparing the relative intensities of ^{12}CO and ^{13}CO to their relative abundances. If the ^{12}CO to ^{13}CO line intensity ratio is much smaller than the assumed abundance ratio then ^{12}CO is expected to be optically thick.

Assuming local thermodynamic equilibrium (LTE) and that a single temperature T applies to the whole cloud, the kinematic temperature is simply this excitation temperature. Morgan et al. (2009) derived the C^{18}O excitation temperature of clouds in addition to ^{12}CO and found significant differences. Since ^{12}CO and C^{18}O probe different parts of the cloud it is not surprising that they will have different excitation temperatures. Typically the interior parts of the cloud, probed by C^{18}O, are expected to be cooler. With its

optical depth known, the $C^{18}O$ excitation temperature can be calculated independently using equation 7.9, giving

$$T_{\rm ex} = 10.54 \left\{ \ln \left[1 + \frac{10.54\,(1 - e^{-\tau_{18}})}{T_{\rm B} + 0.221\,(1 - e^{-\tau_{18}})} \right] \right\}^{-1} . \tag{7.11}$$

The total column density for a given molecular species is calculated following the method given in Scoville et al. (1986), whereby the optical depth is integrated over the line profile. For CO molecules, assuming a rigid rotor and that all levels are represented by a single excitation temperature, the column density over all levels is

$$N = \frac{3k_{\rm B}}{8\pi^3 B\mu^2} \frac{e^{hB{\rm J}_l({\rm J}_l+1)/k_{\rm B}\,T_{\rm ex}}}{({\rm J}_l + 1)} \frac{T_{\rm ex} + hB/3k_{\rm B}}{(1 - e^{-h\nu/k_{\rm B}\,T_{\rm ex}})} \int \tau_v dv \tag{7.12}$$

where B and μ are the rotational constant and permanent dipole moment of the molecule respectively. ${\rm J}_l$ is the lower of the two rotational levels for the transition being considered. The rotational constant and permanent dipole moment of $C^{18}O$ are 54.891 GHz and 0.11 Debye respectively. When using equation 7.12 in this Chapter I use the average value of τ_{18} calculated via Equations 7.5 and 7.6 and use the FWHM of the line to replace the velocity integral. With the $C^{18}O$ column density known, the H_2 column density $N\,(H_2)$ can then be found using an assumed (and, since in this case it is prescribed, correct) abundance of $C^{18}O$ relative to H_2, namely 1.7×10^{-7} (the prescribed value is given in Table 7.2 and was taken from Goldsmith et al. 1997).

Following Urquhart et al. (2006) (assuming spherical symmetry) I estimate the cloud average number density $n_{\rm H_2}$ using the column density via

$$n_{\rm H_2} = \frac{\pi^3 N\,({\rm H_2})}{8R} \tag{7.13}$$

where R is the cloud radius. Equation 7.13 is derived by integrating the column density over the assumed uniform density sphere and dividing by the circular surface presented to the observer. Finally the mass of the cloud can be estimated using

$$M_{\rm cloud} = \frac{4\pi R^3}{3} n_{\rm H_2} \mu m_{\rm H} \tag{7.14}$$

where R, $m_{\rm H}$ and μ are the cloud radius, atomic hydrogen mass and mean molecular weight respectively. I follow Urquhart et al. (2006) and use a value of $\mu = 2.3$, which assumes 25 per cent abundance of helium by mass.

In addition to the above mass calculation which assumes spherical symmetry and uniform density, the mass can also be calculated by integrating the inferred column density over a given solid angle. That is, the total mass of molecular hydrogen of over all pixels i in a given region is

$$M_{\rm cloud} = \frac{\mu m_{\rm H}}{X(j)} \sum_i a_i N_i(j) \tag{7.15}$$

Table 7.2: The parameters used in statistical equilibrium and datacube generation calculations

Parameter (Unit)	Value	Description
$v_{\rm turb}$ (km s^{-1})	0.2	Turbulent velocity
$N_{\rm v}$	200	Number of velocity channels
dv (km s^{-1})	0.1	Span of each velocity channel
$N_{\rm pix}$	401^2	Number of pixels per channel
θ ($''$)	2.5	Angular width per pixel
tolerance	1×10^{-2}	Statistical equilibrium convergence checking tolerance
$n_{\rm C^{18}O}/n_{\rm H_2}$	1.7×10^{-7}	$C^{18}O$ abundance (Goldsmith et al. 1997)
$n_{\rm ^{13}CO}/n_{\rm H_2}$	2.7×10^{-6}	^{13}CO abundance (Pineda et al. 2008, and references therein)
$n_{\rm ^{12}CO}/n_{\rm H_2}$	8.0×10^{-5}	^{12}CO abundance (Magnani et al. 1988, and references therein)
D (pc)	1000	Distance of observer

where $X(j)$ is the abundance of species j relative to molecular hydrogen and a_i is the pixel area.

7.6 Results and discussion

7.6.1 Synthetic data cubes

Cube construction

I generated ^{12}CO, ^{13}CO and $C^{18}O$ data cubes from the results of statistical equilibrium calculations in the manner described in sections 7.3 and 7.4. A total of nine statistical equilibrium calculations were run, one for each isotopologue considered at the three distances of the ionizing star from the cloud (see section 7.3.1 for details of the model). The maximum velocity magnitude in the data cubes is 10 km s^{-1} and each velocity channel spans 0.1 km s^{-1}. A summary of the statistical equilibrium and datacube calculation parameters is given in Table 7.2. The abundance of each species in Table 7.2 is a constant value relative to H_2, determined through a literature search.

Edge-on morphology

^{12}CO images of the clouds for an observer edge-on to the BRC, convolved to the appropriate Gaussian beam size, are given in Figures 7.2, 7.3 and 7.4 for the low, medium and high flux models respectively. Overlaid are ^{13}CO and $C^{18}O$ intensity contours. These images and contours are constructed by integrating the data cubes using the STARLINK software GAIA. The contours are chosen to give the best representation of the distribution of emission throughout the BRCs. The ionizing star is located off the left hand edge of the images.

The low flux ^{12}CO images (Figure 7.2) are dominated by the bright bow, with weaker emission in the wings of the cloud. There is also some weaker emission behind the bow in the cloud. The integrated ^{13}CO and $C^{18}O$ contours trace the ^{12}CO morphology well. The peak $C^{18}O$ contours extend further into the neutral gas away from the bright rim

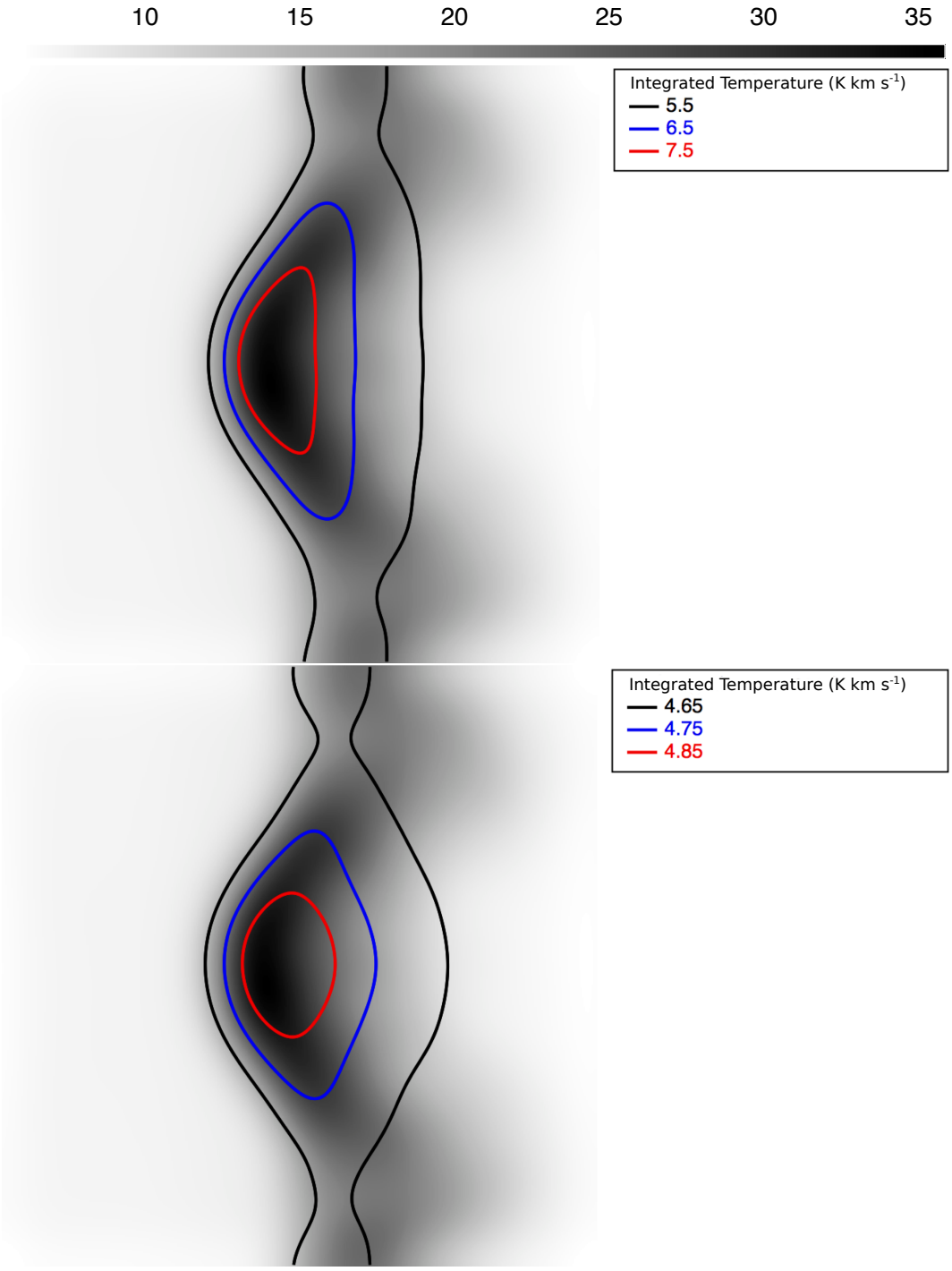

Figure 7.2: Low flux model data cube ^{12}CO images (greyscale) smoothed to a Gaussian beam representative of the JCMT and integrated over velocity channels. The image temperature scale is given by the greyscale bar in integrated brightness temperature units (K km s^{-1}). The contours are ^{13}CO (top) and C^{18}O (bottom). These images are all 4.87 pc to a side.

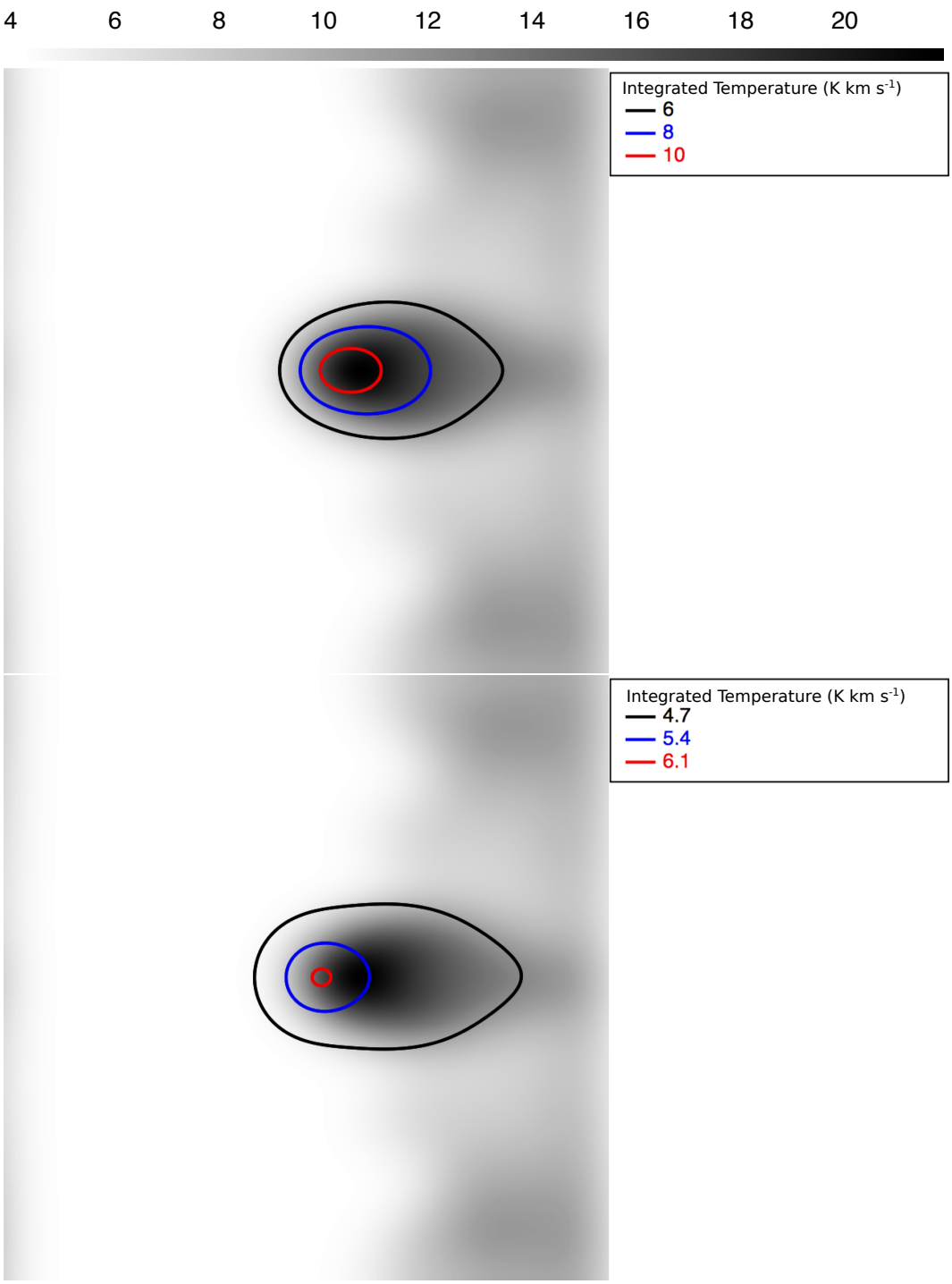

Figure 7.3: Medium flux model data cube ^{12}CO images (greyscale) smoothed to a Gaussian beam representative of the JCMT and integrated over velocity channels. The image temperature scale is given by the greyscale bar in integrated brightness temperature units (K km s^{-1}). The contours are ^{13}CO (top) and C^{18}O (bottom). These images are all 4.87 pc to a side.

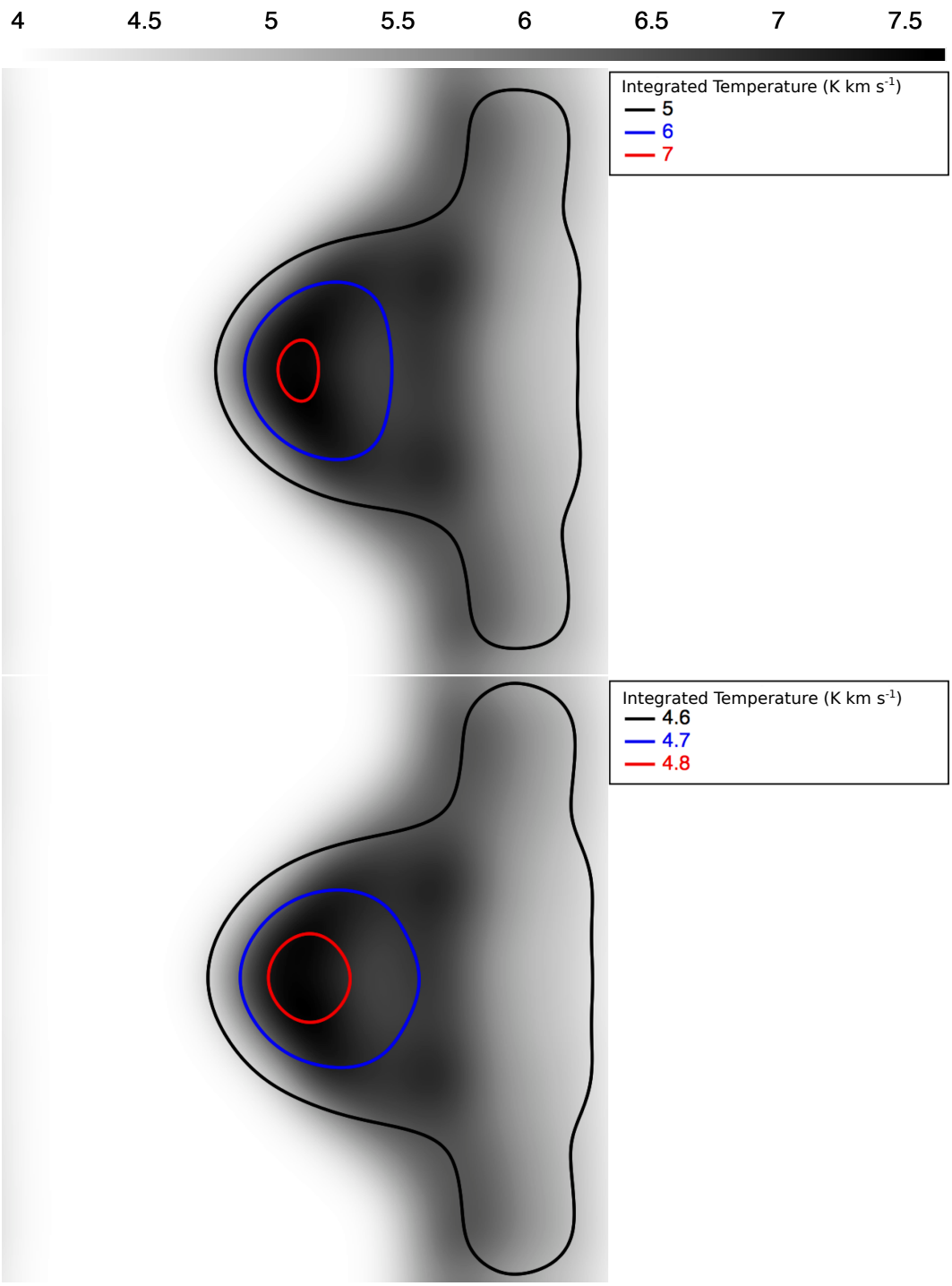

Figure 7.4: High flux model data cube ^{12}CO images (greyscale) smoothed to a Gaussian beam representative of the JCMT and integrated over velocity channels. The image temperature scale is given by the greyscale bar in integrated brightness temperature units (K km s^{-1}). The contours are ^{13}CO (top) and C^{18}O (bottom). These images are all 4.87 pc to a side.

due to the lower critical density of the line. In the radiation hydrodynamic calculations instabilities arose resulting in fingers with dense tips in the wings of the BRC (Haworth & Harries 2012). Those dense tips are not individually resolved in these data cubes due to the beam size used, rather they appear to contribute to the more widespread emission in the wings of the BRC.

The medium flux ^{12}CO images (Figure 7.3) show a dense core at the tip of the cloud and a tail that gives the object a cometary appearance. There is also fairly widespread emission about the cometary object which is due to foreground material, rather than material coinciding with the BRC itself. A channel map of the medium flux model over the velocity range -7.02 to $+0.05\,\mathrm{km\,s^{-1}}$ is given in Figure 7.5. I only include a channel map into the negative velocity range because there is no significant visual difference in the corresponding positive velocity channels. At low velocities (the right hand panel of Figure 7.5) most of the emission comes from the undisturbed material in the inner core at the tip of the cloud, as well as from the layers of the shell driving into the cloud perpendicular to the line of sight. At higher velocities the components of the shell driving into the shell along the line of sight dominate. At high negative velocities the shell from the near side of the cloud is observed and at high positive velocities the shell from the far side of the cloud is observed.

The high flux ^{12}CO images consist of a BRC which has a fairly dim bow compared to the low and medium flux models. The weaker extended emission behind the main cloud is therefore more easily visible due to the reduced contrast. There is also a lot of visible foreground material that is not directly associated with the BRC, towards the right of the image. The relative dimness of the high flux model compared to the other two models is because less material was accumulated during the high flux radiation hydrodynamic calculation in Haworth & Harries (2012). The ^{13}CO and C^{18}O contours have fairly similar morphology, again tracing the ^{12}CO extent of the gas well.

In general, although the optically thin and thick lines may be focused on slightly different components of the cloud (depending on the density structure) each line traces a similar extent of the cloud for all models. It is therefore only necessary to use the combination of lines considered in this section to determine the average cloud conditions.

7.6.2 Edge-on line profiles

I split the edge–on image of each cloud into a series of 20 equally sized boxes over which I calculate the average line profiles. These boxes are 50 by 50, 20 by 40 and 40 by 50 pixels for the low, medium and high flux models respectively. The box sizes are chosen to provide optimal coverage of the BRC. Signatures in profiles such as these are used to infer the kinematic behaviour of the gas by observers but the cause of these signatures is not always clear. The interpretation of line profile features is usually based on simple theoretical models. Since I have directly modelled the RDI process and know the thermal and kinematic conditions I can attempt to clarify the origin of some of these signatures. The 20 line profiles are shown for each model cloud across all three considered molecular

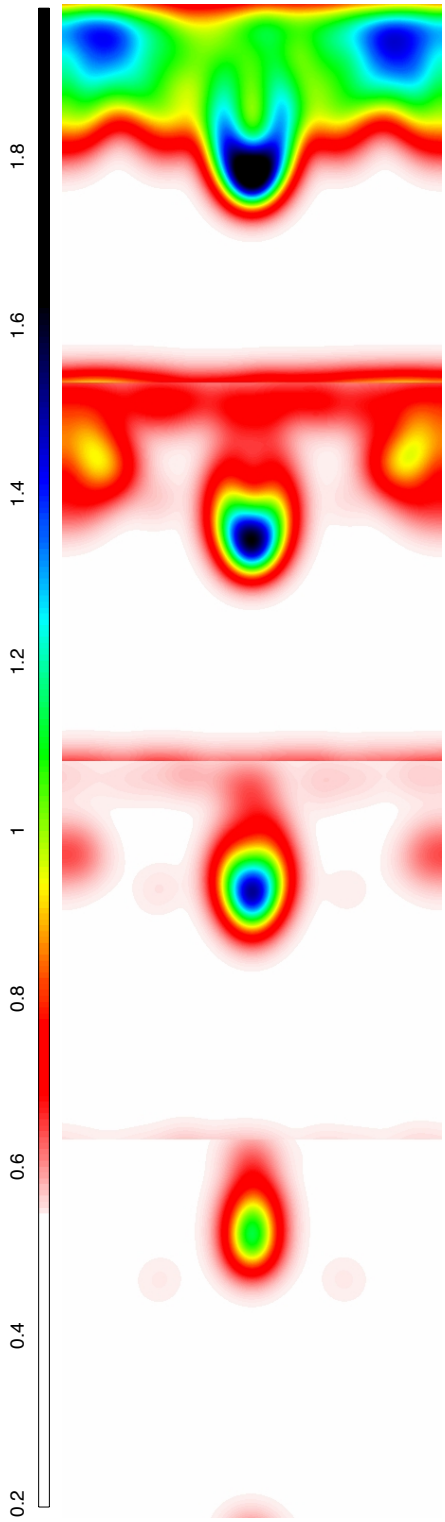

Figure 7.5: A pseudocolour channel map of the medium flux model in ^{12}CO. The channels, from left to right, are at $-7.02, -4.70, -2.27$ and $0.05\,\mathrm{km\,s^{-1}}$. The colourbar represents the brightness temperature scale in Kelvin. Each channel is 4.87 pc to a side.

species in Figure 7.8.

General features of the edge-on line profiles

At this viewing angle the line profiles typically consist of multiple components. The primary component is a peak of small width centred on $0\,\mathrm{km\,s^{-1}}$ which is due to turbulently broadened emission from the stationary gas both within the cloud and from the back/foreground material. The secondary components are due to the swept up shell of material driving into the cloud, in agreement with findings from LOS velocity profiles calculated in Tremblin et al. (2012b).

The profiles are all symmetric about the horizontal mid–plane of the BRC. There is no helical structure or apparent rotation of the cloud as is observed in some elephant trunks (Carlqvist et al. 1998, 2003; Gahm et al. 2006). This result is unsurprising since the starting conditions of my RDI models were axisymmetric. Rotating elephant trunks form via instability (Schneps et al. 1980; Chauhan et al. 2011a) or the exposure of a turbulent medium to ionizing radiation (Gritschneder et al. 2009b, 2010; Ercolano et al. 2012; Tremblin et al. 2012a) rather than RDI. Unless the formation of trunks from a collection of initial inhomogeneities gives rise to a different velocity structure (Mackey & Lim 2010) it seems that the product of RDI of larger scale existing objects is the BRC, which is a distinct object from the narrower, relatively rapidly rotating elephant trunks. The velocities in most profiles are in a similar range to those identified in LOS velocity profiles of the RDI models of Gritschneder et al. (2010). Some of the cloud-averaged profiles from Urquhart et al. (2009) also show secondary features that span the velocity range illustrated here, for example SFO81, which shows two secondary peaks separated by around $9\,\mathrm{km\,s^{-1}}$. The range in velocities between the peaks in the line profiles observed in Urquhart et al. (2009) are too large to be the result of self absorption. In my the models this large velocity range is due to the systematic bulk shell motions relative to the low velocity gas encompassed by the shell.

Features in the line profiles due to the shell have their intensity determined by the density at which the line becomes optically thick. The peak velocity of the shell feature depends on the viewing angle of the observer and the propagation direction of the shell. For example if the shell is travelling perpendicularly to the observer viewing angle then the velocity of the shell peak will be slower than if the observer is viewing the shell along its propagation vector. In the low flux case the shell layers give rise to broad shoulders about the central peak of relatively low intensity compared to the central peak. In the medium flux case the shell contributions to the line profile manifest themselves as separate peaks, since the shell is sufficiently dense and travelling sufficiently fast for the secondary peaks to be isolated from the turbulently broadened emission of the stationary cloud. In the high flux model the shell layer is thinner and propagating more slowly so the distinction between the uncompressed cloud and shell is not as clear. The peaks due to the shell in these models increase and decrease in strength as the observer moves to different viewing angles, as discussed further in section 7.6.3.

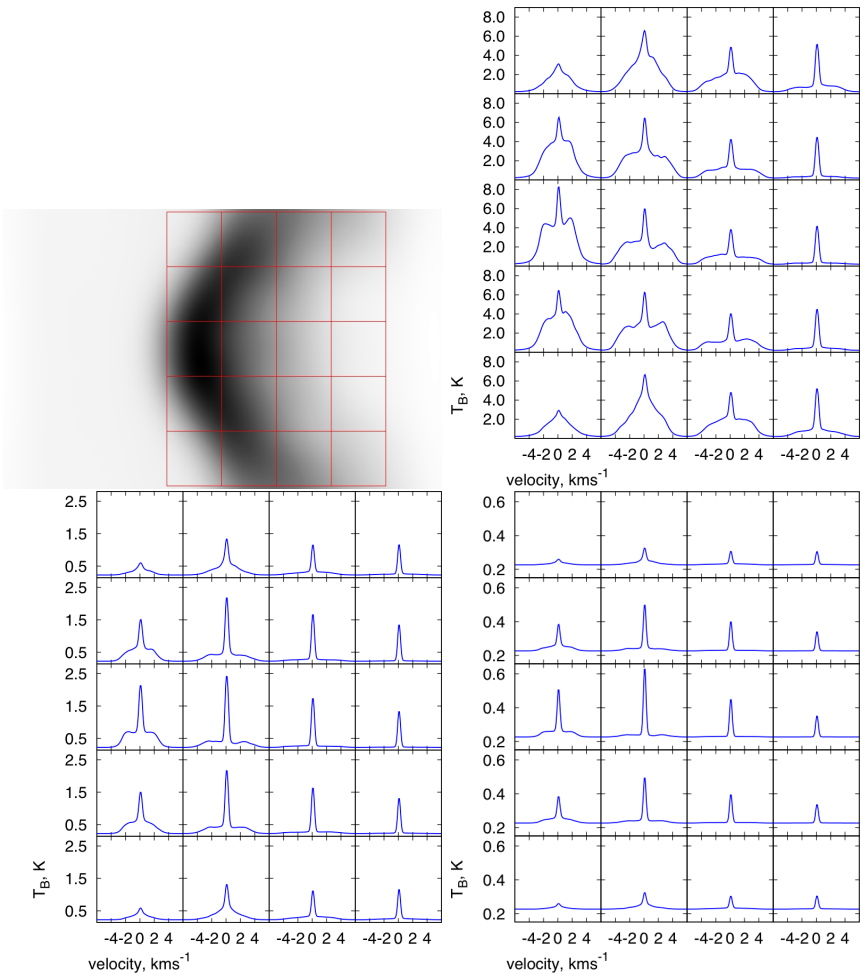

Figure 7.6: Line profiles for regions of the low flux model. The top left image shows the region locations. The profiles are ^{12}CO (top right), ^{13}CO (bottom left) and C^{18}O (bottom right).

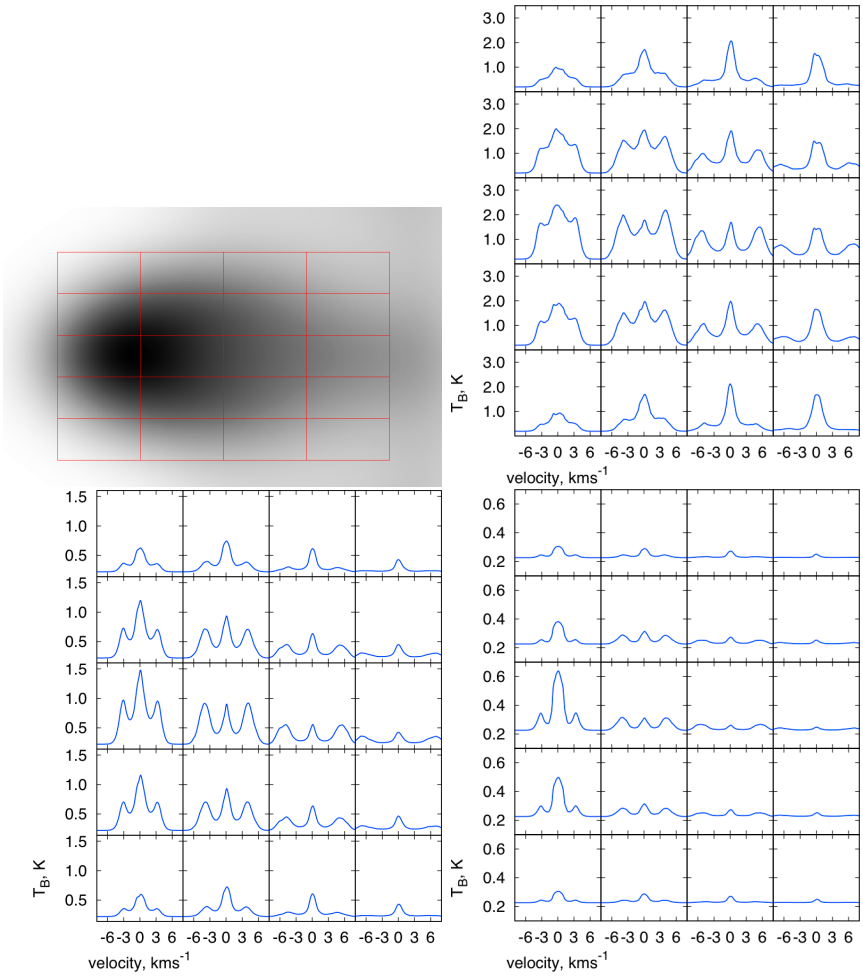

Figure 7.7: Line profiles for regions of the medium flux model. The top left image shows the region locations. The profiles are ^{12}CO (top right), ^{13}CO (bottom left) and C^{18}O (bottom right).

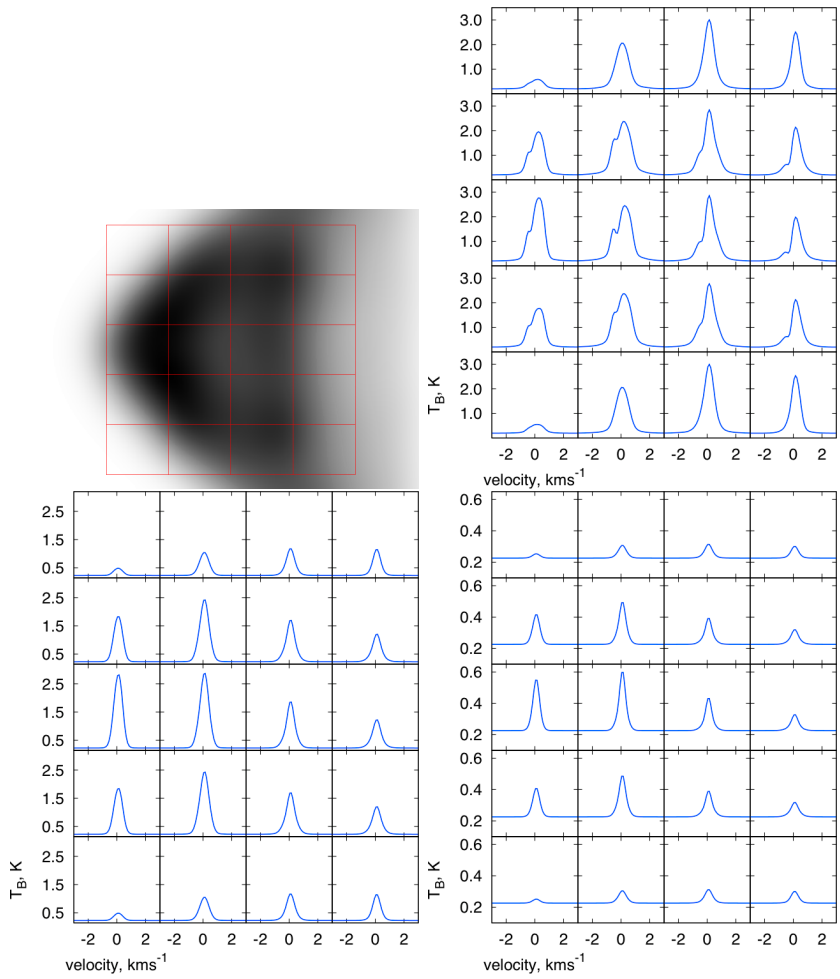

Figure 7.8: Line profiles for regions of the high flux model. The top left image shows the region locations. The profiles are ^{12}CO (top right), ^{13}CO (bottom left) and C^{18}O (bottom right).

The position of the boxes with the most intense line profile peak in the low and high flux models in Figure 7.8 do not correlate between ^{12}CO and C^{18}O. In the medium flux model, the position of the most intense ^{12}CO and C^{18}O profile peaks do correlate, being situated towards the tip of the cometary object in the left most column of the middle row. This implies that in the high and low flux model the optically thick and thin lines are predominantly probing different parts of the clouds. In the medium flux case the optically thick and thin line both probe the same part of the cloud.

Edge-on asymmetries

Another interesting feature is that asymmetries in the ^{12}CO line profiles at this edge-on viewing angle are predominantly red. That is, non-Gaussian features with $v > 0\,\mathrm{km\,s^{-1}}$ are stronger than those with $v < 0\,\mathrm{km\,s^{-1}}$. An example of red asymmetry from Figure 7.8 is the central row of the medium flux model in ^{12}CO where the shells are most directly propagating towards and away from the observer. The reason for this red-asymmetry is the dense shell of material that is driving into the cloud. The BRC observed from this viewing angle is a three-component system, with a central (and ambient) gas cloud, a near-shell propagating away from the observer into the cloud (red-shifted) and a far-shell propagating towards the observer into the cloud (blue-shifted). The optically thick emission from each component will only be from the closest layer to the observer at a given velocity. The interior edge of the driving shell is typically at a lower density than the exterior and central regions of the shell so the blue peak in the line profile is from lower density interior gas and is therefore weaker. At the frequency of the CO molecular transitions considered here, dust absorption plays a negligible role in attenuating the observed intensity from the far shell layer. Asymmetries become more pronounced at different viewing angles. For example, as the observer moves to view the BRC face on the shell will be denser and moving more directly along the observer's line of sight and the profile will be more red-asymmetric. This is discussed further in section 7.6.3.

Envelope expansion with core collapse

An alternative explanation for the red-asymmetry in BRC line profiles is the envelope expansion with core collapse (EECC) model, in which the cloud is a two component system with a collapsing core and an expanding outer shell, (e.g. Keto et al. 2006; Gao & Lou 2010; Lou & Gao 2011; Fu et al. 2011). Figure 7.9 shows a slice through the medium flux model density distribution and has a contour corresponding to the neutral atomic hydrogen fraction being equal to 0.1 overlaid. This figure clearly illustrates that the gas outflowing towards the observer is all too ionized to harbour molecular gas (see section 7.3). The contributor to the line profile must be the neutral part of the driving shell, the gas contained within it and any neutral foreground material. The EECC models of Gao & Lou (2010), Lou & Gao (2011) and Fu et al. (2011) describe well smaller isolated starless cores that are not being driven by the surroundings but following my result probably do

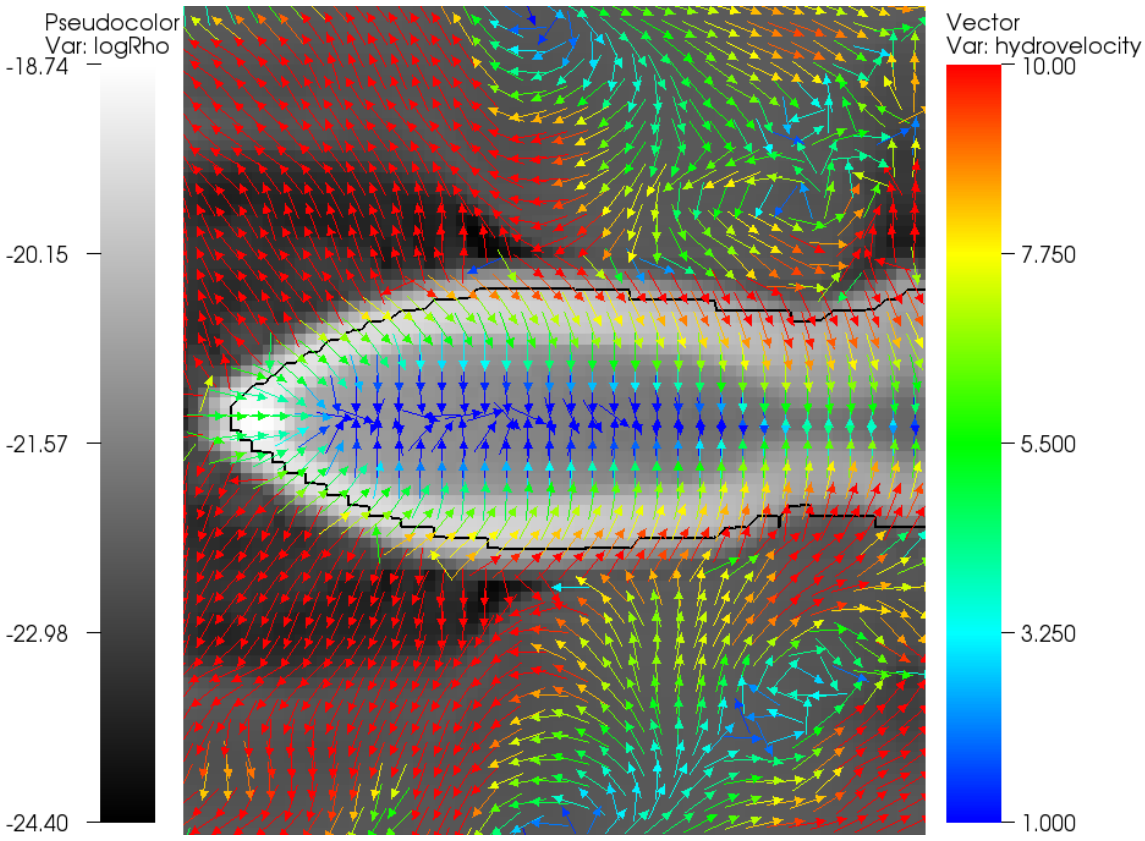

Figure 7.9: A slice through the logarithmic density distribution of the medium flux model. Overlaid are velocity vectors and a contour corresponding to a neutral atomic hydrogen fraction of 0.1. Material external to this contour around the cloud will not contribute to the molecular line data cubes because the gas is ionized. Note that the vortices in the hot gas are Kelvin-Helmholtz instabilities resulting from shear between the driving flow and photo-evaporative outflow. The greyscale bar is the logarithmic density in $\log_{10}(\mathrm{g\,cm^{-3}})$ and the colour bar is for the velocity vectors in $\mathrm{km\,s^{-1}}$. This cut is 3.9 by 2.6 pc.

not extend to BRCs and RDI, where the high velocity motions of the dense shell dominate the line profile.

Comparison of line profiles with observations

SFO 81 is a BRC studied in Urquhart et al. (2009) and has a triple-peaked ^{12}CO profile suggesting it may be viewed edge on. Obtaining line profiles over smaller regions of this cloud, in the manner of this section, would help to confirm this.

Urquhart et al. (2009) also present a number of other profiles that have similarities to those here, SFO 59, 60, 73, 80, 81, 86 and 87 are all multi-peaked in ^{12}CO. Interestingly, Urquhart et al. (2009) suggest that SFO 80, 81 and 86 are all unlikely to be triggered because a PDR is not readily observed at 8 μm (these observations were primarily made using the Midcourse Space Experiment satellite, Price et al. 2001). SFO 73 and 87, however, do have a visible PDR at 8 μm and are expected to be sites of triggering. What the profiles of the apparently un–triggered clouds (SFO 80, 81 and 86) have in common,

compared to SFO 87, is that the stronger (or only visible) of the secondary peaks is blue shifted (the SFO 73 line profile is too complex to compare with the others). If these blue shifted secondary peaks are due to the shell, then my results imply that the observer is viewing the cloud from behind with the shell moving towards them. As such it is less surprising that the PDR is not so readily visible, as it would be on the opposite side of the (potentially optically thick) cloud to the observer. SFO 87 has a strong secondary red peak, suggesting the shell is moving away from the observer and the cloud is being viewed face on. This is supported by the fact that the PDR is readily visible for SFO 87. I conclude that not viewing a substantial PDR at shorter wavelengths may not be sufficient to rule out triggering in a BRC. Follow up analysis with longer wavelength Herschel or Spitzer archival data could help to identify a PDR in the BRCs where one was not identified at $8\,\mu$m.

There are also a number of wings and shoulders identified in the line profiles given in Urquhart et al. (2009), such as SFO 51, 55, 71 and 79 that resemble the features of the low flux and high flux models at this inclination and all models at higher inclinations.

It should be noted that although these edge–on profiles best illustrate the various contributing components of the BRC, the form of a profile changes rapidly with viewing angle. For example, the three strong peaks of the medium flux profile will be dominated by a single peak due to the shell with non–Gaussian wings as the observer moves in front or behind of the BRC. That an edge-on viewing angle is comparatively rare is the reason that single peaked profiles tend to occur more frequently in observations to date (Morgan et al. 2009; Urquhart et al. 2009).

7.6.3 The effect of viewing angle on line profiles

I generated data cubes for ^{12}CO and C^{18}O from -90 degrees (face on to the BRC) to 90 degrees (behind the BRC) in intervals of 15 degrees. A schematic of these viewing angles is given in Figure 7.10. Due to the large volume of data it is impractical to replicate the overlaid grid analysis presented for the edge on viewing angle in section 7.6.2 for each inclination. I therefore focus on the overall variation in the average line profile over the cloud.

The variation of the line profile peak intensity velocity

I plotted the velocity at which the average line profile over the cloud is at maximum intensity (hereafter referred to as velocity for brevity) as a function of viewing angle for both the ^{12}CO and C^{18}O lines across all models in Figure 7.11.

In the low flux model (the top panel of Figure 7.11) the optically thin C^{18}O line is constant as a function of viewing angle, whereas the optically thick line varies in velocity dramatically. As discussed in section 7.6.2, this is because the shell is optically thin to the the C^{18}O line and so the line profile peak comes from the interior cloud at all viewing angles. The shell is optically thick to the ^{12}CO line meaning that the line profile will change with viewing angle as the motion of the shell along the line of sight changes. Both

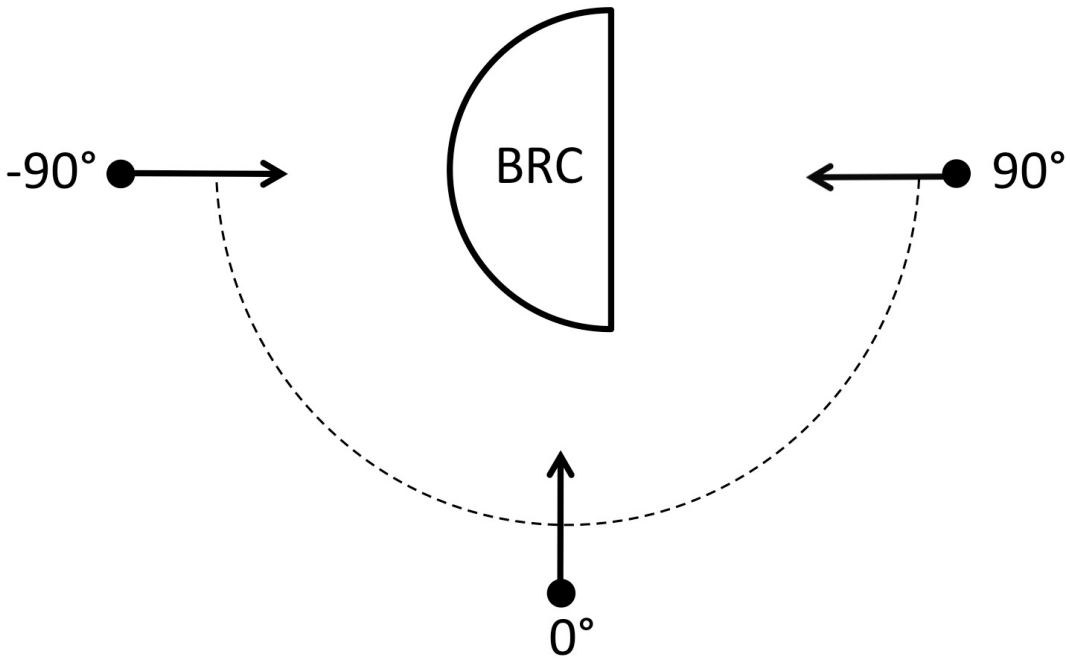

Figure 7.10: A schematic of the viewing angle convention used. At $-90°$ the observer is facing the bright rim of the cartoon class A cloud. At 90° the observer is behind the cloud.

the shell and central cloud are identified in the optically thick and thin line profiles, but the relative strengths differ.

The high flux model shows similar behaviour to the low flux model, with the optically thick and thin peaks separated, but it is not as extreme. This is because the shell accumulated before driving into the cloud had lower momentum than in the other models, meaning that the shell rapidly reached pressure equilibrium with the cloud. The shell only continues to propagate into the cloud due to the rocket motion resulting from a weak photo-evaporative outflow and so the velocities are lower.

In the medium flux model the shell is sufficiently dense that it is optically thick to both the ^{12}CO and C^{18}O lines. Therefore both line profile peaks come from a region of the BRC with similar kinematic properties and their peak velocities vary with viewing angle in the same way.

Examples of ^{12}CO and C^{18}O cloud-averaged profiles at a viewing angle of -60 degrees are given in Figure 7.12. These illustrate the points discussed in this section, showing that the low and high flux models' optically thin lines stay centred at low velocity whereas the medium flux peak moves to follow the optically thick line. The medium and high flux model optically thick and thin line peaks are only slightly separated at this inclination, whereas the low flux peaks are widely separated by $2.9\,\mathrm{km\,s^{-1}}$

The variation of the optically thin line profile FWHM

The C^{18}O FWHM (which is used to calculate the column density, c.f. equation 7.12) remains fairly constant at about $0.5\,\mathrm{km\,s^{-1}}$ in the low and high flux models. This is

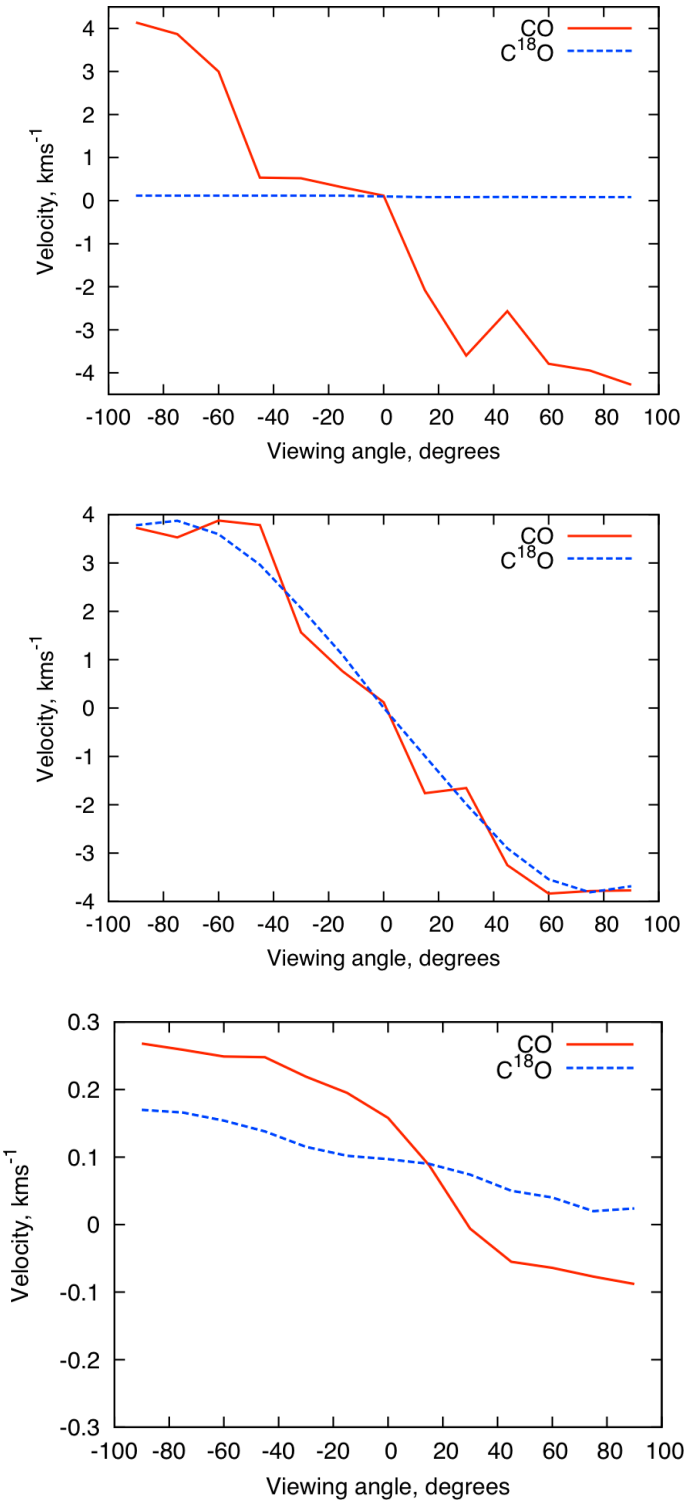

Figure 7.11: The variation of the velocity at which the average line profile over the cloud is at maximum intensity with viewing angle for the low (top), medium (middle) and high (bottom) flux models.

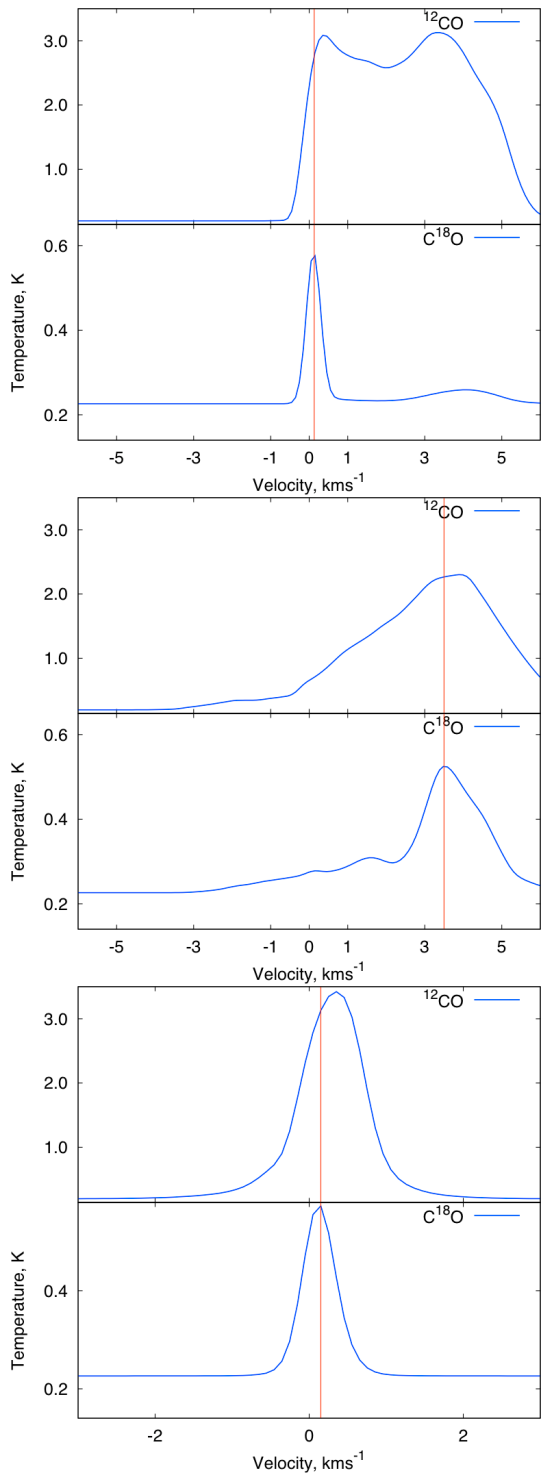

Figure 7.12: ^{12}CO and C^{18}O line profiles at a viewing angle of -60 degrees for the low, medium and high flux models from top to bottom. The vertical lines run through the optically thin line profile peak.

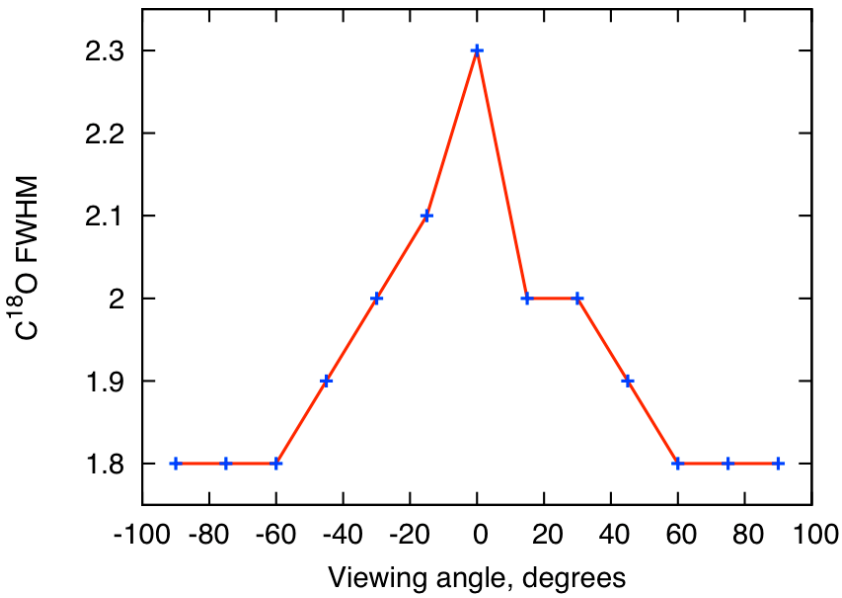

Figure 7.13: The variation of the medium flux model $C^{18}O$ FWHM with viewing angle.

because the optically thin line profile peak is determined by the central cloud at all viewing angles.

Conversely, the FWHM of the medium flux $C^{18}O$ line exhibits a maximum at low viewing angle, decreasing by up to 20 per cent as the observer moves to face the object from behind or face on. This is illustrated in Figure 7.13. The profiles for which these FWHM are calculated are averaged over a constant number of pixels across viewing angles, centred on the area of peak emission and not diluted by the ambient medium. This variation in FWHM is hence not due to varying the size of the region over which the profile is averaged, modifying the size of the line profile peak. Rather, the reason for this variation in the FWHM is that the shell is optically thick to $C^{18}O$. As the observer moves to higher viewing angles a single, denser component of the shell than that seen edge–on dominates the profile. There is also a smaller distribution of velocities about the peak since only a single shell is contributing to the line profile rather than two. The result is a slightly stronger peak that has a smaller FWHM. This variation in the line profile is illustrated in Figure 7.14, where the medium flux $C^{18}O$ profile is shown as the observer moves from 0 degrees to -90 degrees in 30 degree intervals.

The variation of the line profile symmetry parameter

The symmetric nature of a profile can be quantitatively expressed using the profile symmetry parameter δV based on an optically thick and an optically thin line, defined as

$$\delta V = \frac{V_{\text{thick}} - V_{\text{thin}}}{\Delta V_{\text{thin}}} \tag{7.16}$$

where V_{thick}, V_{thin} and ΔV_{thin} are the source-averaged spectrum peak velocities of the thick and thin lines and the FWHM of the optically thin line respectively (Mardones et al. 1997).

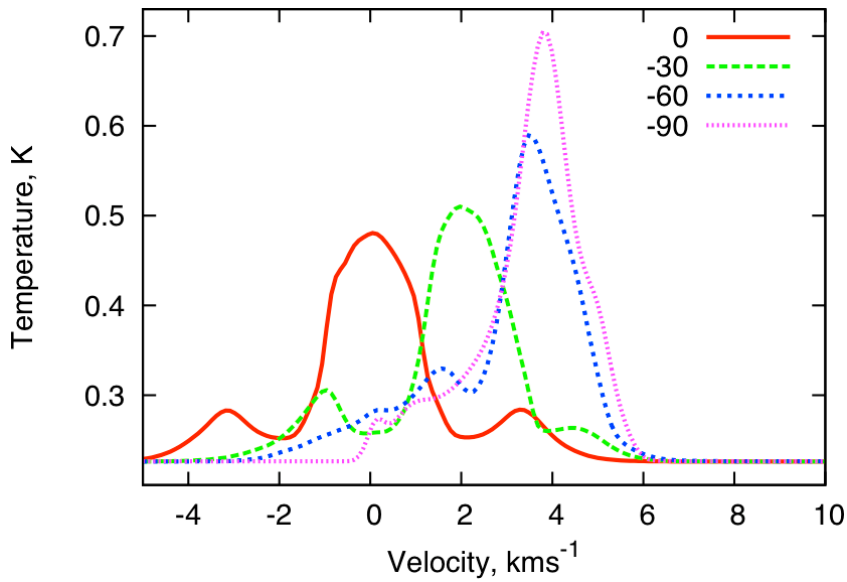

Figure 7.14: The variation in $C^{18}O$ line profile with viewing angle for the medium flux model.

This value gives an indication of the asymmetry in a line profile, with negative values blue-asymmetric and positive values red-asymmetric. Mardones et al. (1997) suggest that values in the range $-0.25 < \delta V < 0.25$ should be considered symmetric. This is usually applied to a single optically thick line with self absorption to determine whether the red or blue motions are predominantly self absorbed. The optically thin line would have a similar linewidth as the thick line and typically $|\delta \mathrm{V}| < 1$. In this Chapter, although both the optically thin and thick lines come from the BRC, they sometimes probe different regions (the shell and the cloud behind the shell) and so the optically thin and thick line peaks may be located at different positions giving rise to larger values of δV. Equation 7.16 is therefore more of a peak separation function than a symmetry function in this Chapter, though I still refer to profiles as symmetric or asymmetric depending on the value of δV. I calculate δV for all three clouds over each viewing angle to see if there is a systematic variation. The results of this analysis are given in Figure 7.15.

The low flux and high flux models show a systematic transition in δV with viewing angle. For viewing angles where the observer is looking face on to the BRC (< 0 degrees using the convention in Figure 7.10), δV shows that there is no or strong red-asymmetry. When the observer is behind the BRC (> 0 degrees using the convention in Figure 7.10) δV shows that there is no or strong blue-asymmetry. As already discussed, this is due to the near shell motion (probed by the optically thick line) relative to the interior cloud motion (probed by the optically thin line). The low values of δV are similar to those found in, for example, De Vries et al. (2002). The large values arise when the shell peak becomes stronger than the low velocity central cloud peak. Calculations of δV have not yet been performed for BRCs where the optically thick and thin lines are widely separated and would therefore give rise to larger values. Some of the profiles given in Urquhart et al. (2009) visually suggest a large separation between the optically thick and thin line peaks,

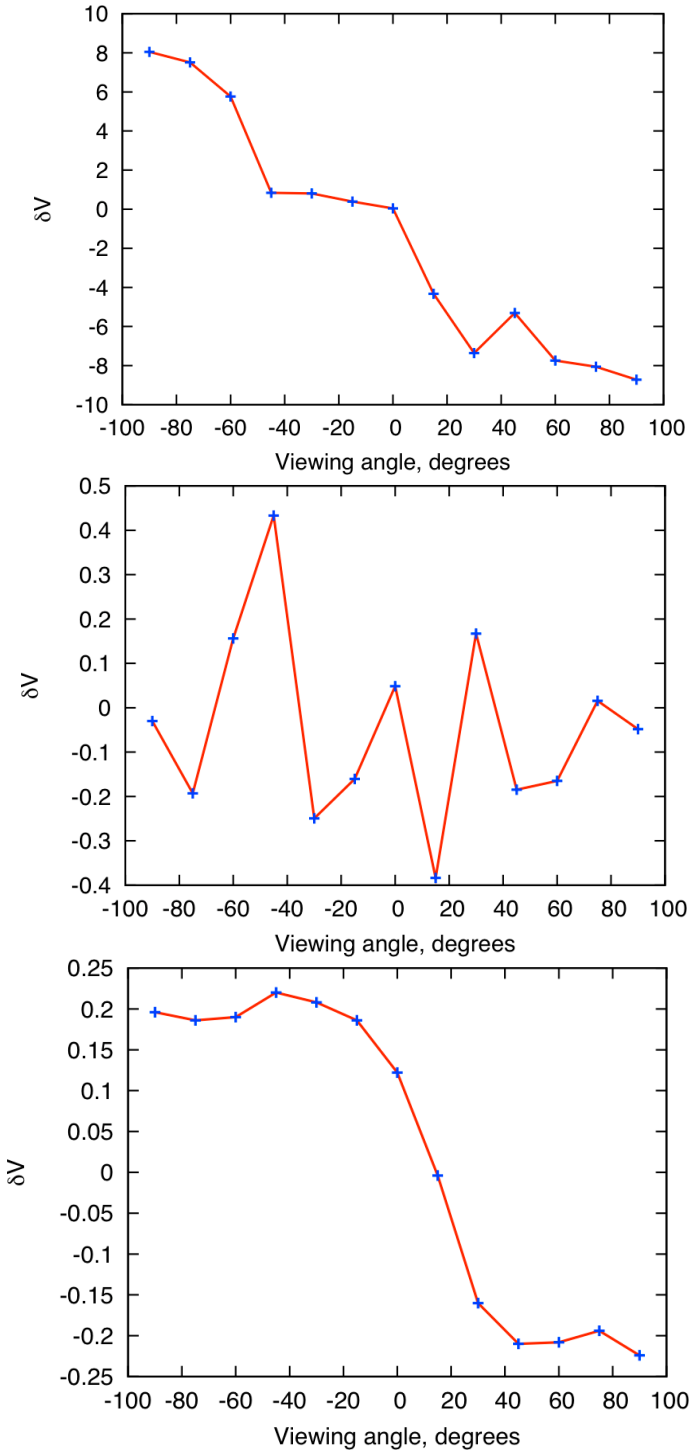

Figure 7.15: The variation of the profile symmetry with viewing angle for the low (top), medium (middle) and high (bottom) flux models. The asymmetry parameter δV (equation 7.16) is determined by the difference between the lines of Figure 7.11 divided by the FWHM of the $C^{18}O$ line.

such as those in SFO 71 and 73.

In the medium flux model there is no clear transition between the dominance of red or blue-asymmetry. This is because the shift in velocity demonstrated in Figure 7.11 is similar for the optically thin and thick lines since they both trace the dense shell region of the cloud. Red and blue-asymmetric profiles can still arise in the medium flux model (for example at 15 and -45 degrees in Figure 7.15), though typically the profiles are symmetric. The values of δV obtained for the medium flux cloud are very similar to those obtained for type B-C BRCs in De Vries et al. (2002).

Given the above, the only way in which a BRC will have a blue-asymmetric profile is if it is viewed from the rear and the shell is not sufficiently dense to dominate the profiles of both the optically thick and thin lines. Requiring that the BRC be viewed from behind (with a viewing angle > 0 degrees using the convention given in Figure 7.10) would reduce the chances of observing a blue-asymmetric line profile by 50 per cent. This is further reduced depending on the shell densities of real BRCs. These results do therefore provide an explanation for the lack, but not complete absence of, blue-asymmetric BRCs and rather a dominance of symmetric profiles.

7.6.4 Molecular cloud conditions

I applied the diagnostics detailed in section 7.5 to each of the clouds to calculate the mass, temperature and column density at an edge–on inclination (0 degrees using the convention given in Figure 7.10). The brightness temperature of the cloud that is used in equation 7.5 is the peak of the source-averaged spectrum with the background signal subtracted. I used GAIA to obtain a single averaged spectrum for each BRC and fit it with a Gaussian profile to obtain the peak value and FWHM. The radii of the clouds in the low, medium and high flux models were estimated to be 0.51, 0.19 and 0.8 pc respectively from their spatial extent in the simulated images.

The inferred properties are all presented in Table 7.3, along with the conditions from the model grid for comparison. The mass calculated assuming spherical symmetry (equation 7.14) is given by M_{sph} and the mass calculated by integrating the column density (equation 7.15) is given by M_{int}.

The optical depths are similar to those found observationally by, for example, Urquhart et al. (2006), Morgan et al. (2009) and given in Urquhart et al. (2009). Other than for ^{12}CO in the low flux model, the excitation temperatures are consistent underestimates of the prescribed neutral gas temperature of 10 K. It is often assumed that the BRC is in LTE and that therefore the ^{12}CO excitation temperature can be used to describe the kinetic temperature of the cloud. The results here suggest that this could be inaccurate by up to a factor of 1.6. The column densities are also similar to those found observationally, for example Morgan et al. (2009) and Urquhart et al. (2009). My values are slightly lower than those from Urquhart et al. (2006), due to the higher ^{12}CO excitation (and hence kinetic) temperatures that they obtain, of order 30 K. Urquhart et al. (2006) attribute this to some internal heating mechanism such as a young stellar object (YSO) or ultra compact (UC) H II region which are not present in my models. Rather, for fully neutral gas I prescribe a minimum temperature in the photoionization calculation of 10 K. The inferred column densities correspond reasonably well to the column density from the model grid, agreeing to within 11, 43 and 32 per cent for the low, medium and high flux models respectively.

When assuming spherical symmetry, all of the inferred masses are larger than the actual mass in the region over which the diagnostics were performed. The discrepancy ranges from a factor of 5 to 11 under this assumption. For the integrated column density method the agreement is much better, with agreement to within one solar mass in the low flux case up to a factor 2.25 in the medium flux case.

In Haworth et al. (2012)/Chapter 6 I calculated the mass and temperature of the same clouds using greybody fitting of the cloud SED. Comparing to the results here to those from from Haworth et al. (2012), calculating the cloud temperature based on greybody fitting of the system SED is a more accurate technique than the molecular line diagnostics, typically agreeing to within 1-2 K. This is because the former diagnostic is based on more information, over a larger frequency range from the cloud and also makes fewer assumptions in converting observational intensities to a temperature. For the SED

fitting temperature diagnostic, the main assumptions are an index which describes the frequency dependency of dust emissivity and that the SED can be fitted as a greybody. This diagnostic does also probe the whole cloud. However in the molecular line temperature diagnostic (see section 7.5, equations 7.5 through 7.11) assumptions include that the optical depths of ^{13}CO and C^{18}O can be related by their abundances (equation 7.6), that the cloud is in LTE and that a single temperature applies to the whole cloud. A single line will also only give a diagnostic temperature for the subset of the cloud that it probes. The masses calculated using molecular line diagnostics are more accurate, differing at most by a factor of 2.25 in the integrated column density method compared with a difference of up to a factor of 4 via SED fitting. This is because SED fitting assumes a constant dust to total mass conversion factor between different BRCs.

A measure of stability against collapse of a BRC is given using the virial theorem, comparing the IBL and neutral cloud pressures (Hartmann 2009; Haworth et al. 2012). In general, the cloud masses have been overestimated here. Given this, the neutral cloud pressure and hence the stability against collapse may also be overestimated when using neutral cloud properties based on molecular line calculations.

Table 7.3: The cloud conditions calculated using ^{12}CO, ^{13}CO and C^{18}O. The columns are, from left to right: which model the conditions have been calculated for, the optical depth of ^{13}CO and C^{18}O, excitation temperatures for ^{12}CO and C^{18}O, the column density calculated from synthetic observations, the column density from the model grid, the C^{18}O FWHM, the cloud mass calculated assuming spherical symmetry, the cloud mass calculated by integrating the column density over the cloud and the known cloud mass from the model grid.

Model	τ_{13}	τ_{18}	T_{12} (K)	T_{18} (K)	$\log(N(H_2))$ (cm^{-2})	grid $\log(N(H_2))$ (cm^{-2})	FWHM, $\Delta\nu_{18}$ (km s^{-1})	M_{sph} ($M_\odot$)	M_{int} ($M_\odot$)	M_{grid} ($M_\odot$)
Low	2.81	0.18	12.6	6.4	21.11	21.16	0.47	100	19	19
Medium	2.56	0.16	6.4	4.5	21.61	21.37	1.88	45	9	4
High	1.72	0.11	6.6	6.9	20.99	20.82	0.60	185	36	21

7.7 Summary and conclusions

I have generated synthetic molecular line observations of the models of RDI from Chapter 5. Using data of the ^{12}CO, ^{13}CO and C^{18}O (J = 2 $\rightarrow$ 1) transitions I have analyzed line profiles over the imaged BRCs and replicated standard diagnostics to calculate the BRC properties. Using the derived conditions and line profiles I have searched for signatures of RDI and tested the accuracy of the diagnostics. I have also investigated the variation of BRC line profiles with observer viewing angle. I draw the following main conclusions from this work:

1. The synthetically imaged BRCs have a similar morphology to real BRCs. The optically thin and thick line integrated intensities all trace a similar extent of the cloud in each model.

2. The lack of blue-asymmetry observed in BRC line profiles can be explained by the shell of material that drives into the cloud. If the shell is very dense then it may be optically thick to both ^{12}CO and C^{18}O. If this is the case then the profiles of both lines are dominated by emission from the shell and have very similar peak velocities that result in a symmetric profile. In the intermediate case when the shell is less dense the optically thick line profile is dominated by the high velocity shell and the optically thin line dominated by the low velocity cloud interior to the shell. This results in an asymmetric line profile. For asymmetric profiles, when the observer is facing the BRC the shell is moving away into the cloud and there will be a red asymmetry. If the observer views the BRC from behind then the motion of the shell will be towards the observer and there will be a blue asymmetry. If the shell is sufficiently weak then it will not contribute to the profile and is likely that RDI will not be occurring.

3. By examining the known motion of material in the neutral gas from the model grid I rule out envelope expansion with core collapse (EECC) as the cause of the asymmetry in the simulated line profiles. This is because expansion from the outer layers of the BRC towards the observer (a key feature of the EECC model) is from gas that is ionized, meaning no molecular gas exists in these regions and they cannot contribute to the line profile.

4. The profiles that I obtain exhibit shoulders and wings that resemble observations (see Figure 7.8). At edge-on viewing angles both the near and far shell, as well as the gas interior to the shells, contributes to the profile. This gives rise to more complex profiles with up to three peaks. That such complex profiles exist in observations to date, for example the profiles of SFO 59, 60, 73, 80, 81, 86 and 87 from Urquhart et al. (2009), is evidence of a shell contributing to the line profile. These systems should be investigated more closely using spatially resolved profiles. At other inclinations the profile is typically either invariant (for the optically thin line) or becomes dominated by a single peak due

to the shell with non-Gaussian wings (for the optically thick line). Such profiles are most common in observations due to the higher probability of viewing a BRC at an inclination that is not edge on.

5. For BRCs, failing to identify a PDR at shorter wavelengths does not necessarily rule out RDI. If the cloud line profile has a secondary strong blue peak then the shell may be driving towards the observer, something that (according to the models here) only happens if the observer is behind the BRC. As such the PDR is on the opposite side of the cloud so may be more difficult to detect if the foreground cloud is optically thick. Examples of this could be SFO 80, 81 and 86 which were identified as not likely being sites of triggering in Urquhart et al. (2009) at $8\,\mu$m (primarily using Midcourse Space Experiment data), but have secondary blue peaks. Conversely SFO 87 (with a secondary red peak that suggests the shell is moving away from the observer and the BRC is viewed face on) does have a PDR identified. Analysis of the clouds where no PDR was detected at $8\,\mu$m using longer wavelength data such as that taken with Herschel or Spitzer may help to identify a PDR.

6. The cloud conditions that I infer by replicating the diagnostics of, for example Urquhart et al. (2006) and Morgan et al. (2009), yield results that are similar to those found observationally. The inferred kinetic temperature differs from the prescribed temperature by up to a factor of 1.6. The column densities for low, medium and high flux models agree with those from the model grid to within 11, 43 and 32 per cent respectively. The cloud masses calculated assuming spherical symmetry are overestimates by up to a factor of 11. Integrating the column density over a region to determine the mass yields much more accurate results, at worst differing from the grid mass by a factor of 2.25 and agreeing more closely for the other models. By comparing with the results from Haworth et al. (2012) I conclude that calculation of cloud temperatures via greybody fitting of the SED is more accurate. However, the mass calculation is more accurate using molecular line diagnostics because the SED fitting assumes a constant dust to total mass conversion factor between clouds.

8

Conclusions and the future

This thesis has detailed some key features and new developments of the TORUS radiation transport and hydrodynamics code and its application to problems in radiative feedback. In this Chapter I provide an overview of the key conclusions and discuss future avenues for research.

8.1 TORUS

TORUS has been developed to treat hydrodynamics, self–gravity and photoionization and to combine them together using operator splitting to perform radiation hydrodynamics calculations. This new functionality has been extensively checked using standard tests for the hydrodynamics, photoionization, self–gravity and radiation hydrodynamics and is shown to work well. TORUS has also been developed to be flexibly and efficiently parallelized using MPI (distributed memory), openMP (shared memory) or hybrid parallelization schemes. The existing octree grid structure has also been developed to be dynamically adaptive for hydrodynamic simulations where the resolution requirements on the computational grid vary in time.

8.2 Astrophysical Applications: Radiatively Driven Implosion

Both pre–existing and newly implemented features of TORUS have been used in this thesis to study the formation of bright rimmed clouds (BRCs) in the radiatively driven implosion (RDI) scenario.

8.2.1 Radiation hydrodynamic models of RDI

I have run three–dimensional RHD calculations of RDI using TORUS in which I systematically constrain the effect of treating a polychromatic radiation field and the diffuse radiation field (as opposed to monochromatic radiation with no diffuse field). I find that inclusion of polychromatic radiation does not change the calculation results much, but that treatment of the diffuse field does.

Previous works have suggested that the effectiveness of compression of a pre–existing clump increases in proportion to the ionizing flux incident upon the clump. I find that the more important factor is the strength (density and velocity) of the shell of material swept up by the ionization front prior to impacting the pre–existing clump. A high ionizing flux that immediately envelopes the clump results in it fizzing away as it is slowly photo–evaporated. A lower ionizing flux that accumulates a shell of material will compress the clump more effectively. As well as having more momentum, a dense shell will also be subject to strong photo–evaporative outflows, the rocket–motion from which further drives the shell into the clump. Part of the reason that the diffuse field leads to different results compared to models that do not treat it is that photo–evaporative outflows can be established over larger regions of the shell driving into the cloud (since some are otherwise shadowed). This shows the importance of assessing our approximations in RHD applications.

8.2.2 Observational diagnostics

I postprocessed the results of the RHD RDI models to produce simulated observations. The objectives of this were two–fold; to test the diagnostics used by observers and to look for observational signatures of the RDI process. This is done by comparing the characteristics of the model inferred from the simulated data with the known properties on the model grid.

Firstly I tested the diagnostic that compares the pressure in the neutral gas of a BRC to the surrounding ionized gas pressure. If the neutral pressure is the smaller of the two then this suggests that the cloud is being compressed. I calculated the neutral gas conditions using fitting of a simulated SED following the widely used approach of Hildebrand (1983). I found that the biggest source of uncertainty in the Hildebrand calculation comes from the assumed dust–to–gas mass conversion factor, which in my calculations gave rise to errors of a factor of a 3.6. I also calculated the ionized gas properties using diagnostics from Lefloch et al. (1997). Overall, I found that comparing the external and internal pressures of BRC's does give a valid representation of the dynamical state of cloud and can be used to help identify RDI.

I also used the molecular line transport functionality in TORUS implemented by David Rundle to post–process the calculations and produce synthetic CO data cubes. I

tested standard diagnostics of CO that are used to infer conditions such as the excitation temperature, column density and mass of the gas and give advice (with quantitative backing) on which approaches are most accurate. For example, integrating the column density over pixels to calculate the mass of a BRC was found to give much more accurate results than assuming spherical symmetry (out by a factor of 2 rather than 10). Finally I investigated the molecular line profiles of BRC's and found that a shell driving into the cloud might provide an observational signature that could be used to identify RDI in real systems. A BRC will have some relatively undisturbed neutral gas and then additional velocity components due to the shell. A multi–peaked profile is therefore evidence for this. This observational signature has since been identified and will be published soon in Tremblin et al. (in prep).

8.3 Future research

There are a number of prospective avenues for my future research, many of which are already under development. Here I provide an overview of these ideas.

8.3.1 Lyman continuum flux estimates from radio continuum observations

In this thesis I have shown that applying the diagnostics used by observers to simulated observations can provide both useful tests of the accuracy of the diagnostics. Simulated observations can also be used to make observational predictions from numerical models. This project is in the same vein, considering a different diagnostic used to study ionized bubbles.

Throughout the galaxy bubbles of ionized gas are observed around massive stars. Rubin (1968) developed the following relation between the number of ionizing photons emitted by the exciting star $N_{\mathrm{ly},*}$ and the radio continuum flux S_ν

$$\begin{aligned} N_{\mathrm{ly},*} \geq \; & 4.76 \times 10^{65} \left(\frac{\nu^{0.1}}{\mathrm{GHz}}\right) \left(\frac{D^2}{\mathrm{pc}}\right) \left(\frac{T^{-0.45}}{\mathrm{K}}\right) \\ & \times \left(\frac{S_\nu}{\mathrm{erg\,cm^{-2}\,s^{-2}\,Hz^{-1}}}\right) \end{aligned} \tag{8.1}$$

which is usefully independent of the geometry of the H II region provided that the medium is optically thin to photons at the frequency of observation. The inequality is present because some ionizing photons will not contribute to the equilibrium photoionization state of the bubble, but will be absorbed by dust or escape through density bounded components of the bubble.

Usually equation 8.1 is used to estimate the spectral class of the ionizing star, or the number of stars of an assumed spectral class, required to ionize the bubble using the massive star parameter models of Panagia (1973), Vacca et al. (1996) or Martins et al. (2005).

Watson et al. (2008) identified candidate stars responsible for exciting three bubble

H II regions (N10, N21 and N49 from Churchwell et al. 2006) and classified them using spectral energy distribution models. They then compared the expected Lyman continuum flux from stars of the inferred spectral class with that inferred from radio observations using equation 8.1. They found that the radio continuum diagnostic gives an underestimate of around a factor of two, which is now the standard assumed uncertainty when employing equation 8.1.

This underestimate is attributed to ionizing photons escaping the system or being absorbed by dust, though which of these is responsible is currently under contention. Beaumont & Williams (2010) and Li et al. (2013) make molecular line observations of bubbles and find that bubbles are actually more likely to be cylindrical than spherical due to the apparent lack of fore and background molecular line emission from the region interior to the bubble. This might imply that photon loss through density bounded surfaces at the caps of the cylinder is quite prevalent. Conversely the findings of others such as Everett & Churchwell (2010) and Deharveng et al. (2010) suggest that dust emission is prevalent throughout bubbles and hence dust absorption is likely partially responsible for the underestimate. It is also possible that the assumptions behind equation 8.1 (for example it assumes hydrogen–only gas) might be responsible for some difference.

It is important to understand more clearly the discrepancy between the Lyman continuum flux inferred from radio diagnostics and that expected from the ionizing stars for two main reasons. Firstly it is useful to understand the accuracy of the diagnostic. Secondly it might be possible to use any discrepancy as a further diagnostic of the structure of ionized bubbles. For example, if they are cylindrical and the underestimate is dominated by photons escaping the system, it might be possible to infer the fraction of the bubble that is density bounded by relating that fraction to the underestimate.

In this project I will test equation 8.1 using radiation transport modelling. I aim to test the accuracy of the diagnostic by applying it to simulated observations of a simple model bubble, thus comparing the assumptions in equation 8.1 with those in a modern radiation transport code. If necessary I will also provide a correction to the relation. Finally I will explore the diagnostic potential of a discrepancy between the number of Lyman continuum photons inferred from radio diagnostics and that expected for the stars suspected of ionizing a bubble.

8.3.2 Further tests of radiation hydrodynamic models

I will continue to investigate the impact of approximations in RHD models. Beyond the diffuse radiation field I will investigate the effect of moving from hydrogen–only gas to one that includes helium and metals. I can also constrain the effect of using a full thermal balance over the simplified function of hydrogen ionization fraction used in Chapter 5. Due to the highly computationally expensive nature of doing full photoionization I am running these models in two dimensions. The basic idea is to run a parameter space of approximations and resolution, to check for any convergence and to provide insight into what we should be focussing on with our limited computational resources. Is it better to

apply resources to obtaining higher resolution, or more accurate treatment of the physics in the model?

8.3.3 The starbench code comparison project

I am collaborating with users of different codes in a code comparison project called STARBENCH. I organised the first STARBENCH meeting, which was held in Exeter in April 2013. The format for the workshop was for attendees to perform a set of pre–defined tests prior to the workshop and for the results to be discussed at the meeting. We found nothing too unsurprising in hydrodynamic–only calculations however there was very little agreement in radiation hydrodynamic tests. This is either due to differences in the calculation run (due to ambiguity in the test description) or differences in the codes. We are now proceeding with refined versions of 2–3 of the original tests which we intend to take towards publication in code comparison papers.

We will also be holding STARBENCH–2 in Germany scheduled for Autumn 2014, which will address new tests looking at other components of numerical star formation. For example turbulence, accretion and treatment of sink particles. We have secured a 5000 euro grant to support PhD student attendance at this meeting from DFG Priority Program 1573 (ISM-SPP).

8.3.4 Photo–evaporation of protoplanetary discs: thermal sweeping

I will investigate the thermal sweeping mechanism in protostellar discs, first discovered in numerical models by Owen et al. (2012a). This is the main project that I will be pursuing in a postdoctoral position at the Institute of Astronomy in Cambridge. Transition discs are protoplanetary discs with an inner gap near the star, first identified via a deficiency in near–IR continuum flux and subsequently confirmed using interferometric observations. This observed inner gap suggests that protoplanetary discs are dispersed from the inside out, most likely either through photo–evaporation or planet formation. The interior edge of the disc is subject to heating from X–rays. As the gap expands the width of the X–ray heated region also increases. Owen et al. (2012a) found that if the disc mid–plane pressure drops below a critical value and the width of the X–ray heated interior disc reaches the point where it is equivalent to the disc height then the X–ray heated component becomes dynamically unstable and moves perpendicular to the disc midplane. This warm plume of gas proceeds to sweep away the remaining mass in the disc on short timescales (of order a few hundred years). This mechanism provides a means for rapidly dispersing the last 10–20 per cent of a protoplanetary disc mass.

Owen et al. (2012a) did not set out to investigate the thermal sweeping mechanism, rather discovering it by accident. I will start by investigating some of the questions proposed by Owen et al. (2012a), but also have some other ideas

- Do calculations by other codes actually give rise to thermal sweeping? The first step will be to reproduce one of the original thermal sweeping calculations and check for

differences.

- For higher mass star–disc systems, thermal sweeping is predicted to only engage at later times. I can test this.
- What is the link between thermal sweeping and debris discs? Can we make observational predictions about the structure of debris discs from our models.
- Perhaps move to 3D calculations using an inhomogeneous disc and see what this does to both the thermal sweeping mechanism and the subsequent observational signatures.

In order to perform RHD models of photo–evaporative feedback in protoplanetary discs I will have to develop TORUS so that it is X–ray enabled, such as Ercolano et al. (2008). This requires inclusion of Compton scattering, additional atomic data for key X–ray lines and a treatment of inner shell photoionization. Once these are implemented I will initially reproduce the original model in which thermal sweeping was observed in Owen et al. (2012a). From there I eventually intend to run a three–dimensional calculation of the thermal sweeping process and to compare the resulting remnant disc with observations of debris discs.

8.3.5 Investigate stellar populations in radiative feedback calculations

I will continue to investigate the impact of radiative feedback in star forming regions. I intend to run calculations which include sink particles to investigate the stellar populations that result from the radiative feedback process. I also intend to investigate how sensitive these populations are to the approximations employed. This project is more long–term than the others already discussed and has not been started yet. It will require the use of the AMR grid since high resolution is required around the sites that sink particles (implemented in TORUS recently by Tim Harries) are inserted onto the grid. This is also probably the most computationally expensive future calculation.

8.4 Closing words

I wish to close by saying that I have really enjoyed contributing to TORUS and applying it to problems in star formation. It has been great to get to use such a diverse range of physics and numerical and observational techniques in this thesis. I have also been fortunate to be part of a field populated by fantastic people who I have enjoyed meeting and sometimes working with. I look forwards to continuing to collaborate with them and also to meeting new people as I branch out into studying the photo–evaporation of proto–planetary discs.

9
Bibliography

Acreman, D. M., Dobbs, C. L., Brunt, C. M., & Douglas, K. A. 2012, MNRAS, 422, 241

Acreman, D. M., Douglas, K. A., Dobbs, C. L., & Brunt, C. M. 2010a, MNRAS, 406, 1460

Acreman, D. M., Harries, T. J., & Rundle, D. A. 2010b, MNRAS, 403, 1143

Agertz, O., Moore, B., Stadel, J., et al. 2007, MNRAS, 380, 963

Alexander, R. D., Clarke, C. J., & Pringle, J. E. 2006, MNRAS, 369, 229

Arce, H. G., Borkin, M. A., Goodman, A. A., Pineda, J. E., & Halle, M. W. 2010, ApJ, 715, 1170

Arthur, S. J. & Hoare, M. G. 2006, ApJS, 165, 283

Artymowicz, P. 2000, in ESA Special Publication, Vol. 451, Darwin and Astronomy : the Infrared Space Interferometer, ed. B. Schürmann, 117

Ballesteros-Paredes, J. 2006, MNRAS, 372, 443

Bally, J., Testi, L., Sargent, A., & Carlstrom, J. 1998, AJ, 116, 854

Barber, P. W. & Hill, S. C. 1990, Light Scattering By Particles: Computational Methods (World Scientific Publishing Co. Pre. Ltd.)

Bastian, N., Covey, K. R., & Meyer, M. R. 2010, ARA&A, 48, 339

Bastian, N., Ercolano, B., Gieles, M., et al. 2007, MNRAS, 379, 1302

Bate, M. R. 2009, MNRAS, 392, 1363

Bate, M. R. 2011, MNRAS, 417, 2036

Bate, M. R. 2012, MNRAS, 419, 3115

Bate, M. R., Bonnell, I. A., & Bromm, V. 2003, MNRAS, 339, 577

Beaumont, C. N. & Williams, J. P. 2010, ApJ, 709, 791

Beltrán, M. T., Massi, F., López, R., Girart, J. M., & Estalella, R. 2009, A&A, 504, 97

Bertoldi, F. 1989, ApJ, 346, 735

Bertoldi, F. & McKee, C. F. 1990, ApJ, 354, 529

Bik, A., Lamers, H. J. G. L. M., Bastian, N., Panagia, N., & Romaniello, M. 2003, A&A, 397, 473

Bisbas, T. G., Bell, T. A., Viti, S., Yates, J., & Barlow, M. J. 2012, MNRAS, 427, 2100

Bisbas, T. G., Wünsch, R., Whitworth, A. P., & Hubber, D. A. 2009, A&A, 497, 649

Bisbas, T. G., Wünsch, R., Whitworth, A. P., Hubber, D. A., & Walch, S. 2011, ApJ, 736, 142

Blitz, L. & Rosolowsky, E. 2006, ApJ, 650, 933

Bok, B. J. & Reilly, E. F. 1947, ApJ, 105, 255

Bonnell, I. A., Bate, M. R., Clarke, C. J., & Pringle, J. E. 2001, MNRAS, 323, 785

Bonnell, I. A., Dobbs, C. L., & Smith, R. J. 2013, MNRAS, 430, 1790

Bonnell, I. A., Larson, R. B., & Zinnecker, H. 2007, Protostars and Planets V, 149

Bowen, I. S. 1927, Nature, 120, 473

Bressert, E., Bastian, N., Gutermuth, R., et al. 2010, MNRAS, 409, L54

Buckle, J. V., Davis, C. J., Francesco, J. D., et al. 2012, MNRAS, 422, 521

Burrows, C. J., Stapelfeldt, K. R., Watson, A. M., et al. 1996, ApJ, 473, 437

Caplan, J., Deharveng, L., Peña, M., Costero, R., & Blondel, C. 2000, MNRAS, 311, 317

Carlqvist, P., Gahm, G. F., & Kristen, H. 2003, A&A, 403, 399

Carlqvist, P., Kristen, H., & Gahm, G. F. 1998, A&A, 332, L5

Cashwell, E. & Everett, C. 1959, A Practical Manual on the Monte Carlo Method for Random Walk Problems. (First Prepared as an Account of U.S. Government Sponsored Work Carried Out by [the Authors] ... and O.W. Rechard, at Los Alamos Scientific Laboratory, Los Alamos, New Mexico.)., International tracts in computer science and technology and their application

Casoli, F. & Combes, F. 1982, A&A, 110, 287

Castor, J., McCray, R., & Weaver, R. 1975, ApJL, 200, L107

Castor, J. I. 2004, Radiation Hydrodynamics, ed. Castor, J. I.

Chabrier, G. 2003, PASP, 115, 763

Chabrier, G. & Hennebelle, P. 2010, ApJL, 725, L79

Chauhan, N., Ogura, K., Pandey, A. K., Samal, M. R., & Bhatt, B. C. 2011a, PASJ, 63, 795

Chauhan, N., Pandey, A. K., Ogura, K., et al. 2011b, MNRAS, 415, 1202

Chauhan, N., Pandey, A. K., Ogura, K., et al. 2009, MNRAS, 396, 964

Choudhury, R., Mookerjea, B., & Bhatt, H. C. 2010, ApJ, 717, 1067

Churchwell, E., Povich, M. S., Allen, D., Taylor, M. G., & et al. 2006, ApJ, 649, 759

Condon, J. J., Cotton, W. D., Greisen, E. W., et al. 1998, AJ, 115, 1693

Conti, P. S., Crowther, P. A., & Leitherer, C. 2008, From Luminous Hot Stars to Starburst Galaxies (Cambridge University Press)

Crowther, P. A., Schnurr, O., Hirschi, R., et al. 2010, MNRAS, 408, 731

Dale, J. E. & Bonnell, I. 2011, MNRAS, 414, 321

Dale, J. E. & Bonnell, I. A. 2012a, MNRAS, 422, 1352

Dale, J. E. & Bonnell, I. A. 2012b, MNRAS, 2723

Dale, J. E., Bonnell, I. A., & Whitworth, A. P. 2007, MNRAS, 375, 1291

Dale, J. E., Ngoumou, J., Ercolano, B., & Bonnell, I. A. 2013, ArXiv e-prints

Davé, R. 2008, MNRAS, 385, 147

De Vries, C. H., Narayanan, G., & Snell, R. L. 2002, ApJ, 577, 798

Deharveng, L., Peña, M., Caplan, J., & Costero, R. 2000, MNRAS, 311, 329

Deharveng, L., Schuller, F., Anderson, L. D., et al. 2010, A&A, 523, A6

Deharveng, L., Zavagno, A., & Caplan, J. 2005, A&A, 433, 565

Dent, W. R. F., Matthews, H. E., & Ward-Thompson, D. 1998, MNRAS, 301, 1049

Dobbs, C. L., Burkert, A., & Pringle, J. E. 2011, MNRAS, 417, 1318

Dobbs, C. L., Pringle, J. E., & Burkert, A. 2012, MNRAS, 425, 2157

Dove, J. B., Shull, J. M., & Ferrara, A. 2000, ApJ, 531, 846

Draine, B. T. & Lee, H. M. 1984, ApJ, 285, 89

Duarte-Cabral, A., Dobbs, C. L., Peretto, N., & Fuller, G. A. 2011, A&A, 528, A50

Dullemond, C. P., Dominik, C., & Natta, A. 2001, ApJ, 560, 957

Dullemond, C. P. & Johansen, A. 2007, Notes Lecture Hydrodynamics: Numerical Methods and Applications, Heidelberg University

Elmegreen, B. G. 2008, ApJ, 672, 1006

Elmegreen, B. G. 2011a, in EAS Publications Series, Vol. 51, EAS Publications Series, ed. C. Charbonnel & T. Montmerle, 19–30

Elmegreen, B. G. 2011b, ArXiv e-prints

Elmegreen, B. G. 2011c, in EAS Publications Series, Vol. 51, EAS Publications Series, ed. C. Charbonnel & T. Montmerle, 45–58

Elmegreen, B. G. 2012, ArXiv e-prints

Elmegreen, B. G., Kimura, T., & Tosa, M. 1995, ApJ, 451, 675

Elmegreen, B. G. & Lada, C. J. 1977, ApJ, 214, 725

Ercolano, B., Barlow, M. J., Storey, P. J., & Liu, X. 2003, MNRAS, 340, 1136

Ercolano, B., Dale, J. E., Gritschneder, M., & Westmoquette, M. 2012, MNRAS, 420, 141

Ercolano, B. & Gritschneder, M. 2011a, in IAU Symposium, Vol. 270, Computational Star Formation, ed. J. Alves, B. G. Elmegreen, J. M. Girart, & V. Trimble, 301–308

Ercolano, B. & Gritschneder, M. 2011b, MNRAS, 413, 401

Ercolano, B., Young, P. R., Drake, J. J., & Raymond, J. C. 2008, ApJS, 175, 534

Everett, J. E. & Churchwell, E. 2010, ApJ, 713, 592

Ferland, G. 1995, in The Analysis of Emission Lines: A Meeting in Honor of the 70th Birthdays of D. E. Osterbrock and M. J. Seaton, ed. R. Williams & M. Livio, 83–+

Ferland, G. J., Korista, K. T., Verner, D. A., et al. 1998, PASP, 110, 761

Fruscione, A., McDowell, J. C., Allen, G. E., et al. 2006, in Society of Photo-Optical Instrumentation Engineers (SPIE) Conference Series, Vol. 6270, Society of Photo-Optical Instrumentation Engineers (SPIE) Conference Series

Fryxell, B., Olson, K., Ricker, P., et al. 2000, ApJS, 131, 273

Fu, T.-M., Gao, Y., & Lou, Y.-Q. 2011, ApJ, 741, 113

Gahm, G. F., Carlqvist, P., Johansson, L. E. B., & Nikolić, S. 2006, A&A, 454, 201

Gahm, G. F., Persson, C. M., Mäkelä, M. M., & Haikala, L. K. 2013, A&A, 555, A57

Gao, Y. & Lou, Y.-Q. 2010, MNRAS, 403, 1919

Garcia-Segura, G. & Franco, J. 1996, ApJ, 469, 171

Gibson, J. 2009, Parallel Programming with MPI, The Numerical Algorithms Group, HECToR

Gieles, M., Moeckel, N., & Clarke, C. J. 2012, MNRAS, 426, L11

Glover, S. C. O., Federrath, C., Mac Low, M.-M., & Klessen, R. S. 2010, MNRAS, 404, 2

Goldsmith, P. F., Bergin, E. A., & Lis, D. C. 1997, in IAU Symposium, Vol. 170, IAU Symposium, ed. W. B. Latter, S. J. E. Radford, P. R. Jewell, J. G. Mangum, & J. Bally, 113–115

Gomez, G. C. & Vazquez-Semadeni, E. 2013, ArXiv e-prints

Goodwin, S. P., Nutter, D., Kroupa, P., Ward-Thompson, D., & Whitworth, A. P. 2008, A&A, 477, 823

Gritschneder, M., Burkert, A., Naab, T., & Walch, S. 2010, ApJ, 723, 971

Gritschneder, M., Naab, T., Burkert, A., et al. 2009a, MNRAS, 393, 21

Gritschneder, M., Naab, T., Walch, S., Burkert, A., & Heitsch, F. 2009b, ApJ, 694, L26

Haque, A. 2006, Sedov Analytical Solution Program: http://flash.uchicago.edu/ ahaque/sedov.html

Harries, T. J. 2000, MNRAS, 315, 722

Harries, T. J. 2011, MNRAS, 416, 1500

Harries, T. J., Babler, B. L., & Fox, G. K. 2000, A&A, 361, 273

Harries, T. J. & Howarth, I. D. 1997, A&AS, 121, 15

Harries, T. J., Monnier, J. D., Symington, N. H., & Kurosawa, R. 2004, MNRAS, 350, 565

Hartmann, L. 2009, Accretion Processes in Star Formation: Second Edition, ed. Hartmann, L. (Cambridge University Press)

Hatchell, J., Wilson, T., Drabek, E., et al. 2013, MNRAS, 429, L10

Haworth, T. J. & Harries, T. J. 2012, MNRAS, 420, 562

Haworth, T. J., Harries, T. J., & Acreman, D. M. 2012, MNRAS, 426, 203

Heiner, J. S. & Vázquez-Semadeni, E. 2013, MNRAS, 429, 3584

Henney, W. J., Arthur, S. J., de Colle, F., & Mellema, G. 2009, MNRAS, 398, 157

Hensler, G. 2011, in IAU Symposium, Vol. 270, Computational Star Formation, ed. J. Alves, B. G. Elmegreen, J. M. Girart, & V. Trimble, 309–317

Herbig, G. H. 1962, ApJ, 135, 736

Hester, J. J. et al. 1996, AJ, 111, 2349

Hildebrand, R. H. 1983, QJRAS, 24, 267

Hillier, D. J. 1991, A&A, 247, 455

Hoare, M. G. & Franco, J. 2007, Massive Star Formation, ed. T. W. Hartquist, J. M. Pittard, & S. A. E. G. Falle, 61

Hogerheijde, M. R. & van der Tak, F. F. S. 2000, A&A, 362, 697

Holman, K., Walch, S. K., Goodwin, S. P., & Whitworth, A. P. 2013, MNRAS, 432, 3534

Hopkins, P. F. 2012, MNRAS, 423, 2037

Huggins, W. & Miller, W. A. 1864, Royal Society of London Philosophical Transactions Series I, 154, 437

Jørgensen, J. K. 2004, A&A, 424, 589

Kahn, F. D. 1974, A&A, 37, 149

Kelvin, W. T. 1871, Philosophical Magazine, 42, 362

Kennicutt, Jr., R. C. 1983, ApJ, 272, 54

Kennicutt, Jr., R. C. 1998, ApJ, 498, 541

Kennicutt, Jr., R. C. & Evans, II, N. J. 2012, ArXiv e-prints:1204.3552

Kerton, C. R., Martin, P. G., Johnstone, D., & Ballantyne, D. R. 2001, ApJ, 552, 601

Kessel-Deynet, O. & Burkert, A. 2003, MNRAS, 338, 545

Keto, E., Broderick, A. E., Lada, C. J., & Narayan, R. 2006, ApJ, 652, 1366

Kim, C.-G., Ostriker, E. C., & Kim, W.-T. 2013, ArXiv e-prints

Kroupa, P. 2002, Science, 295, 82

Kroupa, P. 2012, ArXiv e-prints

Krumholz, M. R., Klein, R. I., McKee, C. F., & Bolstad, J. 2007, ApJ, 667, 626

Krumholz, M. R., Klein, R. I., McKee, C. F., Offner, S. S. R., & Cunningham, A. J. 2009, Science, 323, 754

Kuiper, R., Klahr, H., Beuther, H., & Henning, T. 2012, A&A, 537, A122

Kuiper, R., Klahr, H., Dullemond, C., Kley, W., & Henning, T. 2010, A&A, 511, A81

Kuiper, R. & Klessen, R. S. 2013, A&A, 555, A7

Kurosawa, R., Harries, T. J., Bate, M. R., & Symington, N. H. 2004, MNRAS, 351, 1134

Lada, C. J. 1985, ARA&A, 23, 267

Lada, C. J. & Lada, E. A. 2003, ARA&A, 41, 57

Lagrois, D., Joncas, G., & Drissen, L. 2012, MNRAS, 420, 2280

Langer, W. D. & Penzias, A. A. 1990, ApJ, 357, 477

Larson, R. B. 1969, MNRAS, 145, 271

Lee, C. W., Myers, P. C., & Plume, R. 2004, Journal of Korean Astronomical Society, 37, 257

Lee, C. W., Myers, P. C., & Tafalla, M. 2001, ApJS, 136, 703

Lee, H.-T. & Chen, W. P. 2007, ApJ, 657, 884

Lee, H.-T., Chen, W. P., Zhang, Z.-W., & Hu, J.-Y. 2005, ApJ, 624, 808

Lee, J.-E. & Kim, J. 2009, ApJL, 699, L108

Lefloch, B. & Lazareff, B. 1994, A&A, 289, 559

Lefloch, B., Lazareff, B., & Castets, A. 1997, A&A, 324, 249

Leinhardt, Z. M. 2008, in Astronomical Society of the Pacific Conference Series, Vol. 398, Extreme Solar Systems, ed. D. Fischer, F. A. Rasio, S. E. Thorsett, & A. Wolszczan, 225

Li, J.-Y., Jiang, Z.-B., Liu, Y., & Wang, Y. 2013, Research in Astronomy and Astrophysics, 13, 921

Löhner, R. 1987, Computer Methods in Applied Mechanics and Engineering, 61, 323

Lord, S. D. & Young, J. S. 1990, ApJ, 356, 135

Lou, Y.-Q. & Gao, Y. 2011, MNRAS, 412, 1755

Lucy, L. B. 1999, A&A, 344, 282

Luhman, K. L. 2012, Annual Review of Astronomy and Astrophysics, 50, 65

Mac Low, M.-M. & Klessen, R. S. 2004, Reviews of Modern Physics, 76, 125

Mackey, J. & Lim, A. J. 2010, MNRAS, 403, 714

Mackey, J. & Lim, A. J. 2011, Bulletin de la Societe Royale des Sciences de Liege, 80, 391

Magnani, L., Blitz, L., & Wouterloot, J. G. A. 1988, ApJ, 326, 909

Mardones, D., Myers, P. C., Tafalla, M., et al. 1997, ApJ, 489, 719

Martins, F., Schaerer, D., & Hillier, D. J. 2005, A&A, 436, 1049

Mathis, J. S., Rumpl, W., & Nordsieck, K. H. 1977, ApJ, 217, 425

Matsumoto, T., Hanawa, T., & Nakamura, F. 1997, ApJ, 478, 569

Matzner, C. D. 2001, in Astronomical Society of the Pacific Conference Series, Vol. 243, From Darkness to Light: Origin and Evolution of Young Stellar Clusters, ed. T. Montmerle & P. André, 757

Maury, A. J., André, P., & Li, Z.-Y. 2009, A&A, 499, 175

McKee, C. F. & Ostriker, E. C. 2007, ARA&A, 45, 565

McKee, C. F. & Zweibel, E. G. 1992, ApJ, 399, 551

McLeod, A. D. & Whitworth, A. P. 2013, MNRAS, 431, 710

Mellema, G., Iliev, I. T., Alvarez, M. A., & Shapiro, P. R. 2006, 11, 374

Miao, J., White, G. J., Nelson, R., Thompson, M., & Morgan, L. 2006, MNRAS, 369, 143

Miao, J., White, G. J., Thompson, M. A., & Nelson, R. P. 2009, ApJ, 692, 382

Mie, G. 1908, Ann. Physik, 25

Mihalas, D. & Mihalas, B. W. 1984, Foundations of radiation hydrodynamics

Miura, R. E., Kohno, K., Tosaki, T., et al. 2012, ApJ, 761, 37

Mizuta, A., Kane, J. O., Pound, M. W., et al. 2006, ApJ, 647, 1151

Molinari, S., Swinyard, B., Bally, J., et al. 2010, A&A, 518, L100

Moore, T. J. T., Urquhart, J. S., Morgan, L. K., & Thompson, M. A. 2012, ArXiv e-prints

Morgan, L. K., Thompson, M. A., Urquhart, J. S., & White, G. J. 2008, A&A, 477, 557

Morgan, L. K., Thompson, M. A., Urquhart, J. S., White, G. J., & Miao, J. 2004, A&A, 426, 535

Morgan, L. K., Urquhart, J. S., & Thompson, M. A. 2009, MNRAS, 400, 1726

Myers, P. C., Linke, R. A., & Benson, P. J. 1983, ApJ, 264, 517

Nagy, Z., Van der Tak, F. F. S., Ossenkopf, V., et al. 2013, A&A, 550, A96

Narayanan, G., Heyer, M. H., Brunt, C., et al. 2008, ApJS, 177, 341

Ng, K. C. 1974, Chem. Phys., 61, 2680

Nussbaumer, H. & Storey, P. J. 1983, A&A, 126, 75

Nutter, D. & Ward-Thompson, D. 2007, MNRAS, 374, 1413

Offner, S. S. R., Klein, R. I., & McKee, C. F. 2008, ApJ, 686, 1174

Offner, S. S. R., Lee, E. J., Goodman, A. A., & Arce, H. 2011, ApJ, 743, 91

Ogura, K., Sugitani, K., & Pickles, A. 2002, AJ, 123, 2597

Ohlendorf, H., Preibisch, T., Gaczkowski, B., et al. 2012, A&A, 540, A81

Okada, Y., Güsten, R., Requena-Torres, M. A., et al. 2012, ArXiv e-prints

Onodera, S., Kuno, N., Tosaki, T., et al. 2010, ApJL, 722, L127

Oort, J. H. & Spitzer, Jr., L. 1955, ApJ, 121, 6

Ossenkopf, V. & Henning, T. 1994, A&A, 291, 943

Osterbrock, D. E. 1989, Astrophysics of gaseous nebulae and active galactic nuclei, ed. Osterbrock, D. E.

Owen, J. E., Clarke, C. J., & Ercolano, B. 2012a, MNRAS, 422, 1880

Owen, J. E., Ercolano, B., & Clarke, C. J. 2011, MNRAS, 412, 13

Owen, J. E., Ercolano, B., & Clarke, C. J. 2012b, ArXiv e-prints

Padoan, P. & Nordlund, Å. 2002, ApJ, 576, 870

Padoan, P., Nordlund, A., & Jones, B. J. T. 1997, MNRAS, 288, 145

Palla, F. & Stahler, S. W. 1991, ApJ, 375, 288

Palmeirim, P., André, P., Kirk, J., et al. 2013, A&A, 550, A38

Panagia, N. 1973, AJ, 78, 929

Paumard, T., Genzel, R., Martins, F., et al. 2006, ApJ, 643, 1011

Pequignot, D., Petitjean, P., & Boisson, C. 1991, A&A, 251, 680

Peraiah, A. 2001, An Introduction to Radiative Transfer: Methods and Applications in Astrophysics

Perna, R. & Lazzati, D. 2002, ApJ, 580, 261

Peters, T., Banerjee, R., & Klessen, R. S. 2008, Physica Scripta Volume T, 132, 014026

Pineda, J. E., Caselli, P., & Goodman, A. A. 2008, ApJ, 679, 481

Polychroni, D., Schisano, E., Elia, D., et al. 2013, ArXiv e-prints

Preibisch, T. & Zinnecker, H. 2007, in IAU Symposium, Vol. 237, IAU Symposium, ed. B. G. Elmegreen & J. Palous, 270–277

Price, D. J. 2008, Journal of Computational Physics, 227, 10040

Price, S. D., Egan, M. P., Carey, S. J., Mizuno, D. R., & Kuchar, T. A. 2001, AJ, 121, 2819

Rayleigh, L. 1900, Proceedings of the London mathematical society, 14, 170

Reach, W. T., Rho, J., Young, E., et al. 2004, ApJS, 154, 385

Redman, M. P., Keto, E., Rawlings, J. M. C., & Williams, D. A. 2004, MNRAS, 352, 1365

Renka, R. 1988a, 14, 149

Renka, R. 1988b, 14, 151

Rhie, C. M. & Chow, W. L. 1983, AIAA Journal, 21, 1525

Richling, S. & Yorke, H. W. 1998, A&A, 340, 508

Roberts, J. F., Rawlings, J. M. C., & Stace, H. A. 2010, MNRAS, 408, 2426

Roberts, W. W. 1969, ApJ, 158, 123

Roe, P. L. 1985, in Large-Scale Computations in Fluid Mechanics, ed. R. L. Lee, R. L. Sani, T. M. Shih, & P. M. Gresho, 163–193

Rogers, H. & Pittard, J. M. 2013, MNRAS, 431, 1337

Rohlfs, K. & Wilson, T. L. 1996, Tools of Radio Astronomy

Röllig, M., Abel, N. P., Bell, T., et al. 2007, A&A, 467, 187

Rubin, R. H. 1968, ApJ, 154, 391

Rundle, D., Harries, T. J., Acreman, D. M., & Bate, M. R. 2010, MNRAS, 407, 986

Salpeter, E. E. 1955, ApJ, 121, 161

Sandford, II, M. T., Whitaker, R. W., & Klein, R. I. 1982, ApJ, 260, 183

Santos-Lima, R., de Gouveia Dal Pino, E. M., & Lazarian, A. 2013, MNRAS, 429, 3371

Scannapieco, C., Tissera, P. B., White, S. D. M., & Springel, V. 2006, MNRAS, 371, 1125

Schmidt, M. 1959, ApJ, 129, 243

Schneps, M. H., Ho, P. T. P., & Barrett, A. H. 1980, ApJ, 240, 84

Schöier, F. L., van der Tak, F. F. S., van Dishoeck, E. F., & Black, J. H. 2005, A&A, 432, 369

Scoville, N. Z., Sargent, A. I., Sanders, D. B., et al. 1986, ApJ, 303, 416

Sedov, L. I. 1946, Journal of applied mathematics and mechanics, 10, 241

Shepard, D. 1968, in In ACM '68: Proceedings of the 1968 23rd ACM national conference, 517–524

Shu, F., Najita, J., Galli, D., Ostriker, E., & Lizano, S. 1993, in Protostars and Planets III, ed. E. H. Levy & J. I. Lunine, 3–45

Shu, F. H., Adams, F. C., & Lizano, S. 1987, ARA&A, 25, 23

Shull, J. M. & van Steenberg, M. 1982, ApJS, 48, 95

Smith, M. D. & Rosen, A. 2005, MNRAS, 357, 1370

Smith, N., Bally, J., & Brooks, K. J. 2004, AJ, 127, 2793

Smith, R. J., Shetty, R., Stutz, A. M., & Klessen, R. S. 2012, ApJ, 750, 64

Sod, G. A. 1978, J. Comput. Phys., 27, 1

Spitzer, L. 1978, Physical processes in the interstellar medium, ed. Spitzer, L.

Spitzer, L. 1998, Physical Processes in the Interstellar Medium, ed. Spitzer, L.

Stahler, S. W. & Yen, J. J. 2010, MNRAS, 407, 2434

Sugitani, K., Fukui, Y., & Ogura, K. 1991, ApJS, 77, 59

Sugitani, K. & Ogura, K. 1994, ApJS, 92, 163

Symington, N. H., Harries, T. J., & Kurosawa, R. 2005, MNRAS, 356, 1489

Tannirkulam, A., Monnier, J. D., Harries, T. J., et al. 2008, ApJ, 689, 513

Taylor, G. 1950a, Proc. R. Soc., 201, 192

Taylor, G. 1950b, Royal Society of London Proceedings Series A, 201, 159

Terquem, C., Papaloizou, J. C. B., & Nelson, R. P. 2000, in Astronomical Society of the Pacific Conference Series, Vol. 219, Disks, Planetesimals, and Planets, ed. G. Garzón, C. Eiroa, D. de Winter, & T. J. Mahoney, 19

Teyssier, R. 2002, A&A, 385, 337

Thompson, M. A., Urquhart, J. S., Moore, T. J. T., & Morgan, L. K. 2012, MNRAS, 421, 408

Thompson, M. A. & White, G. J. 2004, A&A, 419, 599

Thompson, M. A., White, G. J., Morgan, L. K., et al. 2004, A&A, 414, 1017

Tremblin, P., Audit, E., Minier, V., Schmidt, W., & Schneider, N. 2012a, A&A, 546, A33

Tremblin, P., Audit, E., Minier, V., & Schneider, N. 2012b, A&A, 538, A31

Tsamis, Y. G., Rawlings, J. M. C., Yates, J. A., & Viti, S. 2008, MNRAS, 388, 898

Tüllmann, R., Rosa, M. R., Elwert, T., et al. 2003, A&A, 412, 69

Turner, N. J. & Stone, J. M. 2001, ApJS, 135, 95

Urquhart, J. S., Morgan, L. K., & Thompson, M. A. 2009, A&A, 497, 789

Urquhart, J. S., Thompson, M. A., Morgan, L. K., & White, G. J. 2004, A&A, 428, 723

Urquhart, J. S., Thompson, M. A., Morgan, L. K., & White, G. J. 2006, A&A, 450, 625

Vacca, W. D., Garmany, C. D., & Shull, J. M. 1996, ApJ, 460, 914

Verner, D. A. & Ferland, G. J. 1996, ApJS, 103, 467

Verner, D. A., Ferland, G. J., Korista, K. T., & Yakovlev, D. G. 1996, ApJ, 465, 487

Vidali, G., Roser, J., Manicó, G., et al. 2005, Journal of Physics Conference Series, 6, 36

Vink, J. S., Harries, T. J., & Drew, J. E. 2005, A&A, 430, 213

Vishniac, E. T. 1983, ApJ, 274, 152

Von Helmholtz, H. 1868, Monthly Reports of the Royal Prussian Academy of Philosophy in Berlin, 23, 215

von Neumann, J. & Richtmyer, R. D. 1950, Journal of Applied Physics, 21, 232

Walch, S. K., Whitworth, A. P., Bisbas, T., Wünsch, R., & Hubber, D. 2012, MNRAS, 427, 625

Wang, W., Liu, X.-W., Zhang, Y., & Barlow, M. J. 2004, A&A, 427, 873

Watson, C., Povich, M. S., Churchwell, E. B., et al. 2008, ApJ, 681, 1341

Weaver, R., McCray, R., Castor, J., Shapiro, P., & Moore, R. 1977, ApJ, 218, 377

Williams, J. P. & Cieza, L. A. 2011, ARA&A, 49, 67

Williams, R. J. R. 2002, MNRAS, 331, 693

Woltjer, L. 1972, ARA&A, 10, 129

Wood, K., Mathis, J. S., & Ercolano, B. 2004, MNRAS, 348, 1337

Yorke, H. W. & Sonnhalter, C. 2002, ApJ, 569, 846

Yusef-Zadeh, F., Morris, M., & White, R. L. 1984, ApJ, 278, 186

Zavagno, A., Deharveng, L., Comerón, F., et al. 2006, A&A, 446, 171

Zel'Dovich, Y. B. & Raizer, Y. P. 1967, Physics of shock waves and high-temperature hydrodynamic phenomena, ed. Zel'Dovich, Y. B. & Raizer, Y. P.

Zinnecker, H. & Yorke, H. W. 2007, ARA&A, 45, 481

10
List Of Publications

First author publications

1. **Radiation hydrodynamics of triggered star formation: the effect of the diffuse radiation field**, Thomas J. Haworth & Tim J. Harries, 2011, MNRAS,420, 562

2. **Testing diagnostics of triggered star formation**, Thomas J. Haworth, Tim J. Harries & David M. Acreman, 2012, MNRAS, 426, 203

3. **Assessing molecular line diagnostics of triggered star formation using synthetic observations**, Thomas J. Haworth, Tim J. Harries, David M. Acreman & David A. Rundle, 2013, MNRAS, 431, 3470

Conference proceedings

1. **Testing models of triggered star formation: theory and observation**, Thomas J. Haworth, Tim J. Harries & David M. Acreman, 2013, The Labyrinth of Star Formation

2. **Radiation hydrodynamics simulations of massive star formation using Monte Carlo radiation transfer**, Tim J. Harries, Thomas J. Haworth & David M. Acreman, 2013, The Labyrinth of Star Formation

A

Unit Directory

A.1 Unit Types

To avoid conflicts between quantities with the same physical units but different calculation units a selection of unit types have been established to ensure that input unit conversion occur properly. These different unit types are given in Table tbl:unittypes

A.2 Units

Within each unit type are a list of available units, thes are added to the parameters file after a quantity which has units. For example, to specify that the calculation end time has been given in seconds the user would include

```
tend 1.d16 s
```

Table A.1: Table of unit types.

Unit type	Default
distance	1×10^{10} cm
wavelength	1 Å
dust	1 μm
angle	radians
mass	grams
time	seconds
temperature	Kelvin
luminosity	Ergs per second

in the paramters file. The different units available for each unit type are given below. Note that these are case sensitive.

- Distances
  1. Default value: 10^{10} centimetres
  2. cm - 10^{10} centimetres
  3. m - 10^{10} metres
  4. au - Astronomical units
  5. pc - parsecs
  6. rSol - solar radii
- Wavelengths
  1. Default value: Angstroms
  2. A - Angstroms
  3. nm - Nanometers
  4. um - Microns
  5. mm - Millimetres
- Dust Grain Sizes
  1. Default value: microns
  2. A - Angstroms
  3. nm - Nanometers
  4. um - Microns
  5. mm - Millimetres
- Angles
  1. Default value: radians
  2. rad - radians
  3. deg - degrees
  4. arcmin - arcminutes
  5. arcsec - arcseconds
- Masses
  1. Default value: grams
  2. g - grams
  3. mSol - solar masses

4. kg - kilograms

- Time
  1. Default: seconds
  2. s - seconds
  3. yr - years
  4. kyr - kiloyears
  5. Myr - megayears
- Temperature
  1. Default: Kelvin
  2. K - Kelvin
- Luminosity
  1. Default: Ergs per second
  2. ergsec - ergs per second
  3. lSol - solar luminosities
- Velocities
  1. Default: cm s^{-1}
  2. cms - cm s^{-1}
  3. ms - m s^{-1}
  4. kms - km s^{-1}
  5. c - fraction of light speed
- Densities